TEM Investigations of Deformation Mechanisms in Nanocrystalline Metals and Multilayered Composites

Ankush Kashiwar

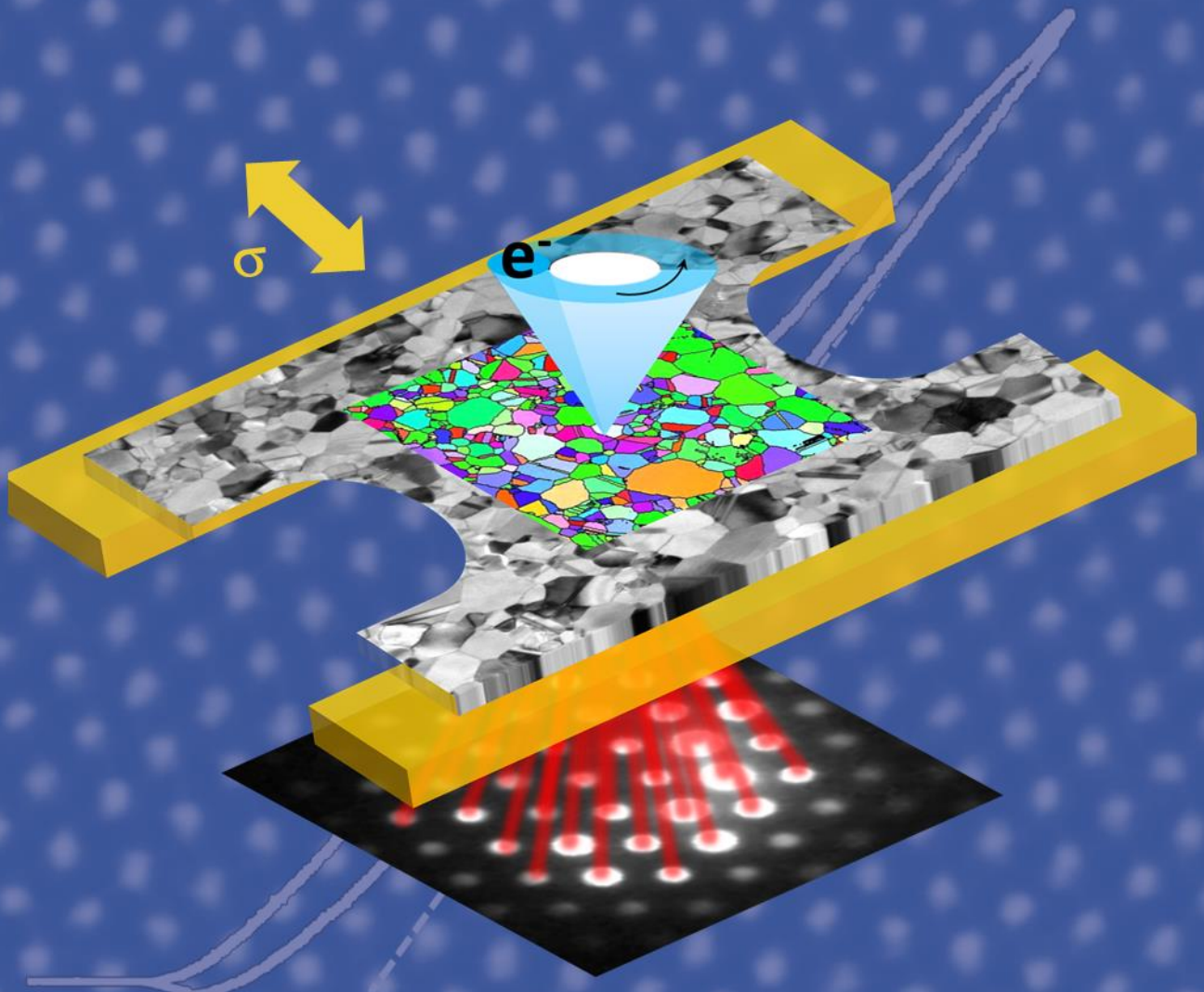

stress [MPa]

strain [%]

Supervisors:
Prof. Dr. rer. nat. Christian Kübel
Prof. Dr.-Ing. Horst Hahn

TEM Investigations of Deformation Mechanisms in Nanocrystalline Metals and Multilayered Composites

TECHNISCHE UNIVERSITÄT DARMSTADT

Dissertation Approved by

the Department of Materials- and Geosciences,

Technical University of Darmstadt

in Fulfillment of the Requirements of the Degree of

Doctor of Engineering (Dr.-Ing.)

by

Ankush Kashiwar

M.E. in Materials Engineering

Referee: Prof. Dr. rer. nat. Christian Kübel

Co-referee: Prof. Dr.-Ing. Karsten Durst

Date of Submission: 17.11.2021

Date of Examination: 14.02.2022

Darmstadt 2022

Abstract

In the last few decades, nanostructuring has driven significant attention towards the development of novel metallic materials with advanced mechanical properties. Nanocrystalline (nc) metals are a class of nanostructured materials with grain sizes smaller than about 100 nm. These exhibit outstanding mechanical strength and fatigue properties compared to their coarse-grained (cg) counterparts. These are promising candidates for application as structural or functional materials. Nc metals in the form of thin films are employed as hard coatings on bulk components, structural components, and conductive layers in various micro-/nanoscale devices. These structural components and devices are often subjected to cyclic stresses or fatigue loading. Under these cyclic stresses, nc metals tend to exhibit the Bauschinger effect (BE). The strength loss during the BE is of great importance concerning the strength-ductility trade-off in nc metals. Furthermore, contact surfaces of the engineering components in service often undergo relative motion and are subject to both friction and wear. These extreme loading conditions demand nc metals with tailored interfacial characteristics for improved tribological performance. Aiming at ensuring high reliability and mechanical robustness for optimum performance of these components, there has been a strong motivation for understanding the mechanical properties and governing deformation mechanisms in nc metallic materials. This thesis aimed at in-depth investigation of microstructures at micro-/nanoscales using state-of-the-art *in situ* and *ex situ* transmission electron microscopy (TEM) to develop a closer link between the deformation structure and underlying deformation mechanisms in some nc metallic materials.

The thesis has primarily focused on the *in situ* TEM nanomechanics of the BE and rotational deformation of grains in nc palladium thin films. A sputtered thin film of nc Pd was deformed inside TEM by cyclic loading-unloading experiments and the evolving microstructure was studied in real-time under different TEM imaging modes. The stress-strain response of the film exhibited a characteristic non-linear unloading behavior confirming the BE in the film. The corresponding bright-field TEM imaging revealed evidence of partially reversible dislocation activity. Towards a quantitative understanding of the deformation structure in real-time, *in situ* nanomechanical testing was coupled with precession-assisted automated crystal orientation mapping in scanning TEM (ACOM-STEM). Global ACOM-STEM analysis offered crystal orientation of a large number of grains at different states of deformation and confirmed partially reversible rotations of nanosized grains fitting to the observed BE during loading and unloading. Analysis of intragranular rotations showed substantial changes in the sub-structure within most of these grains indicating a dominant role of dislocation-based processes in driving these rotations. Globally, an unusually random evolution of texture was seen that demonstrated the influence of deformation heterogeneity and grain interactions on the resulting texture characteristics in nc metals. In the quest of understanding the grain interactions, local investigations based on annular dark-field STEM imaging during loading-unloading showed reversible changes in the contrast of grains with sets of adjoining grains exhibiting a unique cooperative rotation. Local analysis of the density of geometrically necessary dislocations (GNDs) showed the formation of dislocation pile-up at grain boundaries due to the generation of back-stresses during unloading. Critical observations of the evolution of GND density offered greater insights into the mechanism of cooperative grain rotations and these rotations were related to grain structure and grain boundary characteristics.

In addition to understanding the influence of grain structure and grain boundaries, the thesis has further investigated the role of heterointerfaces in sputtered Au-Cu and Cu-Cr nanocrystalline multilayered composites (NMCs) deformed under cyclic sliding contact. The microstructural evolution in the NMCs was investigated at different deformation states by classical TEM imaging, ACOM-STEM as well as energy-filtered TEM (EFTEM). Au-Cu NMC with an initial high density of twin boundaries deformed by stress-driven detwinning with a concurrent change in grain structure in both Au and Cu. The formation of a vortex structure was observed due to plastic flow instabilities at Au-Cu interfaces that led to codeformation and mechanical intermixing. Cu-Cr NMC showed a preferential grain growth in Cu layers whereas no noticeable change in the grain sizes was seen in Cr layers. The phase maps revealed sharp interfaces between Cu and Cr layers indicating no intermixing between the immiscible phases. EFTEM results exposed the cracking processes in Cr layers with a concurrent migration of Cu in the cracks. Overall, the thesis has attempted to analyze the competing deformation processes and relate these with the microstructural heterogeneity in terms of grain structure and GB and interfacial characteristics in nc metallic materials.

Acknowledgements

I would like to express my sincere acknowledgments to my doctoral thesis supervisors Prof. Christian Kübel and Prof. Horst Hahn. I am highly grateful to them for their supervision, constant motivation, and support through the course of scientific research that was conducted during my Ph.D. I am indebted to them for the knowledge, skills, and expertise in electron microscopy and materials science that I gained under their guidance.

The Institute of Nanotechnology (INT) at Karlsruhe Institute of Technology (KIT) and the Department of Materials- and Geosciences at the Technical University of Darmstadt, Germany are acknowledged for providing access to all the necessary facilities and resources required during the Ph.D. research. Karlsruhe Nano Micro Facility (KNMF) is acknowledged for providing access to the laboratory for electron microscopy and spectroscopy at KIT. I acknowledge the German Academic Exchange Service (DAAD) for offering me a full-time doctoral scholarship under the 'Research Grants: Doctoral Programmes in Germany 2015/16'. German Society for Electron Microscopy (DGE), Wilhelm and Else Heraeus Foundation, and KIT are acknowledged for offering travel grants towards several international conferences and workshops that I attended during my Ph.D.

I extend my gratitude to Prof. Ruth Schwaiger and Dr. Zhaoping Luo for their collaboration on nanocrystalline multilayered composites that significantly expanded the scientific horizons of this thesis work. I would like to thank Dr. Aaron Kobler for his support during the initial stages of my research endeavors. The data processing and analysis routines developed by him were immensely vital towards the completion of this thesis work. I thank Dr. Mohammad Hammad Fawey and Dr. Sabine Schlabach for introducing and training me in the specimen preparation strategies for *ex situ* and *in situ* studies by focused ion beam. I am thankful to Dr. Maryam Mohri and Dr. Sree Harsha Nandam for introducing me to the thin film deposition by magnetron sputtering. I thank Dr. Xiaoke Mu and Dr. Di Wang for training me on the TEM and introducing me to precession-based ACOM-STEM and EFTEM. Further, I would like to thank all the members of the electron microscopy and spectroscopy group at INT, KIT for their friendly cooperation and support through the course of my Ph.D., and the invaluable time that I spent with them to develop my stature as a professional researcher.

I am obliged to Dr. Edgar Rauch and Prof. Muriel Veron for their extensive support related to critical aspects of ASTAR orientation and phase mapping through the course of my Ph.D. I thank Dr. Edgar Rauch for his valuable feedback on chapter 3 of this thesis. I thank Dr. Ralf Hielscher for his support related to MTEX-based analysis. I acknowledge Dr. Julia Ivanisenko and Dr. Frédéric Mompiou for several scientific discussions related to deformation mechanisms in nc and UFG metals that added to a deeper understanding of this subject. I thank Dr. Sanjit Bhowmick, Dr. Douglas Stauffer, and Dr. Rhys Jones for their scientific and technical support on PI95 TEM PicoIndenter and various challenging aspects related to *in situ* nanomechanical testing. I thank Dr. Jing Lu for her technical support related to precession electron diffraction using Topspin.

I would like to extend my heartfelt gratitude towards my current research supervisors Prof. Hosni Idrissi, Prof. Dominique Schryvers, and Prof. Aude Simar for supporting my research at Electron Microscopy for Materials Science (EMAT), University of Antwerp, and Institute of Mechanics, Materials and Civil Engineering (IMMC), Université catholique de Louvain in Belgium. Their kind support and motivation were extremely vital during the final stages of the preparation of this thesis. I thank Dr. Dorothee-Vinga Szabó, Dr. Sabine Schlabach, Dr. Andrey Mazilkin, Dr. Andrey Orekhov, Dr. Armand Béché, Jort Van Den Kieboom, and Saleh Gholam for editing and correcting different sections of this thesis. I extend my friendly gratitude to all the colleagues from EMAT and IMMC for their cooperation and support. I am especially indebted to my master's thesis supervisor Prof. Dipankar Banerjee and all the professors and teachers from my alma mater for their guidance in the past. I am grateful to His Grace Advaita Gaura Hari Prabhuji, Doyal Govinda Prabhuji, Tattvavati Mataji, Vimal Prasad Prabhuji, and Purushottam Tirtha Prabhuji for always directing me to the path of righteousness. I will never forget the association and the amazing times I spent with some of my friends in Belgium: Jort, Souvik, Ferran, Hadi, Saleh, Leon, and Saffiye. At last, I dedicate this thesis to my family members who have been a constant source of inspiration and who always stood by my side during difficult times. I will never be able to recompense for what they have given up for my interests. I would like to offer my humble obeisances to my mother and my motherland, Bharatvarsha.

Table of Contents

List of Figures

List of Tables

List of Abbreviations

ACOM-STEM	Automated crystal orientation mapping in STEM
ADF	Annular dark-field
BE	Bauschinger effect
BFTEM	Bright-field TEM
BSE	Back-scattered electron
BCC	Body-centered cubic
CCD	Charge-coupled device
Cg	Coarse-grained
CBED	Convergent beam electron diffraction
CGR	Cooperative grain rotation
CTB	Coherent twin boundary
DFTEM	Dark-field TEM
DP	Diffraction pattern
EDS	Energy dispersive spectroscopy
EELS	Electron energy loss spectroscopy
EFTEM-SI	Energy-filtered transmission electron microscopy spectrum imaging
EM	Electron microscopy
ETD	Everhart-Thornley detector
FCC	Face-centered cubic
FIB	Focused ion beam
GB	Grain boundary
GBS	Grain boundary sliding
GIS	Gas injection system
GND	Geometrically necessary dislocation
HAADF	High angle annular dark-field
HR-STEM	High resolution scanning transmission electron microscopy
HRTEM	High-resolution transmission electron microscopy
IF	Interstitial-free
IPF	Inverse pole figure
MEMS	Microelectromechanical systems
MC	Minicondenser
Nc	Nanocrystalline
NEMS	Nanoelectromechanical systems
NMC	Nanocrystalline multilayered composite
PED	Precession electron diffraction
PTP	Push-to-pull
PF	Pole figure
SAD	Selected electron diffraction
SAED	Selected area electron diffraction
SE	Secondary electron
SEM	Scanning electron microscopy
SF	Stacking fault
SFE	Stacking fault energy
SPED	Scanning precession electron diffraction
SSD	Statistically stored dislocation
STEM	Scanning transmission electron microscopy
TB	Twin boundary
TEM	Transmission electron microscopy
UFG	Ultra-fine grained
µP-STEM	Microprobe STEM

1 Introduction

Metallurgy and metalworking have played a pivotal role in the evolution of human civilization since the copper, bronze, and iron ages. The first copper processing based on smelting dates back to 5000 BC. Copper and bronze were used for tools, arts, aesthetics, as means of payment, and household utilities. In the 4th millennium BC, the metalworkers had already mastered the smithing of meteoric iron, an alloy harder and more brittle compared to copper [1]. In the quest for stronger and more durable materials, early blacksmiths invented steel in 1300 BC. Craftsmen in the 3rd century BC started smelting wrought iron with charcoal to produce 'wootz' steel, which was followed by the emergence of tough and highly resilient Damascus steel [2]. The advent of steam engines in the 18th century enabled the operation of blast furnaces for the mass production of iron. Iron and steel-making boosted the industrial revolution. Today, steel contributes to all sectors of the global economy. Modern steel-making technologies are aimed at manufacturing products with reduced weight, costs, energy consumption, and CO_2 emissions. For light-weight materials, the last two centuries have also seen the emergence of aluminum and titanium-based alloys. These are key materials in the aerospace and defense sectors due to their high strength-to-weight ratio. The technology of designing new metallic and composite materials with superior properties continues to flourish (Figure 1-1). Since the end of the 20th century, metallic materials are used in chips for computers and various nanoscale devices, e.g. in micro or nanoelectromechanical systems (MEMS/NEMS), sensors, and actuators. Metals and alloys influence global trends including economy, public health, agriculture, energy efficiency, and access, environment, and sustainability.

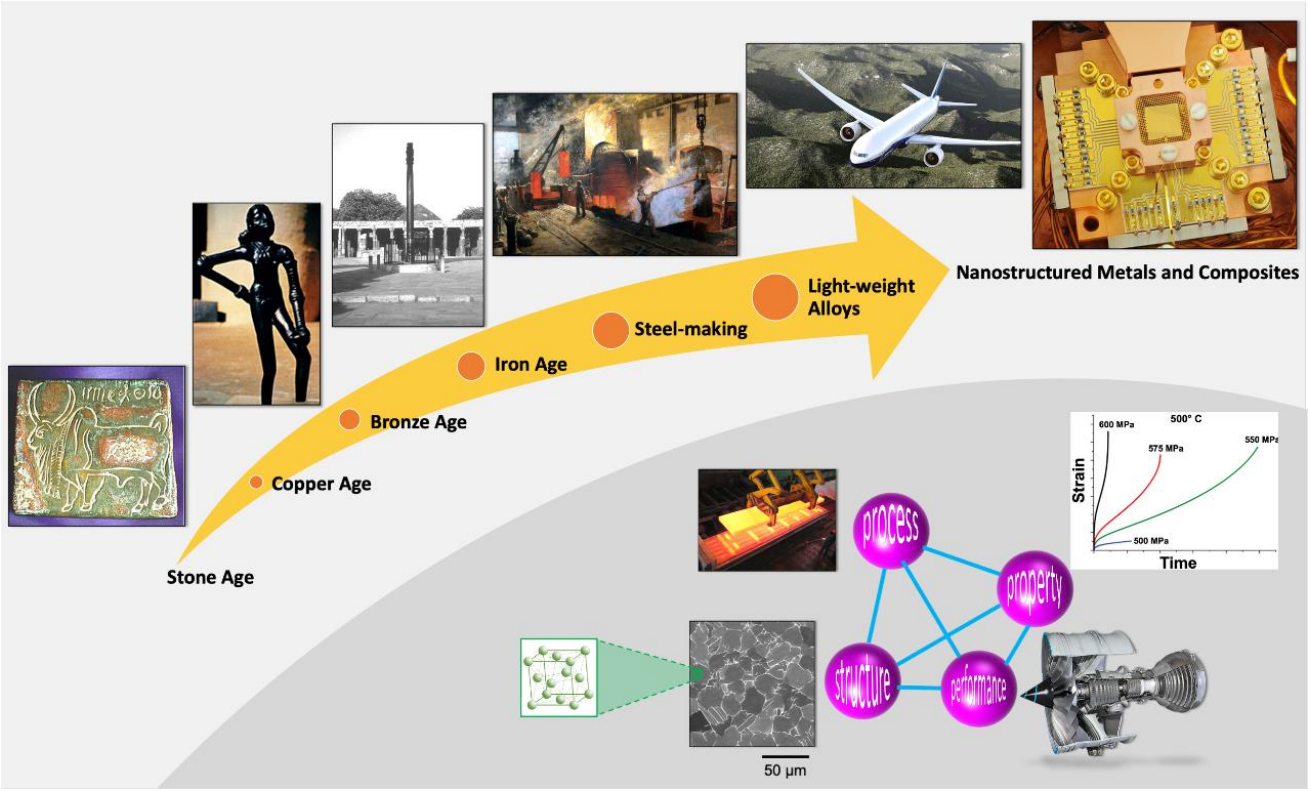

Figure 1-1 **Upper:** Depiction of the evolution of metal-making technology over the ages. From left to right: An inscribed copper plate (c. 2600-2000 BC) from Indus valley civilization [3]. A bronze statue (c. 2500 BC) of a dancing girl discovered at Mohenjo-daro, presently in Pakistan [4]. 1600 years old corrosion-resistant iron pillar in Delhi, India [5]. An oil painting by E.F. Skinner showing the mass production of steel (c. 1916) by Bessemer process at Penistone Steel Works, South Yorkshire, England [6]. A commercial Boeing 777 airplane employing advanced titanium and aluminum-based alloys and composites [7]. A gold chip surrounded by a copper enclosure and gold mesh used for quantum computing [8]. **Lower:** Materials science tetrahedron illustrating the relationship between process, structure, property, and performance with an example of a commercial creep resistant titanium alloy for application in fan-blades of aero-engines (Image courtesy: [9–12]).

In the pursuit of designing novel metallic materials, the last few decades have witnessed a strong drive towards the nanostructuring of metals and alloys. Nanocrystalline (nc) metals are a class of metallic materials with structural features with dimensions in at least one direction of less than 100 nm [13–20]. Nc metals in the form of thin films are often employed as hard coatings on bulk components [21]. These are used as structural components in MEMS/NEMS or as conductive layers in microelectronic devices [22,23]. Nc metals also received significant attention as bulk materials in the past four decades due to their appealing mechanical properties [24–28]. They are well-known for their ultra-high yield [29–31] and tensile [32] strengths, fracture strength and toughness [30,33–35], enhanced fatigue properties [33,36–38], and superior wear resistance [39,40]. However, they typically also exhibit very limited ductility [35]. Figure 1-2 (a) shows the strength-elongation trade-off comparison of nc metals with classical ferrous and non-ferrous alloys. Nc metals exhibit far superior strength compared to Al and Cu alloys as well as IF and dual-phase steels. Their strength almost surpasses state-of-the-art martensitic and TWIP steels and competes with that of metallic glasses. However, due to the limited ductility, the elongation to failure for nc metals is considerably less compared to most of these alloys of commercial interest. Despite the tremendous potential, this lack of ductility in nc metals limits their practical utility [15,19]. For their practical utilization in engineering applications, efforts have been made to improve the ductility by a variety of nanostructuring approaches [19,22,30,35,41–45]. These materials could serve as promising components in upcoming applications like flexible displays, wearable electronics, electronic skins, or flexible solar cells [16,17]. To ensure the high reliability and longevity of these components and devices in service, a detailed understanding of the deformation characteristics in these materials is essential. This has motivated strong research to investigate the mechanical properties and the underlying deformation mechanisms in this class of materials.

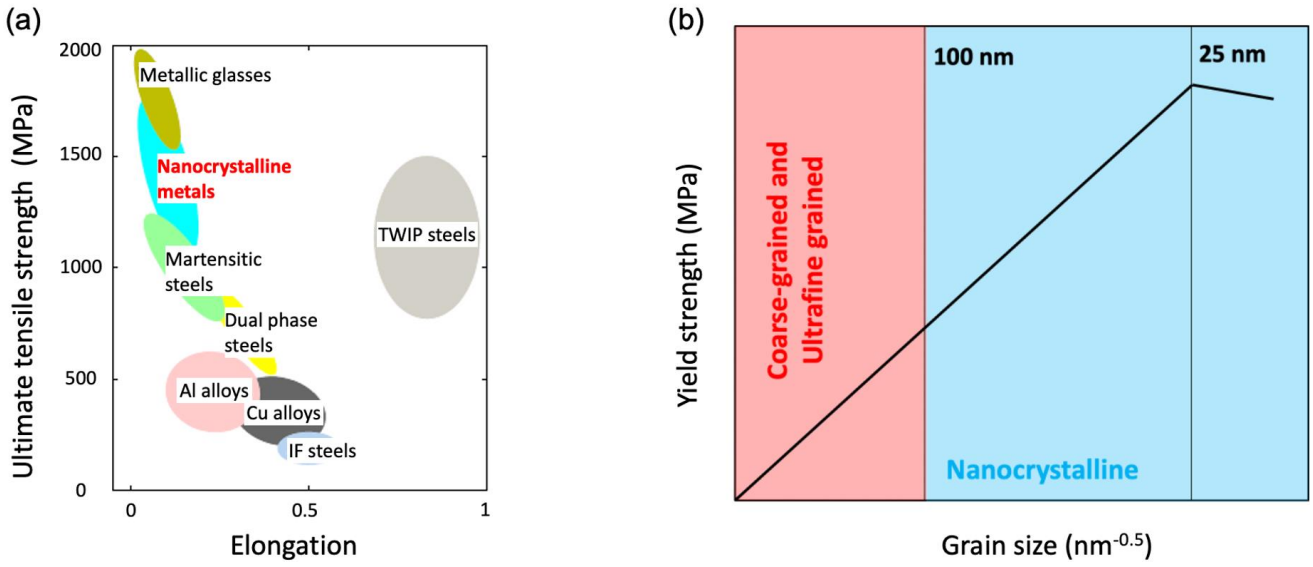

Figure 1-2 (a) Plot comparing the tensile strength versus elongation to failure of nanocrystalline metals with other materials (modified from [46]), (b) schematic of a Hall-Petch plot showing the variation of yield strength versus inverse square root of grain sizes in coarse-grain and nanocrystalline regime (concept adopted from [27,47,48]).

The macroscopic behavior and properties of materials are controlled by their structure at the meso- and nanoscale down to the atomic scale (Figure 1-1). Reducing the grain size to the nano-scale regime as well as increasing the fraction of defects has been proven to considerably influence the properties of materials. For instance, as seen in the classical Hall-Petch plot (Figure 1-2 (b)), the yield strength of the material increases as the grain size is reduced down to 100 nm or below. The increased fraction of grain boundaries (GBs) in nc metals offers greater resistance to the motion of dislocations responsible for plasticity, thereby leading to their enhanced strength. Thus, the microstructural characteristics become critical in controlling the plastic deformation mechanisms and the resulting mechanical behavior of nc metals.

To shape the final product and to modify the microstructure and thus the mechanical properties, metallic materials are subjected to plastic deformation processes. The deformation processing routes include forging, rolling, extrusion, sheet forming, wire drawing, pipe forming, etc. These operations involve complex and often repetitive mechanical and/or thermal treatments of the materials. The stress-strain relations are strongly influenced by the deformation history of the material. The stress-strain curve of a metallic material generally exhibits an anisotropic flow behavior. This anisotropy becomes important as the direction of loading is reversed during deformation e.g. during straining and compression. Due to the anisotropy of plastic deformation, the flow stress during the reverse loading is found to be lower than that during the loading in the forward direction [49]. This phenomenon of exhibiting a directionality in the strain hardening is known as the Bauschinger effect (BE) [50].

Some of the important factors that need to be taken into account for the plastic working of metals include strain-induced anisotropy (the deformation texture), latent work hardening, the evolution of defects, and the BE [51]. Looking in particular at the BE, the strength of a component may be reduced considerably if the operational stresses are in the reverse direction compared to the working stress during the production of the component for materials exhibiting a strong BE. This strength loss during reverse deformation is of practical significance, especially in the manufacturing processes that utilize cold forming methods [52]. The BE is critical for several industrial applications and enormous efforts have been made to develop suitable approaches or models for an in-depth understanding of the BE and various factors influencing it [53]. Apart from the relevance of the BE for the plastic working of bulk components, it is also important for the mechanical properties of nc thin metal films, e.g. during repetitive loading, which affects the performance and lifetime of coatings and MEMS/NEMS devices. Therefore, an in-depth analysis of the BE and its origin in nc thin metal films is essential for refining the current theories of plasticity to design materials with superior mechanical properties [49].

Apart from the mechanical properties in the bulk, these become critical at the surfaces since the surfaces and sub-surfaces of the components are exposed to different and often extreme loading conditions compared to the bulk. The contact surfaces in devices and engineering components under relative motion are subject to both friction and wear. The behavior of these components under frictional loading is dependent on their mechanical and tribochemical properties as well as the microstructural characteristics of their surfaces. Designing metals and alloys with improved tribological performance, while retaining other properties like electrical conductivity becomes essential for device applications. For metallic materials, surface nanostructuring has been proven to enhance their friction and wear properties. The wear performance of nc metals is far better than cg metals. The ultralow wear rates in nc metals could be achieved by improving their ability to resist sub-surface plastic deformation, nucleation of defects, and ultimately the evolution of microstructures in response to cyclic sliding contact [54]. A promising approach in this direction is designing multicomponent or multilayered composite thin films. The incorporation of metal-metal interfaces offers the possibility to design materials with tailored mechanical and tribological properties [55]. Understanding the tribochemical interactions and the underlying deformation characteristics at metal-metal interfaces could benefit the design and manufacturing of robust multicomponent or multilayered nanoscale devices.

This thesis is dedicated to the experimental investigation of plastic deformation mechanisms in nanocrystalline (nc) metals and nc multilayered composite (NMC) thin films subjected to small-scale deformation. To understand these mechanisms, the thesis primarily focuses on the evolution of deformation structures at nanoscales using *in situ* and *ex situ* transmission electron microscopy (TEM) techniques. From the TEM-based microstructural analysis, the thesis has attempted to explore plasticity mechanisms associated with the BE in nc metal thin films. Furthermore, the thesis aims to understand the elementary deformation mechanisms at the metal-metal interfaces under cyclic tribological loading that lead to the evolution of unique microstructures in NMCs. With the state-of-the-art capabilities of the *in situ* and *ex situ* nanomechanical testing and advanced electron microscopy tools, the thesis has attempted to analyze the interplay of various deformation processes and build a closer link of these processes with the nanostructures in materials. In a broader context, the thesis aims at developing an in-depth understanding of the structure-property relationship at nanoscales for designing nanocrystalline materials with superior mechanical characteristics.

1.1 Nanocrystalline versus Coarse-grained Metals

Plastic deformation of metallic materials leads to a permanent change in their shape or dimensions in response to an externally applied load. Plastic strain introduced in a material depends on the deformation path and the defined stress state. The deformation behavior of materials is typically described based on the stress-strain relationship. Understanding the deformation characteristics is critical for designing deformation processing routes as well as for assessing the mechanical properties of materials for engineering purposes.

The deformation characteristics of nc metals are significantly different from their coarse-grained (cg) counterparts. As a comparison, Figure 1-3 shows schematically the engineering stress-strain responses of an nc and a cg metal. A typical engineering stress-strain curve of a cg polycrystalline metal or alloy is characterized by an elastic regime, followed by a transition to the plastic regime. Microplasticity corresponds to all inelastic deformation processes that occur before the macroscopic yielding and is often not detected by the conventional macroscopic mechanical testing methods [56,57]. This phenomenon is attributed to plastic yielding, which is not initiated simultaneously in all the grains [58]. The yield strength (σ_y) characterizes the onset of plastic deformation. In general, nc metals exhibit significantly greater yield strength compared to their cg counterparts. However, in nc metals, deviations from the macroscopic linear elastic behavior are observed at low stresses [56,58]. It is also noticeable that the inelastic deformation in nc metals occurs over a wider range of strain before the macroscopic yielding. Thus, nc metals exhibit an extended microplastic regime compared to their cg counterparts [58–64].

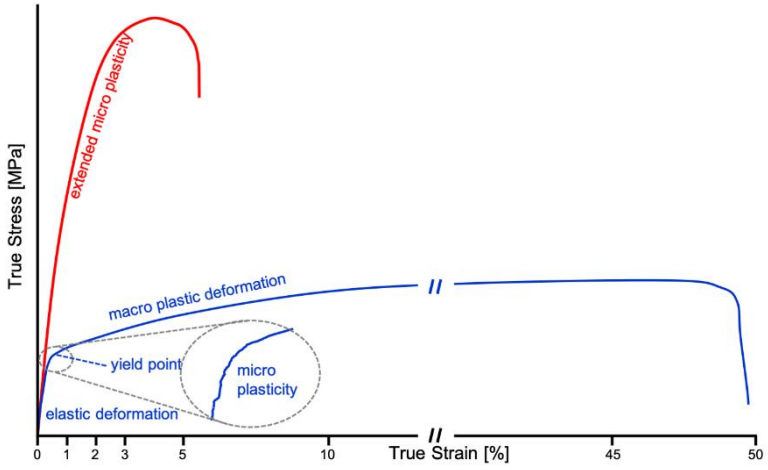

Figure 1-3 Schematic of the stress-strain responses of nc (red curve) and cg (blue curve) metallic materials (concept adopted from [56,58,65]).

The ductility of a metal is the ability to deform plastically without failure via fracture under tensile stress [66]. It is controlled by the competing plastic deformation and fracture processes as well as the resistance to plastic flow localization [43]. Nc metals tend to show limited ductility compared to their cg counterparts. The reduced ductility of nc metals is associated with their limited strain hardening capacity that restricts the uniform elongation and is potentially responsible for their plastic instability [66–68]. The lower strain hardening is a direct consequence of the limited dislocation storage capacity due to very small grain sizes [66].

1.2 Classical Deformation Processes in Metallic Materials

The plastic flow behavior of metals is controlled by the microscopic deformation processes. Deformation by slip is a common mode of plastic deformation in metals. Deformation slip in metal single crystal involves irreversible shearing of parts of a crystal over one another along specific crystallographic planes (slip

planes) and along certain directions (slip directions) [69]. The observed shear strength required for the slip process in a metal single crystal is lower than the ideal or theoretical shear strength due to the presence of defects. Dislocations are line defects responsible for slip processes that lead to plastic deformation in metals.

Polycrystalline metals and alloys consist of an aggregate of differently oriented grains, secondary phases, or precipitates which are separated by extended defects like grain boundaries (GBs) and interfaces (Figure 1-4). In addition, there are defects present within the grains which include dislocations, stacking faults, sub-grain boundaries, twin boundaries (TBs), etc. These defects significantly influence the plastic deformation behavior of the individual grains and the mechanical properties of polycrystalline aggregates due to their interactions with moving dislocations. As metals deform, the dislocations tend to multiply thereby increasing their density. In absence of any sources generating dislocations, a well-known mechanism by which dislocations multiply is by the operation of Frank-Read sources. It involves generation of new dislocations from the existing ones. The Frank-Read source operates by bulging of dislocation in response to stress-field leading to its expansion in the form of a loop to produce a new dislocation. The multiplication of dislocations and their interaction with existing dislocations in the lattice as well as other defects eventually lead to strain hardening in metallic materials.

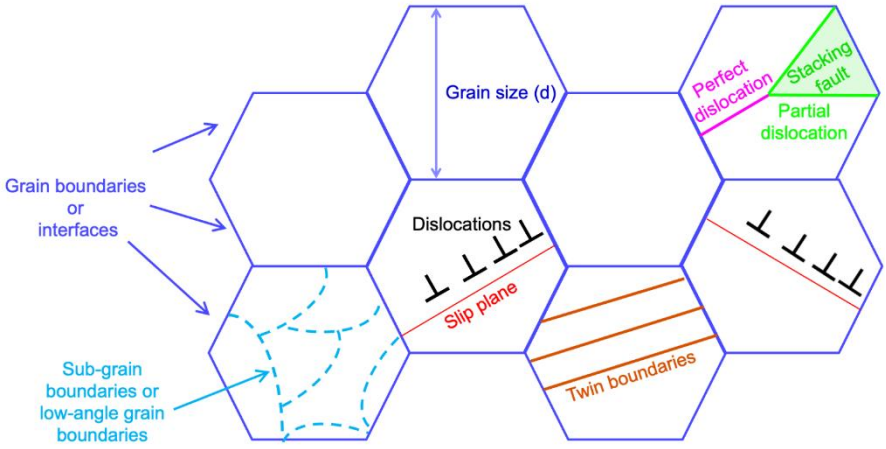

Figure 1-4 Schematic showing grain boundaries, interfaces, sub-grain boundaries, twin boundaries, perfect and partial dislocations, and stacking fault in polycrystalline metallic material with average grain size d. The dislocations are shown to glide along the slip plane and are hindered by GBs to form a pile-up.

Grain Boundary Strengthening

GBs and interfaces play a key role in the strengthening of metallic materials by acting as barriers for dislocation motion. This is shown schematically by the formation of dislocation pile-up at the GBs in Figure 1-4. The spacing or density of the GBs or interfaces in the materials directly affects the hardness and the yield strength. For polycrystalline metals with conventional grain sizes (several micrometers), the yield stress (σ) is related to the grain size (d) by the Hall-Petch relationship as [48,70]:

$$\sigma = \sigma_o + kd^{-1/2} \qquad 1\text{-}1$$

where σ_o is the lattice friction stress required to move individual dislocations and k is a constant. According to the Hall-Petch relation (Eq. 1-1), the yield strength varies as the inverse square root of the grain size. A reduction in grain size leads to an increased fraction of GBs that provides higher resistance to the motion of dislocations. Therefore, the yield strength increases as the grain sizes are reduced. The GB strengthening is also the basis for enhanced strength in nc metals. Figure 1-2 (b) shows a schematic plot representing the variation of yield strength with the inverse-square root of grain sizes. As the grain size is

reduced from the cg to the nc regime, the yield strength increases almost continually up to at least 25 nm. This shows that the dislocation-based hardening mechanisms are actively contributing to the strengthening in the nc regime (below 100 nm). However, below a certain critical grain size (typically about 25 nm) nc metals tend to soften and follow an inverse Hall-Petch relation [27,71], indicating the activation of alternative mechanisms governing the deformation processes. As broadly classified by Carlton and Ferreira, a variety of models or mechanisms have been proposed to explain the inverse Hall-Petch relation which includes dislocation-based, GB shearing, GB diffusion-based, and two-phase-based models [72]. Thus, in nc metals, the strengthening mechanisms are far more complex than those associated with the classical dislocation-based hardening in cg metals.

Bauschinger Effect

The Bauschinger effect (BE), discovered by Bauschinger in 1881 [50], refers to the anisotropic flow behavior of a metallic material during forward and reverse loading. This is illustrated in Figure 1-5 by the classical stress-strain curve of a bulk metallic material subjected to tensile and compressive loading. Trace OAB shows the loading path where A marks the forward (tensile) yield stress. Trace BC shows the unloading path which is typically linear elastic for conventional cg materials and the slope of it corresponds to Young's modulus (E). CDE shows the loading path along the reverse direction where D marks the reverse (compressive) yield stress, the magnitude of which is less than that of the forward yield stress, unlike the CD'E' path in which the yield stress at D' is equal to that of A if an isotropic hardening is assumed. Due to directionality in the strain hardening, the BE leads to the reduction in the yield stress during reverse straining after being plastically deformed in the forward direction [62].

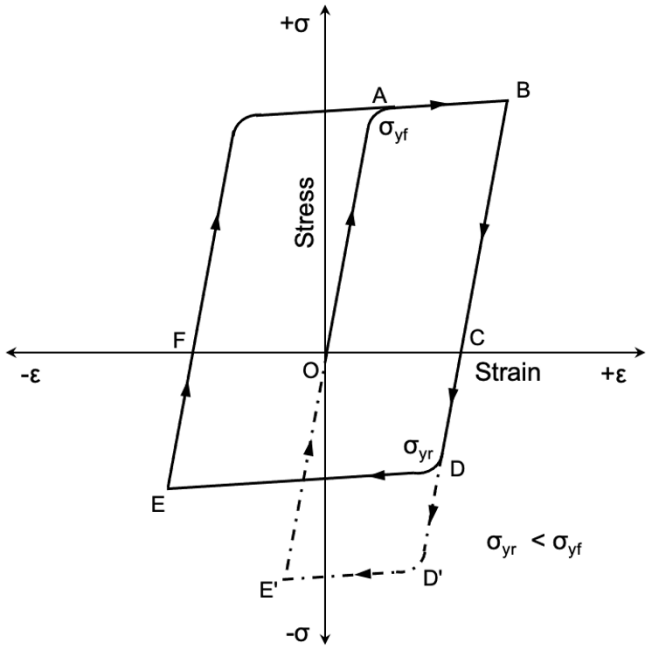

Figure 1-5 Schematic showing the Bauschinger effect in metals. σ_{yf} and σ_{yr} are the forward and reverse yield stresses, bold traces show the BE and the hysteresis loop whereas the dotted trace shows the reverse loading path assuming an isotropic hardening (modified from [49] and [65]).

Several theories have been proposed in the past to define and explain the BE in metallic materials [65,73–76]. Most of these theories are primarily based on the dislocation theory. The anisotropy in the plastic deformation resulting in the BE is primarily caused by back-stresses. The back-stresses are generated due to the dislocation pile-up formation at the GBs during deformation. Based on the back stress effects associated with the dislocation pile-ups, Abel and Muir [77] proposed two approaches to explain the BE. The first approach is based on Seeger's theory of work hardening [78]. Seeger's theory is based on the effects of long-range stresses that build up during deformation. The long-range stresses arise as a result

of the accumulation of dislocations in the principal glide planes. These stresses oppose the equally forward and reverse motion of dislocation thereby leading to the plastic anisotropy during tension and compression. It has been shown experimentally that the deformed state of metal single crystals is partially unstable, and this instability is reflected in the form of a large BE. The second approach is based on Orowan's theory [79,80] which suggests that anisotropy in the resistance to the motion of dislocations is introduced by pre-straining. After a certain amount of pre-strain, the dislocation motion is easier in the opposite direction as the back-stresses associated with the dislocations accumulated during pre-straining assist their backward motion which leads to the BE.

The plastic anisotropy under cyclic deformation is remarkably different for cg and UFG metals. Höppel et al. performed microyielding experiments with cyclic loading/unloading and reloading of bulk cg and UFG Al [81]. The microyielding curves for cg Al do not show a noticeable change in the plastic strain during unloading/reloading (Figure 1-6 (a)). The unloading and reloading curves almost overlap with each other. Interestingly, notable inelastic backward/forward strains were observed during unloading/reloading of UFG Al compared to cg Al as seen in Figure 1-6 (b). These differences in the microyielding behaviors were accounted for in a model that considered the effect of dislocation emission at GBs and the build-up of deformation-induced long-range back stresses that lead to inelastic strain recovery. Using *in situ* TEM testing, Mompiou et al. presented clear experimental evidence of the partial re-emission of dislocations from GBs and their reverse motion upon unloading in tensile deformed UFG Al (Figure 1-6 (c)) [64]. This elucidated the unusually large inelastic reverse deformation upon unloading, which is not observed in the cg counterparts. These results have raised strong interest in the dislocation-based processes leading to the BE in nc and UFG metals.

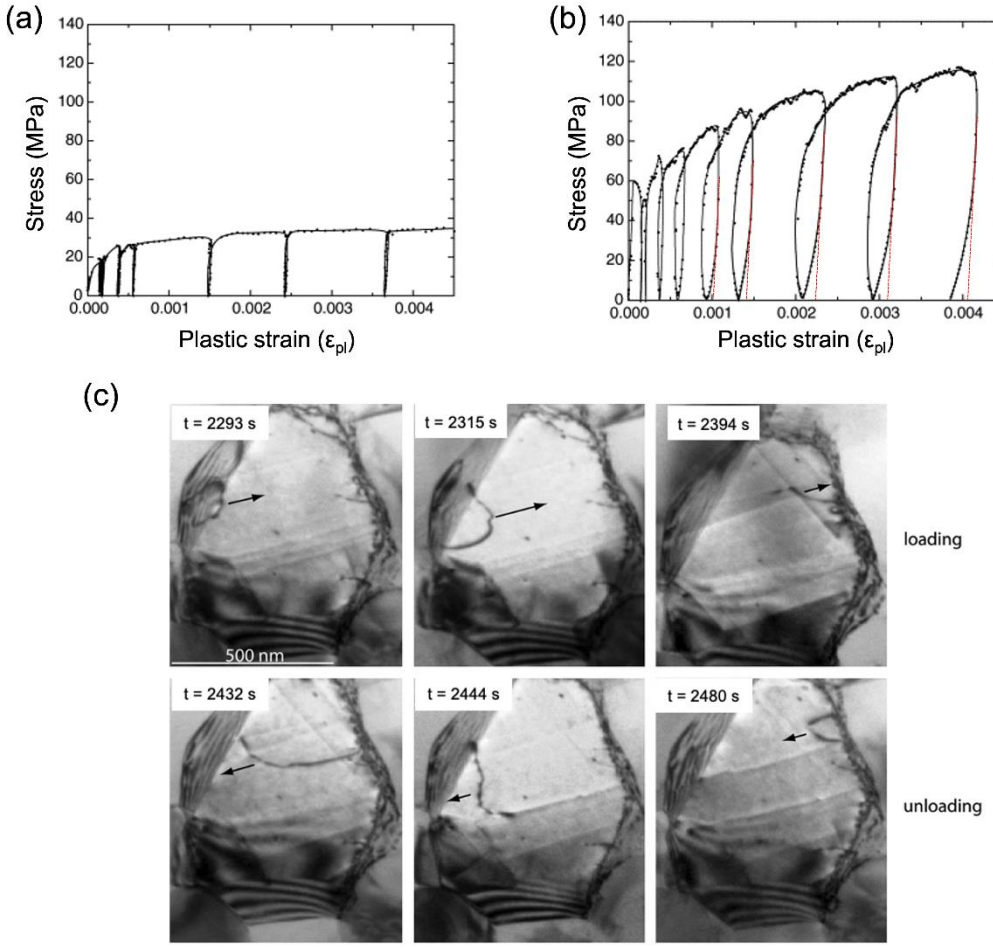

Figure 1-6 Micro-yielding curves for: (a) coarse-grained Al, (b) ultrafine-grained Al (modified from [81]), and (c) bright-field TEM images showing back and forth motion of dislocation between two opposite GBs in a UFG Al during *in situ* TEM loading and unloading experiments [64].

Apart from the bulk materials, the BE in thin metallic films has gained strong attention in the last two decades. Due to the dimensional and microstructural constraints and the presence of free surfaces, thin films exhibit a mechanical behavior different from their bulk counterparts [49]. However, unlike bulk specimens, thin films cannot be subjected to external compressive stress after straining in tension as straining in the reverse direction leads to buckling. Accordingly, modified Bauschinger tests have been introduced. These include simple loading-unloading tests to study internal stresses in thin films [49,59,62,82]. These studies have shown that the stress-strain response of thin metal films deviates from the elastic behavior with a significant reverse plastic flow during unloading, even when the films are still under tension [49,62,82]. In other words, the plastic strain in the film upon unloading is considerably less than expected [62] if an ideal elastic strain recovery would be assumed (Figure 1-7).

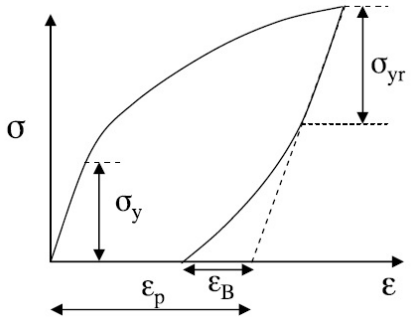

Figure 1-7 Schematic of the typical engineering stress-strain response of the BE in metallic thin films or nanocrystalline film subjected to loading-unloading cycle. σ_y: forward yield stress; σ_{yr}: reverse yield stress; ε_p: expected plastic strain if the specimen traced an elastic unloading path; ε_B: recovered plastic strain defined as the difference between expected and actual plastic strain. A lower σ_{yr} leads to larger ε_B and hence a more pronounced BE [49].

In their first experimental report, Xiang and Vlassak showed the BE in passivated thin metal films with relatively larger grains size of 1-2 μm using plain strain bulge tests [49]. A dislocation-based mechanism was proposed to explain the BE in the passivated films. During tensile loading of a passivated film, dislocations pile up at the film/passivation interface leading to significant back-stresses as shown in Figure 1-8 (a). These back-stresses in the film lead to the gliding of dislocations in opposite direction resulting in a non-linear unloading curve. On the contrary, unpassivated thin films showed little or no reverse flow even after completely unloading the specimen. According to their model, in unpassivated or free-standing thin films many dislocations can exit the film at the free surfaces, and therefore the BE is not significant.

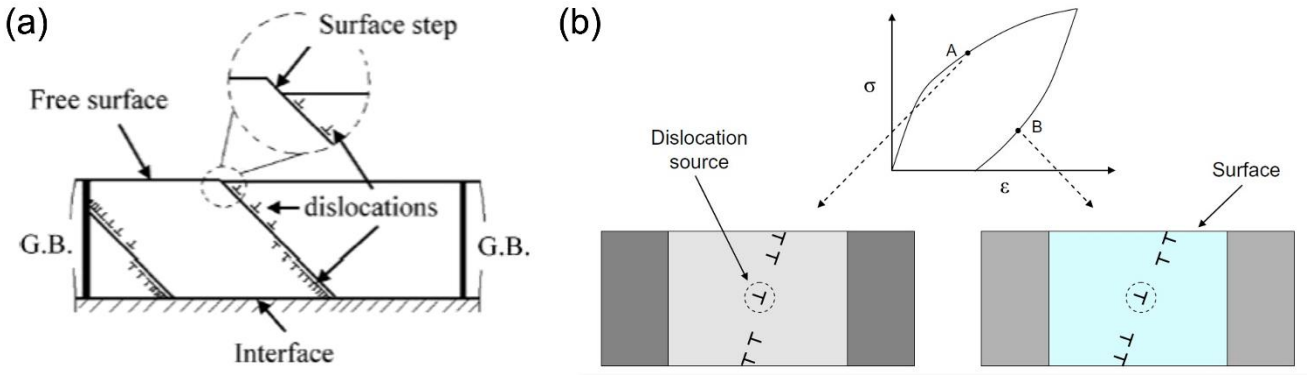

Figure 1-8 (a) Schematic showing the interaction of dislocations with GBs as well as free surfaces and interfaces in passivated thin films [49], and (b) A conceptual mechanism for BE in free-standing or unpassivated metal films with columnar grains. The figure shows the stresses in a large and two surrounding smaller grains. Grey and blue colors indicate tensile and compressive stress respectively while darker shades represent higher magnitude [63].

Subsequently, Rajagopalan et al. experimentally reported BE upon unloading free-standing metal films [63]. However, the thicknesses (200-400 nm) and grain sizes (~ 200 nm) of the films examined were smaller compared to the ones studied by Xiang and Vlassak. In their following report, Rajagopalan et el. reported an extended microplasticity in microstructurally heterogeneous free-standing nc gold (Figure 1-9 (a)) and aluminum thin films that lead to the build-up of internal stresses inducing a large BE during unloading [61]. Using *in situ* TEM studies, a significant dislocation activity was observed in some larger grains in these films whereas smaller grains showed little dislocation slip-based processes when the overall plastic strain in the film was over 0.3%, well above the conventional limit of 0.2% for the macroplastic deformation. This was considered as evidence for the microplastic deformation. On the other hand, for microstructurally homogeneous aluminum films with grains oriented favorably for dislocation glide and reduced plastic incompatibilities, such a microplastic deformation, and BE was found to be minimal (Figure 1-9 (b)).

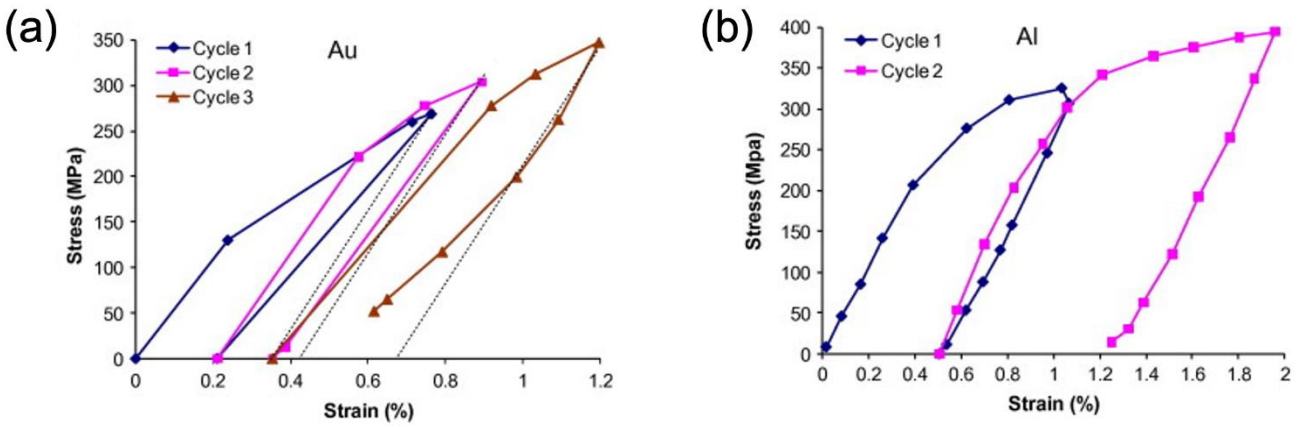

Figure 1-9 (a) The stress-strain response for nc gold film during *in situ* TEM deformation for three cycles. The stress-strain curves deviate from the elastic unloading path (indicated by dashed black lines) during all three deformation cycles. (b) The stress-strain measurements for nc aluminum film during *in situ* TEM deformation, showing a relatively sharp elastic-plastic transition and an almost elastic unloading behavior for two cycles (modified from [61]).

The above experimental results were supported by simulations that showed that the extended microplasticity and BE are a result of an inhomogeneous stress distribution caused by microstructural heterogeneity. A conceptual mechanism was proposed to explain the distinct BE in free-standing films with grain sizes in UFG and nc regime as illustrated in Figure 1-8 (b). This mechanism has considered the variation in grain sizes and orientation resulting in an inhomogeneous stress distribution leading to the BE. Figure 1-8 (b) shows the stresses in a large and two surrounding smaller grains at two points, A and B, during loading and unloading, respectively. The large grain is representative of grains that undergo significant plastic deformation while the smaller grains are symbolic of grains that undergo little plastic activity. During loading, the large grain starts deforming plastically at low stresses, whereas the smaller grains accommodate the strain elastically. As the external load increases, the stresses in the smaller grains keep increasing. However, the stress in the larger grain remains low (no significant hardening from dislocation entanglements) as the dislocations can escape to the surface. This leads to highly inhomogeneous stress distribution in the film. Furthermore, once the larger grains start deforming plastically the stress-strain slope reduces markedly. During the initial stages of unloading both the large and the smaller grains unload elastically. However, as the unloading progresses, the larger grain goes into compression as it was under much smaller stress at the start of unloading. This compressive stress leads to reverse plastic deformation in the larger grain (as the dislocations are of opposite sign) and hence the BE.

The increased interaction of dislocations with GBs in small-grained materials has been the basis of most of the theories explaining the inelastic behavior, anisotropic plastic response, and the BE. However, the conventional theories or models solely based on dislocation slip processes may not be valid to explain the

anomalous plasticity in nc metals. A principal reason for that is the multiple concurrent deformation mechanisms apart from the dislocation-based processes that are often reported to control the plasticity. Moreover, if the dislocation-based processes are dominant and assumed to control the plasticity, their complex interactions with GBs need to be taken into consideration.

Grain Rotation and Texture

The deformation slip within individual grains in polycrystalline metals is typically accompanied by their rotation leading to a change in the crystal orientation [65,69,83]. The grain rotation in cg metals is often accomplished by microscopic dislocation glide on multiple active slip systems [84]. Within bulk metallic materials, rotation of the grains leads to the evolution of deformation texture. The development of deformation texture means that the intensity of certain stable orientations (deformation texture components) increases at the expense of unstable orientations [83].

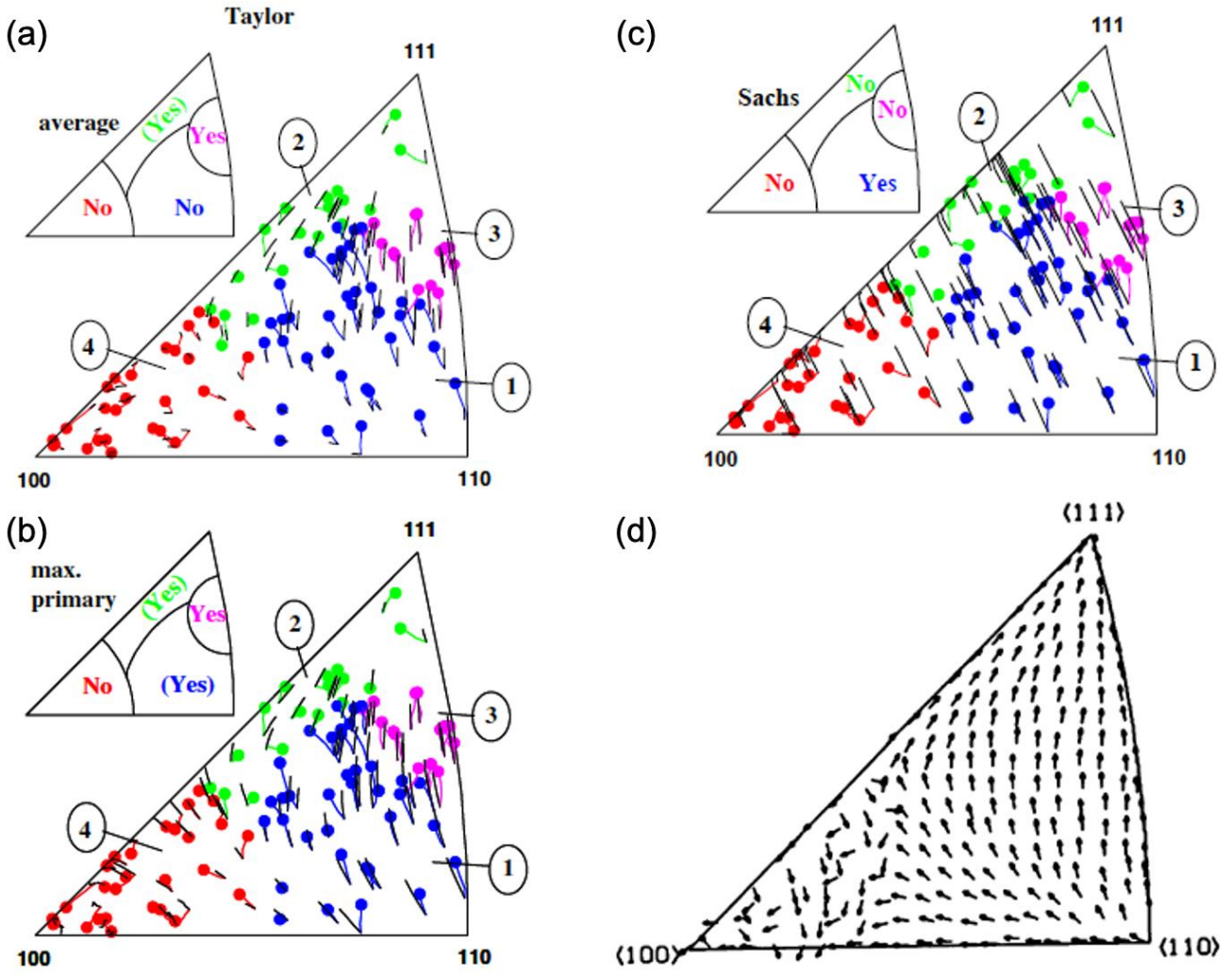

Figure 1-10 Comparison of the experimentally observed rotation of the tensile axes with standard models shown in an inverse pole figure: (a) Taylor model using the average of different solutions to the ambiguity problem (either 6 or 8 slip systems are active), (b) Taylor model using the maximum primary slip, (c) Sachs model, and (d) self-consistent prediction of the rotation of the tensile direction of Al on tensile elongation from 3% to 5% showing the direction of the rotations. For (a)-(c) the black lines show the predicted and the colored lines show the experimental rotation data whereas in (d) only the predicted rotation directions are shown (adopted and modified from [85]).

In cg metals, the rotation of grains during plastic deformation is dominated by their orientation with respect to the straining direction and the resulting texture can be predicted well by classical plasticity models such as the Taylor or Sachs models or self-consistent approaches [85–89]. The first statistically significant measurements of a large number of individual micron-sized grains rotating during deformation of a bulk specimen were reported by Margulies et al. using 3D X-ray diffraction characterization [90]. They compared their experimental results with classical predictions as shown in Figure 1-10. Comparison with the Taylor model showed significant discrepancies around the <100> corner and in the middle of the stereographic triangle (Figure 1-10 (a-b)). The Sachs model showed discrepancies around the <100> and <111> corners (Figure 1-10 (c)), whereas self-consistent approaches predicted large variations of the rotation behavior in the <100> corner, but did not predict the experimentally observed rotation directions (Figure 1-10 (d)) [85,90].

The Taylor model is based on the assumption that each grain experiences the same strain as the surrounding bulk material, equal to the macroscopic plastic strain, and accommodates the strain via the five independent slip systems, which are required to describe the state of strain in FCC metals [87,89,91,92]. The validity of the critical resolved shear stress for simultaneous activation of these five independent slip systems at the same external stress state and the equilibrium of the stress state has been questioned [93]. Alternatively, the Sachs model assumes a uniform external stress state for each grain and predicts crystallographic slip only for those slip systems where the critical resolved shear stresses are approached according to Schmid's law [89]. However, the Sachs model does not include constraints for shape changes induced by the activation of different slip systems in differently oriented grains and therefore does not guarantee a shape equilibrium between deforming grains and their neighbors [89,94]. The classical texture models do not consider the influence of GB-mediated processes, which do not lead to the development of a strong preferential texture. Furthermore, the interaction of dislocations with GBs is enhanced as the grain size is reduced to the nc regime, thereby leading to far more complex textures compared to those predicted by classical models.

Grain Interactions in Metallic Materials

The classical theories of crystal plasticity predict the rotation of grains based on macroscopic mechanical boundary conditions and crystallographic parameters of grains. However, the deformation processes within a grain are likely to be influenced due to the generation of locally varying mechanical boundary conditions that may be different from the macroscopic mechanical boundary conditions [95]. In general, the earliest plasticity models are known to predict the textures that are too sharp compared to the deformation textures measured by X-rays or neutrons [96]. This discrepancy has been attributed to the basic assumptions of these models that ignore complex interactions between grains as well as deformation heterogeneities [96,97]. Grain interaction occurs if the plastic flow process in a grain is influenced by its neighboring grain. Grain interaction as incorporated by Robert and Driver [97] in their model refers to the degree of stress transfer across GBs so that the state of stress of each grain is influenced by the stress state of its surrounding neighbors according to their contact distances. Under severe grain interactions, similarly oriented grains in different locations in the specimen are expected to exhibit a different rotational response, and as a result deviations from the classical model are expected [95].

Panchanadeeswaran et al. performed channel die compression of randomly oriented polycrystalline Al with mean grain size 200 μm and measured the textures by backscattered Kikuchi as well X-Ray diffraction techniques [98]. The experimentally measured global deformation texture matched reasonably well with that predicted by the Taylor model. However, the model failed to predict the orientations at the level of individual grains. Each grain exhibited a wide local orientation spread whereas the model predicted only a single orientation. This fundamental anomaly was attributed to the variations in deformation as a result of the interactions with neighboring grains which are not incorporated in the model. In another report, Kalidindi et al. also demonstrated that the Taylor model was unsuccessful in predicting the rotation of individual grains in Al and were able to model the local deformation at the level of individual grains [99]. Thorning et al. conducted a detailed quantitative investigation of crystal orientation distributions in a single grain in cg Cu to analyze the influence of grain interactions [95]. Their study showed the formation of orientation domains that extended several tens of micrometers around the periphery of the grain. Based

on the detailed analysis of crystal orientation maps, these domains exhibited a correlation with the intersecting GBs, intersecting grains, or domains within the neighboring grains which confirmed the influence of grain interactions. Subsequently, the efforts by Winther et al. offered a greater understanding of grain interaction mechanisms leading to intragranular orientation spread in tensile deformed cg IF steel [96]. In their study, the differences in the rotation of two similarly oriented grains were attributed to long-range grain interactions that lead to deformation heterogeneities within the grains. A qualitative analysis based on the ALAMEL model accounting for grain interactions showed that the interactions observed in their study occur as a result of cooperative shear at GBs.

Various modified models have been introduced in the past decades to account for interactions between a single grain and all their neighbors (assumed as a matrix regardless of the different orientations of each grain) or the detailed interactions between neighboring grains [93,94,96,100–103]. Some of the well-known models accounting for the grain interactions include the LAMEL, ALAMEL, and GIA models. The LAMEL model by Van Houtte et al. [104] considers the interactions of two grains across the faces of elongated grains. The LAMEL model was further generalized to the advanced LAMEL (ALAMEL) model [102] which also takes into consideration the GB plane as a variable. The grain interaction (GIA) model by Crumbach et al. [105] considers the interaction between clusters of grain which was further extended to the GIA-TW-HD model by Mu et al. [101] to take into account twinning-induced texture and strain hardening for predicting textures.

The above-mentioned studies were mainly focused on cg metals with grain sizes of several (tens of) micrometers. Due to the increased fraction of GBs in nc metals and reduced slip length, the grain interactions are expected to be far more pronounced compared to cg metals. Due to strong grain interactions, the rotational response and orientations within individual nano-grains and overall texture in nc metals are likely to be far more complex compared to cg metals. Such interactions between grains in nc metals are barely understood or reported in the literature. These interactions could be influenced by a variety of microstructural characteristics including grain size, the geometry of GBs, the geometric arrangement of the slip systems across GBs, GB character, and the initial orientation of grains. Understanding the detailed influence of these microstructural parameters requires critical investigations using advanced experimental strategies. These investigations could aid to refine the classical theories of dislocation plasticity and texture evolution.

1.3 Understanding Deformation Mechanisms in Nanocrystalline Metals

In nc metals, the motion of dislocations and their multiplication, typically governing the deformation in cg metals is limited by the nano-sized grains [106,107]. Conventional dislocation sources like the Frank-Read sources are generally not found to be operational [26]. As a result, mechanisms involving the multiplication and generation of new dislocations from the existing ones are not particularly active. With the reduction in grain size, the number of dislocations piling up at GBs decreases for a given stress level [47]. As a result, greater stress is required for piling up a similar number of dislocations at GBs. In addition to the dislocation-mediated processes, plasticity in nc metals is accommodated by GB-mediated mechanisms that include GB sliding [108–117], GB migration [118–126], GB diffusion creep [127–129], grain rotation [109,110,118,119,128,130–134] or alternative mechanisms like twinning [106,135] or shear band formation [107,136].

To investigate the different deformation mechanisms in nc metals at micro-/nanoscales, the last few decades have witnessed the development of miniaturized testing strategies. *Ex situ* small-scale mechanical testing methods like nanoindentation, tribological contact, tensile testing, bulge testing, etc. are some of the techniques that have been widely employed to measure the mechanical response of nc metals. These techniques can provide precise control over load, displacement, and temperature. These, however, only enable correlation with the microstructure on an averaged statistical basis by characterizing the initial and selected deformed states and do not provide direct visualization of the evolving microstructural characteristics. Although *ex situ* testing and characterization have yielded valuable insights into the deformation mechanisms of nc metals, *in situ* nanomechanical testing techniques are indispensable for observing the deformation processes in materials in real time.

Since the length scales of the microstructural characteristics are typically in the micro-/nanoscale regime down to atomic scales, the miniaturized testing strategies need to be combined with high-resolution imaging techniques to probe the active deformation mechanisms. Transmission electron microscopy (TEM) has proven to be crucial for the in-depth characterization of materials down to the atomic scale. TEM offers high spatial resolution and sufficient statistical information related to the structure, crystallography, chemical composition, etc. With these capabilities, *in situ* TEM nanomechanical experiments allow for direct mechanistic investigations of various deformation mechanisms in nc metals while measuring the nanomechanical response from the test specimens. The following sections briefly review the different deformation mechanisms in nc metals by specifically focusing on some of the recent *in situ* and *ex situ* TEM studies. These studies illustrate the role of microstructural characteristics in controlling deformation mechanisms and the resulting mechanical behavior in nc metals. Starting with the dislocation-based processes, the mechanics of dislocations at GB and within the grains in a UFG metal are understood. As the grain size is reduced to 20 nm, the deformation is seen to be largely accommodated by the activity of partial dislocations that could lead to a superplastic deformation. Further, with the reduction in grain sizes down to the nc regime, a transition from dislocation-based processes to deformation twinning is quantitively studied. The next study shows the impact of nano twins on activating the GB-mediated processes. Lastly, the role and interplay of both dislocation and GB-mediated processes leading to grain rotations in nc metals are reviewed.

1.3.1 Dislocation-based Mechanisms

Dislocation-based mechanisms in nc metals are complex because dislocation activity is expected within the grains as well as at the GBs. Their interactions with GBs and interfaces strongly depend on the grain size, GB character, their geometry as well as the arrangement slip systems across the GBs. Due to the increased volume fraction of GBs in nc metals, understanding the dislocation-GB interactions becomes important since these influence the dislocation pile-up, plasticity, and strengthening mechanisms that are active at the GBs. Mompiou et al. presented direct evidence for intergranular dislocation plasticity occurring under lower strains in UFG Al [137]. In this mechanism, the dislocation activity is confined within the plane of the GB (Figure 1-11 (a)). Based on a statistical analysis using automated crystal orientation mapping in TEM (ACOM-TEM), it was confirmed that this intergranular plasticity occurs in all types of GBs irrespective of their misorientation. These GBs included low and high-angle GBs as well as some special GBs, indicating that the GBs, in general, act as potential sites for nucleation and propagation of dislocations.

At larger strains (over 2%), due to their progressive accumulation at the GBs, the dislocations are emitted from the GB and propagate within the grain leading to a transition to intragranular plasticity ((Figure 1-11 (b))). From these results, it is understood that the inter-and intragranular plasticity are competing deformation processes and GBs in fine-grained materials accommodate the plastic strain as well as these act as a medium for strain transfer within the grains.

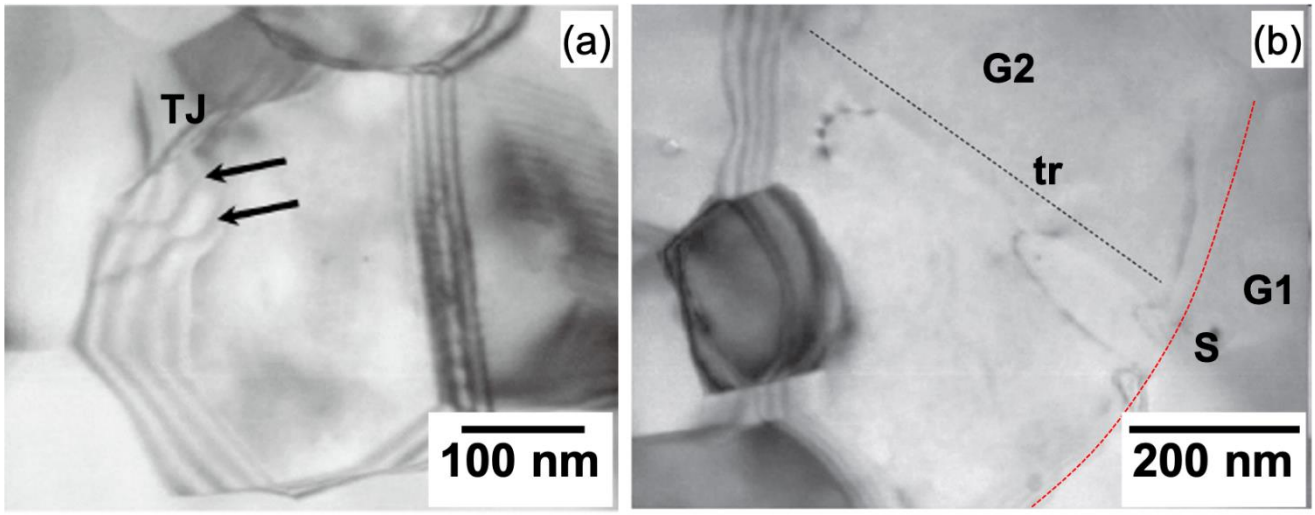

Figure 1-11 (a) Intergranular plasticity mechanism showing nucleation of dislocations from GB-TJ and their propagation inside GB in UFG Al, (b) a source S located at GB 1-2 (marked by the red line) emitting intragranular dislocations in G2 in the plane delimited by its trace tr [137].

Grain size in the nc regime considerably influences the characteristics of dislocations. The operation of full dislocations becomes less active with a reduction in grain sizes. Simulation studies by Swygenhowen et al. [138] and Yamakov et al. [139] and have shown substantial partial dislocation activity for their models for the grain sizes within the nc regime. The activity of partial dislocations is a principal mechanism for ultra-large elongation in nanoscaled crystals (e.g. nanowires). The stacking fault energy (SFE) determines the equilibrium separation of the partial dislocations or the resulting width of the SF. The higher the SFE, the smaller is the separation between the partials. Interestingly, for nc metals with high SFE (e.g. Al), it has been shown that the SF width is much wider compared to their cg counterparts [140]. SFE influences the critical grain sizes below which the deformation mode switches from full dislocations to partial dislocations. Alloying is a potential approach to modify the SFE in materials to influence the activity of partials. Recently, critical atomic-scale observations (Figure 1-12) by Libo et al. during the deformation of Au-Cu nanowires showed gliding of leading and trailing partials leading to the formation of extended dislocations [141]. Due to the activity of these extended dislocations, they were able to achieve ultrahigh strength (~ 2.98 GPa) and superplastic deformation (~185%) at room temperature in these alloyed nanocrystals of size below 20 nm. Thus, tailoring the SFE and thereby activating multiple dislocation activities including those of partials and extended dislocations offer a pathway towards strength-ductility trade-off in nc metals.

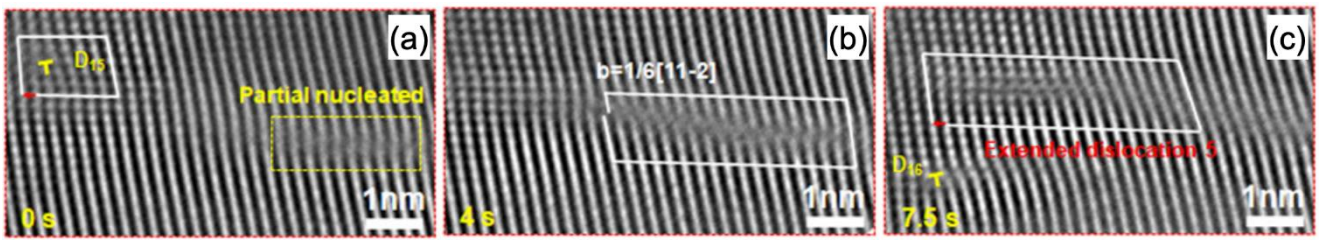

Figure 1-12 (a)-(c) Series of images showing the gliding of leading (D15) and trailing (D16) partials that lead to the formation of an extended dislocation during *in situ* deformation of the Au-Cu nanowire [141].

1.3.2 Deformation Twinning

Another well-established deformation process in cg metals is deformation twinning, which occurs under shear stresses that lead to the cooperative movement of atoms. The tendency of cg metals to twin is closely related to their stacking fault energy (SFE). Metals with lower SFE (e.g., Ag) have a greater tendency to twin compared to those with higher SFE (e.g., Al or Cu). In addition to SFE, atomistic simulations have shown that the stress required for the nucleation of Shockley partial dislocations is strongly dependent on the grain size [139,142]. Thus, the grain size becomes a critical parameter in controlling the twinning in nc metals. Compared to their cg counterparts, deformation twinning becomes a prominent mechanism in nc metals with even medium-to-high SFE (e.g., Cu, Ni, or Al).

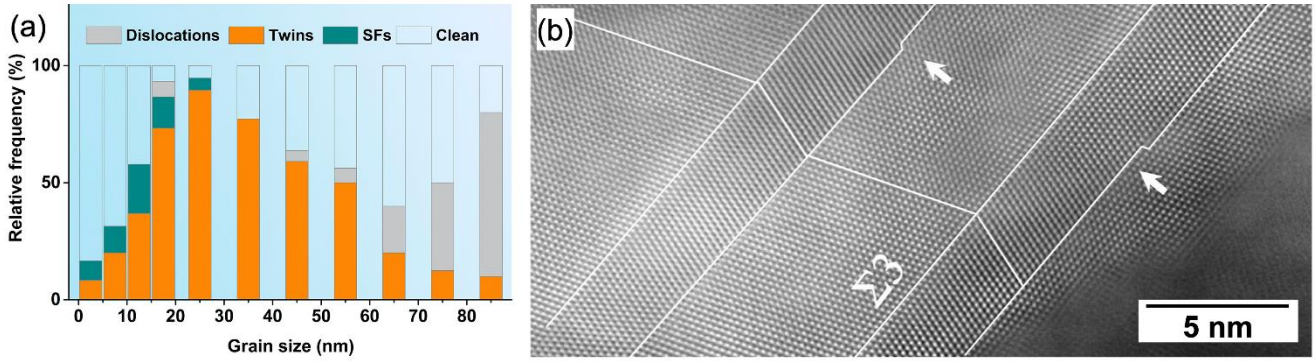

Figure 1-13 (a) Frequency distribution of dislocations, twins, and stacking faults in a deformed gradient nanostructured Ni, (b) HR-STEM image showing the atomic structure of deformation-induced twins [143].

To experimentally study the influence of grain size on twinning, Guo et al. recently conducted *ex situ* TEM investigations on a deformed gradient nanostructured Ni [143]. They have shown a transition from full dislocation slip to twinning depending on the grain size. In their study, ACOM-TEM enabled a statistical analysis of grain sizes and twin boundaries. For grain sizes above 60 nm, the primary deformation mechanism was dislocation slip, whereas extensive twinning was reported for grain sizes in the range of 20 to 60 nm (Figure 1-13 (a)). A high-resolution scanning TEM (HR-STEM) image shows the atomic structure of a few closely spaced Σ3 TBs within a 20 nm grain (Figure 1-13 (b)). The steps at the TBs indicated by arrows are most likely due to their interaction with Shockley partials further confirming their role for the twin formation in nc Ni. From these results, it is concluded that the transition from dislocation slip to twinning involves competition between leading, trailing, and twinning partials that effectively contribute to the twin fractions as the grain sizes are reduced.

1.3.3 Grain Boundary-mediated Processes

Classical grain boundary-mediated processes include GB sliding (GBS), GB migration, or GB diffusion. Grain boundary sliding (GBS) denotes the sliding of two grains over each other in response to external stress with their displacement taking place at or near their mutual interface. Using molecular dynamics simulations, Swygenhoven and coworkers have reported that the plastic deformation in nc Ni with grain sizes less than 10 nm has a regime controlled by GBS [144]. Within this regime, the strain rate was shown to increase with decreasing mean grain size, whereas above a critical grain size, the strain rate was shown to be independent of the grain size, which was considered as a transition to a regime that is intermediate between GBS and intragrain dislocation. Further, theories have also predicted that cooperative GBS and GB migration actively contribute to the enhancement of plasticity and fracture toughness in nc metals.

Most of the previous studies on GBS and GB migration were reported for nc metals without the influence of special GBs. Nanotwins with coherent Σ3 character are known to offer strong resistance to dislocation motion and these could alternatively activate GB-mediated processes. Understanding the influence of Σ3 TBs during deformation could offer insights into competing dislocation and GB-mediated processes. In a recent development, Li et al. reported on *in situ* TEM observation of cooperative GBS and migration in

nanotwinned nc Au thin films. Figure 1-14 shows a series of bright-field TEM (BFTEM) images acquired from a localized region of nc Au film with two crack tips. The cooperative GBS and migration could be noticed from the displacement of the grains across GB 4-5, GB 4-6, GB 6-7, and GB 6-9 and the resulting blunting of both the crack-tips. These results explicitly showed that accommodation of GBS by GB network can be associated with migration of GB interface and triple junctions. Statistical analysis on the grains at the blunting crack-tips indicated that the sizes of most of the twinned grains increased whereas the sizes of those without twins decreased. From these observations, it is concluded that nanotwins promote cooperative GBS, migration, and stress-driven grain growth during the crack-tip blunting processes thereby paving a way towards increased plasticity and fracture toughness in nc metals.

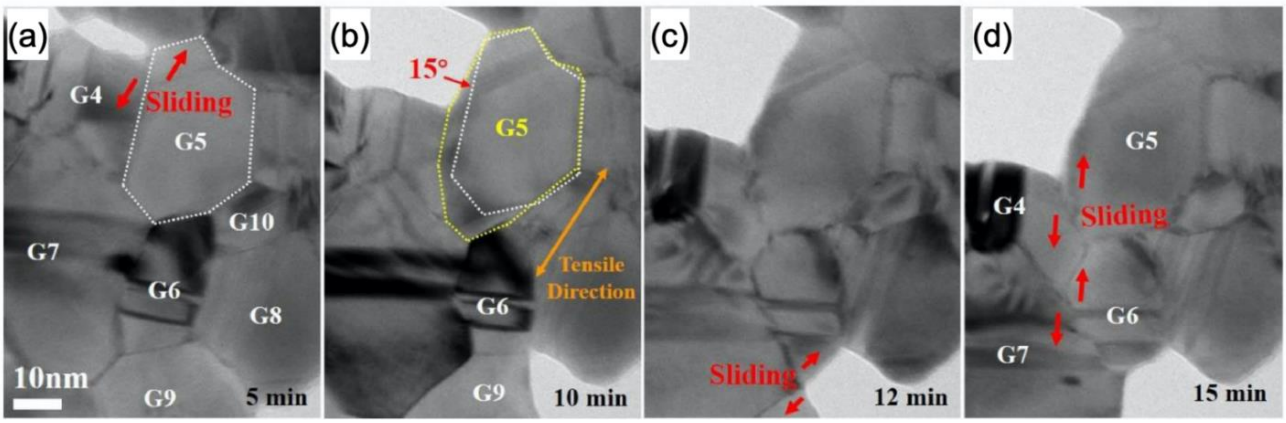

Figure 1-14 Bright-field TEM images showing cooperative GBS and GB migration between nanotwinned grains in nc Au: (a)-(b) sliding across GB 4-5 along with GB migration associated with the blunting of the crack-tip at G5, the initial and final traces of the boundary of G5 are shown in white and yellow. (c)-(d) Cooperative sliding across GB 4-5, GB 4-6, and GB 4-7 along with GB migration associated with the blunting of crack-tip at G6.

1.3.4 Grain Rotation and Deformation Texture

The grain rotation and texture observed experimentally during deformation in nc metals are strongly affected by the different types of deformation mechanisms. It is generally accepted that GB-mediated rotation of grains does not lead to a global texture development [20,84,112]. For example, Ivanisenko et al. reported a GB-mediated process controlling the deformation in nc Pd for grain sizes below 40 nm [107]. In another experimental report, they showed GB-mediated rotational deformation of grains occurring as rigid units for Pd with a mean grain size of 130 nm [117]. In such a GB-driven mechanism, the rotation of grains is not controlled by the classical dislocation slip that leads to the formation of crystallographic texture, and these rotations are considered as 'non-crystallographic' in nature. Shan et al. had also observed such rotations in much smaller grains (~ 10 nm), and explained these to be occurring in conjunction with GB sliding (GBS) [145]. This mechanism involving grain rotation in association with GBS necessitates accommodation of the strain and strain rate incompatibility between a cluster of neighboring grains [117,146]. The classical model by Gutkin et al. shows a crossover from GB sliding to the rotational deformation [109]. This crossover of deformation modes of plastic flow was explained by splitting of the gliding GB dislocations into climbing GB dislocations at GB triple junctions. Using *in situ* HRTEM, Wang et al. had observed simultaneous (collective) rotation of several grains in a direct neighborhood in a coordinated manner and it was explained by the climbing of dislocations into triple junctions or GBs [131]. On the contrary, Yang et al. suggested dislocation-based plasticity as a dominant mechanism even at grain sizes as low as 28 nm and were able to describe the texture development by classical models limiting the number of slip systems [147]. Mompiou et al. have also reported on grain rotations in UFG Al using *in situ* TEM studies. These rotations were shown as a direct consequence of GB dislocations with Burgers vectors out of the plane of the film and occurred as a collective process involving several neighboring grains [148].

Real-time local investigations based on the evolving grain structure become indispensable to untangle the contributions of the active mechanisms that lead to grain rotations. Recently, Chen et al. have shown dislocation-mediated GB migration associated with a climb of dislocations and their reaction in nc Au under

in situ cyclic shear loading inside TEM (Figure 1-15). It was shown that the grain shrinkage is accommodated by dislocation-driven GB migration which is accompanied by coordinated deformation of neighboring grains. These processes resulted in rapid grain rotation together with grain annihilation during reverse shear deformation. These results provide a direct understanding of the complex interplay of dislocation and GB-mediated processes leading to rotation of nanograins occurring during cyclic deformation and add greater insights into fatigue degradation processes in nc metals.

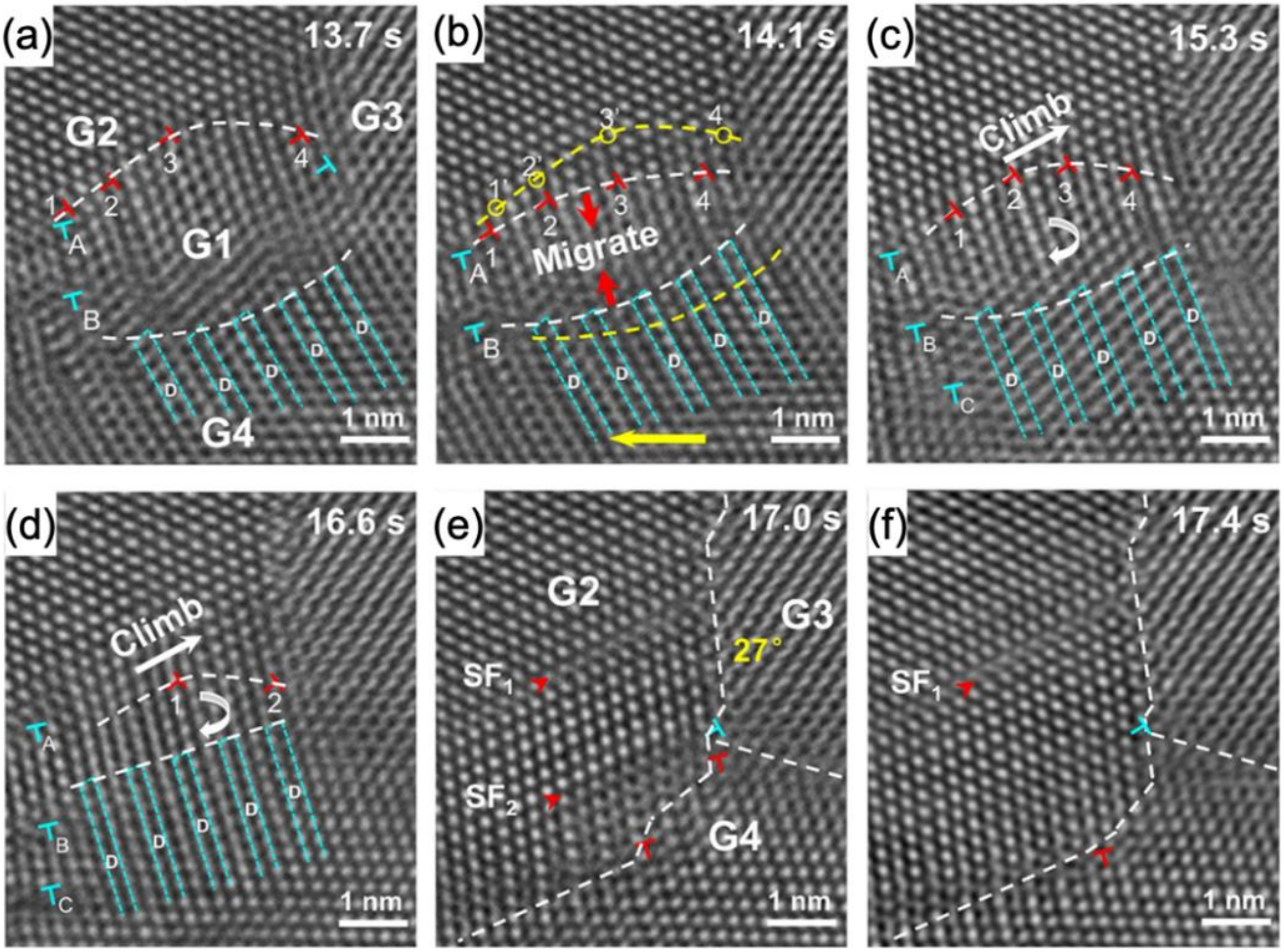

Figure 1-15 Series of HRTEM images during shear deformation showing GB migration, dislocation activity, grain rotation, and annihilation: (a-b) Migration of GB 1-2 and dissociated GB 1-4, (c-d) migration of GB 1-2 associated with collective climbing of GB dislocations leading to clockwise grain rotation of G1, (d-e) reaction of glide dislocations with dislocations on GB 1-2 and SFs in the dissociated GB 1-4 driving the grain rotation and annihilation, (e-f) emission and annihilation of SFs at neighboring GBs.

1.4 Nanocrystalline Multilayered Composites

Apart from grain structure and GB characteristics, further possibilities to tailor nc materials is to incorporate heterophase interfaces between dissimilar materials and alter their structure and chemistry at nano or atomic scales. Nanocrystalline multilayered composites (NMCs) have emerged as a novel class of engineering materials. They are applied as coatings with advanced mechanical, tribological, and chemical properties [149,150]. The metallic multilayer systems offer controllability of dimensions, interface structures, and properties at a near-atomic scale. As a result, these are good model systems to explore the effect of interfaces on the tribological properties at different length scales ranging from nano- to micrometers [151,152]. NMCs typically consist of two or three components deposited alternatively with thickness and grain sizes within 100 nm. Each layer in the composite material has a discrete function of imparting properties like the ability to act as a thermal or diffusion barrier or to impart abrasion resistance [149]. GBs and interphase interfaces in these multilayered systems play an important role in controlling their properties like strength, hardness, fracture, resistance to fatigue, and irradiation damage [151,153]. The strengthening mechanisms in NMCs and their deformation behavior have been proven to be strongly influenced by the layer spacing and coherency of the interfaces [150]. Further, various other factors like shear modulus mismatch, grain size within the layers, structural discontinuity across the interface, and its crystallographic nature also govern their mechanical properties [154].

1.4.1 Strengthening and Plasticity in NMCs

NMCs can exhibit significantly high yield strengths, which can approach 1/3 to 1/2 of the theoretical strength at room temperature [154,155]. For NMCs, the individual layer thickness (λ) is the principal parameter for tailoring the flow strength (σ) by Hall-Petch strengthening [156]. For NMCs composed of stiffer and softer phases (e.g. Cu-Cr), the flow strength is controlled by the softer phase and the strengthening is related to the characteristic dimension of the softer phase [157,158]. The characteristic dimension can be either thickness or grain size depending on whichever is smaller. The ductility of NMCs is dependent on the modulation period (bilayer thickness). Unlike strength, the ductility reduces as the modulation period is reduced [157,159].

Apart from the layer thickness and grain size, another crucial factor that controls the mechanical properties of NMCs is the interfacial structure [155], which can be broadly classified into coherent, semi-coherent, and incoherent systems [150,160]. Coherent interfaces are formed in NMCs with the same crystal structure and specific orientation at the interface. This results in a continuity of slip systems across the interfaces and these are termed as 'transparent' interfaces. Despite the continuity of the slip systems, dislocations are hindered in moving from one layer to the next due to the coherency stresses arising due to lattice mismatch and image stresses due to modulus mismatch [156]. Semi-coherent interfaces form between metals with the same lattice structure but a larger mismatch of the lattice parameters. For semi-coherent interfaces with small misfits ($\leqq$ 5%), gliding dislocations need to overcome large stresses as the misfit dislocations only relax long-range coherency stresses [151]. Interfaces between two phases with different crystal structures are incoherent and offer strong resistance to slip transmission due to the low shear strength of the interfaces and these are called 'opaque' interfaces [161,162].

1.4.2 Deformation Mechanisms in NMCs

In the case of NMCs, the dislocation-based processes could be even more complex due to the presence of two or more types of materials. For multilayers with incoherent interfaces, Misra et al. proposed dislocation-based models for FCC/BCC multilayers, without coherency stresses, to interpret the length scale dependence of the strengthening mechanisms, as shown in Figure 1-16 [163]:

- Dislocation pile-up based mechanisms following the Hall-Petch relationship for layer thickness in or over a sub-micrometer range
- Confined layer slip (CLS) of single dislocation loops for layer thickness in the range of a few tens of nanometers where the dislocation pile-up based Hall-Petch relation explaining the increase in strength with decreasing thickness does not apply
- Interface cutting model for the layer thickness of 1-2 nm

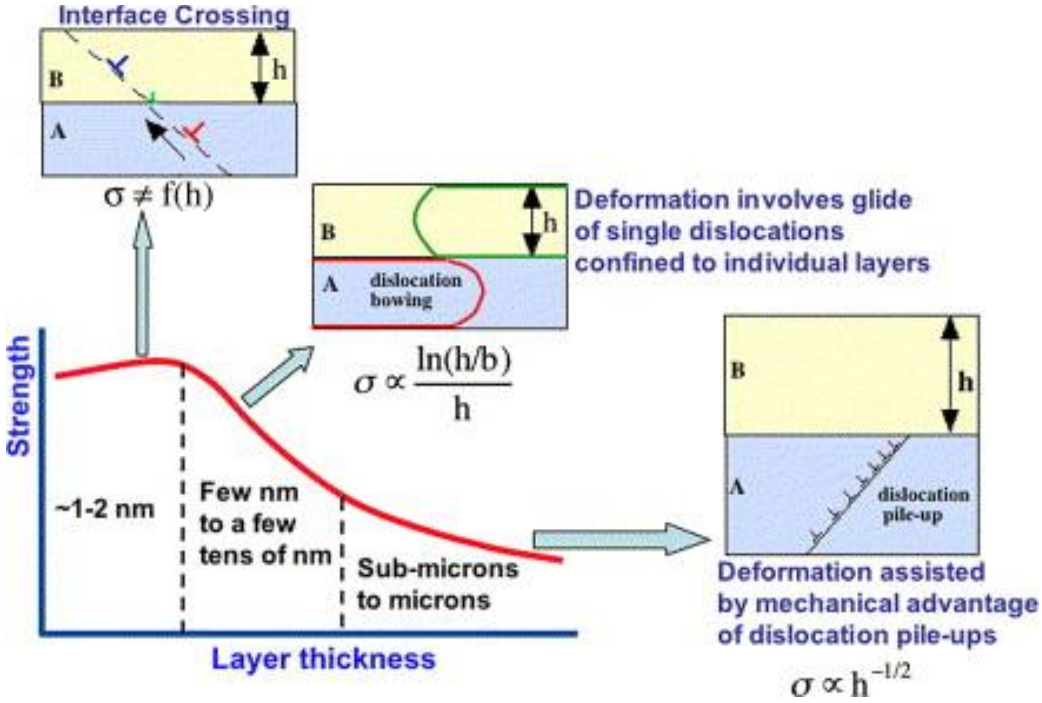

Figure 1-16 Schematic illustration of the dislocation mechanisms in multilayers operative at different length scales (adopted from [163]).

Considering the above predictions, a critical understanding of the deformation processes at the length scales of a few tens of nanometers becomes important to explain the enhanced strengthening in NMCs (Figure 1-16). Nan et al. showed an *in situ* TEM evidence of the CLS mechanism with a cluster of dislocations gliding collectively in the Cu layer close to the indenter during the compression indentation process of nanoscale Cu-Nb multilayers (Figure 1-17). These dislocations are confined within the Cu layer and do not transmit to the neighboring Nb layers. Geometrically, unlike their appearance, it was concluded that these dislocations do not pile up on the same glide plane but are arranged as loops on a set of different glide planes parallel to each other. With the operation of the CLS mechanism, both Cu and Nb layers were shown to co-deform to large plastic strains without crack formation.

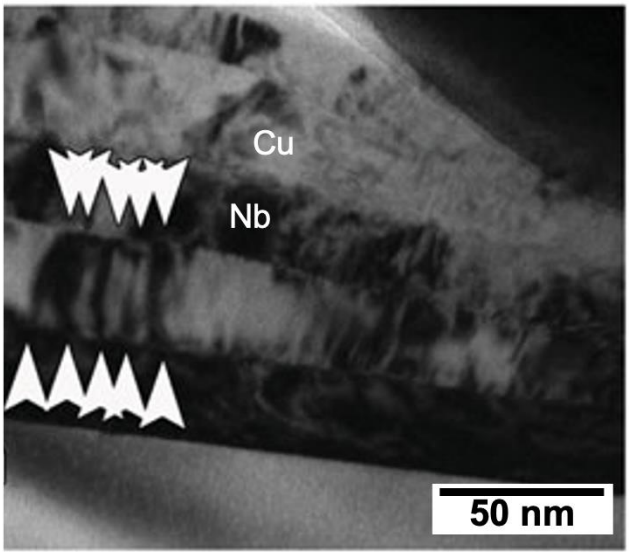

Figure 1-17 Cluster of dislocations gliding collectively in the Cu layer in Cu-Nb multilayers [152].

Due to opaque interfaces in the above study, direct slip transmission or transmission of partial dislocations leading to twinning was not evident. Deformation twinning has been rarely reported in Cu layers in Cu-Nb multilayers even at peak stresses of 2.5 GPa or under shock loading. This indicates that deformation twinning is dependent on the heterophase interfacial characteristics that determine the extent of transmissibility of the twinning partials. Wang and co-workers have shown the twinning is facilitated by interfaces in Ag-Cu eutectic composite in submicron and nc regime [164,165]. With the greater propensity of Ag to twin compared to Cu, the Ag-Cu interfaces were shown to permit the transmission of twinning partials from Ag to Cu to constitute a sustained growth of deformation twins across the interfaces (Figure 1-18). It is seen that the twinned band after transmission not only locally reorients Ag and Cu to twin orientation but also the Ag-Cu interface leading to the instability of interface. These differences in the behavior of Cu-Nb and Cu-Ag multilayers indicate that Cu in both the systems does not act independently of the adjoining component layers and the interfaces play a critical role in controlling deformation mechanisms. This raises a strong interest in deeper investigations of the influence of heterophase interface structure on the deformation characteristics of nanoscale metallic multilayers.

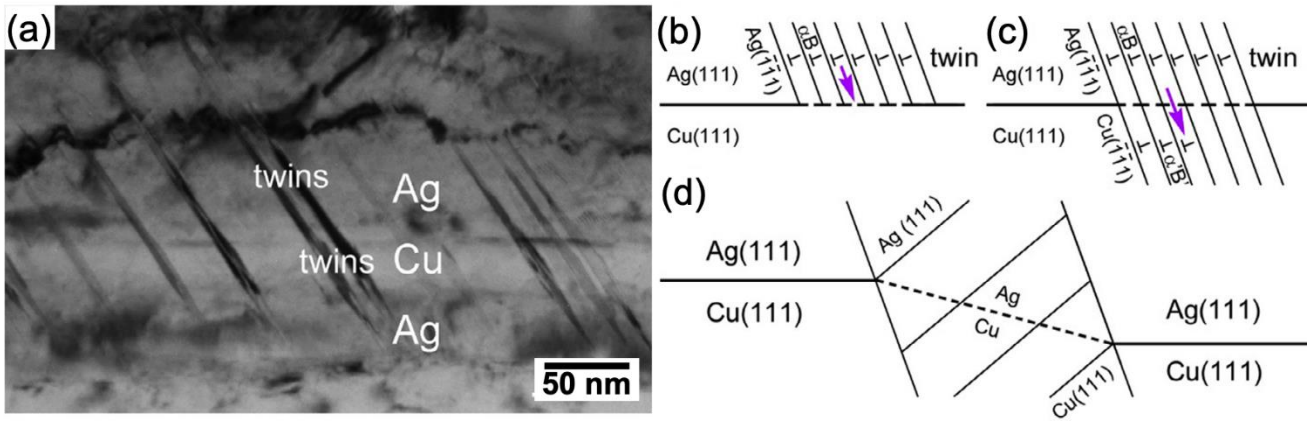

Figure 1-18 (a) TEM image showing the twins transmitted from Ag layer to Cu layer in Ag-Cu nanocomposite subjected to compression. (b)-(c) schematics showing the transmission of twinning partials across the Ag-Cu interface, and (d) schematic of the final interface structure shown by dashed-line after twin transmission (modified from [165]).

1.5 Thesis Goals and Framework

Despite the advancements in experimental and computational techniques, various facets of the deformation behavior in nc metals are not yet explicitly understood. The cooperative interactions between grains and their influence on the deformation processes controlling the elastic-plastic transition during loading and in particular plastic recovery leading to the BE during relaxation in nc thin metal films deserve extensive investigations. One of the principal goals of the thesis was to gain further insights into the elementary deformation mechanisms that lead to plastic recovery during relaxation and the BE in nc palladium thin films. To accomplish that, an *in situ* TEM experimental approach was employed. This approach was aimed at establishing a direct correlation between the cyclic nanomechanical loading behavior and the real-time evolution of the global deformation microstructure to analyze the deformation processes.

In nc metals, both dislocation slip as well as GB-mediated processes lead to rotational deformation of grains. The initial orientation of grains and the global texture considerably influence the overall plastic anisotropy in nc metals. A detailed investigation of the complex interactions of grains with their neighbors becomes critical to understanding grain rotation and the resulting texture characteristics. In addition to a global analysis of the microstructure, local investigations were conducted to understand the complex grain interactions in nc palladium. These investigations were aimed at analyzing the possible contributions from dislocation and GB-mediated processes that lead to the grain rotations during loading and relaxation of the specimen.

Apart from the influence of grain structure and GBs, the thesis further explored the impact of compositional variations and heterointerfaces on the deformation characteristics. This part of the thesis was focused on understanding the microstructural evolution in more complex systems involving NMCs with different interface structures under tribological loading. The main objective here was to study the influence of the interfacial characteristics and various material parameters on the microstructural evolution during sliding contact. To accomplish that, two systems Au-Cu (semi-coherent interfaces) and Cu-Cr (incoherent interfaces) were selected for comparative analysis. Based on the distinct microstructural features in these two systems, the study aimed at unraveling the active deformation mechanisms that are expected to be operative during the sliding contact.

The thesis is divided into seven chapters. Following the motivation for investigating deformation mechanisms in nc metals and NMCs, the basic concepts of plasticity, deformation behavior, and mechanisms in metallic materials are introduced in **Chapter 1**. **Chapter 2** introduces the key experimental methods utilized for the investigations. The techniques for specimen preparation for *in situ* and *ex situ* nanomechanical studies and various transmission electron microscopy (TEM) techniques that were employed in this thesis are described. **Chapter 3** describes the approaches employed for processing and quantitative analysis of the data acquired in the experiments. **Chapter 4** presents the results from *in situ* TEM observation of the Bauschinger effect in nc Pd thin films. *In situ* nanomechanics coupled with the quantitative orientation mapping in the TEM enabled a direct correlation of the nanomechanical response with the evolving microstructure in nc Pd. The results from a reliable quantitative analysis of the global microstructural characteristics are presented to understand the deformation mechanisms governing the BE in nc Pd. **Chapter 5** presents the results from *in situ* TEM observation of cooperative grain rotations in nc Pd. A quantitative analysis of the rotational behavior of some specific grains is presented. Based on these local analyses, the chapter presents detailed mechanistic investigations of the interactions occurring due to the dislocation pile-up formation between some specific pairs of grains leading to their cooperative rotation. **Chapter 6** presents and discusses the results of the microstructural evolution in Au-Cu (FCC/FCC) and Cu-Cr (FCC/BCC) NMC thin films under cyclic tribological loading and explores the deformation mechanisms active in these systems with heterogeneous interface structures. **Chapter 7** concludes and summarizes the main findings and suggests prospective advances towards the nanomechanical investigations of nc materials.

2 Experimental Methods and Data Acquisition

To understand the deformation mechanisms in nc materials, detailed investigations of the deformation microstructure are important. Crucial aspects for the microstructural characterization are the spatial resolution (nm-scale) to identify the relevant deformation processes and the volume of the sample analyzed, which needs to provide sufficient statistical information. In this work, transmission electron microscopy (TEM) was employed for the microstructural characterization as it offers a resolution down to the atomic scale and allows to sample sizes of several micrometers. TEM techniques provide a variety of details on the structure, crystallography, and chemical composition for a comprehensive materials description. In addition, rapid image and data acquisition capabilities in TEM enable time-resolved experiments. *In situ* TEM has become exciting to directly visualize the microstructural evolution in response to strain, temperature, and other stimuli. Altogether, these capabilities make TEM ideal for imaging and analysis of the deformation processes in nc materials.

This chapter introduces the major experimental techniques that were used to investigate the deformation mechanisms in nc materials at the nanoscale. Starting from the sample preparation, magnetron sputtering is presented as a route to prepare thin nc metal films. Methods for specimen preparation, both for *ex situ* and *in situ* TEM characterization, using FIB are briefly introduced. The basics of electron microscopy are summarized by introducing electron-specimen interactions, electron optics, and various operational principles. Finally, *in situ* TEM techniques for heating and small-scale deformation of miniaturized specimens are discussed.

2.1 Preparation of Nanocrystalline Thin Films

Physical vapor deposition (PVD) is a common method for producing thin films with sputter or evaporative sources. It is a bottom-up approach that involves consolidation of material atom-by-atom or layer-by-layer and offers the possibility to design multicomponent and multilayered coating variants with tailored mechanical or tribological properties for surface engineering [55]. It is employed for producing thin films/coatings for a variety of applications including microelectronics, corrosion barrier, and wear-resistant coatings [166].

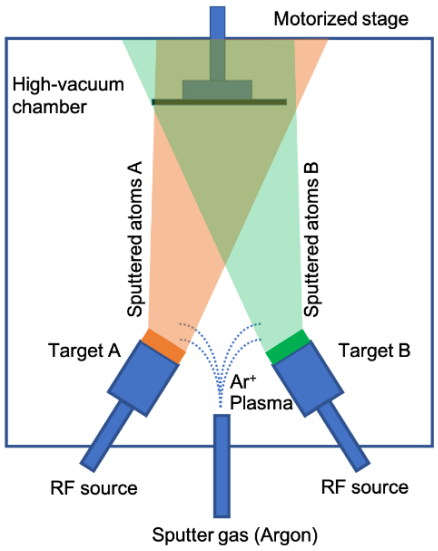

Figure 2-1 Schematic of the set-up of magnetron sputtering with two targets.

In the present work, nc metal and composite thin films were prepared by magnetron sputtering. The magnetron sputtering set-up consists of one or more planar targets that are bombarded by energetic ions (Ar^+). These ions are produced in a glow discharge plasma in front of the targets. The momentum transferred by the Ar^+-ions during the bombardment leads to sputtering of atoms from the target material

under high vacuum (~ 10^{-9} mbar) conditions. These sputtered atoms are deposited on a substrate as thin film. In addition to the target atoms, secondary electrons are also emitted from the surface of the target. These electrons are confined in the vicinity of the target by the magnetic field of magnetrons. This leads to a greater ionization efficiency with a dense and self-sustained plasma, thereby enhancing the sputter and deposition rates (1-10 nm/s) on the substrate [167]. The main advantages of this method include purity and uniformity of the coatings, dense and well-adherent coatings, ease of scaling-up, a large variety of film materials, and broad tunability of film properties [168].

Critical parameters for sputtering include the sputtering gas pressure, sputter power and temperature, and bias of the substrate. These parameters control the sputter yield, growth rate, microstructural characteristics, texture, and residual stresses of the deposited films. The sputter gas pressure and substrate temperature influence the surface mobility of adatoms. Classically, the influence of these parameters on the microstructure of the films is understood from Thornton's diagram based on the energy of the adatoms [166,169]. Thornton's structure zone model for sputter metal coating classifies the microstructure such that increasing the energy of adatoms gradually changes the microstructure from porous columnar grains to a fully recrystallized state [166]. Castrup et al. in their TEM investigations showed that low sputtering gas pressures resulted in a dense equiaxed structure, whereas distinct columns with reduced atomic density at column walls formed at higher pressures [16]. Further, Castrup et al. [16] and Detor et al. [170] have shown a rapid transition from strongly compressive to tensile residual stresses as the sputter gas pressure was increased. Based on the previous literature, the sputter parameters were chosen to obtain films with dense and equiaxed structures with minimal residual stresses.

2.2 Electron Microscopy for Materials Characterization

Ernst Ruska and Max Knoll invented electron microscopy in the early 1930s. In 1932, they introduced the term 'electron microscope' (EM) and proposed the concept of electromagnetic lenses and the formation of images with the aid of electrons [171]. The advent of electron microscopy significantly expanded the capabilities of microscopes to achieve nano- to atomic-scale resolution compared to classical light microscopy. EMs use electrons to illuminate and image materials. These electrons are generated from electron sources. Two types of electron sources are typically employed. Thermionic sources produce electrons when heated to elevated temperatures whereas field emission sources produce electrons by application of high electric potential. The electrons emanated from the source are accelerated at high voltages and focused to form a fine cross-over. The electron gun mainly controls the brightness, coherency, and energy spread of the electron beam. Since electrons are charged particles, EMs use electromagnetic lenses to define their optical paths. The electrons are focused by the force exerted by the electric or magnetic field produced by these lenses. Perfect electromagnetic lenses produce an axially symmetric magnetic field enabling uniform focusing of the electrons.

As the electrons are accelerated at high voltages, they can achieve high velocities approaching a significant fraction of the speed of light. From the wave-particle duality, these charged particles can effectively behave as waves with short-wavelength (λ) given by:

$$\lambda = \frac{h}{\left[2meV\left(1+\frac{eV}{2mc^2}\right)\right]^{1/2}} \qquad 2\text{-}1$$

where m is the rest mass of the electron, e is the charge of a single electron, h is the Planck's constant, V is the applied accelerating voltage and c is the speed of light in vacuum. If the electromagnetic lenses are perfect without any aberrations, the theoretically achievable resolution is diffraction-limited by the collection angle of the lens. The resolution can be defined as the smallest distance at which two individual points on the specimen can be distinguished. It is generally given by the classical Rayleigh criterion as:

$$\delta = 0.61\frac{\lambda}{\mu \sin\beta} \qquad 2\text{-}2$$

where δ is the resolution, λ is the wavelength of the radiation, μ is the refractive index of the medium and β corresponds to semi-angle of collection of the lens. Considering β to be small, the theoretical resolution (R) for the electron waves in vacuum (μ = 1) is expressed using a simplified form of the Rayleigh criterion as:

$$R = 1.22\frac{\lambda}{\beta} \qquad 2\text{-}3$$

In practice, however, the electromagnetic lenses are not perfect and the magnetic field generated by them is not rotationally symmetric. This results in geometrical lens aberrations which include spherical aberration, coma, astigmatism, etc. These aberrations lead to the deviation of electrons from their ideal optical paths and govern the limit of actual resolution achievable in EMs.

2.2.1 Electron-specimen Interactions

High energy electrons hitting a specimen interact strongly with the nucleus and the electron cloud of the atoms present in the material. The beam-specimen interaction generates various signals that contain specific information about the material (Figure 2-2 (a)). The interaction volume of the incident electron beam depends on the electron probe size, the energy of the beam, and the material itself. Secondary electrons (SEs) are low energy (< 50 eV) electrons that are ejected from the atoms of the surface or sub-surface of the specimen after receiving sufficient kinetic energy from the incident electrons. SEs mainly provide information about the topography, shape, or inclination of features on the surface of the specimen [172]. Backscattered electrons (BSEs) arise as a result of the strong interaction of electrons with the nucleus of atoms (Figure 2-2 (b)). As a result, these carry information sensitive to the average atomic number of the phases present in the specimen and offer compositional contrast during imaging. Deceleration of incident electrons due to Coulombic interaction with the atoms of the specimen leads to the generation of Bremsstrahlung or continuum X-rays. During the interaction, the electron beam can eject the tightly bound inner shell electrons, leaving the atoms of the specimen in an excited state. The transition of outer shell electrons to the empty lower energy state can result in the emission of X-rays (Figure 2-2 (b)). Since the difference between the two energy states is characteristic for an element, the emitted photons are termed as the characteristic X-rays. The continuum X-rays constitute the background under the characteristic X-rays in X-ray spectrums. These X-rays are essential components for energy-dispersive X-ray spectroscopy for elemental analysis.

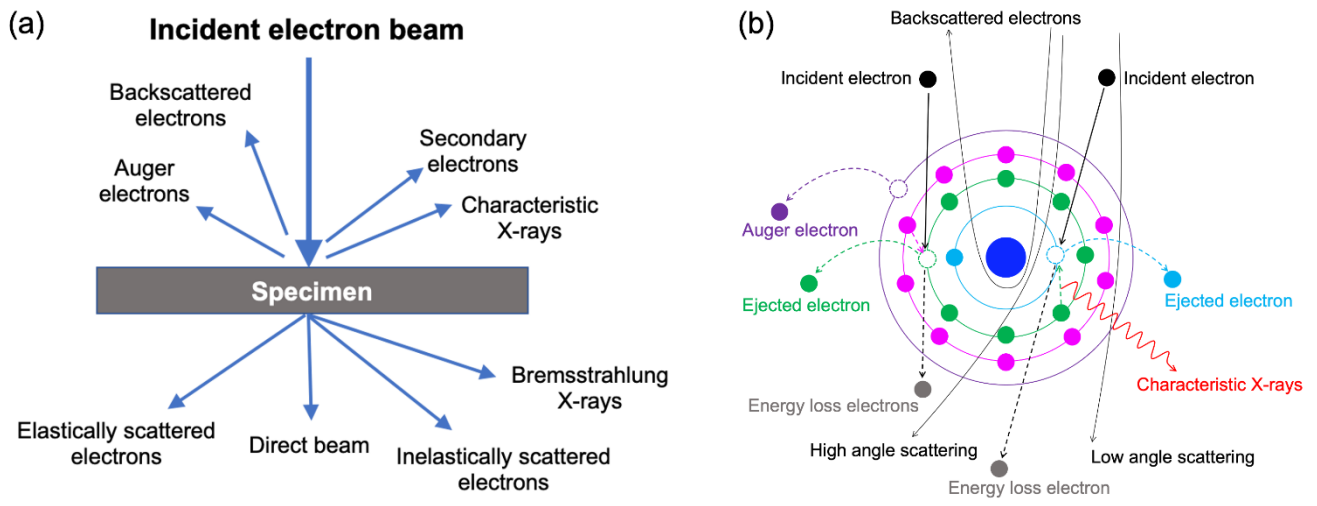

Figure 2-2 (a) Principal signals resulting from the interaction of electron beam with the specimen, and (b) schematic showing interaction of electrons with an isolated atom (modified from [173]).

If the specimen is sufficiently thin (~ 100 nm) to be 'transparent' to electrons, the incident electrons can transmit it. Imaging with the aid of these transmitted electrons forms the basis for transmission electron microscopy (TEM). As the electron beam transmits the specimen, it is scattered in multiple directions (Figure 2-2 (a)). These interactions are either inelastic or elastic depending on whether the incident electrons lose energy or not. The elastically scattered electrons are the major source of contrast in bright-field (BF), dark-field (DF) as well as high resolution (HR) TEM imaging. The elastically scattered electrons can undergo low or high-angle scattering as shown for a single atom in Figure 2-2 (b). Low angle scattering mostly results from the interaction of electrons with the outer electron cloud of an atom. The electrons that mainly scatter elastically at low angles can interfere coherently and result in diffraction. Electrons getting close to the nucleus are strongly attracted by it. These elastic electron-nucleus interactions result in Rutherford scattering to high angles, which primarily depends on the atomic number (Z) of the element. The Rutherford scattered electrons contribute to Z-contrast during imaging in TEM or scanning TEM (STEM).

During transmission, some of the electrons lose energy due to inelastic scattering. The energy distribution of the electrons can be analyzed by electron energy loss spectroscopy (EELS). Inelastically scattered electrons and the signals generated from them primarily provide information about the chemical composition of the specimen. The incident electron loses characteristic energy in knocking out an inner shell electron from an atom characteristic for that element. Depending on the energy lost by the electrons, these can be broadly classified into low or high energy loss regions in the EELS spectrum. The electrons that transmit the specimen without losing energy contribute to the high-intensity zero-loss peak (ZLP). The low-loss region (0-50 eV) corresponds to the excitation of electrons in the delocalized orbitals and consists of information related to the weakly bound valence and conduction band electrons. The high-loss region (50-4000 eV) corresponds to the excitation of localized orbitals in an atom to the unoccupied states above the Fermi level. It provides information related to the strongly bounded core-shell electrons, atomic bonding, band structure, elemental composition, atom-specific radial distribution function, etc.

2.2.2 Crystallography in Materials

Periodicity at the atomic or molecular scale is a fundamental property of crystalline materials. A crystal lattice describes the periodic arrangement of lattice points with translational symmetry. The lattice can be represented using a set of three non-coplanar fundamental translation vectors (Figure 2-3). A unit cell, which can be a single atom or a group of atoms, when placed at each lattice point generates the full periodic crystal structure. The lattice is characterized by the lengths of the fundamental translation vectors a, b, and c and the angles between them α, β and γ. The entire crystal can be generated by translation of the unit cell by the fundamental vectors as:

$$d_{xyz} = x*a + y*b + z*c \qquad 2\text{-}4$$

where d_{xyz} represents the vector joining the origin to the lattice point with coordinates x, y, and z. Crystal structures can be classified into 7 crystal systems and 14 Bravais lattices with varying symmetries. Amongst these the cubic systems possess the highest symmetry.

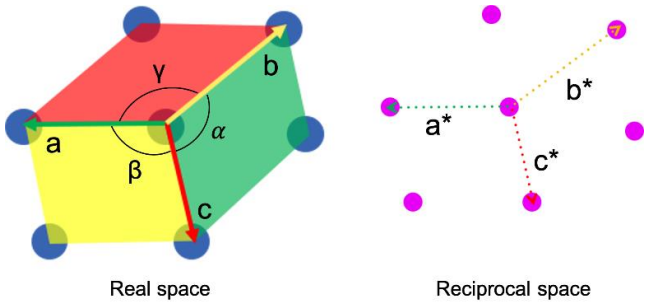

Figure 2-3 Illustration of the crystal lattice in real space and the corresponding lattice in reciprocal space.

Each crystal lattice can be described using crystallographic planes and directions. The crystallographic directions are represented in real space using vectors joining the origin of a unit cell to that of another and are expressed in the form <uvw> [174]. A family of crystallographic planes is defined by Miller indices that are usually represented by a triplet {hkl}. The (hkl) plane parallel and closest to the plane from the same family passing through the origin intercepts the unit translational vectors at a/h, b/k, and c/l [174]. Three crystallographic planes formed by the fundamental lattice translation vectors are shown in Figure 2-3. The crystallographic planes may be used to define the orientation of the crystals in single or polycrystalline samples.

A crystal lattice in real space can be associated with a corresponding lattice in reciprocal space (Figure 2-3). Each point in reciprocal space is represented by a set of lattice planes (hkl) of the crystal lattice in real space. In reciprocal space, a plane (hkl) with the lattice spacing d_{hkl} is represented by a vector of length $1/d_{hkl}$ normal to that plane. The reciprocal lattice vector is constructed by joining the origin to the corresponding reciprocal lattice point. Similar to the crystal lattice, the reciprocal lattice can be generated using the fundamental lattice translation vectors a*, b* and c*, which are mathematically related to the real space vectors as:

$$\left.\begin{aligned} a^* &= \frac{b \times c}{a.(b \times c)} \\ b^* &= \frac{c \times a}{b.(c \times a)} \\ c^* &= \frac{a \times b}{c.(a \times b)} \end{aligned}\right\} \quad 2\text{-}5$$

The present thesis is focused on body-centered cubic (BCC) and face-centered cubic (FCC) materials. Figure 2-4 shows the lattice structure of the BCC and FCC unit cells with atoms as motif located on each lattice point. Since both unit cells belong to the family of cubic lattices, the lattice translation vectors and the angles between them are a = b = c and $\alpha = \beta = \gamma = 90°$

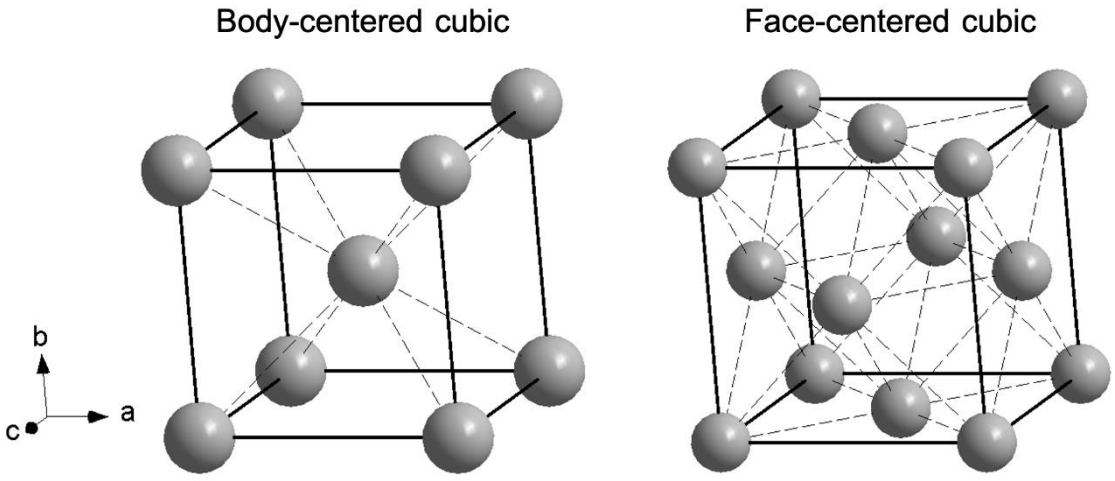

Figure 2-4 Body-centered and face-centered cubic unit cells. Solid lines indicate the edges of the unit cells whereas dashed lines indicate the connectivity between pairs of atoms.

The BCC unit cell consists of 2 atoms located at positions (0,0,0) and (1/2, 1/2, 1/2). The atom at the origin is located at the corner of the unit cell and it is shared with 8 neighboring unit cells. The second atom is located at the center of the unit cell. The atom at the center is connected to 8 atoms located at the corner of the unit cell. For BCC, the {110} planes are the most densely packed planes and the <111> directions are

the most densely packed directions. Slip during mechanical deformation occurs on the {110} as well as the {112} and the {123} planes along the <111> directions.

The FCC unit cell consists of 4 atoms each located at (0,0,0), (1/2, 1/2, 0), (0, 1/2, 1/2) and (1/2, 0, 1/2). The atom at the origin is located at the corner of the unit cell and is shared with 8 neighboring unit cells. The other 3 atoms are located at the center of each face of the unit cell. Each atom at these faces is shared between 2 unit cells. The atoms at the center of each face are connected to 4 atoms at the corners as well as 8 atoms that are at the center of the orthogonal faces. Thus, the atoms at the face center have the coordination number 12. FCC has a greater packing fraction or atomic density compared to the BCC unit cell. The ideal stacking sequence of the atomic layers in FCC structure is in the form ABCABC… which constitutes the typical cubic close-packed structure. For FCC, the {111} planes are the close-packed planes and the <110> directions are the close-packed directions. They constitute the primary slip system during mechanical deformation.

2.2.3 Electron Diffraction

Electron diffraction occurs due to coherent elastic scattering of incident electrons by specimen along with certain directions. To interpret electron diffraction, the electrons are treated as plane waves illuminating the specimen. The incident plane wavefront propagating along a given direction can be expressed using a time-independent term as:

$$\boldsymbol{\Psi}_i (r) = \boldsymbol{\Psi}_o e^{2\pi i k r} \qquad 2\text{-}6$$

where $\boldsymbol{\Psi}_i (r)$ is the wave function describing the incident wavefront, $\boldsymbol{\Psi}_o$ is the amplitude of the wave, k is the wave vector and r is the distance propagated by the wave. The plane electron wave elastically scattered by an atom can be described by a spherical wave function as:

$$\boldsymbol{\Psi}_{sc} (r, \theta) = \boldsymbol{\Psi}_o f (\theta) \frac{e^{2\pi i k r}}{r} \qquad 2\text{-}7$$

where $\boldsymbol{\Psi}_{sc} (r, \theta)$ is the wave function describing the scattered wavefront, θ is the angle of scattering, f (θ) is the atomic scattering factor, which depends on the atomic number (Z). The resultant wavefront ($\boldsymbol{\Psi}_r$) is the sum of the incident and scattered wavefronts:

$$\boldsymbol{\Psi}_r = \boldsymbol{\Psi}_i + \boldsymbol{\Psi}_{sc} = \boldsymbol{\Psi}_o \left[e^{2\pi i k r} + f (\theta) \frac{e^{2\pi i k r}}{r} \right] \qquad 2\text{-}8$$

Figure 2-5 (a) shows a parallel beam of electrons traveling along paths P1 and P2, incident at an angle θ to crystal planes with interplanar spacing d. As the rays are inclined to the planes, it is seen that P2 travels a different distance compared to P1. From the geometry, a path length difference of d sin θ is introduced between the rays as the parallel rays are incident on the two crystal planes. The difference in the path length results in a change in the phase of the waves. Constructive interference of the waves occurs if the path length difference is an integral multiple of the wavelength (Figure 2-5 (b)). On the other hand, when completely out of phase, they cancel each other and lead to destructive interference. The waves resulting from the constructive interference are termed as the diffracted beams and these occur only in certain directions defined by Bragg's law expressed as:

$$\lambda = 2 * d_{hkl} \sin \theta \qquad 2\text{-}9$$

where λ is the wavelength of the electron wave and d_{hkl} is the interplanar spacing between the planes with Miller indices hkl.

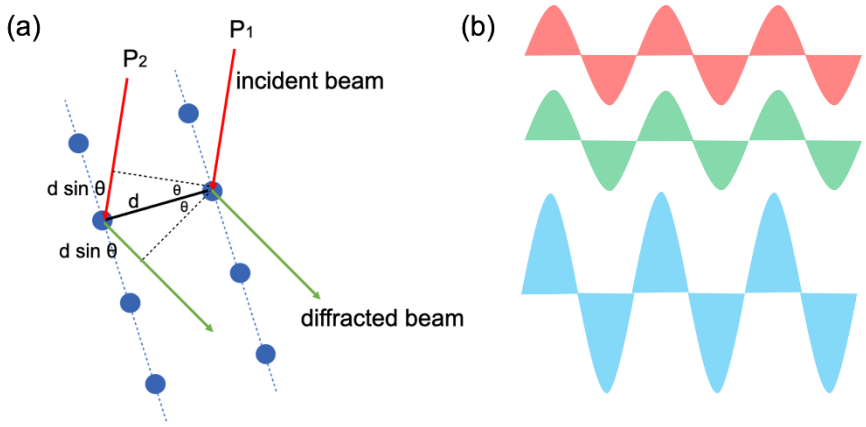

Figure 2-5 (a) Illustration of diffraction of the waves scattered by crystal planes, and (b) sinusoidal waves with a phase difference of integral multiple of 2π reinforce each other leading to constructive interference.

Bragg's law (Eq. 2-9) derived using the crystal lattice in real space can be expressed using reciprocal space or k-space as well. To realize that, two wave vectors K_i and K_d in the direction of the incident and scattered waves are considered in Figure 2-6. The length of these vectors is $1/\lambda$. Diffraction of plane waves occurs if these are coherent. The vector (K) describes the difference between incident and scattered wave:

$$K = K_d - K_i \qquad 2\text{-}10$$

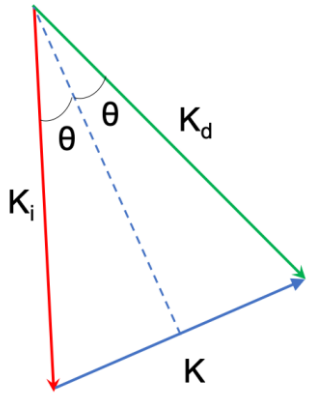

Figure 2-6 Illustration of the incident and diffracted wave vectors in k-space.

From the geometric arrangement of the vectors K_i, K_d, and K in Figure 2-6:

$$|K| / 2 = |K_i| \sin\theta = |K_d| \sin\theta = \sin\theta / \lambda \qquad 2\text{-}11$$

$$|K| = 2 \sin\theta / \lambda \qquad 2\text{-}12$$

At the Bragg condition (Eq. 2-9) with $\theta = \theta_B$,

$$1/\lambda = 1 / 2d_{hkl} \sin \theta_B \qquad 2\text{-}13$$

Eq. 2-12 and Eq. 2-13 lead to

$$|K| = 1 / d_{hkl} = g_{hkl} \qquad 2\text{-}14$$

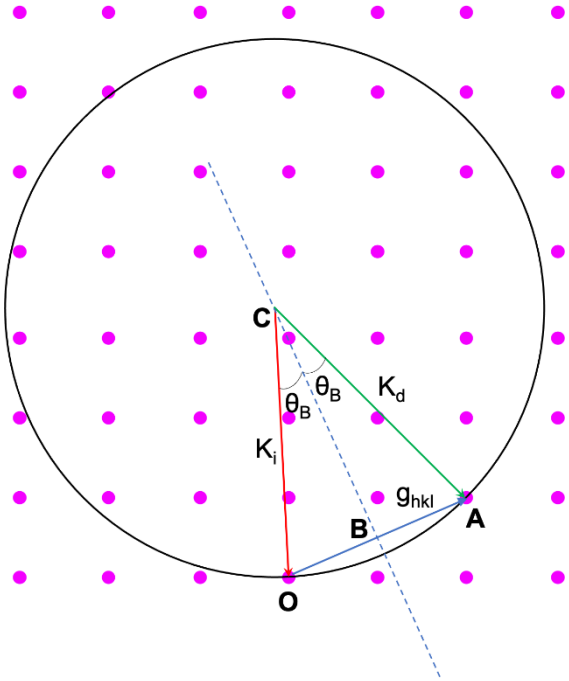

Figure 2-7 Illustration of Bragg's law in reciprocal space using the Ewald sphere of reflection.

The Ewald sphere construction is a convenient approach to visualize the Bragg conditions in the 3D reciprocal space. The Ewald sphere is a sphere of radius $1/\lambda$ that passes through the origin O of the reciprocal lattice and is represented by a circle in 2D. The incident wave vector K_i is drawn passing through O and it defines the center C of the sphere (Figure 2-7). The scattered wave vectors may be drawn in any direction from C and will have the same length equal to $1/\lambda$. As explained above, constructive interference can occur when $K = K_d - K_i$ corresponds to g_{hkl} with the scattered wave vectors ending on a reciprocal lattice point. This is represented by OA in the present case. From the geometry in Figure 2-7, CB bisects angle ACO. It is perpendicular to g_{hkl} and thus represents a plane perpendicular to g_{hkl}. Therefore, $K_d - K_i$ represents a vector OA which is perpendicular to the (hkl) plane. For any point of the reciprocal lattice that intersects the Ewald sphere, the Bragg condition is satisfied for the set of planes corresponding to the point of intersection. Thus, at the Bragg diffraction condition:

$$K = K_d - K_i = g_{hkl} = ha^* + kb^* + lc^* \qquad 2\text{-}15$$

The reciprocal lattice can be treated as an array of points in 3D if the specimen is perfect and infinite in all directions. However, in practice, TEM specimens are thin (< 200 nm) along the direction parallel to the incident electron beam. The small thickness of the specimen in real space leads to an elongation parallel to the incident beam in reciprocal space (Figure 2-8). These elongated diffraction spots are often termed as 'rel-rods' and their length is inversely proportional to the thickness of the specimen. If the Ewald sphere

intersects these rel-rods, Bragg's reflection can still be excited even if the Bragg condition is not exactly satisfied. The intensity of these reflections is dependent on the extent of their deviation from the exact Bragg condition. This deviation can be quantified using the excitation error s. From Figure 2-8, K is expressed as:

$$K = g + s \qquad 2\text{-}16$$

s in the above equation may be changed by tilting the specimen or by tilting the beam. Tilting the beam shifts the Ewald's sphere as K_i is tilted whereas tilting the specimen moves the reciprocal lattice itself.

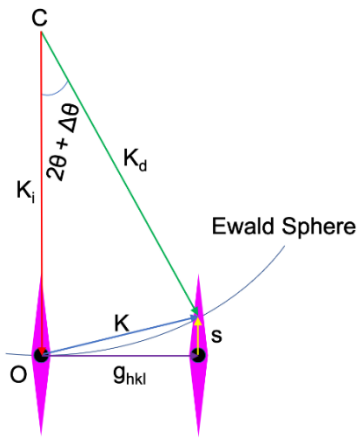

Figure 2-8 Illustration of excitation error and the diffraction at 'non-Bragg' condition.

The intensity of the diffraction spots arises as a result of scattering from atoms present in the crystal unit cell. To evaluate the intensities, contributions from the atoms in the crystal unit cell are taken into account. In kinematical diffraction theory, the intensities are described by superimposing the wave functions scattered from each atom considering the specific position in the unit cell. From Eq. 2-7, the intensity of the scattered waves from an atom can be summed for all the atoms in the unit cell and the scattered wave function for the cell ($\boldsymbol{\Psi}_{cell}$) can be calculated as:

$$\boldsymbol{\Psi}_{cell} = \frac{e^{2\pi i k r}}{r} \sum_{m=1}^{n} f_m \exp(2\pi i K.r_m) \qquad 2\text{-}17$$

Using the above formulation, a simplified form of the structure factor related to scattered waves from the cell can be expressed as:

$$F_{cell}(\theta) = \sum_{m=1}^{n} f_m(\theta) \exp(2\pi i K.r_m) = \sum_{m=1}^{n} f_m(\theta) \exp(2\pi i g_{hkl} . r_m) \qquad 2\text{-}18$$

where F_{cell} is called the structure factor of the unit cell that expresses the amplitude and the phase shift of the reflection corresponding to hkl, f_m is the atomic scattering factor, n is the number of atoms in the unit cell, θ is the scattering angle, K is the change in the wave vector, r_m is the position each atom in the unit cell, g_{hkl} is the reciprocal lattice vector for a given lattice plane. The intensity of the reflection g_{hkl} is proportional to the square of the corresponding structure factor F_{hkl}. The kinematic approach, thus, allows predicting the intensities of the Bragg reflections, which are important for identifying crystal structure as well as crystal orientations.

2.3 Scanning Electron Microscopy and Focused Ion Beam

Scanning electron microscopy (SEM) is a technique in which a finely focused electron beam is scanned over a specific region of a sample with a defined step size. As shown in the schematic (Figure 2-9), an SEM consists of an electron gun, an electromagnetic lens system, and a detection system. The beam is generated by an electron source and typically accelerated with a voltage in the range of 1 to 30 kV. The condenser lens demagnifies the electron beam cross-over produced by the gun. The scanning coils deflect the beam and move it along discrete points to generate a rectangular raster on the specimen. Finally, the objective lens further demagnifies and focuses the electron probe on the specimen. The electron beam scanning the sample interacts with a localized region of the sample and generates SEs, BSEs, AEs, X-rays, etc. SEs and a fraction of BSEs are collected by an Everhart-Thornley detector (ETD). It is asymmetrically located with respect to the sample inside the SEM and is highly directional in collecting the electrons. Mainly the low energy SEs are collected by applying a positive bias to the ETD. The BSEs are mainly detected with the aid of a dedicated BSE detector located almost symmetrically above the specimen to collect electrons with a high take-off angle with high collection efficiency [172]. A through-the-lens detector (TLD) efficiently collects SEs with the aid of the magnetic field of the objective lens to direct the SEs to a detector inside the column. The X-rays are collected by an energy dispersive X-ray spectrometer (EDS) which consists of a solid-state silicon drift detector that absorbs X-ray photons and an X-ray spectrum is produced with the aid of a charge-to-voltage converter.

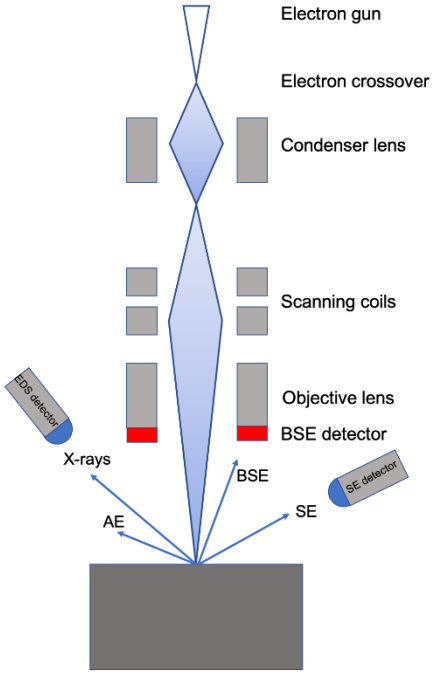

Figure 2-9 Schematic of SEM showing the electron source, lenses, and the detection system.

A focused ion beam (FIB) system is similar to an SEM considering the operational procedure. One of the basic differences is that the beam scanned over the sample is an ion beam. Typically, a finely focused ion beam is generated from a gallium liquid metal ion source (LMIS) [175,176]. A dual-beam FIB comprises both a scanning electron beam and a scanning Ga^+ ion source inclined at a defined angle (typically 52°) to it. The ion beam is used for precise milling or patterning at the micro-/nanoscale while the electron beam is used for imaging. Further, a dual-beam FIB can be equipped with a gas injection system (GIS) for depositing metals and insulators. The combination of an SEM and a FIB in one equipment thus provides a versatile micro- and nanoscale fabrication and analytical tool.

In the present work, a FEI Strata 400S Dualbeam system was employed for conventional as well as *in situ* TEM specimen preparation. For the preparation of a conventional TEM lamella, a protective Pt layer is

initially deposited on the region of interest. This is followed by milling around this region to form rectangular trenches. The dimensions of these trenches depend on the size of the desired lamella. The lamella is partially cut from the specimen using the ion beam. A micromanipulator is navigated and brought close to a corner of the lamella and welded, typically using Pt. The lamella is then detached from the bulk and lifted from the specimen. Afterwards, the specimen is transferred and welded to a TEM grid. Final thinning of the lamella is performed from both sides using Ga^+ ions by sequential under- and over-tilting the stage.

One of the critical aspects to be considered during specimen preparation is the implantation of Ga^+ and the resulting FIB-induced damage. The impact of the high-energy Ga^+ on the specimen does not only lead to the removal of material by sputtering but also the formation of a damage layer at the surface and gallium implantation [177]. The damage may result in amorphization of the specimen, incorporation of point defects or dislocations and it may extend several tens of nanometers in the specimen. The extent of this damage is governed by the ion beam energy, the incidence angle during milling as well as the ion current. Therefore, the TEM specimens for the present study were prepared by milling using the following parameters:

- adjusting the over and under-tilt of the stage (tilted by 52°) in the range of ± 5° to produce a uniform sample thickness
- reducing the accelerating voltage in steps from initially 30 kV to 16 kV, 8 kV, and 2 kV for the final polishing
- reducing the beam current from a few nA to a few tens of pA as the thinning progressed.

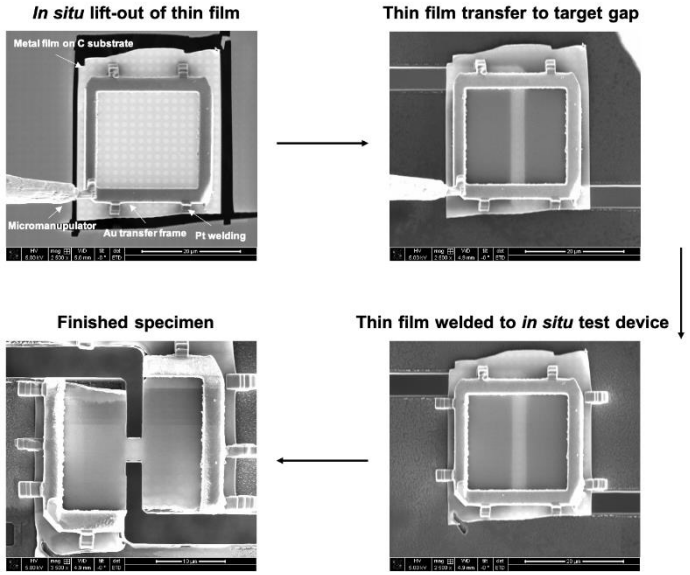

Figure 2-10 Procedure for *in situ* lift-out of a thin film, transfer and mounting it on an *in situ* testing device inside FIB.

The FIB-induced damage and ion implantation become even more critical for the transfer and preparation of *in situ* TEM specimens. Figure 2-10 shows the transfer process of a thin metallic film to an *in situ* straining device inside the FIB. The *in situ* transfer is achieved with the aid of a rectangular transfer frame made of gold. The frame is initially attached to the micromanipulator, which is brought in contact with the film and welded to it. The transfer frame offers good mechanical stability to the film and allows for its parallel placement on the device with minimum bending or folding. During this transfer process, the specimen is not exposed to the ion beam to prevent damage or Ga^+ implantation. The film along with the frame is transferred and attached to the *in situ* devices using Pt. Pt is deposited using the e-beam, which has proven to minimize contamination. A portion of the transfer frame and the thin film is milled through the gap of the device to produce a thin film specimen of desired dimensions for *in situ* TEM experiments. As a last step in the preparation, the *in situ* specimens in the present study were cleaned using a Fischione 1040 NanoMill, which uses Argon ions at low voltages of less than 500 eV. This facilitated the removal of any residual Pt contamination that occurred during the preparation.

2.4 Transmission Electron Microscopy

Transmission electron microscopy (TEM) is a technique in which a beam of high-energy electrons illuminates and transmits a thin specimen. The transmitted electrons are used to form images, diffraction patterns, and energy loss spectra that allow for obtaining information related to the structure and chemistry of the materials down to the atomic scale. The instrumental set-up of a TEM consists of an electron gun, a series of electromagnetic lenses, and a detection system as schematically shown in Figure 2-11. The electron gun extracts electrons from the source and generates a fine cross-over. The gun cross-over acts as an object for the first condenser lens (C1). The primary role of the C1 lens is to form a demagnified image of this cross-over which acts as an object for the second condenser lens (C2). The C1 lens controls the spot size in TEM. A higher spot size means a greater lens current, smaller beam size, and reduced beam current. The C1 and C2 lenses operate together to control the intensity and size of the illuminated area with the aid of the condenser aperture. The C1 and C2 lenses work in conjunction with the upper objective (pre-field) lens to illuminate the specimen in parallel or convergent beam mode. The electron beam after transmitting the specimen is collected by the lower part of the objective lens, which operates to form a diffraction pattern at its back-focal plane and an image at the intermediate image plane. To see an image or diffraction pattern from the specimen, the strength of the intermediate lens is adjusted such that the image or the back-focal plane of the objective lens acts as the object plane of the intermediate lens (as seen in Figure 2-12). The image or diffraction patterns are projected on a viewing screen, charge-coupled device (CCD) camera, or other detectors using the projector lens system. The energy loss electrons are collected by an image filter to produce EELS spectra and energy-filtered images.

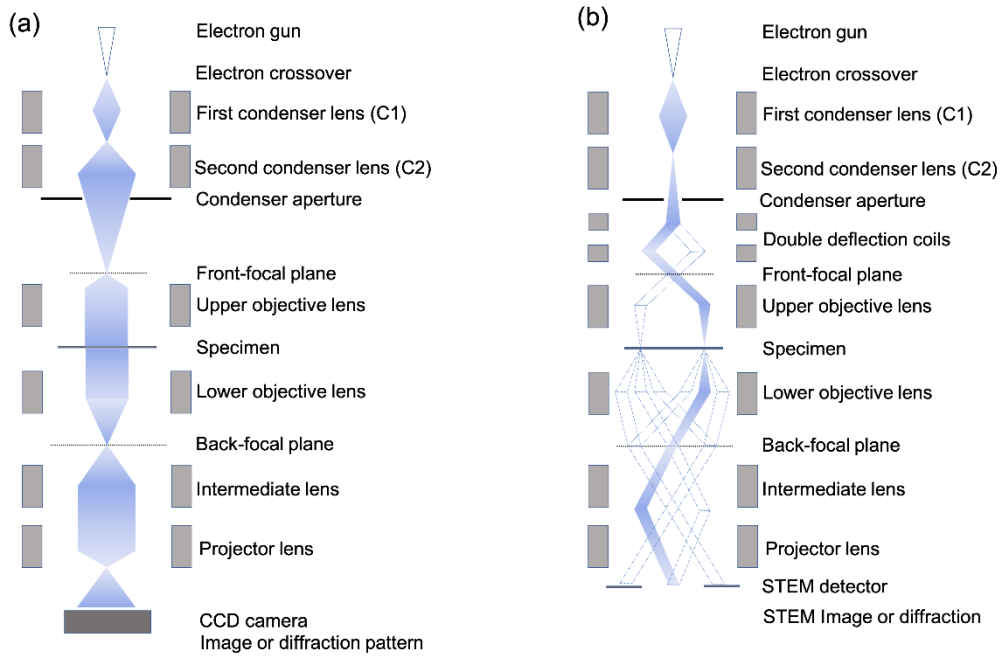

Figure 2-11 Ray diagrams illustrating the optics in a conventional TEM showing the electron source and electromagnetic lenses constituting the illumination, imaging, and projection system in (a) TEM mode and (b) STEM mode.

In the present study, two transmission electron microscopes, a Tecnai F20 ST and a Titan 80-300 from the FEI company were employed for the structural and compositional characterization. The Tecnai operated at 200 kV and the Titan operated at 300 kV were equipped with a two- and three-condenser lens system, respectively. Both microscopes were used for classical TEM imaging, electron diffraction, and scanning TEM using a high angle annular dark-field (HAADF) detector. The Tecnai was further equipped with a DigiSTAR system from NanoMEGAS which was mainly used for automated crystal orientation and phase mapping. The Titan was used to perform energy-filtered TEM spectral imaging (EFTEM-SI) for thickness mapping as well as compositional characterization by elemental mapping.

2.4.1 TEM Imaging and Diffraction

For TEM imaging (Figure 2-11 (a)), the C1 lens produces a demagnified image of the cross-over before the C2 lens. The C2 lens further focuses and forms an image of the C1 cross-over on the front focal plane of the upper objective lens. The upper objective lens then illuminates the specimen with a parallel beam of electrons. Figure 2-12 shows the optical ray diagrams illustrating the image and diffraction pattern formation in a TEM. All rays scattered in the same direction from the object are focused by the objective lens at the same point on the back-focal plane to form a diffraction pattern whereas all rays emanating from the specimen are focused by the objective lens to meet on the conjugate (image) plane of the objective lens, thereby forming an image of the specimen. Coherent interference between the direct and diffracted beams from the specimen results in the formation of contrast in the images [178]. The direct and/or diffracted beams are selected with the aid of an objective aperture which is inserted in the back-focal plane of the objective lens. The scattered electrons selected using the objective aperture in the back-focal plane are an effective source for image formation. The size of the aperture controls the spatial frequencies in Fourier space that are allowed to form the image and thus limit the spatial resolution during imaging.

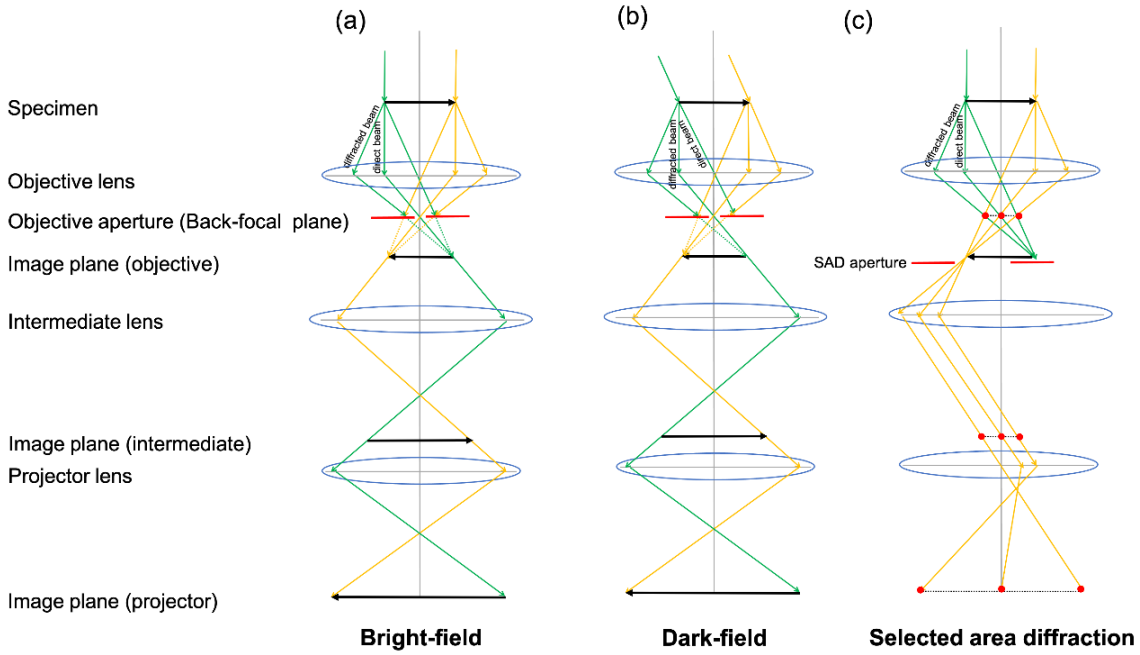

Figure 2-12 Ray diagrams describing the optics in parallel illumination modes: (a) BFTEM, (b) DFTEM, and (d) SAED.

If the direct beam is selected to form the image, a bright-field (BF) image (Figure 2-12 (a)) is formed, whereas blocking the direct beam and selecting one or more diffracted beams forms a dark-field (DF) image (Figure 2-12 (b)). For the dark-field (DF) imaging (Figure 2-12 (b)), the electron beam is tilted with respect to the optic axis so that the desired diffracted beams are parallel to the optic axis. To obtain a diffraction pattern from a specific region of the sample, a selected area diffraction (SAD) aperture (Figure 2-12 (c)) is inserted in the image plane of the objective lens to select the region of interest. The SAD aperture allows only the rays emanating from a specific region and excludes the rays that do not illuminate this region. Since the object and image planes are conjugate to each other, inserting the SAD in the image plane is equivalent to inserting a 'virtual' aperture in the plane of the specimen. The microscope is then switched to diffraction mode to form a diffraction pattern on the CCD or screen.

The images formed under parallel illumination, typically in the BFTEM, exhibit amplitude contrast. This contrast is sensitive to the atomic number and thickness (mass-thickness contrast) as well as due to the Bragg-scattering (diffraction contrast). For crystalline specimens, this contrast is mostly sensitive to the local changes in the diffraction conditions due to defects (dislocations or stacking faults), strain fields, composition, thickness, etc.

2.4.2 Scanning Transmission Electron Microscopy

In scanning transmission electron microscopy (STEM) mode, a focused probe of (sub)nanometer size is formed on the specimen and the illumination is convergent. In STEM mode, the beam scans parallel to the optic axis of the TEM without changing its direction. To achieve parallel scanning, two pairs of deflection coils deflect the beam such that the beam pivots at the front-focal plane of the upper objective lens (Figure 2-11 (b)). In STEM, the convergence angle determines the minimum probe size that can be formed at the specimen. The smallest probe diameters are obtained using large condenser apertures resulting in a convergence angle of ~10 mrad for uncorrected microscopes [150] and for C_S corrected STEM systems it is in the range of 15 to 50 mrad [179]. The convergence angle (θ_c) determines the limit of diffraction broadening (d_d) of the probe, expressed as $0.61\,\lambda/\theta_c$ (Eq. 2-2). Apart from d_d, the effective size of the probe is influenced by contributions from aberrations. Spherical aberration leads to a distortion of the wavefront causing the waves away from the optic axis to bend more than those closer to it. As a result, the rays emanating from a point in the object plane do not converge at the same point in the image plane and the point is imaged as a disk. The minimum diameter (d_{sa}) of this disk is obtained in the plane of least confusion. d_{sa} determines the resolution limit due to the spherical aberration and is given as $0.5C_s\theta_c^3$, where C_s is the spherical aberration coefficient. Chromatic aberration leads to a dispersion of the beam depending on the energy of the electrons. They are focused on different planes depending on their energy. Electrons with lower energy are more strongly focused than those with higher energy, leading to a disk of least confusion (d_c), given as $(\Delta E/E_o)C_c\theta_c$, where C_c is the chromatic aberration coefficient, ΔE is the change in energy of electrons from the initial energy of the beam, E_o. Apart from aberrations, the disk of least confusion can arise as a result of an error in focusing (Δf). Δf corresponds to the difference in the focal length of the objective lens and the focal length needed to focus the probe on the specimen. The contribution, d_f, to the probe size due to defocus is given as $2\theta_c\Delta f$. For a source with geometrical size (d_s) and taking into account lower-order aberrations, the total probe size (diameter, d_o) can be expressed by adding the quadrature of various contributions to d_o as [178]:

$$d_o^2 = d_s^2 + d_d^2 + d_{sa}^2 + d_c^2 + d_f^2 \qquad 2\text{-}19$$

The smallest probe size is obtained by simultaneously minimizing all the quantities in Eq. 2-19 and corresponds to a convergence in which the superimposed contribution from the demagnified electron source size, aberrations, and diffraction effects at the beam limiting aperture is minimal [180].

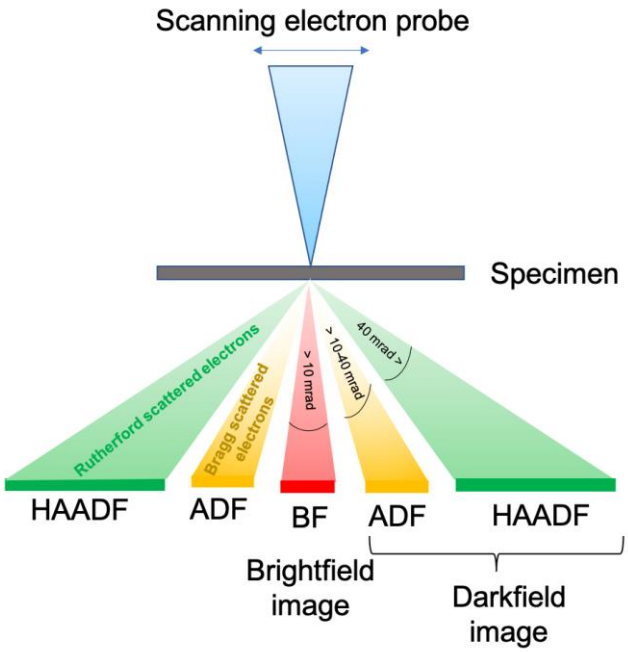

Figure 2-13 Schematic of the scanning probe and the detection system in STEM mode.

For acquiring an image, at each point during scanning, a STEM detector collects the electrons scattered in a certain angular range and records the intensity in an image (Figure 2-13). While the geometry of the detector is fixed, the electrons scattered at a specific range of angles may be suitably adjusted by the camera length 'L' that determines the collection angle. The bright-field (BF) detector collects the electrons scattered at low angles (< 10 mrad) to form BF images. The annular dark-field (ADF) detector collects the electrons scattered at intermediate (typically 10-40 mrad) scattering angles. These signals have a significant contribution from Bragg diffraction and thus allow to distinguish between different phases or crystallites of different orientations [181]. On the other hand, electrons scattering at sufficiently high angles (40 mrad or greater) contain information due to the Rutherford as well as thermal diffuse scattering and are collected by the high angle annular dark-field (HAADF) detector. The contrast obtained due to these electrons is sensitive to the atomic number 'Z' of the elements present in the specimen [182].

With small probe sizes, the convergent electron beam can be employed to acquire diffraction from small volumes to perform spatially high-resolution diffraction experiments [183]. Due to the convergence of the beam in conventional or nanoprobe STEM, each diffraction spot appears as a disk. The diameter of the diffraction disk is proportional to the convergence angle. Each point within the disk corresponds to a distinct direction within the cone of illumination. Large convergence angles of several mrad lead to overlapping diffraction disks. This makes the diffraction disks difficult to interpret, especially if the crystal is out of zone axis orientation and a limited number of disks are present in the diffraction pattern. As a result, nanoprobe STEM imaging with large convergence angles is not suited for orientation identification of the individual grains in nc materials.

Quasi-parallel probes with reduced convergence angles can be formed by using STEM imaging in microprobe mode. Figure 2-14 represents the optics of the probe formation in microprobe (red rays) as well as in nanoprobe (green rays) STEM modes. In nanoprobe mode, the upper objective lens produces a strongly demagnified image of the C1 crossover on the specimen. In microprobe mode, a mini condenser (MC) lens is used unlike in the nanoprobe mode for which the lens current is inverted in the FEI twin-lens systems. In this mode, the C2 lens setting remains the same as in nanoprobe mode and a beam cross-over is formed above the MC lens. The MC lens uses this crossover and works in combination with the upper objective lens to form a probe on the specimen. From Figure 2-14, it is understood that reducing the strength of the C2 lens and a strong excitation of the MC lens can reduce the convergence angle.

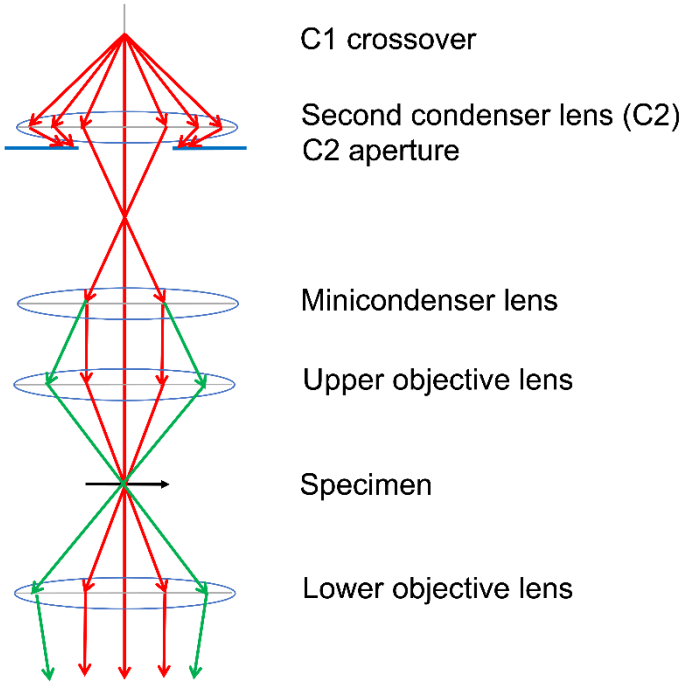

Figure 2-14 Ray diagram illustrating the optics of forming a quasi-parallel probe in microprobe STEM mode (red rays). As a comparison, green rays are indicating the nanoprobe STEM mode.

The C2 aperture plays a critical role in selecting the electrons that emanate from the C1 crossover and are transferred by the C2 lens. From both the green and red rays (Figure 2-14), it is understood that the size of the C2 aperture defines the maximum acceptance or collection angle of the beams transferred by the C2 lens. The strength of the C2 and MC lenses and the C2 aperture size control the convergence angle. In nanoprobe mode, even with the smallest condenser aperture, the convergence angle obtained at the specimen is still larger compared to the microprobe mode. The beam convergence is reduced using a smaller condenser aperture (30-50 μm) to produce a semi-convergent beam in the range 0.5-2 mrad [184,185]. With the low convergence angles and achievable probe sizes of 1 nm, microprobe STEM imaging is a useful approach for STEM diffraction mapping of nc materials. As a sufficient number of diffraction spots can be obtained, this approach is well-suited for reliable identification of the orientation of crystallites that are randomly oriented including the ones away from zone-axis orientations.

2.4.3 Precession Electron Diffraction

Precession electron diffraction (PED) is a technique developed by Vincent and Midgley in the mid-1990s [186]. This technique enables the acquisition of electron diffraction patterns whose intensities appear to be less sensitive to dynamic scattering effects thereby making the diffracted intensities more suitable for solving crystal structures [187]. This was achieved by rocking the incident electron beam in a hollow conical above the specimen and compensating by additional hollow conical de-rocking below the specimen as shown in Figure 2-15. By de-rocking below the specimen, the circular motion of the reflections is arrested to produce a stationary diffraction pattern that has the same geometry as a conventional pattern [188]. This procedure is known as the double-conical beam-rocking, which is equivalent to precessing the specimen at a fixed angle around the beam direction as the diffraction pattern is recorded [186].

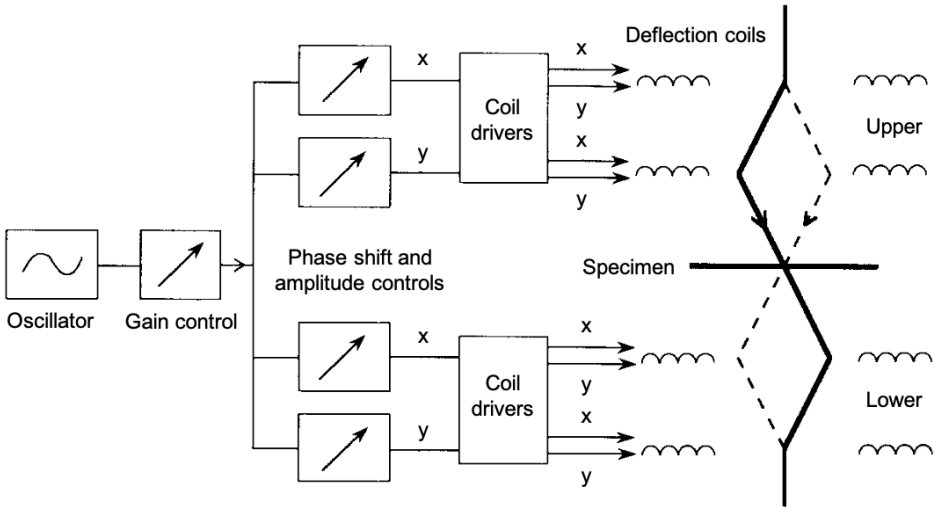

Figure 2-15 Block diagram of the electronics driving the double-conical scanning system for the deflection coils above and below the specimen (modified from [186]).

For thin TEM specimens, the reciprocal lattice points are elongated and the diffracted intensities depend on the excitation error s (Figure 2-8). A small change in the specimen tilt affects the resulting intensities for classical diffraction patterns without precession. In PED, the Ewald sphere systematically moves and spans over a specific angular range in 3D reciprocal space (Figure 2-16). As the Ewald sphere moves, it intersects multiple reciprocal lattice points thereby exciting several reflections compared to the case of a beam without precession. In addition, for almost all reflections, the Ewald sphere covers the entire range of excitation errors for which Bragg's reflections are still visible. As a result, the intensities in a PED pattern are integrated through the Bragg condition. The diffraction intensities closer to kinematic conditions facilitate the identification of crystal symmetry. Furthermore, the constantly precessing beam suppresses multiple scattering events that result in dynamical diffraction. Thus, the intensities of reflections are closer to those under kinematical conditions.

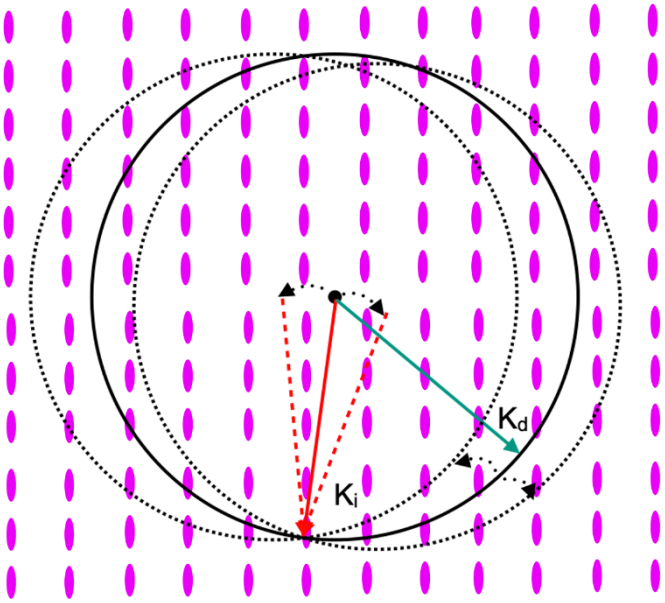

Figure 2-16 Excitation of multiple Bragg's reflections due to the precession of incident electron beam.

A large number of diffraction spots and their kinematic intensity distribution make PED an ideal approach for orientation determination by template matching [189]. Scanning precession electron diffraction (SPED) can be employed to obtain information spanning several micrometers of the specimen area with a nanometer spatial resolution. Thus, SPED is used to extract quantitative crystal orientation and phase information from a large number of crystallites with sizes in the nanoscale regime.

2.4.4 Automated Crystal Orientation Mapping in STEM

Automated crystal orientation mapping in STEM (ACOM-STEM) is a technique in which a probe of electron scans the specimen with or without precession and acquires the electron diffraction patterns from each point. The electron diffraction patterns are collected either using a CCD camera or a fast frame capture camera [188,190]. Scanning and precession are controlled by a dedicated external device for PED, called the DigiSTAR™ system from NanoMEGAS company, Brussels, Belgium, for which the TEM itself does not need to be equipped with an additional scanning system [190–193]. A schematic of the ACOM-STEM is shown in Figure 2-17 indicating the coils used for performing the scanning and precession functions. These functions are controlled by the Topspin™ user interface.

In the present work, this technique was employed in microprobe (μProbe) STEM mode on a FEI Tecnai F20-ST TEM operated at 200 kV. A fine probe of approximately 1 nm is formed in this mode with a quasi-parallel beam of electrons using a condenser aperture of 30 μm leading to a semi-convergence angle of around 1 mrad. The precession of the beam is accomplished using two pairs of coils above the specimen named beam deflection coils upper X and Y and beam deflection coils lower X and Y (Figure 2-17) that induce a circular rotation of the electron beam on the front-focal plane of the upper objective lens. To perform this rotation, the signals that are sent to each deflection coil are generally of a sinusoidal form. Thus, the parameters defining each signal are the amplitude, the phase, and the offset (Figure 2-15) [186,194]. Depending on these parameters, a varying range of precession angles can be achieved. In the present work, precession angles were used in the range 0.3° to 0.5°. As discussed in the previous section, the precession of the electron beam is 'descanned' below the specimen to get a stationary diffraction pattern. The stationary diffraction pattern is projected on a fluorescent screen and imaged using the Stingray camera with a typical acquisition rate of 100 frames per second. As illustrated in Figure 2-18, at each beam position, the corresponding diffraction pattern is recorded and an image can be formed by using a virtual aperture in the Topspin™ user interface.

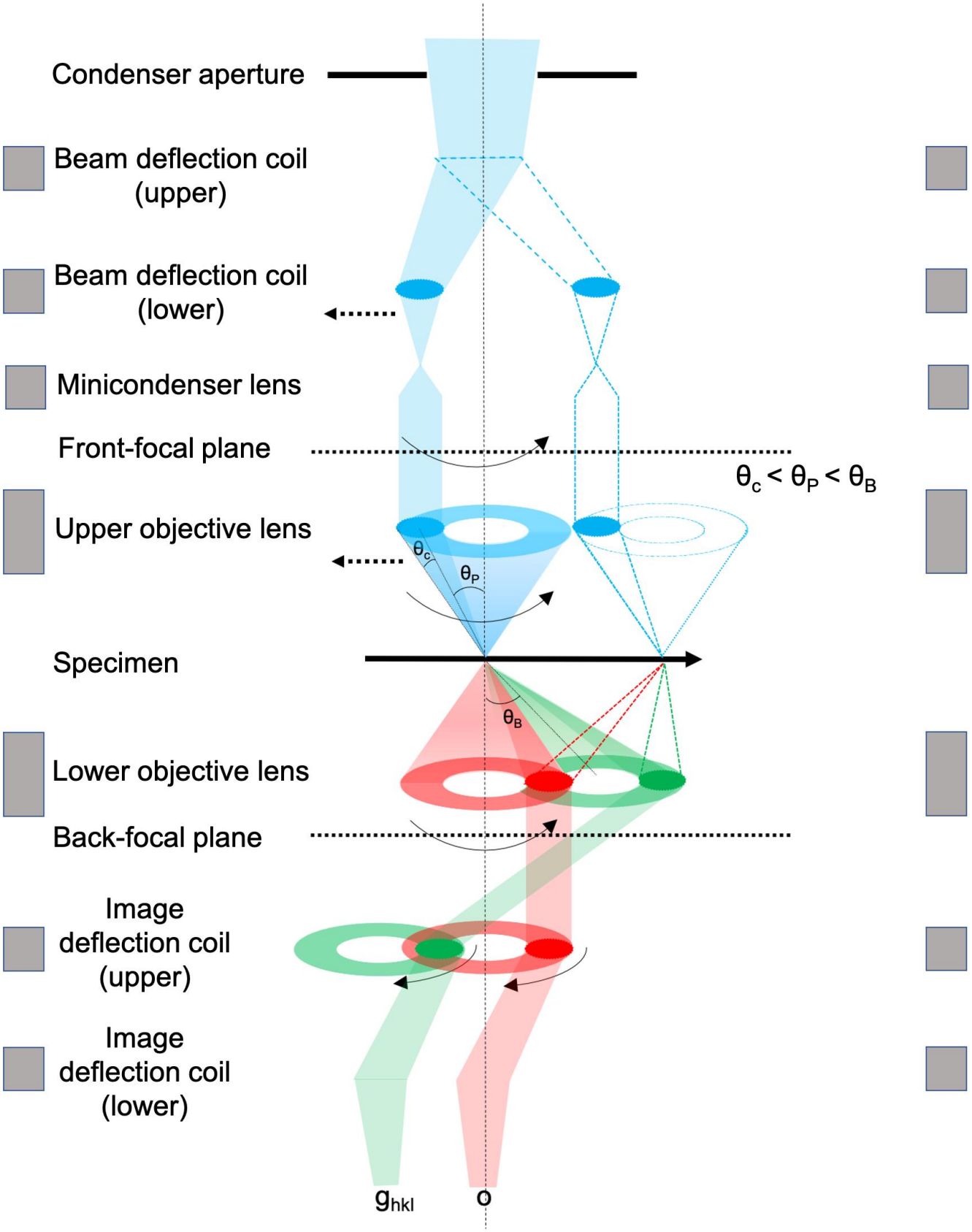

Figure 2-17 Ray diagram illustrating the automated crystal orientation mapping in microprobe STEM mode with the precessing electron beam.

The typical step size used is in the range 1-4 nm depending on the desired resolution for the features of interest and a typical sampling size is 2 µm × 2 µm. Since each pixel in the resulting 2D image consists of a 2D diffraction pattern, the technique is sometimes also referred to as 4D STEM. The details regarding indexing of the diffraction data to obtain orientation and phase maps will be introduced in the next chapter. The major advantages of the ACOM-STEM may be summarized as follows:

- the spatial resolution of 1 nm and angular resolution of about 0.4° for a single measurement with reasonable statistics for reliable quantification
- precession of the incident electron beam leads to excitation of a larger number of reflections which enables more accurate orientation determination
- precession allows for the acquisition of diffraction patterns with near-kinematical conditions by integrating the intensities over a large interval of the excitation error and suppressing dynamic diffraction effects
- full crystallographic orientation information including both in and off-zone axis orientations unlike classical imaging techniques like DFTEM, BFTEM, nanobeam diffraction or CBED
- operation in µProbe STEM mode allows for the acquisition of fast overview/reference images without switching from diffraction to image mode making it more suitable for *in situ* TEM investigations to obtain correlative information from a local area of the specimen
- from the crystallographic information obtained from each crystallite, a more comprehensive quantitative understanding of various microstructural parameters like accurate grain size distribution, GB character (e.g. twin boundaries and CSL boundaries), GB misorientation distribution, intragranular misorientation, global texture analysis, the spatial distribution of phases, etc. is achievable

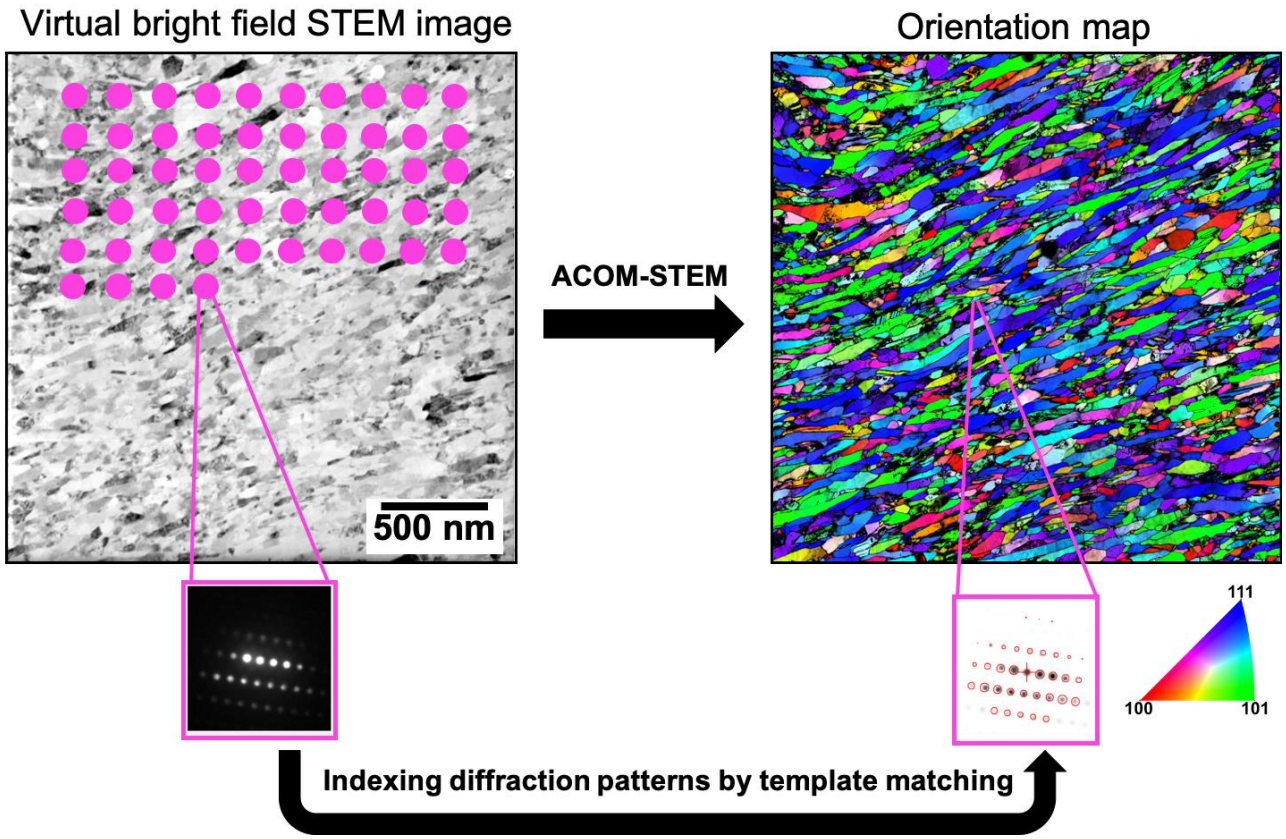

Figure 2-18 Application example of precession assisted automated crystal orientation mapping in TEM showing orientation mapping of a deformed FCC high entropy alloy revealing the structure with several hundred nanoscaled grains with an average grain size of 50 nm, sample provided by Benjamin Macdonald, University of California, Irvine, USA. The mapping was performed using µProbe STEM mode with step size 2 nm, precession angle 0.5°, camera length 80 mm and the total area scanned was 2.4 µm × 2.4 µm. The virtual bright-field STEM image is formed by using the central beam in the electron diffraction patterns during acquisition.

2.4.5 Energy Filtered Transmission Electron Microscopy

Electron energy loss spectroscopy (EELS) is a technique used for analyzing the energy distribution of the electrons transmitting the specimen. The inelastically scattered electrons provide information about the atomic and electronic structure of the material and produce images with contrast sensitive to chemical composition. In the Titan 80-300, the EELS setup primarily consists of a magnetic prism installed below the viewing screen of the TEM. The prism collects the electrons from the projector crossover and separates them in the form of a spectrum based on their energy loss. The electrons with higher energy loss are deflected stronger compared to the low-loss or zero-loss electrons, forming a spectrum in the dispersion plane with the electron intensity analyzed versus the energy loss. The electrons coming from the projector crossover could be selected by a variable entrance aperture before they enter the prism. The size of the projector crossover and entrance aperture is critical in defining the energy resolution in EELS. A small crossover and a smaller aperture offer a better energy resolution by excluding the electrons traveling off-axis at larger angles, thereby minimizing the influence of aberrations. The scattering cross-section of the electrons is highly sensitive to the scattering angle and electrons with a given energy loss are scattered within a specific angular range. As a result, the collection angle of the spectrometer becomes crucial in governing the intensities in the EELS spectrum which is important for quantitative analysis. In TEM/STEM diffraction modes, the collection angle is controlled by the size of the entrance aperture, whereas in the TEM image mode, it is controlled by the size of the objective aperture [173].

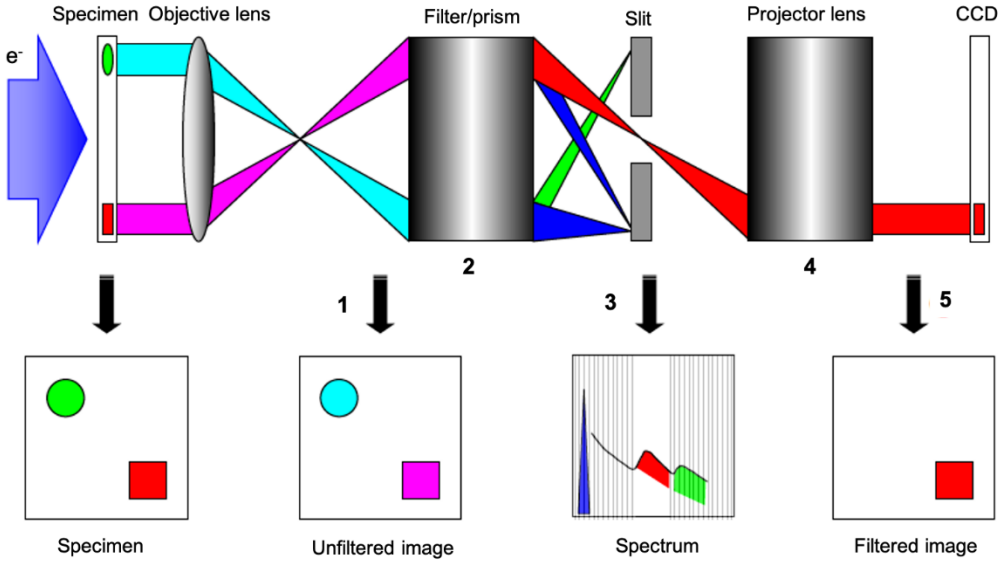

Figure 2-19 Schematic ray diagram showing the step-wise formation of a filtered image using an image filter in EFTEM (modified from [173]).

The inelastically scattered electrons with a specific energy that are dispersed by the spectrometer can be selected or filtered using an energy selecting slit. Energy filtered transmission electron microscopy (EFTEM) is a technique by which these filtered electrons can be used to form images or diffraction patterns (DPs). Figure 2-19 illustrates a schematic for the formation of an energy-filtered image in five steps using an image filter. In step 1, an unfiltered image or DP is formed by the objective lens before the filter. In step 2, the magnetic prism collects these specific electrons that form image/DP and disperses them to form the energy spectrum. In step 3, an energy slit of defined width is used to select a part of the spectrum and filter the electrons within a given range corresponding to specific energy loss. The filtered electrons are then collected by a projector lens to form an energy-filtered image/DP. Lastly, the image or DP formed by the projector is detected by the CCD camera. The energy slit is located at the dispersion plane of the filter. To visualize the spectrum instead of the filtered image, the slit is removed and the focus of the projector lens is changed to project the dispersion plane onto the CCD. Important aspects of EFTEM imaging are the contrast enhancement and the quality of the resulting image. The contrast and the image quality can be

enhanced by selecting a narrow energy window during energy filtering which suppresses the influence of chromatic aberrations. An important advantage of the EFTEM is that it allows the zero-loss and inelastic filtering of the images/DPs which significantly enhances the contrast by removing the inelastically scattered electrons. Further, selecting the electrons with specific energy loss allows to tune the contrast at any energy and obtain images with compositionally sensitive information. In the present study, a Gatan Imaging Filter (GIF) Tridiem installed at the Titan 80-300 was used to acquire thickness and elemental maps using the EFTEM imaging.

Thickness maps can be produced in EFTEM by acquiring an unfiltered and a zero-loss image from the same area of the specimen. The thickness determination is based on the mean free path length of electrons for inelastic scattering. The mean free path length (λ) for inelastic scattering corresponds to the average distance traveled by the electron between inelastic scattering events in the specimen. It primarily depends on the energy of the incident beam and the material itself. If t is the thickness of the specimen, the average number of times an electron is scattered inelastically is t/λ. The probability for no inelastic scattering events to occur (P) based on the Poisson statistics is given by:

$$P = \exp(-t/\lambda) = I_o / I_t \qquad 2\text{-}20$$

Based on the above formulation, the relative thickness map can be computed as:

$$t/\lambda = -\ln(I_o / I_t) \qquad 2\text{-}21$$

where I_o is the integrated intensity of the zero-loss peak obtained from a zero-loss filter image, I_t is the total integrated intensity of the entire spectrum obtained from the unfiltered image.

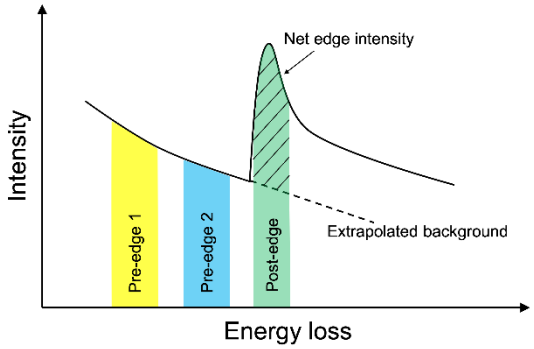

Figure 2-20 Schematic showing background subtraction based on the three-window method for evaluation of the net intensity of an ionization edge in EFTEM elemental mapping.

For elemental mapping using EFTEM, filtered images can be generated using the core energy loss corresponding to inner-shell ionization edges. In this core-loss imaging, the areas of the specimen that contain a specific element give rise to the corresponding ionization edge and appear brighter in the filtered image. The most crucial aspect in the EFTEM elemental mapping is the accurate identification of the edges and evaluation of their intensities. This is achieved by subtracting the background of the intensity versus the energy-loss curve. For subtracting the background in the present study, the three-window method was employed. In this method, three energy-filtered images are acquired. Two of these images are acquired using the filter energy before the ionization edge of interest and are called the pre-edge images. The third image is acquired using the filter energy which is almost next to the edge of interest and is called the post-edge image. The two pre-edge windows are used to calculate the background. The post edge window is used to subtract the extrapolated background from the total intensity to calculate the edge intensity (Figure 2-20). The procedure of background removal is done for each pixel after aligning all three images to obtain the elemental maps.

2.5 *In Situ* TEM Heating

In situ heating experiments allow for detailed insights into the grain structure evolution by time-resolved mapping of the grain boundaries, their mobility, character, grain sizes, and their crystallographic orientations. In the present work, a Gatan 652 *in situ* TEM heating holder was employed to tailor the grain structure of nc thin metal films for subsequent *in situ* TEM nanomechanical testing. For these *in situ* heat treatments, the material to be investigated was directly deposited on conventional carbon-coated TEM grids and loaded on the specimen cradle of the heating holder. The holder operates on the principle of calibrated resistive heating of a small furnace, where the TEM grid is mounted [195]. In the present work, a smart heater control was used with a ramping time of a few minutes to reach the target temperature (350° C) as well as for cooling down to room temperature.

2.6 *In Situ* TEM Nanomechanics

In situ TEM straining has been proven to be an indispensable technique for the observation of deformation processes in a variety of materials in real-time [197]. Since the 1950s, *in situ* TEM nanomechanical testing stages have been developed and customized by various research groups. These stages allow for straining, indentation, tribological (scratch) testing, etc., and some of these operate even at elevated temperatures. These testing methods allow for investigating size effects on the mechanical behavior by tailoring the physical dimensions or microstructural parameters of the specimen like the thickness, diameter, grain sizes, etc.

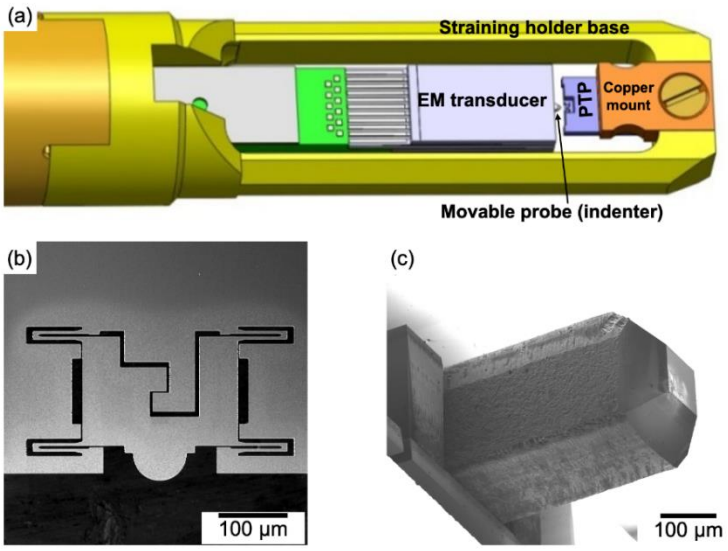

Figure 2-21 (a) Schematic of the tip of a PI 95 PicoIndenter straining holder (modified from [198]), (b) SEM image of a PTP device, (c) SEM image of a 100 µm wide movable probe of a flat punch transducer.

In the present work, a PI 95 TEM PicoIndenter holder from Bruker, MN, USA was employed. A schematic of the tip of the holder is shown in Figure 2-21 (a). The main components of the nanomechanical straining system include an electromechanical (EM) transducer with a moveable probe, an actuator, a displacement sensor, a mechanical positioner, a piezo positioner and a controller as shown in the block diagram in Figure 2-22 (a) [199]. The EM transducer is a MEMS-based capacitive device that consists of a force/displacement sensor with a micromachined comb drive that enables actuation and sensing [200]. It consists of two pairs of electrostatic actuator combs or electrodes (Figure 2-22 (b)). As these electrodes are biased, the electrode at the center moves in the direction of indentation. This leads to a change in the gap between the movable and fixed electrodes, resulting in a change in the capacitances between these. The change in the capacitance is detected by the displacement sensor based on which the displacement of the movable electrode is measured. The force is measured based on the electrostatic force generated by the comb drive actuators due to the change in capacitance between the electrodes. The capacitive function of the actuator combs provides high sensitivity, a large dynamic range, and a linear force or displacement output signal. In

addition, the system comprises a MEMS-based push-to-pull (PTP) linear mechanical transformer (Figure 2-21 (b)). The PTP device transforms an external pushing force into a tensile force on a specimen mounted on it. The PTP transformer is mounted on a copper mount and the entire assembly can be detachably mounted on the straining holder base with the aid of a small screw (Figure 2-21 (a)). The fabrication of the miniaturized specimens on the PTP is achieved by *in situ* FIB lift-out and transfer (Figure 2-10).

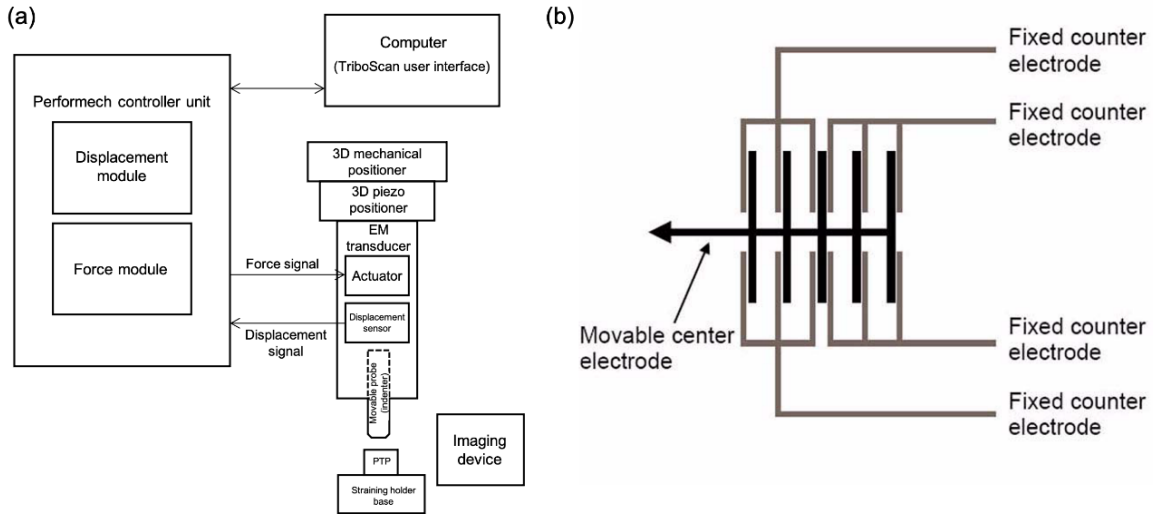

Figure 2-22 (a) Block diagram of the nanomechanical test system from Bruker (modified from [199]), (b) MEMS-based transducer actuation diagram showing the electrostatic actuator combs [200].

The indentation is achieved with the aid of a 100 µm wide movable probe (also called the 'flat punch' as shown in Figure 2-21 (c)) that is integrated into the EM transducer assembly (Figure 2-21 (a) and Figure 2-22 (a)). The probe can be manually positioned and aligned with respect to the PTP device using the 3D mechanical positioner at the other end of the holder before inserting the holder in the TEM. Further fine alignment of the probe is achieved using the 3D mechanical positioner together with the 3D piezo positioner after inserting the holder in the TEM and adjusting the eucentric height of the specimen on PTP. The load function can be defined to conduct the nanomechanical testing in load control or displacement control mode with varying loading or displacement rates. In addition, there is also a possibility to perform the tests in a dynamic or quasi-static fashion to synchronize the straining experiments with the acquisition time of the specific TEM imaging technique with or without drift correction. This enables time-resolved imaging of the intricate deformation events and when coupled with multiple TEM imaging modes/cameras facilitates the acquisition of correlative information from the same specimen without the relaxation of the specimen. The nanomechanical response of the specimen can be simultaneously measured during the imaging further enabling a direct correlation of the local and time-resolved deformation events with the mechanical behavior of the specimen as a whole.

A challenging aspect of the *in situ* nanomechanical experiments is the overall stability and drift of the holder assembly and the specimen. The mechanical drift is dependent on various factors like vibrations, thermal fluctuations, etc. The drift can significantly influence the measured mechanical response and its reliability. During rapid straining experiments, it may be essential to measure the amount of drift. To enable reliable measurement of the systematic drift, it is important to avoid any manual interaction to adjust the position of the probe with the aid of a 3D mechanical positioner during the actual experiment. The measurement of the systematic drift is introduced in the next chapter. The drift becomes critical if the experiments are performed in combination with ACOM-STEM imaging which typically requires a holding time of 45-60 min between the consecutive straining states. It may vary significantly if the experiments are conducted for longer durations (several hours or over days). Thus, in this case, to minimize the effects of drift the specimen is allowed to stabilize for several minutes after each loading step and before acquisition of the ACOM-STEM map.

3 Methods: Data Processing and Quantitative Analysis

A systematic methodology for the data processing using advanced software programs becomes indispensable for quantitative analysis of the results obtained from both *in situ* and *ex situ* TEM studies. The present chapter provides an introduction to some basics of crystallographic orientation, its representation, and interpretation. A systematic approach for visualization and processing of the data is discussed for a reliable quantitative understanding to characterize the deformation mechanisms in the nc metals and NMCs. Lastly, the evaluation scheme for *in situ* TEM nanomechanical testing is briefly described. Several factors including challenges in processing and interpretation of the data are highlighted.

3.1 Orientation in Space

3.1.1 Description of Crystal Orientation

The orientation of a crystal in space is defined as the position of the crystal coordinate system (C_C) of the crystal with respect to the specimen coordinates system (C_S). The crystal orientation can be mathematically expressed as [201]:

$$C_C = g \,.\, C_S \qquad 3\text{-}1$$

'g' in Eq. 3-1 is the orientation or rotation matrix, that transforms the specimen coordinate system into the crystal coordinate system. Figure 3-1 shows several grains in a bright-field STEM image in which the orientation of each grain is symbolically represented using unit cells in the specimen reference.

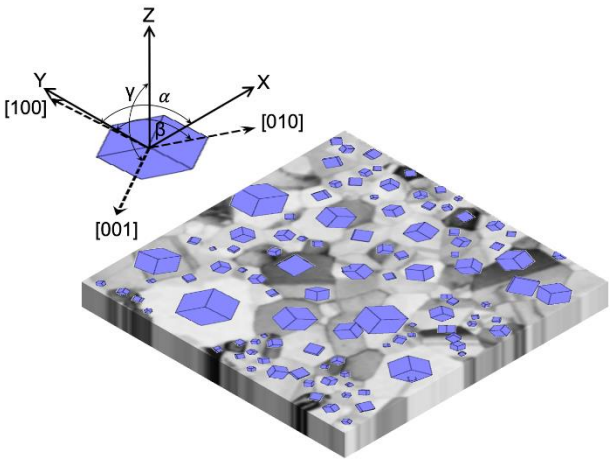

Figure 3-1 Illustration of grains in nc Pd. Each grain is represented by cubic unit cells with their respective orientations in the specimen reference frame with cartesian coordinates X, Y and Z. Inset shows a crystal representing the relationship between the specimen coordinates X, Y, and Z with respect to the crystal coordinates [100], [010] and [001] with angles α, β and γ between them.

In the present study, the principal axes of the specimen coordinates are designated as X, Y, and Z according to the cartesian coordinate system (Figure 3-1). It is to be noted that the Z-axis in the present study is chosen to be parallel to the optic axis of the TEM. Thus, if the specimen is not tilted, Z-axis represents the normal to the specimen, and X and Y are two mutually perpendicular directions in the plane of the specimen. The inset in Figure 3-1 shows the coordinate system of grain with crystal coordinate axes [100], [010] and [001] that are inclined at angles α, β and γ with respect to the axes of the specimen X, Y and Z. From Eq. 3-1, the rotation matrix 'g' transforms the specimen coordinates and allows the crystal directions to be expressed by directions in the specimen to which these are parallel. In the present study, the orientations are described by the Euler angles as defined by Bunge [202].

3.1.2 Representation of Orientations and Texture

A common method of representing the orientation of individual grains is to plot the poles of crystal planes {hkl} with respect to the specimen coordinates on a stereographic projection. A stereographic projection allows the representation of a 3D crystal and its orientation on a 2D projection plane. Figure 3-2 (a) shows a pole figure representing {hkl} poles on a stereographic projection from one of the grains in Figure 3-1. Here X, Y, and Z are the principal axes in the specimen reference and the red markers indicate the poles obtained from the intersection of the plane normals with a reference sphere and projecting them on a plane normal to the Z-axis. Figure 3-2 (b) shows the same pole figure (PF) superimposed on the Wulff net. The stereographic projections retain the angular relationships between planes and directions in the crystal and are angle true.

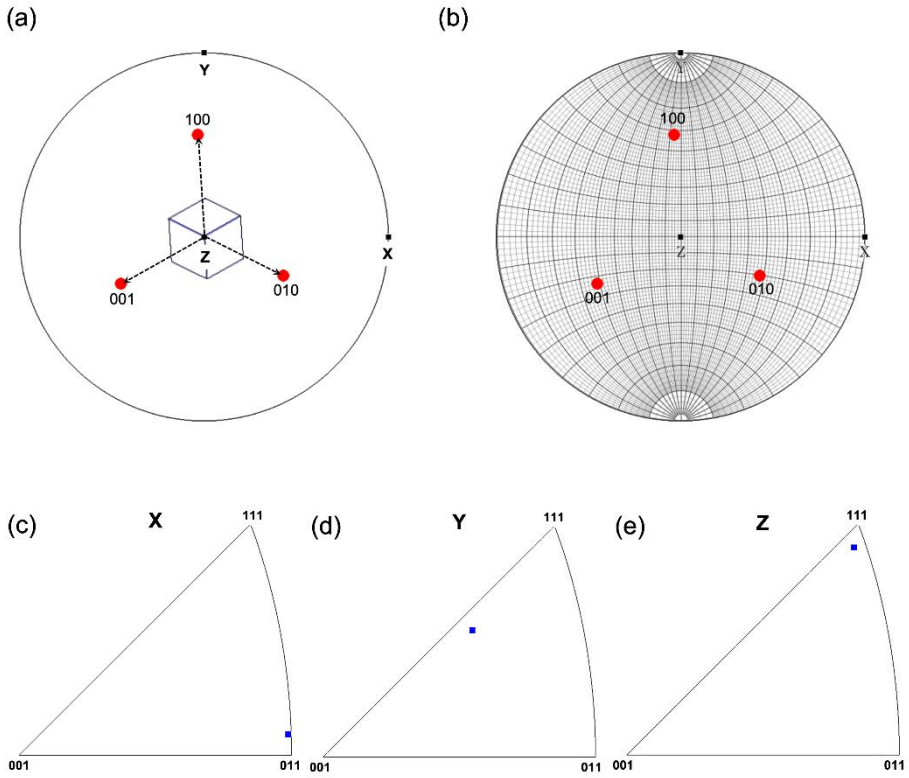

Figure 3-2 (a) (100) pole figure with the projected directions from a crystal, (b) {100} poles superimposed on the Wulff net, (c)-(e) inverse pole figures showing the X, Y, and Z specimen axes in the crystal reference.

Another approach of representing the orientations is to plot the poles X, Y, and Z of the specimen coordinate system with respect to the crystal coordinate system on a stereographic triangle. Figure 3-2 (c)-(e) show a standard unit stereographic triangle with corners corresponding to [100], [110] and [111]. All symmetry-equivalent crystal directions can be represented on this plot. The blue markers in these plots represent the position of specimen X, Y, and Z directions in the reference frame of crystal with the orientation shown in Figure 3-2 (a)-(b). Plotting these figures involves the operation of expressing the specimen directions in the frame of crystal, which is the reverse operation performed for plotting the pole figures. Thus, Figure 3-2 (c)-(e) are referred to as the inverse pole figures (IPFs). Using these methods, the orientations from several grains can be plotted and their densities can be represented on PFs and IPFs to visualize the overall texture of a specimen. Figure 3-3 represents the densities of (100), (110), and (111) using colormaps on PFs and the orientation densities of specimen X, Y, and Z axes on IPFs. From the pole figures, it is noted that the majority of the grains have their (111) planes almost parallel to Z or normal to the plane of the film leading to a sharp maximum close to the Z-axis. The film, thus, exhibits a preferential (111) texture along the growth direction.

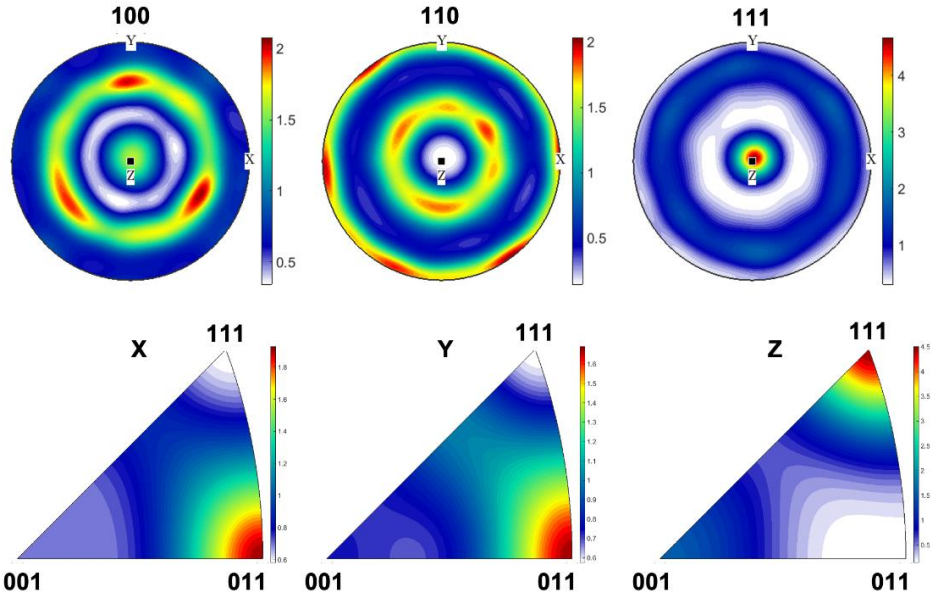

Figure 3-3 Texture plots showing the density of {100}, {110} and {111} poles on pole figure and the orientation density for X, Y, and Z specimen axes on inverse pole figure with the aid of colormaps. The densities are plotted for the same sample as shown in Figure 3-1.

3.2 Orientation Mapping with ASTAR

The data acquisition procedure by ACOM-STEM using Topspin was introduced in 2.4.4. A fast frame acquisition camera allows to capture spot diffraction patterns at each pixel and these are stored in a *.blo ('block') file. The primary information that is obtained from the spot diffraction patterns by ACOM-STEM is the crystal orientation and phases present in the specimen. Both the crystal orientation and phases are identified by a systematic indexation procedure using the ASTAR software package, NanoMEGAS, Brussels, Belgium. The package consists of three programs namely: DiffGen, Index, and MapViewer. The following sections introduce the concepts and steps involved in the indexing and obtaining reliable orientation maps.

3.2.1 ASTAR Indexing by Template Matching

Templates are diffraction patterns simulated under kinematic conditions for the known phases and orientations [193]. The simulation procedure assumes that reduction in the intensity of the diffraction spots at the non-Bragg condition is proportional to the excitation error 's' (Figure 2-8). The DiffGen (Diffraction Generator) is used to generate 'template banks'. These banks consist of computed spot patterns for sets of Euler angles spanning the entire Euler space defined by the crystal symmetry. The templates representing the spot patterns are calculated for all possible orientations with a defined rotation step for the expected phases in the specimen [192]. The key parameters that are defined for generating the templates in DiffGen include [203]:

- **TEM voltage** that defines the electron wavelength and the radius of Ewald sphere;
- **Max angle** that corresponds to the maximum Bragg angle used for generating the diffraction spots ($2\theta_{max}$), and it determines the angle above which the diffraction spots corresponding to d-spacing of less than $\lambda/2\sin\theta_{max}$ are not visible;
- **Excitation error** which determines the maximum value of 's' or the closeness of a reflection with respect to the Ewald sphere needed for it to be visible;
- **Step count** that defines the number of steps that are used to generate template patterns between the fundamental directions ([100], [110], and [111]) in reciprocal space and governs the angular resolution for orientation measurements.

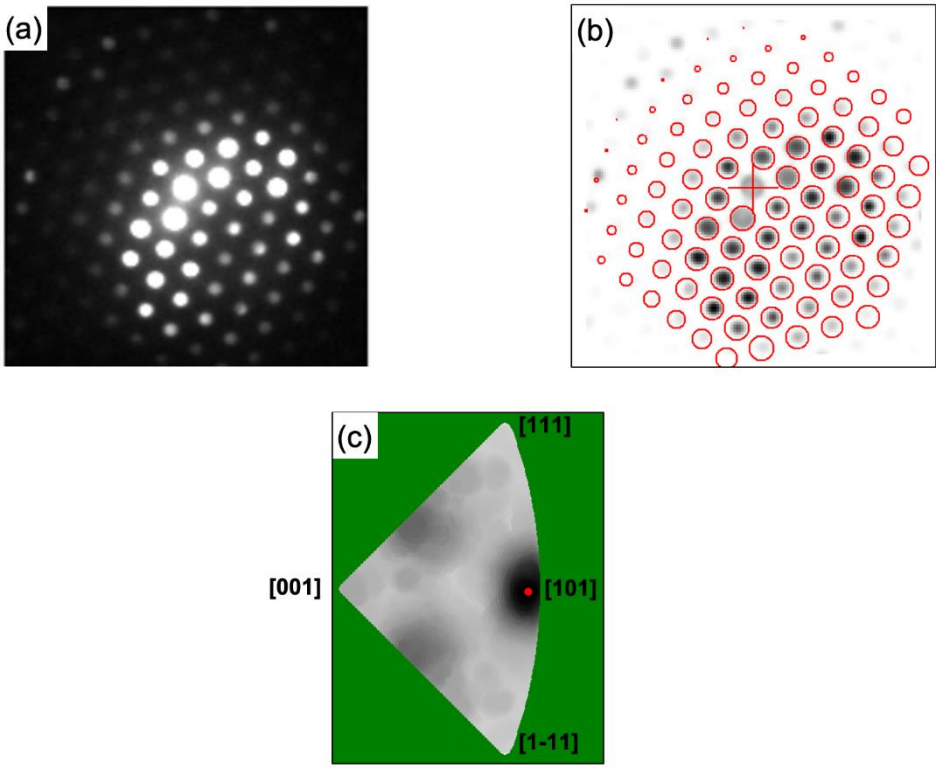

Figure 3-4 Illustration of the template matching procedure: (a) spot diffraction pattern obtained experimentally, (b) best matching template (in red) superimposed on the spot pattern, and (c) index map representing the correlation indices as grey levels for all the orientations on the IPF. The maximum index value (1217) is shown by the red marker and the corresponding reliability is 40. As seen from the index map, the orientation of the spot pattern is close to [101].

The template matching procedure is performed using the Index program by importing the block file and the template bank. The procedure involves comparison of each spot diffraction pattern (Figure 3-4 (a)) with the measured templates in the bank and determines the degree of matching for a given template given by the cross-correlation index (Qi) [192,193]:

$$Q_i = \frac{\sum_{j=1}^{m} P(x_j,y_j)T_i(x_j,y_j)}{\sqrt{\sum_{j=1}^{m} P^2(x_j,y_j)}\sqrt{\sum_{j=1}^{m} T_i^2(x_j,y_j)}} \qquad 3\text{-}2$$

P(x,y) in the above equation is the intensity function representing the diffraction pattern and each template 'i' given by the function T(x,y). The template matching with the highest value of Q corresponds to the solution (Figure 3-4 (b)). The correlation indices for each template are normalized by the highest value and these are converted to grey levels to represent on the IPF (Figure 3-4 (c)). The correlation index map in Figure 3-4 (c) allows to qualitatively visualize the reliability of the solution. A single dark region on the IPF is indicative of a safer unique single solution. If there are additional darker regions, it would indicate possible multiple solutions leading to low reliability. Thus, corresponding to each indexed solution a reliability factor is assigned as [192,193]:

$$R_i = 100\left(1 - \frac{Q_{i2}}{Q_{i1}}\right) \qquad 3\text{-}3$$

where Q_1 and Q_2 are correlation indices of the two highest and distinct maxima. Unreliable solutions can be disregarded by imposing a filter with a certain minimum threshold for reliability. In practice, a value of 15 is considered as a threshold for the fidelity of the solution.

3.2.2 ASTAR Parameter Optimization for Indexation

Since indexing involves cross-correlation to match experimental and simulated diffraction patterns [190], the Index program [204] allows for enhancement in the image quality and visibility by optimization of image processing parameters and filters. Following are some of the critical parameters that optimized during indexation:

- **Softening loops:** number of times the filter is applied to the image
- **Spot enhance loops:** number of times the filter is applied to each spot
- **Spot detection radius:** radius of the circle centered at each pixel on which the average intensity is calculated
- **Normalize:** scales up the image in the full range of 255 grey levels
- **Noise threshold:** determines the maximum value below which intensities of all the pixels with values less than the selected maximum value are set to zero
- **Gamma correction:** a power-law transform that determines the strength of intermediate intensities and enhances the image quality
- **Polar image max work radius:** defines the maximum reciprocal lattice vector considered for the template matching

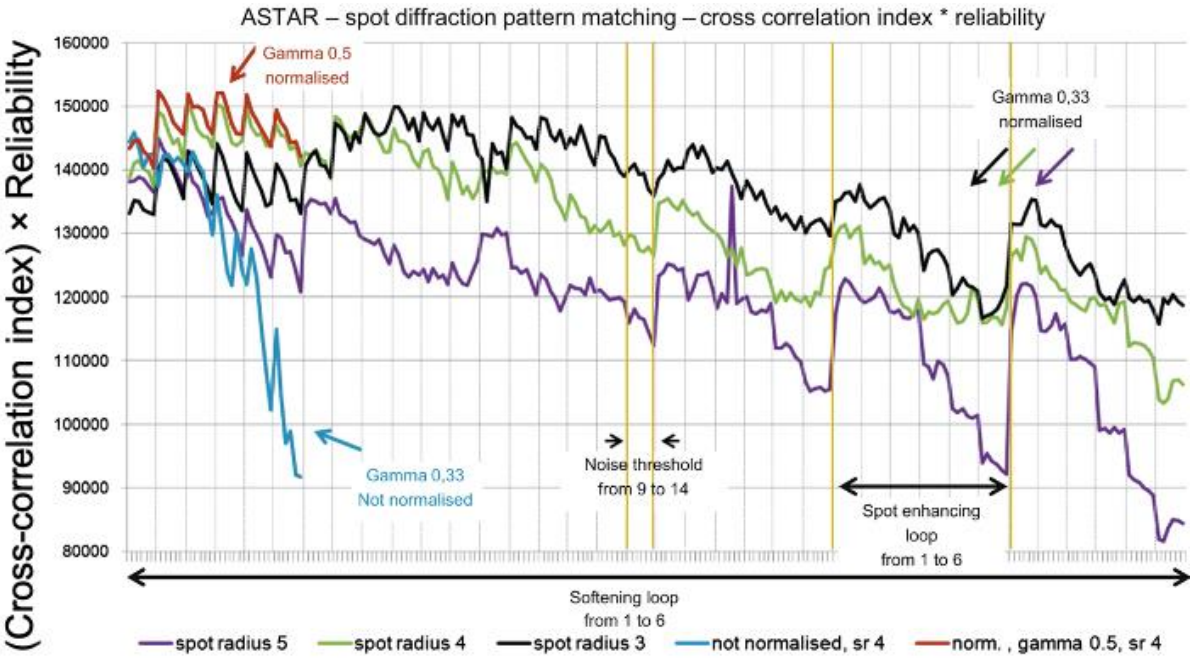

Figure 3-5 Analyses of the influence of the matching parameters used in ASTAR (indexing program) to find the match for the spot diffraction pattern with the bank of templates. After matching the patterns, the product of cross-correlation index and reliability for all pixels in an orientation map is summed up and plotted against the matching parameters. The vertical grid lines separate a block in which the "noise threshold" varies from 9 to 14. After each of such blocks the "spot enhancing loop" is increased by one. After six of such blocks, the "softening loop" is increased from one to six. Summarized, the "noise threshold" varies from 9 to 14, the "spot enhancing loop" and the "softening loop" vary from one to six. Results for different "spot radius" (sr), "gamma" of 0.5 or 0.33, and "normalization" on or off are plotted (adopted from [205]).

Kobler et al. conducted a parametric study by systematic variation of the above parameters and found that each of these parameters can noticeably influence both index and reliability. Figure 3-5 shows the influence of these parameters on the product of index and reliability [205]. In addition, Figure 3-6 shows the effect of changing the level of normalization keeping other parameters constant. As the normalization is increased, a twinned crystallite (shown by arrow) widens. Such effects showing widening or shrinking can be seen in a few other crystallites as well. These effects arise due to tilting of the twin boundaries or in

general any random grain boundary with respect to the incident electron beam. Depending on the degree of tilting, the number of reflections in the diffraction patterns from two neighboring grains and their intensities vary in the overlapping region. Normalization scales the grey values in diffraction patterns to full 8-bit grayscale values available in the Index. In addition, a threshold for normalization can be defined so that every grey value above it is set to the maximum value. With the increasing value of normalization, the threshold intensity for the diffraction patterns decreases. As a result, the diffraction spots with weaker intensities are enhanced and contribute strongly towards the cross-correlation leading to indexation with lower reliability which is seen in the region marked by an arrow in Figure 3-6. These effects make the data interpretation challenging and need to be accounted for when analyzing the deformation mechanisms involving GB-related processes during *in situ* TEM deformation.

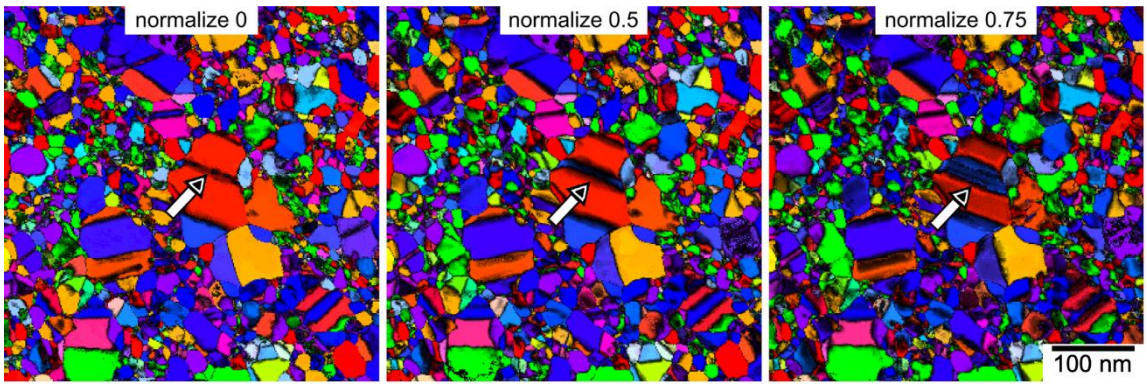

Figure 3-6 Illustration of the effect of change in normalization on the resulting orientation maps (adopted from [206]).

3.2.3 ASTAR Data Visualization

The results of indexation obtained from the Index as '.res' files can be visualized in the Mapviewer [207] which allows for orientation and phase analysis. The Index program processes 4D STEM data in which each pixel in a 2D STEM image (Figure 3-7 (a)) has spot diffraction data embedded in it. During indexation, each pixel on the image is assigned information related to phase and crystal orientation which could be represented on the Mapviewer using different maps. These maps facilitate correlation and comparative analysis at the pixel level. The main results that are used for the representation of the indexed data are shown in Figure 3-7 for a single-phase material. Figure 3-7 (a) shows a bright-field STEM image formed from the 4D STEM data using a virtual aperture that collects the signals from direct (undiffracted) beam in the diffraction patterns. It is called the virtual bright-field STEM image and represents contrast that is typically sensitive to diffraction and to a certain extent to the Rutherford scattering. The index and reliability values are assigned to each pixel during the indexation. Accordingly, index and reliability maps (Figure 3-7 (b)-(c)) can be obtained. These are represented as grayscale images, and the grey levels are adjusted by appropriate selection of the minimum and maximum of index and reliability.

The crystallographic orientation that matches best for the experimental data for each pixel is represented according to the color code displayed on the fundamental triangle with corners corresponding to [100], [110], and [111]. Using the color code, the orientation maps can be obtained along the axes X_C, Y_C, and Z_C according to the crystal coordinate system shown in Figure 3-7 (d)-(f), where Z-axis is considered parallel to the optic axis of the TEM. Since these maps use IPF color code for display, these are also termed as 'IPF maps'. All the orientation maps presented in chapters 4 to 6 are displayed according to the ASTAR color code. The orientation maps are displayed by superimposing the corresponding index and orientation reliability maps with suitably scaled grey levels. These superimposed maps facilitate visualization of the pixels within grains that are indexed with a reasonable or acceptable orientation index and reliability. These parameters may be used to filter the pixels or the grains that are poorly indexed enabling a reliable quantitative analysis. In addition to orientation maps, for materials with more than one phase, each pixel is also identified by the phase to which it belongs, and the phase maps may be displayed as well. These maps are shown in chapter 6, which presents the data related to NMCs.

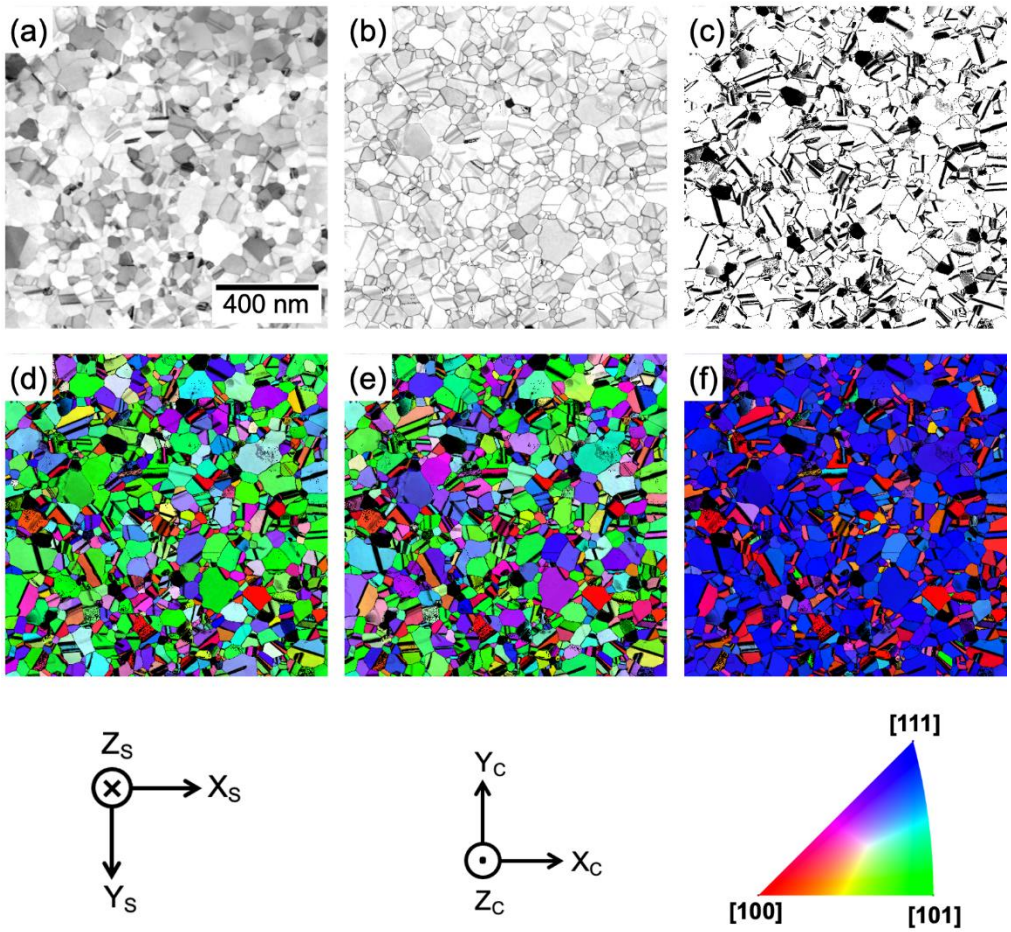

Figure 3-7 Illustration of the data visualization using ASTAR Mapviewer: (a) virtual bright-field STEM image, (b) index map with a minimum of 400 and maximum of 1100, (c) reliability map with a minimum of 10 and maximum of 25, (d) IPF map along X_C, (e) IPF map along Y_C and (f) IPF map along Z_C. All the IPF maps are shown by overlaying the index and reliability maps. X_S, Y_S, and Z_S axes represent the coordinate system for the specimen reference frame whereas X_C, Y_C, and Z_C axes represent the coordinate system for the crystal reference frame. Standard IPF color code is shown on the fundamental triangle with corners [100], [110], and [111]. The coordinate systems and color code are specific to ASTAR.

A critical aspect in visualizing and analyzing the orientation maps is to check for the scan rotation correction which if not implemented would most likely lead to an erroneous display of orientations and affect the entire analysis performed using the '.ang' files that store the orientation and phase information for every pixel. Any rotation between the diffraction pattern and real-space image needs to be corrected to ensure accurate alignment of the crystallographic directions with real space for each grain.

3.2.4 Correction for 180° Ambiguity

Given the quasi-parallel beam (probe) precessing at an angle of 0.5° or less, the spot diffraction patterns consist of reflections corresponding to low Bragg angles. This results in the excitation of reflections that are usually confined only in the zero-order Laue zone (ZOLZ). The absence of reflections from the higher-order Laue zone (HOLZ) could result in the ambiguity of orientations during indexation. The 180° ambiguity problem specifically arises for the orientation determination of spot patterns with a highly symmetric axis about which two possible orientations that are rotated by 180° could not be distinguished. Figure 3-8 shows a spot pattern from a grain of steel with [111] orientation. Due to the absence of higher-order reflections, two possible orientations are identified by the Index program that are rotated by 180° with respect to each other leading to the ambiguity problem in orientation mapping.

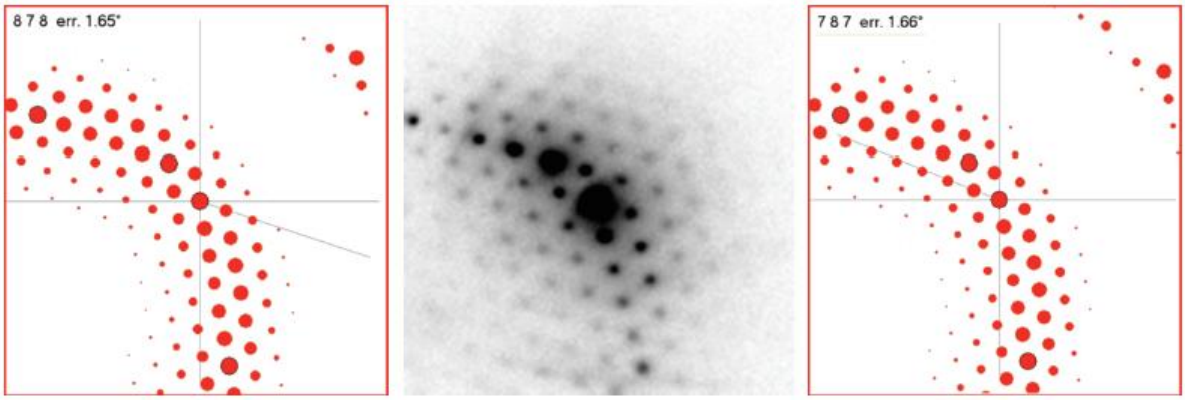

Figure 3-8 Illustration of 180° ambiguity problem based on two possible orientations (left and right) corresponding to the spot pattern shown in the center [208].

For solving the ambiguity problem, the data processing needs to be carried out with version 2.X (V2) of the ASTAR software package. The DiffGen V2 by default generates template banks with additional information related to the 'ambiguity axes' about which the rotation needs to be performed to correct for the ambiguity. The ambiguity is detected by the Index V2 during orientation indexing and each pixel is assigned the corresponding ambiguity parameter (Ambig.) as:

$$Ambig. = 100\left(1 - \frac{I_2}{I_1}\right) \qquad 3\text{-}4$$

where I_1 and I_2 are the cross-correlation indices of the two best solutions with 180° ambiguity between those. 'Ambig.' equal to 100 implies there is no ambiguity for the selected solution and it is reliable whereas 'Ambig.' less than 100 or equal to zero means that there is potential ambiguity for the solution (scaled for 0 to 100). The values of 'Ambig.' can be read at pixel level and can be corrected in the Mapviewer V2. The Mapviewer corrects the ambiguity detected within each grain by extending orientations from the most reliable pixels (highest Ambig.) to the unreliable ones and the correction is performed by rotating the unreliable orientations about the 'ambiguity axis'.

3.2.5 Projection Effects

The TEM specimens of nc metals and NMCs employed in the present study are in the form of deposited thin films or lamellae prepared using FIB milling. In any case, consideration of the projection effects and the misconceptions and artefacts arising from those is critical. This is especially related to the reliability of crystal orientation mapping and precise detection of interfaces (grain or phase boundaries) using ACOM-STEM. The projection effects arise mainly due to the presence of two or more grains through the thickness of the specimen or due to GBs that are inclined with respect to electron beam (Figure 3-9).

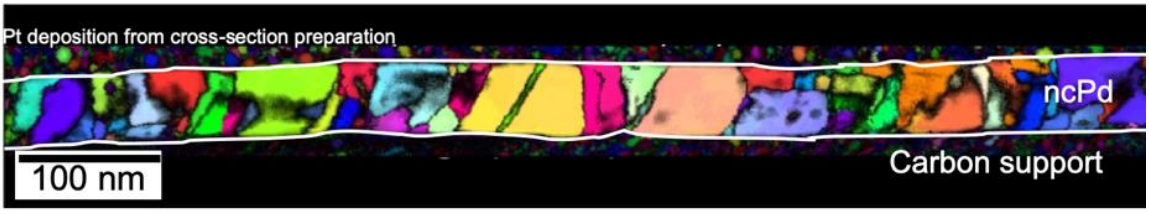

Figure 3-9 Orientation map of a cross-section of nc palladium thin film deposited on carbon substrate showing the projection effects (modified from [206]).

The overlapping microstructural features result in multiple diffraction patterns corresponding to differently oriented grains through the thickness. The tilting or bending of the specimen additionally contributes to the projection effects and the resulting GB detection. Kobler et al. presented a comprehensive analysis on the impact of tilting on the resulting projection effects that determine the visibility of certain microstructural features [206]. A classic example of twin boundary presented by them explains that twin boundaries in the twinned grains appear and disappear and their apparent width varies with the specimen tilting. These effects can lead to erroneous results in the quantitative analysis involving grain size measurements and the determination of GB characteristics. Further, the interpretation of these effects with potential artefacts during deformation as GB-based processes needs to be avoided. These effects need to be prevented or excluded during the *in situ* experimentation and related data analysis.

The diffraction patterns obtained from a single defect-free crystal are expected to be nearly identical whereas an abrupt change in patterns is expected if the scanning beam passes through defects and interfaces. Based on this principle, ASTAR Index V2 provides a feature to generate structural images/maps of specimen directly using the '.blo' file. The contrast in these maps corresponds to the contribution from all structural features in the specimen that affect the local changes in diffraction conditions [209]. These maps can facilitate fast mapping and visualization of the presence of overlapping grains including an estimate for the degree of tilting of interfaces. To generate these images, diffraction correlation is carried out using an algorithm that measures the degree of similarity between diffraction patterns from neighboring points. For each diffraction pattern, this degree of similarity is expressed by the correlation coefficient C (i,j) given as:

$$C(i,j) = \sqrt{\frac{\sum_{x,y}\left[P^{i,j}(x,y) - P^{i+1,j}(x,y)\right]^2 + \sum_{x,y}\left[P^{i,j}(x,y) - P^{i,j+1}(x,y)\right]^2}{2N}} \qquad 3\text{-}5$$

where $P^{i,j}$ and $P^{i+1,j}$ denote the intensities of diffraction patterns obtained from successive or neighboring points with coordinates (i,j) and (i+1,j), (x,y) represent the pixel coordinate within patterns, and N is the total number of pixels within each pattern [210]. The correlation coefficient obtained from each point is represented on a grayscale as a correlation coefficient map.

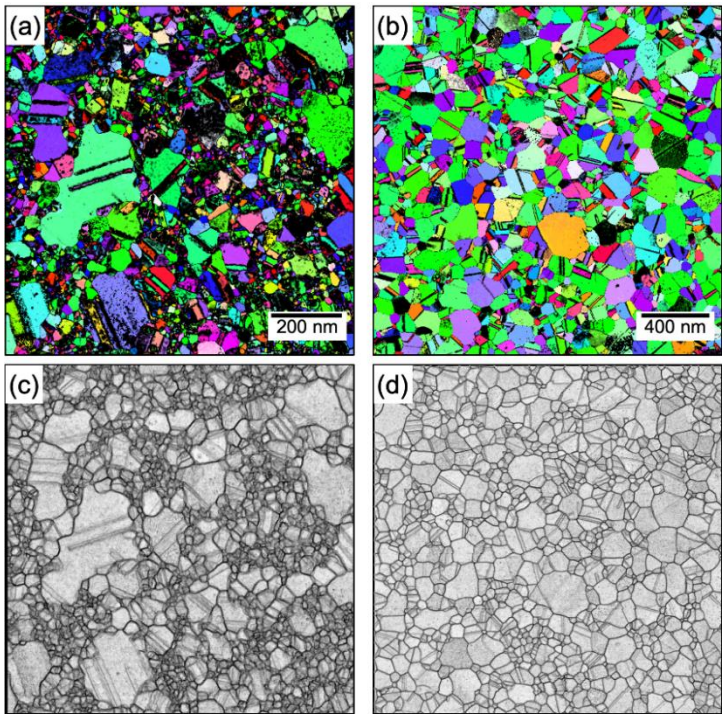

Figure 3-10 Illustration of the effect of grain overlapping on the orientation reliability: (a)-(b) orientation maps from nc Pd thin films with a different grain size distribution, and (c)-(d) corresponding correlation coefficient maps.

As seen in Figure 3-10 (a), a nc Pd thin film shows reduced orientation reliability and the correlation coefficient map (Figure 3-10 (c)) shows various contrast features within the coarser grains indicating the possibility of several finer grains overlapping with those. In addition, the contrast due to GBs is not sharp and these appear wider indicating that they are tilted with respect to the film plane. Figure 3-10 (b) on the other hand shows another nc Pd thin film with relatively better orientation reliability. The corresponding correlation coefficient map (Figure 3-10 (d)) shows lesser contrast features within each grain and GBs are showing sharp contrast indicating that this specimen exhibits minimum projection effects. Thus, these maps are helpful to some extent in detecting the projection effects.

3.3 Data Processing

ASTAR Mapviewer provides several features for extracting basic quantitative information from the ACOM-STEM results such as grain sizes, pole figures, detection of grain boundaries, etc. However, before any quantitative analysis is performed, systematic data processing becomes necessary using appropriate filters to ensure that the data is free from noise and unreliable data points. Matlab-based open-source and versatile software toolbox MTEX provides means to analyze, program, model, visualize and interpret the crystallographic orientation data [211]. Some of the features of MTEX were utilized in the present study. In addition, an MTEX-based in-house program 'Grain Evaluation' by A. Kobler [205,206,212] was employed. This program is especially dedicated to post-processing and analysis of the ACOM-STEM data from *in situ* TEM studies. The 'Grain Evaluation' is compatible with MTEX-3.5.0 and is operated with MATLAB R2013b whereas some additional data analysis without the 'Grain Evaluation' was performed with a higher version, MTEX-5.2.beta2, operated in MATLAB R2017b. In addition to the MTEX, the ATEX software [213] was employed specifically for the estimation of GND density based on the Nye tensor approach.

3.3.1 Alignment of Reference Frames

The 'angle' ('.ang') files with the 3 Euler's angle, orientation index and reliability, phases, and their reliability at each data point with (x,y) coordinates are exported from the Mapviewer. These are by default exported according to the ASTAR convention of reference frames. A comparison between the ASTAR and MTEX conventions for both spatial and crystal reference frames is shown in Figure 3-11. It is seen that the crystal and spatial reference frames in the case of ASTAR do not coincide with each other unlike in the case of MTEX. The crystal reference frame in the case of ASTAR is identical to that of MTEX, unlike the spatial reference frame which is rotated by 180° about X-axis. Thus, for importing the '.ang' files obtained from the Mapviewer, the spatial reference frame must be aligned appropriately for the visualization and processing of the data. The alignment is achieved using the command 'convertSpatial2EulerReferenceFrame' in MTEX followed by suitable rotation (90° clockwise about Z-axis in the present case) of the resulting map to align it with the ACOM map in ASTAR.

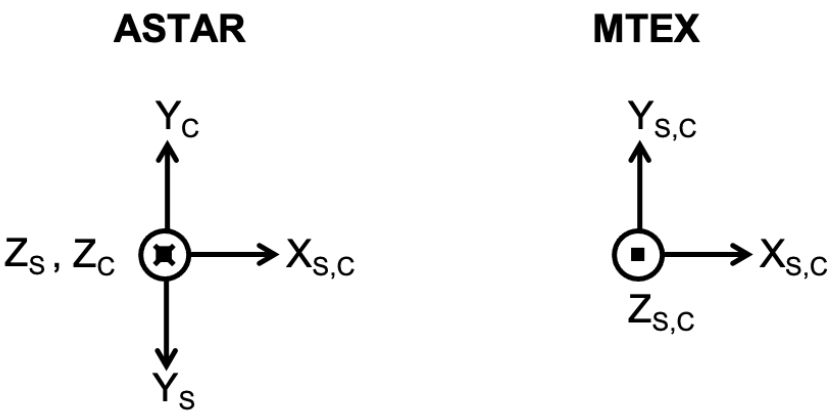

Figure 3-11 Comparison of reference frames for the crystal and spatial coordinates in ASTAR and MTEX.

It should be noted that the alignment procedure described above is not required while working with the 'Grain Evaluation' as it is programmed to incorporate the alignment to coincide with the two reference frames. It is necessitated while directly importing the '.ang' files in MTEX without the aid of 'Grain Evaluation'.

3.3.2 Grain Evaluation: A Program for Automated Data Processing

Data processing using the 'Grain Evaluation' involves a stepwise filtering procedure followed by quantitative analysis as shown in Figure 3-12 and is discussed below.

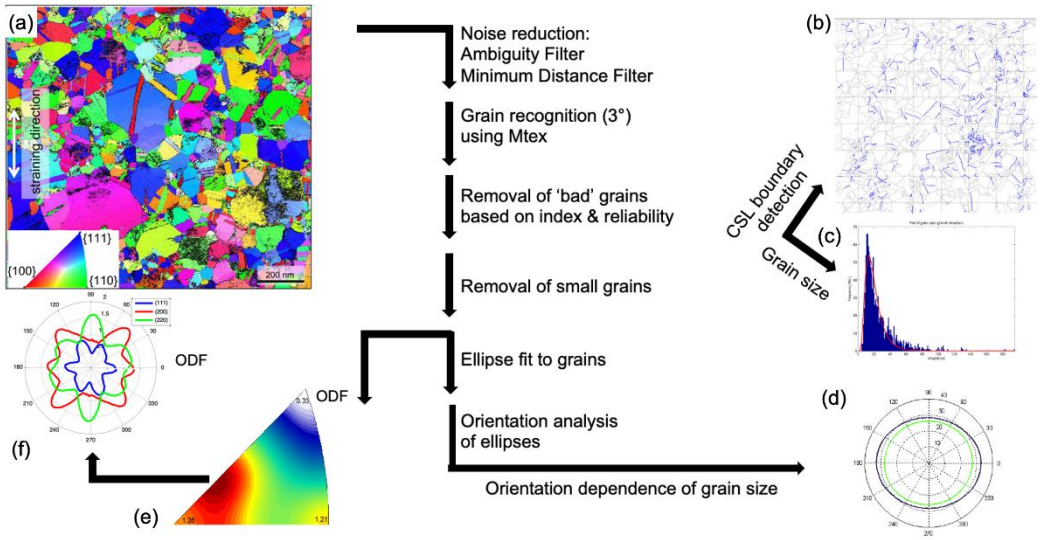

Figure 3-12 Data procession scheme of the orientation maps: (a) Orientation map overlaid with reliability of the initial state (inset: color code of the crystal orientation), (b) detection of twin boundaries (shown in blue), (c) grain size statistics, (d) averaged diameter of the ellipse of crystallites represented as a function of the specimen direction Φ within x–y plane relative to the straining direction for the initial (green) and deformed (black) states, (e) Orientation density function on IPF (color code: red, max density; white, lowest density), (f) Orientation density function as a 360° polar plot (red: <100>, green: <110> and blue: <111>) (modified from [205]).

Ambiguity Filter

The 'Grain Evaluation' has an option to filter the 180° ambiguity problem. To filter the ambiguity, crystallites with the ambiguity problem are detected with a defined segmentation angle and the script (greater details are provided in [206]) searches for neighboring crystallites with a misorientation greater than the start angle. An important benefit of this function over ASTAR Mapviewer is that it detects and correct ambiguities in a series of orientation maps acquired from the same region, e.g. during *in situ* experiments.

Min. Distance Filter

The min. distance filter is a median filter applied to the crystal orientation data in the imported '.ang' files. The filter treats the 3 Euler's angles as vectors V_i in 3D and calculates the distance from a given pixel V_j to all the pixels V_i within the neighborhood around the central pixel [205,206]. The information of the pixel with the smallest average distance d_{min} is ascribed to the central pixel:

$$d_j = w \sum_{i=1}^{(2n+1)^2} (v_i - v_j)^2 \qquad 3\text{-}6$$

$$d_{min} = Minimum\,(d_{1\ldots(2n+1)^2}) \qquad 3\text{-}7$$

The distance calculation in Eq. 3-6 can be weighted by 'w' which could be the cross-correlation index, the reliability, the phase, or a combination of those. The filter reduces random noise in the orientation maps which enables more refined measurements of orientations at the pixel level.

Processing of ACOM-series for *In Situ* Studies

For the global and local analyses, the ACOM-series needs to be well-aligned to achieve a comparative analysis at the level of individual grains. In the present study, the alignment was performed using IMOD, an open-source software tool dedicated to assembling and aligning the data within multiple types and sizes of image stacks [214]. For aligning the orientation data as stacks of images, separate '.mrc' files were generated for the 3 Euler angles, phases, cross-correlation index, and reliability values obtained from the '.ang' files [205]. These separate '.mrc' series are aligned by X/Y displacements based on the fiducial markers placed typically at the GB triple junctions.

All the data filtering and processing steps in the 'Grain Evaluation' mentioned above can be employed on a series of ACOM maps at the same time to obtain the results for every map for a well-defined set of evaluation parameters. After reducing the noise using min. distance filter and correcting the ambiguity, the program recognizes the grains and detects the grain boundaries for each map. The typical segmentation angle used in the present work was 2-3°. The grains with very small sizes and poor reliability were filtered and not considered for the quantitative analysis. A variety of features are available for the quantitative analysis for each map that includes grain size statistics, orientation density function, texture, GB misorientation, statistics of the twin boundaries, etc. The last important step in the analysis of the ACOM series is the quantitative comparison through the series at the level of individual grains. In this step, each grain is selected in the reference state and its structural evolution is analyzed through the series. In the present study, the average rotation of grains as well as the rotation at pixel level were analyzed for the ACOM series acquired during *in situ* deformation experiments.

Nye Tensor Analysis

The scalar density (ρ_{GND}) of geometrically necessary dislocations (GNDs) can be expressed as an entry-wise norm of the Nye dislocation density tensor (α) [215] divided by the length of the Burgers vector (b):

$$\rho_{GND} = \frac{1}{b}\sqrt{\alpha_{ij}\alpha_{ij}} \qquad 3\text{-}8$$

where α_{ij} corresponds to the curvature components of the dislocation density tensor. For 2D mapping, five curvature components of the Nye dislocation density tensor are obtained, described by Pantleon as [216]: α_{12}, α_{13}, α_{21}, α_{23}, and α_{33}. From these five components, the truncated scalar GND density (ρ_{GND}^{2D}) is computed as [217,218]:

$$\rho_{GND}^{2D} = \frac{1}{b}\sqrt{\alpha_{12}^2 + \alpha_{13}^2 + \alpha_{21}^2 + \alpha_{23}^2 + \alpha_{33}^2} \qquad 3\text{-}9$$

3.4 Data Evaluation for *In Situ* TEM Nanomechanics

The TriboScan user interface records the instantaneous response of the specimen as measured by the PI 95 PicoIndenter. The raw data is recorded as the load and displacement plot and is processed according to the schematic shown in Figure 3-13. The evaluation routine involves correction for drift which is followed by removal of the contribution from PTP to the overall load to obtain a true stress-strain response. The *in situ* nanomechanical experiments are likely to be affected by mechanical drift due to any vibrations, temperature fluctuations, etc. in the testing environment. Although the TriboScan provides an option for drift correction during testing, the drift needs to be checked and corrected while processing the data. The drift correction after testing is most facilitated if any manual interaction is avoided for adjusting the position of the indenter either by 3D mechanical or piezo positioners, as in that case, the drift may be assumed to be systematic.

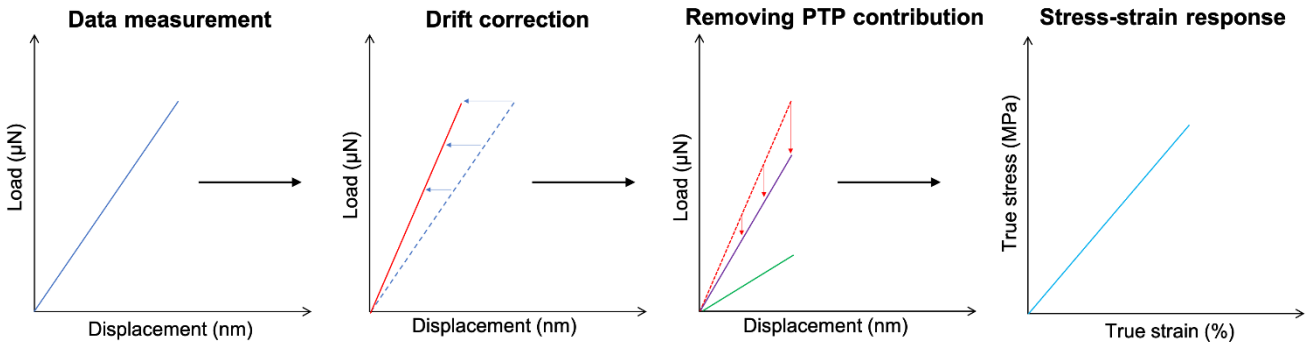

Figure 3-13 Schematic of the data processing routine for evaluation of the nanomechanical response.

Figure 3-14 illustrates the evaluation of the drift corrected load-displacement response from a nanomechanical experiment. Here, the systematic drift of the straining holder was evaluated by careful consideration of the time stamps and the position of the indenter during the experiment. This drift was subtracted from the measured experimental data to correct for the displacement. After the drift correction, the actual load-displacement response of the specimen was calculated by subtracting the PTP contribution which is typically a linear response in most cases. The PTP response was measured by loading the PTP with the same loading rate and mode (displacement-control in the present study) under which the experiments were performed on the film before fracture. Since the PTP contribution was evaluated immediately after the specimen fractured, it ensured that the response was measured under the same drift conditions under which the specimen was tested before it fractured. The true strain in the specimen was evaluated by tracking the displacement of some prominent markers by comparing the images in the initial undeformed stage and during the deformation whereas the true stress is estimated by dividing load at each data point by cross-section area of the specimen.

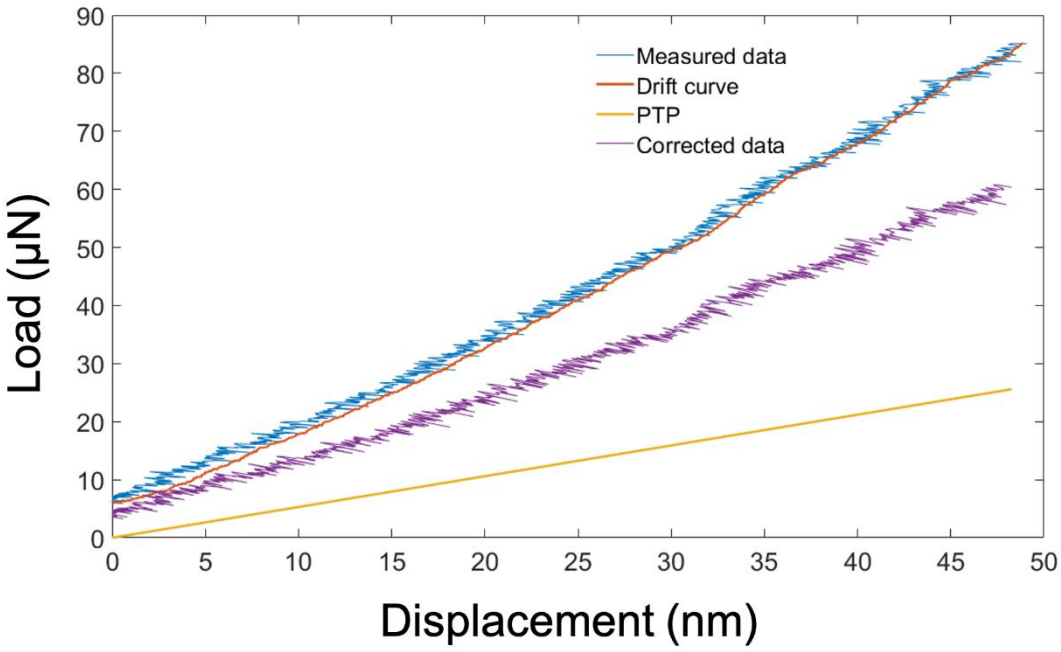

Figure 3-14 Evaluation of the drift corrected load-displacement response from an *in situ* nanomechanical experiment.

4 *In Situ* TEM Investigations of the Bauschinger Effect in Nanocrystalline Palladium

4.1 Introduction

Various aspects of the deformation mechanisms that are associated with the BE in nc metals remain unexplored. In particular, the role of microstructural heterogeneity, the complex interplay of dislocation and GB mediated mechanisms and their impact on the resulting crystal orientation and texture in nc metals need further investigations. For a detailed understanding of the mechanics of nc metals under cyclic deformation, a direct correlation of the relevant deformation mechanisms with the microstructural characteristics needs to be established. Chapters 4 and 5 present the results from *in situ* TEM investigations of the BE and discuss the active deformation mechanisms based on quantitative analysis of the deformed microstructure in nc palladium.

Analysis of grain rotations and the resulting texture in nc metals is a potential approach to gain insights into the active deformation processes. To facilitate that, *in situ* nanomechanical experiments were coupled with ACOM-STEM to map the crystal orientations of a large number of grains in the specimen. The present chapter is focused on a global analysis of the deformation microstructure by investigating a large number of grains that are representative of the specimen under cyclic deformation. These analyses are primarily related to the rotation of grains. Based on the characteristics of global crystallographic texture evolution, this chapter aims to understand the dominant deformation mechanisms that are active in nc thin palladium film showing the BE. To further investigate these rotational characteristics, the next chapter presents the analysis of a selected set of grains that exhibited unusual rotational responses during loading and unloading. Based on the local analysis of these grains, a systematic correlation is established to account for the detailed interactions between the nanosized grains. The presented *in situ* experimental approach is an attempt to directly visualize and quantify the deformation processes in nc thin metal film from a statistical ensemble of grains to the level of individual grains.

4.2 Experimental: Material Synthesis, Methods, Data Acquisition and Processing

4.2.1 Sputtering and Annealing of Nanocrystalline Pd Thin Films

Thin films of nc palladium were prepared by radio frequency magnetron sputtering on carbon-coated TEM grids, which were used as substrates. The sputtering was achieved by 5 cycles of 50 seconds each interrupted for 10 s in a chamber under the base pressure of 10^{-8} mbar, sputter pressure of 0.005 mbar, 60 W sputter power, and substrate-target distance of 15 cm. The thickness of the film was measured using EFTEM and estimated to be around 43 nm and 72 nm considering the mean free paths as 71.3 nm and 119.4 nm from the approximations by Malis et al. [219] and Lakoubovskii et al. [220]. The microstructure of the sputtered film was characterized by BFTEM and ACOM-STEM imaging (Figure 4-1 and Figure 4-2). As seen in Figure 4-1 (a) and Figure 4-2 (a), the as-sputtered films exhibited very fine grain sizes (5-20 nm) with significant projection effects leading to the overlapping of grains and especially of the GBs through the thickness of the specimen. This renders the microstructural investigations by TEM highly challenging, especially using quantitative ACOM-STEM. For an extensive and reliable quantitative TEM analysis, these projection effects need to be excluded. A potential solution to minimize these effects is to adjust the grain sizes by heat treatment leading to the growth of the grains. However, it was found that heat treatment immediately after sputtering did not lead to any significant grain growth. The film was aged in an ambient environment for several months. The aging was proven to enhance the kinetics of grain growth during heat treatment. The strong oxidation resistance of Pd prevented the development of surface passivation that might influence the purity of the film or its mechanical properties. After storing for 18 months under ambient environment, the film was annealed inside FEI Tecnai F20 ST TEM using the Gatan 652 heating holder at 350 °C for 10 minutes. The aging followed by heat treatment resulted in a film with an almost single layer of grains with minimum projection effects.

It is seen that after heat treatment, the film microstructure exhibits a columnar growth with preferential {111} texture, and the mean grain size increases from 5 nm to 90 nm. The columnar growth was confirmed from the correlation coefficient map (Figure 3-10 (d)) in which the majority of the GBs show sharp contrast

indicating that they are almost parallel with the electron beam in the TEM. From Figure 4-1 (b) and Figure 4-2 (b), it is seen that the nc Pd sample shows a wide distribution of grain sizes. The grain size distribution of the annealed film varies from 13 nm to 200 nm, and the area-weighted grain size ranges from 30 nm to 150 nm. The number and area-weighted average grain sizes show log-normal distributions with modes 25 nm and 63 nm.

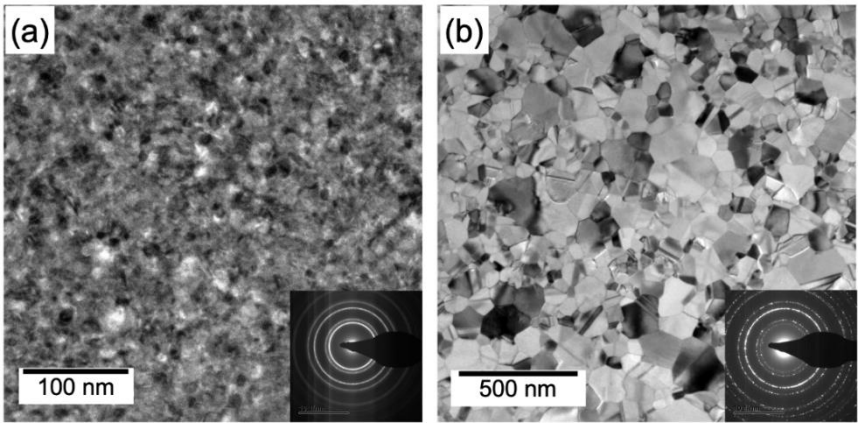

Figure 4-1 BFTEM images of nc Pd: (a) as-sputtered film after aging for 18 months, and (b) after *in situ* annealing of the structure in (a).

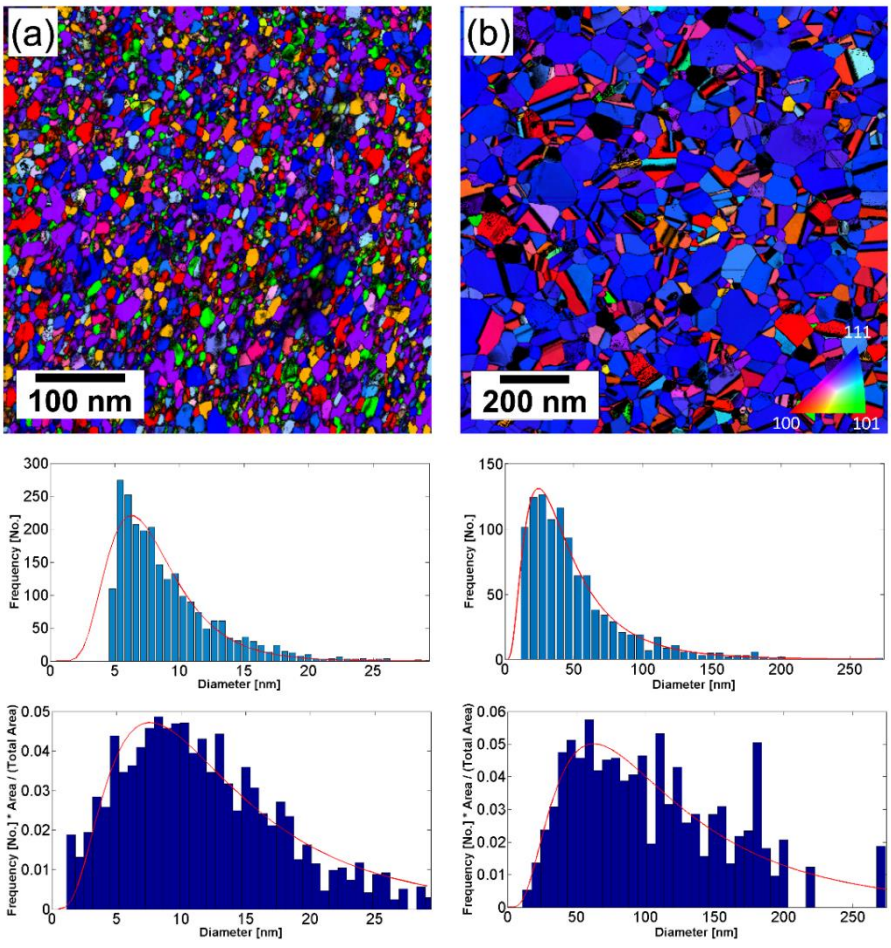

Figure 4-2 IPF maps along the film growth direction and the number and area-weighted average grain size distributions for (a) as-sputtered specimen aged for 18 months, and (b) after *in situ* annealing of the structure in (a).

4.2.2 *In Situ* FIB Transfer and Specimen Preparation for Nanomechanics

An *in situ* lift-out procedure inside the FEI Strata 400S DualBeam FIB was used to transfer the annealed film onto a PTP device from Bruker as shown in Figure 4-3. The procedure involved the lifting of the film using a transfer frame (Figure 4-3 (a)) that prevented bending/buckling of the film during lift-out and transfer to the PTP and facilitated an almost parallel placement of the film on the PTP enabling proper welding using Pt deposition. After transferring the film, the final specimen was prepared with a width (perpendicular to straining direction) of 4 µm and length (along straining direction) 2.5 µm as shown in Figure 4-3 (b) and (c). After the specimen preparation, the PTP was removed from the FIB and mounted on a customized holder, and inserted in the Fischione 1040 NanoMill for final cleaning of the residual Pt contaminants that typically exist in the form of nanoparticles. The final cleaning was achieved by tilting the stage to 8° and setting the ion source energy in the range 300-500 eV. Two *in situ* straining samples were prepared using this method.

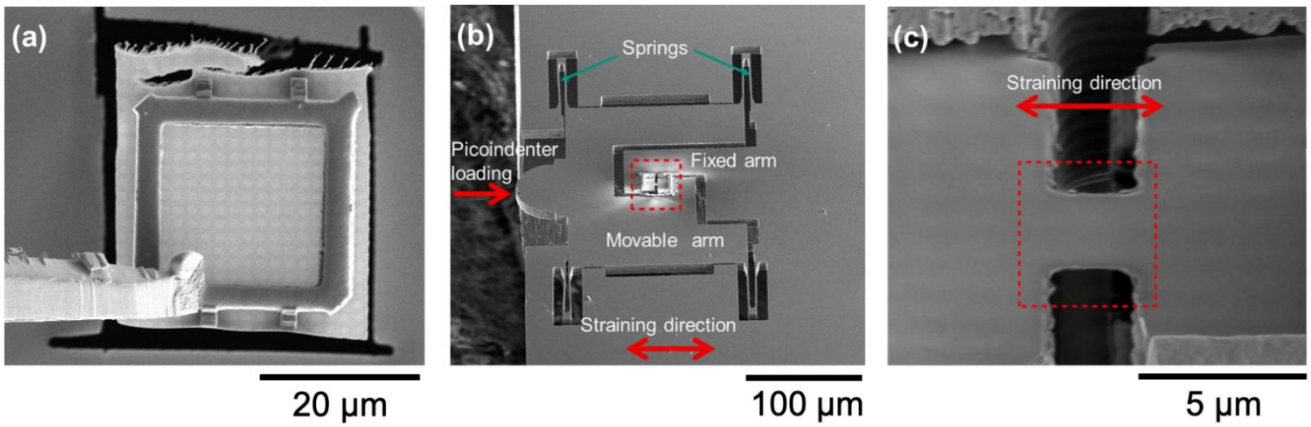

Figure 4-3 SE-SEM images of (a) sputtered Pd thin film lifted using a transfer frame, (b) side-view of the PTP device with 52° stage tilt, the red-dotted box indicates the area where the thin film is transferred and the final specimen is prepared, (c) enlarged view of the final specimen with the region of interest shown using the red-dotted box.

4.2.3 *In Situ* TEM Nanomechanical Experiments

Cyclic loading-unloading experiments were performed on the first thin film sample mounted on the PTP. The *in situ* nanomechanical experiments were performed with the PI95 TEM PicoIndenter from Bruker. The sample was strained along the Y-axis (Figure 4-4 (a)) under displacement-control and subjected to repetitive loading and unloading cycles at the displacement rate of 10 nm/s. After each cycle, the maximum displacement was progressively increased. During mechanical deformation, the specimen was imaged in BFTEM mode with an exposure time of 0.2 s. The cyclic experiments were conducted until the failure of the specimen. The specimen was strained for 6 cycles and the maximum strain achieved until the failure was 1.2%.

The *in situ* nanomechanical response measured during the cyclic loading-unloading experiments of the first specimen was corrected for drift. For a reliable drift correction, any manual interaction with the PicoIndenter for adjusting its position was avoided during experimentation. This ensured that the mechanical drift that existed between the PTP and the indenter remained almost consistent through all the straining cycles. The consistency of the drift was confirmed by monitoring the time stamps while the indenter made contact with the PTP for each cycle. The recorded displacement was then corrected by subtracting the measured drift at corresponding time stamps at each data point. The reliability of the drift correction was confirmed by the overlapping of the loading and unloading curves of the PTP (Figure 4-5), after fracturing of the sample. This ensured the accuracy of the drift correction both during loading and unloading of the specimen. The PTP contribution was subtracted from the overall drift-corrected response to obtain the true nanomechanical response of the sample (Figure 4-6).

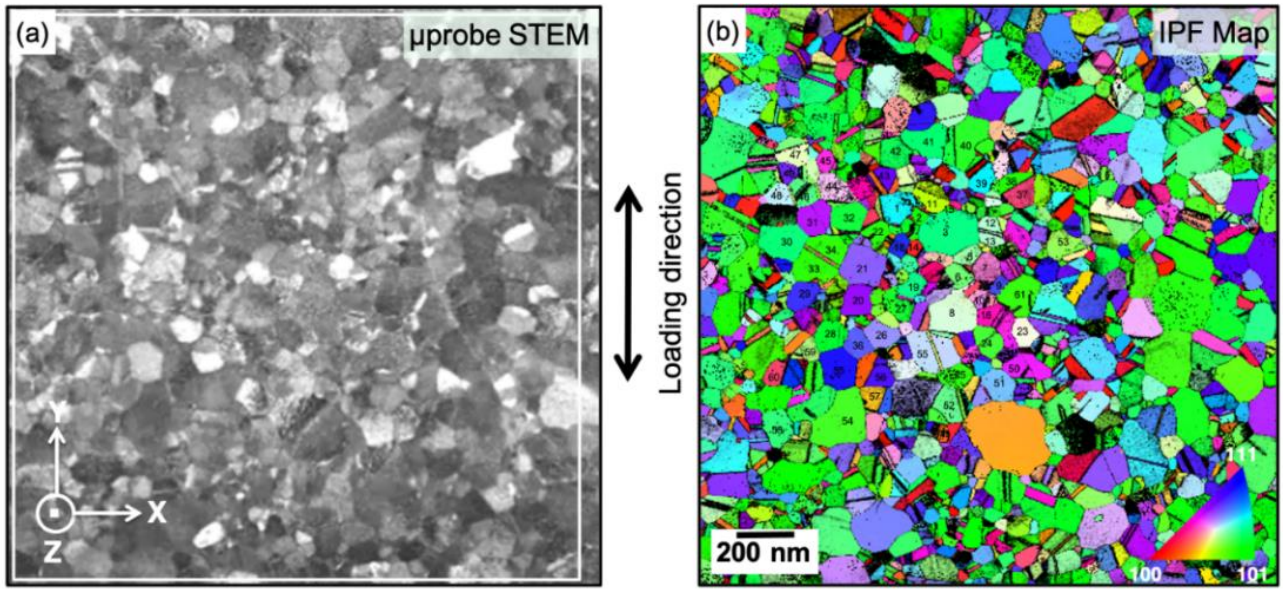

Figure 4-4 (a) μp-STEM image, and (b) reference IPF map along the loading direction acquired using ACOM-STEM from the rectangular region seen in (a). The grains analyzed are numbered.

For the second specimen, the *in situ* TEM cyclic deformation experiments were conducted for two cycles in a displacement-control mode to confirm the BE. Following these experiments, a straining series was recorded using load-control in μP-STEM mode with a condenser aperture of 30 μm leading to the semiconvergence angle of ~ 1 mrad. ACOM-STEM mapping was performed at the spatial resolution of 4 nm and precession angle of 0.4° during holding segments at different loading levels using the NanoMEGAS ASTAR system. Starting from the undeformed state, during each step the load was increased by 100 μN at the rate of 5 μN/s and held constant for 60 min at each holding segment. For the first 15 min of each segment, the specimen was allowed to stabilize following which an ACOM-STEM map was acquired for 40 min. A series of ACOM maps was acquired for one complete cycle (loading and unloading) with a maximum strain of 6.3% and for reloading up to 7.6% before failure of the sample. In addition, μP-STEM images were obtained before and after each ACOM-STEM map using the HAADF detector with a camera length of 80 mm. A reference STEM image at undeformed state is shown in Figure 4-4 (a) and an IPF map along the loading axis is shown in Figure 4-4 (b).

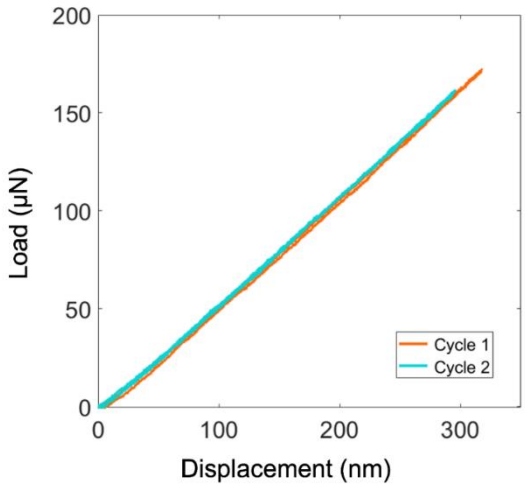

Figure 4-5 Drift-corrected load-displacement response of the PTP device which is overlapping during loading and unloading indicating a fully elastic behavior as shown for two cycles.

4.2.4 Data Processing and Analysis

The ACOM-STEM maps were indexed using proprietary software from NanoMEGAS. The resulting crystal orientation maps were processed for a reliable quantitative analysis of grain rotation using the 'Grain evaluation' program by Kobler [205,206], as discussed in chapter 3. Using the 'Grain evaluation', grain rotation maps were analyzed to exclude the bending or tilting of the specimen. Further, MTEX 5.2.beta2 by Bachmann et al. [211] was employed for the quantitative analysis of individual grain rotations with respect to their rotation angles. The grains were selected from the deformation states in which the specimen did not show any noticeable bending. These analyzed grains are numbered in Figure 4-4 (b).

4.3 The Bauschinger Effect in Nanocrystalline Palladium

Figure 4-6 shows the stress-strain curves obtained after drift correction of load-displacement response during the cyclic deformation experiments. Figure 4-6 (a) shows the cyclic deformation response of 6 loading-unloading cycles and a loading curve, the peak stress of which corresponds to the failure of the specimen. The curves are plotted to represent them continually. This means that each cycle begins at a point on the baseline (zero-stress) where the previous cycle ends. Figure 4-6 (b) shows these 6 cycles as a hysteresis plot where each cycle begins and ends at the origin. The maximum strain achieved for each cycle is indicated in Table 4-1. The maximum stress and strain to failure are 1469 MPa and 1.22%. The strain to failure obtained in the present study is consistent with prior results obtained by Colla et al. who reported 4%, 5.2%, and 2% for nc Pd thin films with thickness 310 nm, 160 nm, and 80 nm [22]. Further, the maximum stress until failure in their case was in the range of 1300 to 1400 MPa for 80 nm thick film which also fits in the present case.

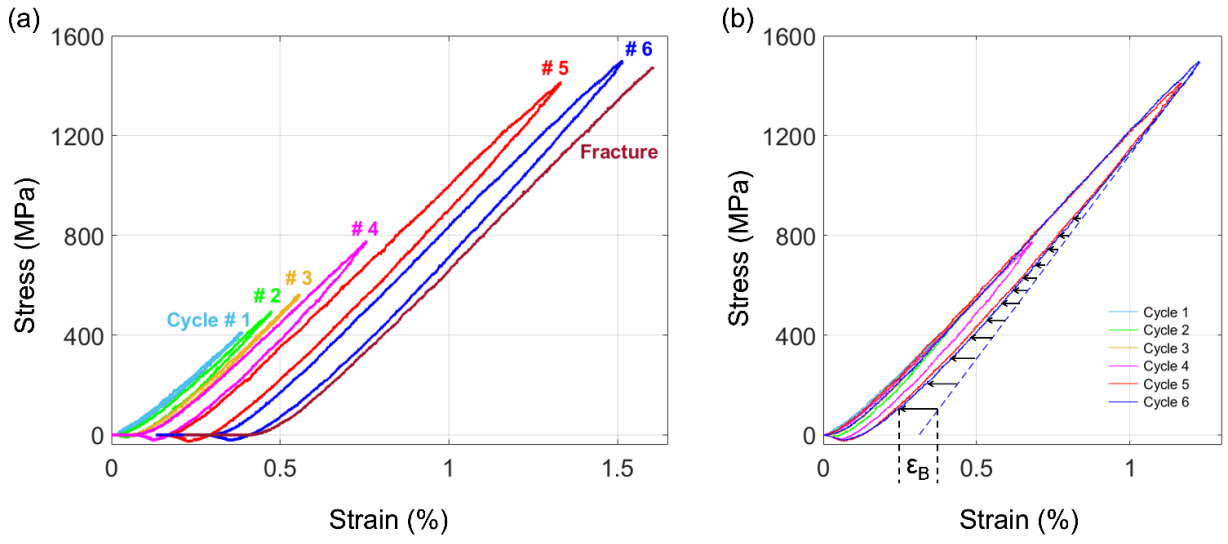

Figure 4-6 (a) Stress-strain response during cyclic loading-unloading experiments after drift correction for 6 cycles along with the curve corresponding to the failure of the specimen, and (b) hysteresis plot for 6 cycles. The deviation of the unloading response from the linear elastic trace (shown by blue dashed line) for cycle 6 is indicated by black arrows.

At lower stress levels (below 100 MPa), it is noted that the slope of the stress-strain curves increases gradually. This means that the mechanical response during the early stages of loading deviates slightly from a perfectly linear elastic behavior. This is expected due to systematic artefacts, that are probably related to the slight unbending of the sample. This can typically also occur due to readjustment of contact between the indenter and the PTP. As the stress in each cycle increases above 100 MPa, the stress-strain response during loading is nearly linear without any noticeable transition from the elastic behavior to the onset of plastic deformation although the maximum strain in the cycle is well above the conventional 0.2% limit. This observation is explained by the extended microplastic regime that is typically shown by nc metals unlike the sharp transition from elastic to plastic deformation in case of cg metals. For cycle 1, as seen in

Figure 4-6 (a), the loading and unloading parts of the curves are seen overlapped with each other, indicating an almost elastic response. From cycle 2 onwards, as the maximum strain increases, separation of the loading and unloading parts of the curves is seen. This separation occurs due to plastic deformation in the film. Another indication for the plastic deformation is the residual strain seen at the baseline as the sample is fully relaxed. This residual strain on relaxation is seen to increase for each cycle which indicates that the amount of permanent plastic deformation in the film increases (Figure 4-6 (b)). The unloading parts of the cyclic curves showed a continuous change in their slope. Like the loading parts, no precise transition from the elastic to the plastic regime is noticed. A straight dashed line is drawn fitting to the initial stages of unloading for cycle 6 (Figure 4-6 (b)). It represents the expected trace of the curve if the specimen showed a perfectly elastic behavior during unloading. The deviation of the unloading response of cycle 6 from the linear response is noticed with reference to this line and it is indicated by black arrows. This non-linear unloading response confirmed that there is plastic deformation in the reverse direction during unloading or in other words, there is plastic recovery. This is evidence for the Bauschinger effect (BE) that leads to plastic recovery during relaxation. The BE was observed for cycles 2 to 5 as well for which the linear fitting is not shown in Figure 4-6 (b).

Cycle	Maximum strain (ε_{max})	Bauschinger strain (ε_B)
1	0.39%	0.02%
2	0.46%	0.03%
3	0.5%	0.04%
4	0.67%	0.07%
5	1.16%	0.13%
6	1.2%	0.13%

Table 4-1 Maximum strain achieved for each cycle and the corresponding Bauschinger strain measured at 100 MPa.

The BE in nc Pd thin film occurring as a result of plastic recovery which is reflected from the characteristic non-linear unloading response (Figure 4-6 (b)) is similar to the one reported by Xiang et al. [49], Höppel et al. [81] and Rajagopalan et al. [61] who observed it for other metallic thin films. Rajagopalan et al. had observed a plastic recovery up to 0.38% for nc Al and 0.07% for nc Au [61]. In the present study, assuming a complete unbending of the specimen at stresses above 100 MPa the plastic recovery or the Bauschinger strain (ε_B) evaluated at 100 MPa from cycle 1 to 6 increases from 0.02% to 0.13% (Table 4-1). Thus, the BE progressively increases as the maximum applied strain is increased. The ε_B is highly sensitive to the loading or strain rate, the maximum strain achieved for each cycle, and the microstructural heterogeneities in the specimen. All these factors influence the generation of stress build-up or deformation heterogeneity in the specimen. As reported previously, the BE is associated with building-up of stresses at GBs and/or film-substrate interface due to pile-up of dislocations [49,61,64,82]. The piling-up of dislocations results in the generation of back-stresses at GBs. These back-stresses lead to a reverse motion of dislocations during unloading and thus, reverse plastic deformation occurs. The BFTEM images (not shown here) acquired during the cyclic deformation in the present study showed partially reversible contrast changes in several grains. Further, after complete relaxation of the specimen on unloading after each cycle, most of the grains continued to exhibit contrast changes for a few seconds. These observations supported the presence of back-stresses on the relaxation of the specimen. The observed contrast changes in the BFTEM images are attributed to complex contributions from the rotation of grains, activity of dislocations as well as thickness and bending effects. The visualization and analysis of dislocations by classical BFTEM in multiple nanoscaled grains with different orientations was not achieved due to the single-tilt capacity of the straining holder and the challenges involved in tilting individual nano-grains to the orientations needed for imaging dislocations. Considering these limitations, the ACOM-STEM results obtained during the cyclic deformation were used to support the evidence for dislocation-based mechanism and the associated BE as discussed in the following sections and chapter 5.

4.4 Analysis of Grain Rotations

Grain rotations and texture characteristics can offer greater insights into deformation mechanisms underlying the observed BE. ACOM-STEM in combination with the loading-unloading experiments provided crystallographic orientation from a large number of grains representative of the specimen as a whole. For analyzing the deformation characteristics, the rotation of a large number of grains was evaluated by careful analysis of the changes in their orientations at each deformation step.

For reliable analysis of grain rotations, the accuracy of orientation measurements for small orientation changes becomes critical. The angular resolution offered by ACOM-STEM is about 1° for a single measurement [193,221]. The precision of the orientation measurements can be improved if an average orientation is considered taking into account all the data points within a grain. For accurate measurement of the grain rotations, the rotation angles were evaluated by considering the mean orientation, obtained by averaging over all the data points within each analyzed grain. As an illustration, Figure 4-7 shows a magnified view of one of the four {111} poles from a grain (grain 3 in Figure 4-4 (b)) for which orientations from all the data points are shown before and after deformation. The information from each data point is represented as a small-dotted marker. The mean orientation is shown by the bigger star-shaped markers of respective colors. The standard deviation of angles evaluated between the mean orientation and orientation from each data point is about 0.1° for both the deformed states. The mean rotation during deformation is 0.5° as highlighted by the dotted arrow. The orientations from data points are broadly clustered into 2 groups indicating the presence of a sub-grain boundary. Thus, the standard deviation consists of contributions from not only the errors in orientation measurement but also other factors like the presence of small-angle boundaries or curvature within the grain. The standard deviation averaged over all the analyzed grains at the reference state (Figure 4-4) is 0.2°. The red error bar at 3.6% strain in Figure 4-8 indicates this average standard deviation of the orientation spread within each analyzed grain. This error bar reflects the upper limit for the reliability of orientation measurements, as it incorporates contributions from the orientation gradients and variations due to small-angle boundaries within grains. As the orientation is averaged over several data points, the precision of measurements over individual grains is considerably enhanced.

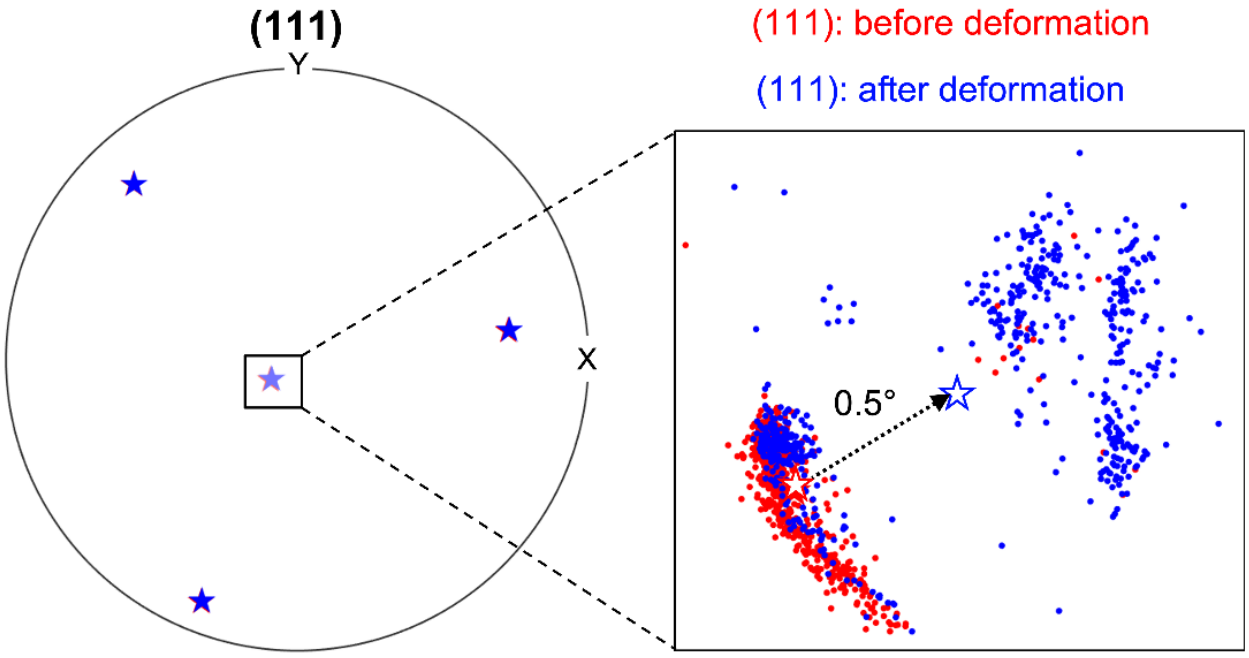

Figure 4-7 A magnified view representing the orientation spread within the grain 3 (shown in Figure 4-4 (b)) plotted on a (111) pole figure. The small red and blue markers denote the orientations at 3.6% and 4.8% strains, whereas the two larger star markers correspond to the mean of the grain orientations at the respective deformed states. X-Y plane corresponds to a plane parallel to the specimen plane according to the coordinate system shown in Figure 4-4 (a).

The orientation refinement algorithm in the NanoMEGAS ASTAR software was used while indexing all the orientation maps. As formulated by Rauch et al., the algorithm ensures a further enhancement in the angular resolution by interpolating the diffraction intensities between successive orientation templates [193]. This results in greater precision of about 0.3° for orientation estimation. The fidelity of the orientation measurements using this approach was further validated by Leff et al. in their analysis [222]. Thus, although pixel-level angular resolution is 1°, together with the orientation refinement and the small standard deviation of 0.2° it is reasonable to analyze the 'mean' change in orientation or rotation of less than 0.5°.

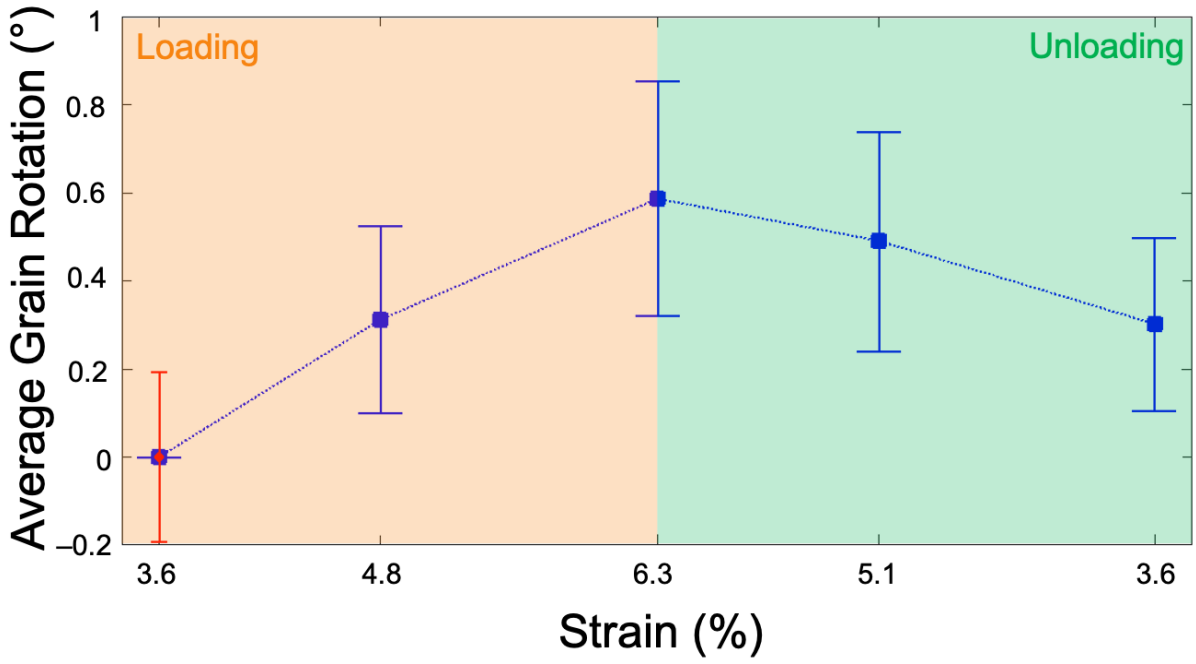

Figure 4-8 Average grain rotation evaluated for 55 grains with blue error bars indicating the standard deviation of the rotation angles evaluated at each deformation step during loading and unloading. The red error bar at 3.6% strain indicates the average standard deviation of orientation changes including the contributions from curvature and small-angle grain boundaries within each analyzed grain.

The results of the analysis are shown in Figure 4-9 as grain rotation maps in which the rotation of each analyzed grain is represented using the color code. The analyzed grains are marked with yellow color in the reference map for which the initial deformation stage at 0% strain was selected. From the rotation maps in Figure 4-9, it is seen that in the early stages of deformation (up to 1.9% strain) during loading majority of the grains exhibit rotations in the range of 2-3 degrees. Often the grains in the close neighborhood are seen to rotate by the same amount as it can be noticed from the same color of these grains. Similar behavior is noticed for the later stages of unloading from 2.2% to 0.7% strain. These observations suggest that there is a systematic bending of the specimen during the early stages of loading and later stages of unloading. The experiments involving the acquisition of ACOM-STEM maps were preceded by some *in situ* deformation experiments to investigate the BE. These prior experiments are likely to introduce some permanent plastic deformation in the specimen. This residual plastic deformation is reflected as the bending or tilting of the specimen once the arms of the PTP are at rest position.

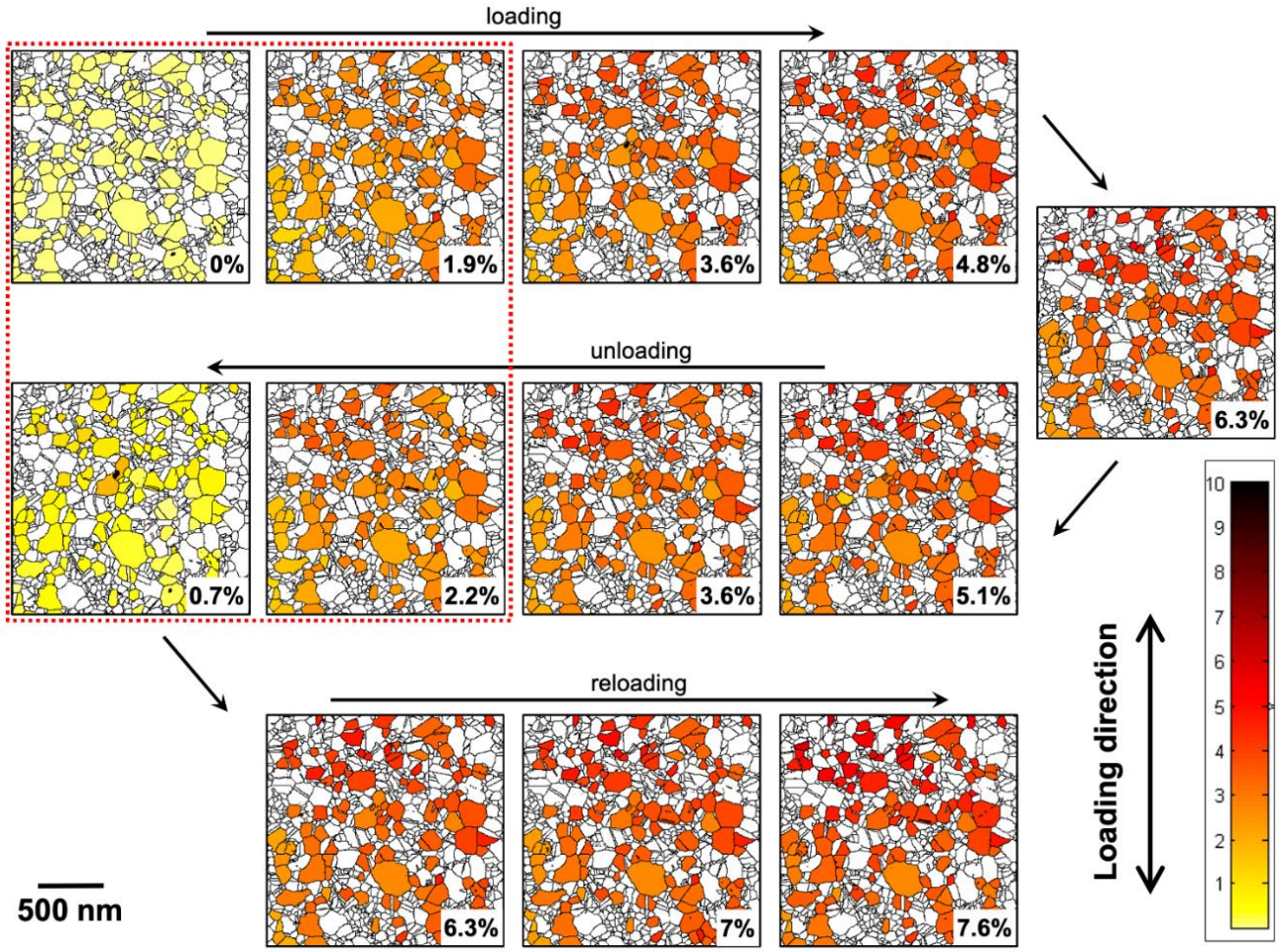

Figure 4-9 Grain rotation maps evaluated for the entire ACOM-STEM series during loading, unloading, and re-loading, and the corresponding strain is indicated (in %) for each deformed state. The colored grains in each map are the ones analyzed and their rotation (in degrees) is colored as indicated by the color bar. Based on the color bar, maximum rotations up to 10 degrees have been presented. The grains that are not colored were not analyzed. The red-dotted square encompasses the rotation maps indicating bending of the sample around an axis approximately 45° to the loading direction due to elongation of the film during earlier straining experiments followed in BFTEM. These maps were excluded from the detailed data analysis.

The thin film specimen, during straining, eventually unbends and becomes flat. Based on this, Figure 4-10 shows the grain rotation maps that were analyzed with 3.6% strain as the reference state, and the straining states below 3.6% strain were excluded. For the observation of very small changes of rotations, these maps were plotted at a much finer scale to represent rotations of less than 1°. From the maps shown in Figure 4-10, it is seen that from 3.6% to 4.8% strain the rotation of the majority of grains is less than 0.5°. Also, the magnitude of these rotations is different for grains located in close neighborhood, unlike the observations from Figure 4-9. Thus, it is reasonable to consider that the bending effects of the specimen for straining states greater than 3.6% are almost negligible. For the quantitative analysis of grain rotations in the present and next chapter, 3.6% strain was selected as a reference state and the straining states below it were excluded.

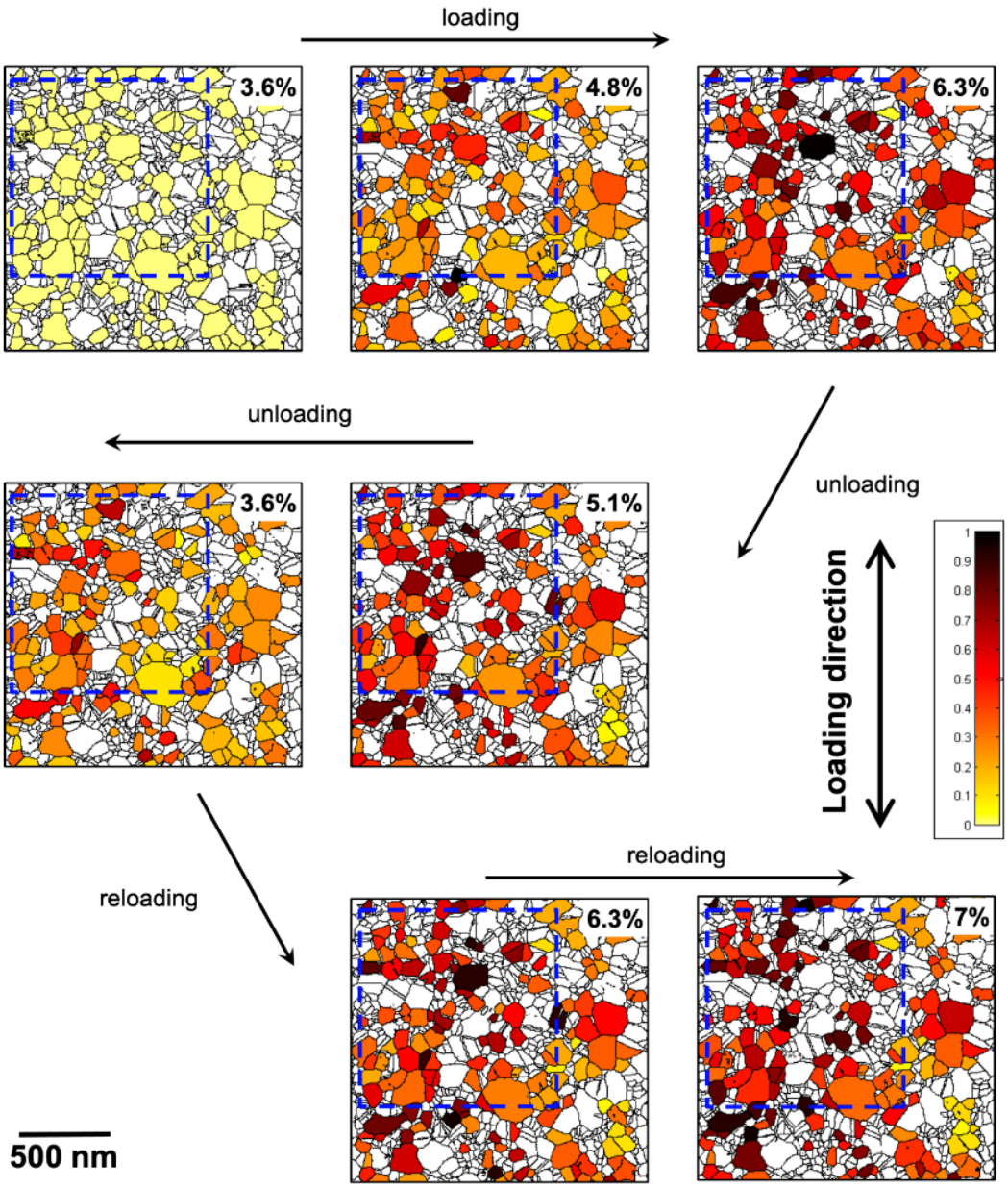

Figure 4-10 Grain rotation map series excluding the bending/tilting stages indicated in Figure 4-9 with the 3.6% strain map as a reference state. The colored grains in each map are the ones analyzed and their rotation (in degrees) is colored as indicated by the color bar. Based on the color bar, maximum rotations up to 1 degree have been presented. No long-range rotation gradient is visible, indicating that no bending/tilting of the sample occurred during this part of the straining series. The blue dotted box shows the region from which the grains were selected for the detailed analysis. They are numbered as shown in Figure 4-4 (b).

Figure 4-11 shows grain rotation maps from the same region as seen in Figure 4-10 and compares the mean rotation of each grain and the rotation at the pixel level, which represents intragranular rotation. Figure 4-11 (a)-(e) show the maps considering the mean orientation of each grain with colors indicating the degree of rotation relative to the orientation at 3.6% strain. It can be seen that the grains show distinct rotation during loading indicating that these rotations are due to mechanical deformation of the sample and not due to bending of the film. As the specimen is unloaded, a reduction in the rotation of the grains is seen. This exemplifies the overall rotational response of the specimen as seen in Figure 4-8, which shows the average deformation-induced grain rotation (excluding the states exhibiting sample bending/tilting) evaluated for 55 grains. Thus, globally, the average grain rotation increases during loading and decreases during unloading.

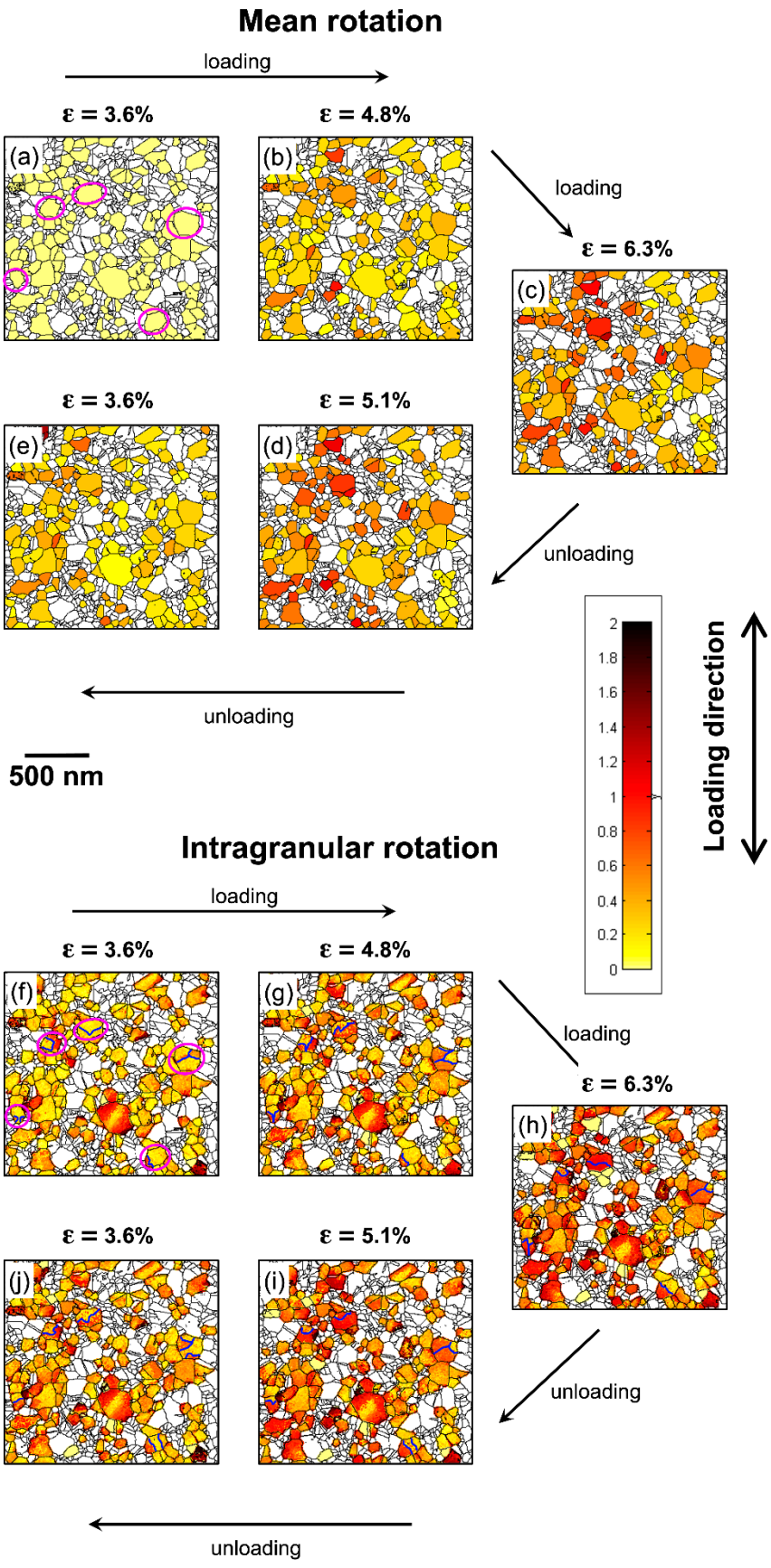

Figure 4-11 (a)-(e) mean grain rotation maps and (f)-(j) intragranular rotation maps at the given strains. Some selected grains (encircled in pink) show re-arrangement of sub-grain boundaries (shown in blue) in (f)-(j).

4.5 Characteristics of Deformation-induced Grain Rotations

Considering the grain size distribution and plastic recovery observed in the sample as BE, operation of both inter- and intragranular plasticity mechanisms driven by dislocations is expected. The grain rotation maps obtained from ACOM-STEM data enabled the realization of the dislocation activity in multiple grains during deformation. The dislocation activity within some of the grains indicated in Figure 4-11 (a)-(e) is expected to drive their rotations. This is supported by the intragranular rotation maps obtained for the same grains (Figure 4-11 (f)-(j)) that reveal significant rearrangement of sub-grain boundaries, providing evidence for intragranular dislocation activity as a mechanism behind the grain rotation. These changes are prominently seen for grains encircled in Figure 4-11 (a) and (f). On unloading (Figure 4-11 (h)-(j)), it is noticeable that the sub-grain boundaries undergo a partially reversible motion. This indicates a reverse motion of dislocations during relaxation due to the generation of back-stresses in the film.

For some of the analyzed grains, most of the pixels within grains show rotation almost equal to their mean rotation without a noticeable change in the sub-grain boundary structure. From these observations, there could be different possible contributions to the grain rotations. Considering the dislocation-based mechanism, this may simply occur if the dislocations are emitted and escaped at another grain boundary or free surfaces in the time interval between consecutive orientation maps. Therefore, not all evolving sub-grain boundaries could be detected experimentally. From the analyzed specimen, the GB sliding or stress-coupled GB migration were not noticeable. As a result, the dislocation-based processes are expected to mainly control the deformation in nc Pd thin film. Furthermore, only geometrically necessary dislocations (GNDs) are expected to contribute to the intragrain rotations whereas the activity of statistically stored dislocation (SSDs) remains unaccounted in the grain rotation analysis. Further investigations on the role of GNDs governing the local deformation characteristics in nc Pd are presented in the next chapter.

So far, in this section, the grain rotation and associated deformation mechanisms in nc Pd were discussed. The magnitude of average grain rotation increased during loading whereas it decreased during unloading. This fits well with the observed mechanical response, characteristic of the BE as shown in Figure 4-6. The BE is accompanied by relaxation due to the reduction and partial reversibility of grain rotations during unloading. The grain rotation was shown to be partly occurring as a result of changes in the sub-grain boundary structure which is attributed to significant intragrain dislocation activity evidenced from the rearrangement of sub-grain boundaries. Overall, the distinct rotation of individual grains, both in terms of magnitude (shown in Figure 4-11 (a)-(e)) and direction (as discussed in the next section), indicates the generation of heterogeneous stress distribution and build-up of back-stresses at the grain boundaries. The heterogeneous stress fields may develop due to heterogeneity in the microstructure due to differences in the grain sizes, a larger grain surrounded by smaller grains. These could also result due to differences in the grain boundary type, grain orientation as well as geometric incompatibility of the slip systems. The microstructural heterogeneity has been shown to play a critical role in driving the BE in thin metallic films, as reported in detail in ref. [61,63,223].

4.6 Global Crystallographic Texture Evolution

In the previous section, a significant contribution of dislocation activity within grains was shown to cause their rotations. The dislocation activity in the presence of strong stress build-up raises an argument on the extent to which the rotation of grains during deformation is dependent on their initial orientation. Therefore, the orientation dependence and directionality of the rotations with respect to the global straining direction were analyzed. Figure 4-12 (a) and (b) show the magnified vector representation of the direction of rotation of the tensile axis on IPF for each analyzed grain during loading from 3.6% to 4.8% and unloading from 5.1% to 3.6%. It is noted in both the figures that the tensile axis for each grain rotates along different directions and often grains with similar crystallographic orientations tend to show different rotation directions. The magnitude of rotations as seen from the length of these vectors in IPF are fairly different. This is observed even for the grains numbered 1 to 10 that are spatially located very close to each other. In addition, the orientation of the tensile axis of some of the grains (e.g. grains 4, 5, 6, and 8) are not very different on the IPF, nevertheless, the magnitude and direction of their rotation are different. These observations suggest that the rotations of grains with respect to the global tensile axis are to a great extent independent of their initial orientations. The different magnitudes of rotations, as suggested in the previous

section, also explain the impact of local stress build-up leading to heterogeneous rotations of the grains. It is further seen that the vectors in most cases point in the exact opposite direction during loading and unloading, indicating a reversible rotation of the grains with respect to the global straining direction. The reverse rotation of most of the grains suggests that although the local stress distribution is heterogenous, on unloading these stresses locally tend to drive the plastic deformation in the reverse direction, or in other words, there is plastic recovery. These results are in good agreement with the observed BE and suggest that the dislocation-driven grain rotations are significantly contributing to the rotations observed in Figure 4-12. For a few grains, it is noted that their tensile axis is not rotating in the exact reverse direction. The rotational responses for these grains may be expected due to complex contributions from either dislocation or GB-based processes or both.

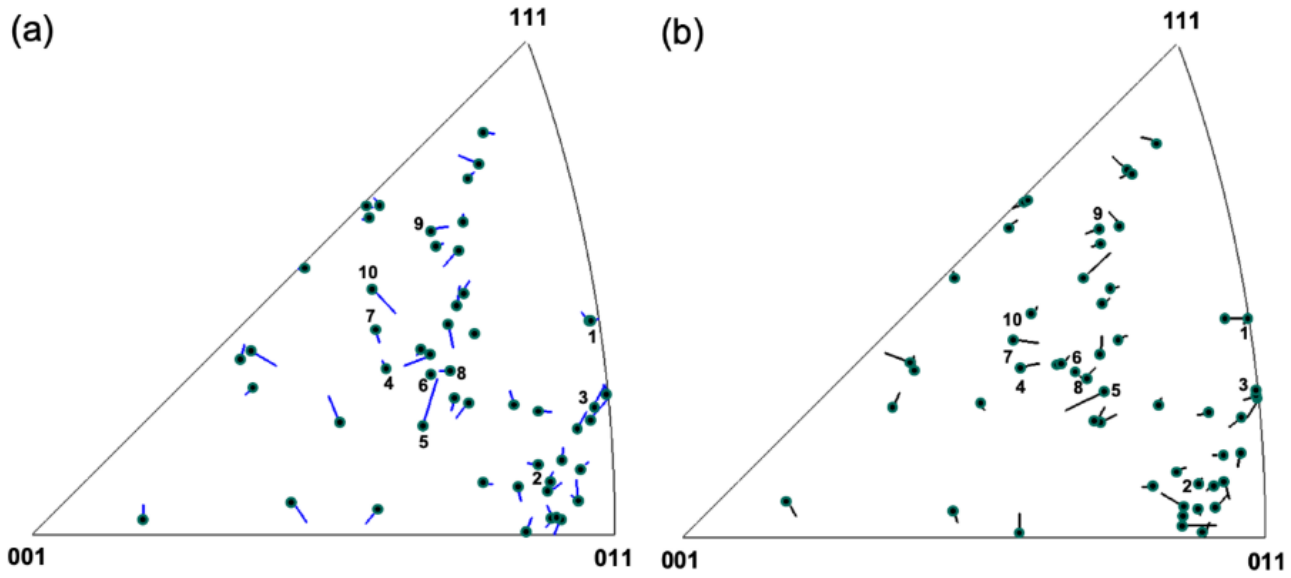

Figure 4-12 Inverse pole figures showing the vectors magnified by 4 times of their absolute length by joining the initial and final positions of the loading axis shown in Figure 4-4: (a) during loading from 3.6% to 4.8% strain, and (b) during unloading from 5.1% to 3.6% strain. Vectors corresponding to the loading axis of grains 1 to 10 as seen in Figure 4-4 are annotated.

Winther and coworkers had made a comprehensive analysis of the lattice rotations of individual bulk grains that were several micrometers large. They were able to experimentally show that rotations of the grains are strongly dependent on their initial orientations with respect to the straining axis [85,86,90]. These rotations were attributed to the dislocation slip-based processes. However, their results showed certain deviations from the Taylor and Sachs models. These deviations were explained based on the interaction of grains and the stress build-up at grain boundaries. Such grain interactions were also reported by others [93,96,100,224] for the cg metals.

Even for nc metals of grain sizes as small as 28 nm, Yang et al. were able to present the dislocation-based plasticity mechanism by both experiments and simulations. However, the amount of strain in their case was as high as 50% [147]. In the present case, the applied strain is much smaller, less than 10%. At these smaller strains, mostly the primary slip systems would be expected to be activated. Thus, if a pure dislocation-based mechanism is assumed to operate without interactions between the grains, the rotation of most of the grains should be strongly dependent on their initial orientations. In that case, the texture evolution would be expected to be in good agreement with the classical models of plasticity. However, in the present study, significant randomization of the texture is seen for a majority of grains. For nc metals, it is generally accepted that a random texture develops if the plastic deformation is dominated by the GB-mediated processes. In contrast, the present study showed that dislocations are driving the majority of the grain rotations, and these are to a great extent influenced by a strong stress build-up at the GBs that leads to the BE. From these results, it is seen that even the operation of dislocation-based processes in presence

of significant interactions between the grains and strongly heterogeneous stress fields could lead to random texture. Detailed interactions between the grains based on dislocation-related processes and their resulting rotation are discussed in the next chapter. From the present study, it may be concluded that an absence of texture development does not necessarily justify the dominance of GB-mediated processes and this could occur due to dislocation-based processes in the presence of strong stress build-up or due to competition of these processes.

4.7 Summary

In situ TEM nanomechanical experiments were performed on nc Pd to measure the cyclic deformation response. Nc Pd showed the Bauschinger effect which was confirmed from the significant plastic recovery that was observed during unloading of the specimen. With the progressively increasing maximum strain for each cycle, the amount of plastic recovery increased indicating that the BE became more pronounced with increased deformation. The combination of these *in situ* experiments with ACOM-STEM yielded further insights into the active deformation mechanisms underlying the observed BE. Detailed quantitative analysis on several grains showed extensive grain rotations as the specimen deformed. On average, the rotations of the grains increased on loading whereas a reduction in grain rotation was observed as the specimen was unloaded indicating that rotation of grains in the specimen exhibiting BE is mostly reversible. The analysis of intragrain rotation maps showed rearrangement of the sub-grain boundaries within grains indicating that the grain rotations are primarily driven by the dislocation activity. The forward and reverse motion of the dislocations explained the increasing and decreasing rotations of the grains which are in agreement with the observed BE. The magnitude of rotations for the grains that are in close neighborhood with each other was found to be different. This is presumably due to the development of heterogeneous stress-field that arises due to the variation in microstructural characteristics like grain sizes, crystal orientation, or GB character. The impact of stress heterogeneity was evidenced on the global texture characteristics. The rotation of tensile axes for the majority of the analyzed grains was found to be independent of their orientation and was mostly random, fitting to both dislocation as well as the GB-mediated processes. For most grains, the rotation of the tensile axis was found to be reversible indicating that the local stress fields on unloading lead to the plastic recovery within these grains. Based on these observations, it was shown that dislocation activity in the presence of heterogeneous stress-field could lead to the random texture during the deformation of nc metals.

5 Grain Interactions in Nanocrystalline Palladium

5.1 Introduction

Several studies in the past have investigated the interaction between grains and proposed models to account for these interactions. Most of these reported studies were focused on cg metals. In nc metals, these interactions are expected to be far more complex due to increased interactions of dislocations with the GBs. In addition, the GB-mediated processes are associated with rotational deformation. To investigate these complex grain interactions, it is essential to locally analyze and establish a correlation between the rotation of grain with its neighbors. For these local investigations, the same nc Pd specimen as probed in chapter 4 was chosen, a cropped region of which is shown in Figure 5-1. Some specific grains were selected from this specimen that showed unusual interactions. Based on the analyses of these interactions, this chapter presents a unique plastic deformation mechanism that involves the cooperative rotation of nanoscaled grains during *in situ* cyclic loading-unloading experiments.

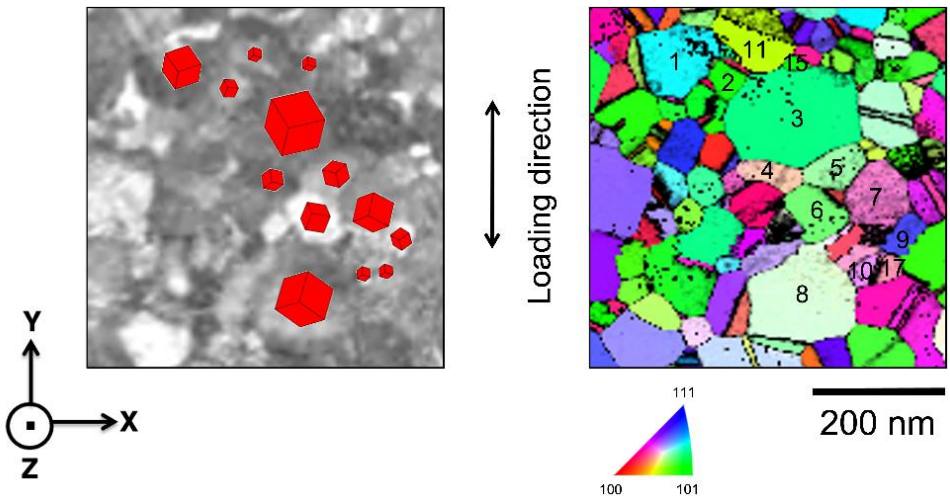

Figure 5-1 Reference area for analysis of grain interactions: (a) µp-STEM image showing unit cells scaled according to grain sizes and representative of crystal orientation of grains, and (b) corresponding IPF map along the loading direction (Y-axis).

5.2 Estimation of GND Density

The Nye tensor analysis was performed for estimating the GND density using the ATEX software programmed by Beausir and Fundenberger [213]. For analysis of the GND density, a kernel orientation filter was applied with 1 neighboring pixel and the maximum exclusion angle of 5°. The maximum disorientation angle used for the analysis was 5° and a smoothing level of 2 was applied for the reduction of noise. The maximum value of the entry-wise norm of the Nye tensor was scaled to 3 μm^{-1} to obtain the spatial distribution of the scalar GND density as color maps.

5.3 Cooperative Grain Rotations

Microprobe STEM (µp-STEM) with annular dark-field (ADF) imaging offers information sensitive to the diffraction from each grain. The contrast changes in these images are sensitive to change in the crystallographic orientation of the grains during plastic deformation. These contrast changes can be effectively used to track the rotation of grains. The propagation of these contrast changes from one grain to its next neighboring grain with increasing or decreasing global strain is an indication of interaction between the grains. Thus, µp-STEM imaging during *in situ* straining experiments was used to visualize the complex interactions between grains that exhibited step-wise changes in their rotation with one grain rotating after another as the deformation progressed. In the present study, these rotations are referred to as cooperative grain rotations (CGR).

Figure 5-2 shows the µp-STEM image series acquired after the acquisition of each ACOM-STEM map. The STEM series consists of images that were acquired during loading, unloading, and reloading of the specimen. The corresponding strains measured at each step are shown in the images. The purple arrows are indicated for visualization of the approximate direction of propagation of the contrast changes from grain to its neighbor. In Figure 5-2 (a-c), it is seen that during loading from 3.6% to 6.3% the contrast successively changes from grains 6 to 4 to 3 as shown by the arrows. On unloading, in Figure 5-2 (d-f), the contrast changes are seen in the reverse direction from grains 3 to 4 to 6 towards grains 9 and 10. On reloading in Figure 5-2 (g-i), similar changes in the contrast could be seen through the same sets of grains that showed this effect during the initial loading (Figure 5-2 (a-c)). The STEM images in Figure 5-2 were acquired in microprobe mode with a low semi-convergence angle of 1 mrad and a camera length of 80 mm. This results in the collection of mostly the Bragg-diffracted signals from each grain thereby leading to a contrast sensitive to the crystal orientation. Thus, these contrast changes are an indication of grains showing a correlative change in their orientation. It is noted that grains 5 and 7 including some other neighboring grains do not exhibit a significant change in contrast. Furthermore, they do not show any correlation with the systematic and almost reversible contrast changes occurring in grains 3, 4, 6, 9, and 10. The correlative contrast changes occurring in grains 3, 4, 6, 9, and 10 reflect their propensity to undergo a cooperative deformation. As this deformation process is associated with the rotations of grains, it is termed cooperative grain rotation.

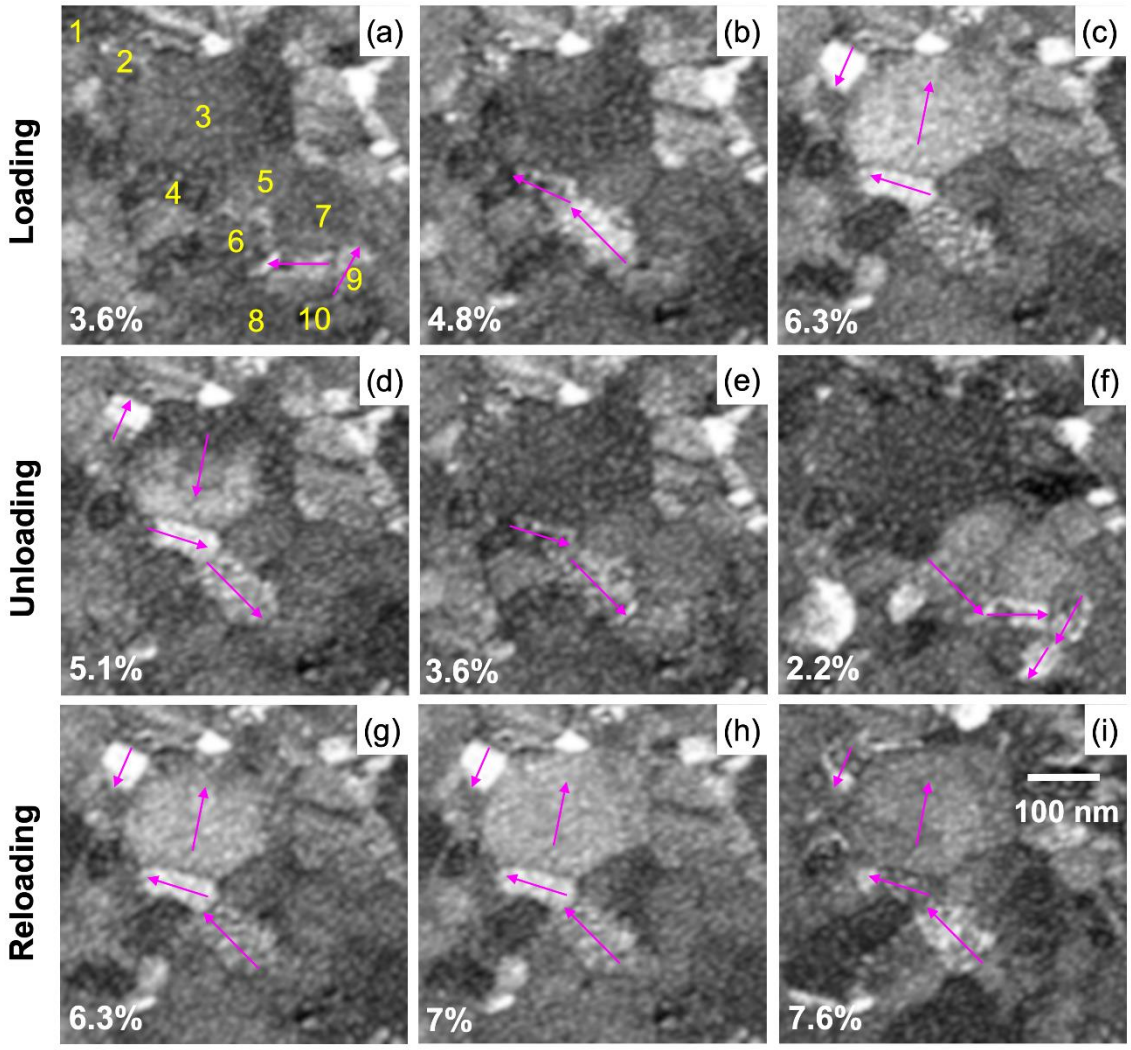

Figure 5-2 Microprobe STEM images acquired after each ACOM-STEM map showing cooperative rotation of grains: (a)-(c) loading, (d)-(f) unloading, and (g)-(i) reloading. The corresponding strains at each deformation state are indicated in the images. The grains in (a) are numbered as in Figure 5-1.

It may be noted that the CGR occurs in a step-wise manner, one grain rotating after another. It does not occur simultaneously or as a collective rotation of multiple grains at the same time. This is unlike the collective rigid body rotation of multiple grains that is usually associated with the GB-mediated processes. As the geometry of the HAADF detector is annular, it may be concluded that the contrast changes seen in Figure 5-2 are due to the rotation of the grains with a strong out-of-plane component. Under these conditions, the rotations with a pure in-plane component are not detected. Figure 5-3 shows the rotation of specimen Z-axis in the crystal reference frame. It is seen that a majority of grains show absolute rotation greater than 0.2° which suggests their strong out-of-plane rotation. The strong out-of-plane components of the grain rotation are expected due to the microstructural constraints including anisotropy of crystal orientation. Due to the strong anisotropy of the crystal orientations along the growth direction for the majority of grains, a set of slip systems with a specific inclination with respect to the growth direction or the plane of the film is preferentially activated. From the orientation of each grain determined using the ACOM-STEM in the previous chapter, the Schmid factor was analyzed for the grains shown in Figure 5-2 (a). The film mostly consists of a single layer of grains with free surfaces. Assuming the back-stresses at the film-substrate interfaces to be relatively small, the stresses on a grain due to its neighbors are mostly confined within the plane of the film. As a simplified approximation, the Schmid factors were evaluated considering a uniaxial stress tensor in the direction of externally applied load which is along the Y-axis according to the coordinate system shown in Figure 5-1. Table A-1 shows the analysis of the Schmid factor for grains 1 to 10. Due to a strong {111} texture in the film, the majority of the grains have their <110> (111) slip systems almost parallel to the film plane. These are referred to as the in-plane slip systems. For the remaining 9 slip systems, the slip planes are comparatively at a much greater inclination with the plane of the film. Accordingly, these have been categorized as out-of-plane slip systems. As seen in Table A-1, for most cases, the in-plane slip components have a relatively lower Schmid factor compared to the out-of-plane slip systems. This is explained by the geometric arrangement of these slip systems. The in-plane slip plane normals are near orthogonal to the loading axis. As a result, the resolved shear stresses on the in-plane slip components are lower. This is also valid for the stresses on a grain due to its neighbors, since these are mostly confined within the film plane, and their contribution to activating the in-plane slip systems is negligible. Thus, for simplified analysis, it is reasonable to consider a uniaxial stress tensor to evaluate the Schmid factors. Since the film is composed of mostly a single layer of grains through the thickness and the grains have a free surface on the top, there is a greater probability of the activation of out-of-plane shear components. This explains the strong tendency of the grains to undergo out-of-plane rotation during deformation.

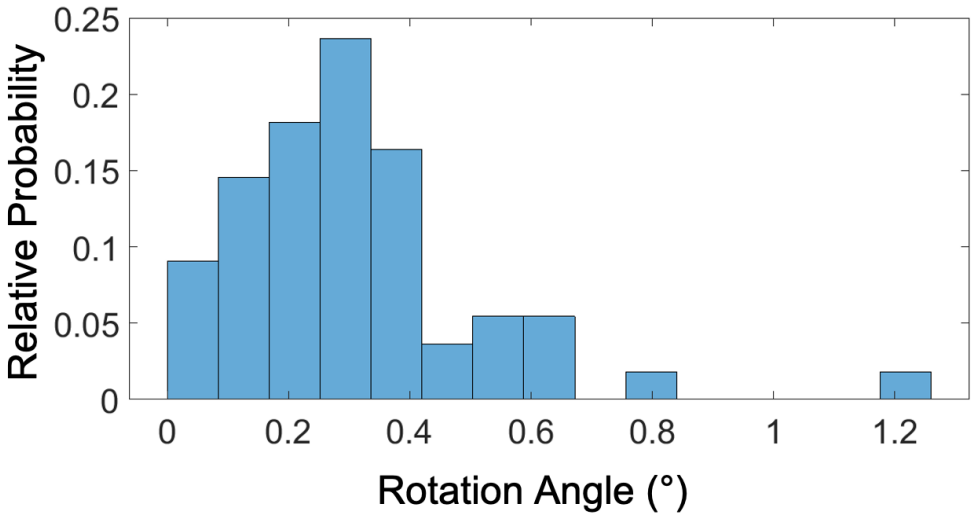

Figure 5-3 Probability distribution of rotation angles of the specimen Z-axis as shown Figure 5-1.

5.4 Local Quantitative Analysis of the Cooperative Grain Rotations

Figure 5-4 shows the local analysis of mean and intragranular rotation from the same area as shown in Figure 5-2. From the color maps in Figure 5-4 (a)-(b) and (b)-(c) it is seen that the amount of rotation from grains 6 to 4 and 4 to 3 gradually increases as the strain is increased. Similarly, a gradual reduction of the rotations could be seen for these specific grains in Figure 5-4 (d)-(e), as the strain is decreased. Figure 5-4 (f)-(j) show significant rearrangement of sub-grain boundaries for these grains during loading and to a certain extent, this is also reversible on unloading. These observations qualitatively support the deformation heterogeneity resulting from dislocation activity within these grains and at the GBs. Thus, cooperative and mostly reversible rotation of grains occurs during the plastic deformation in nc Pd. The reversibility in the grain rotations fits the localized plastic recovery and the Bauschinger effect seen for the same specimen as a whole in the previous chapter.

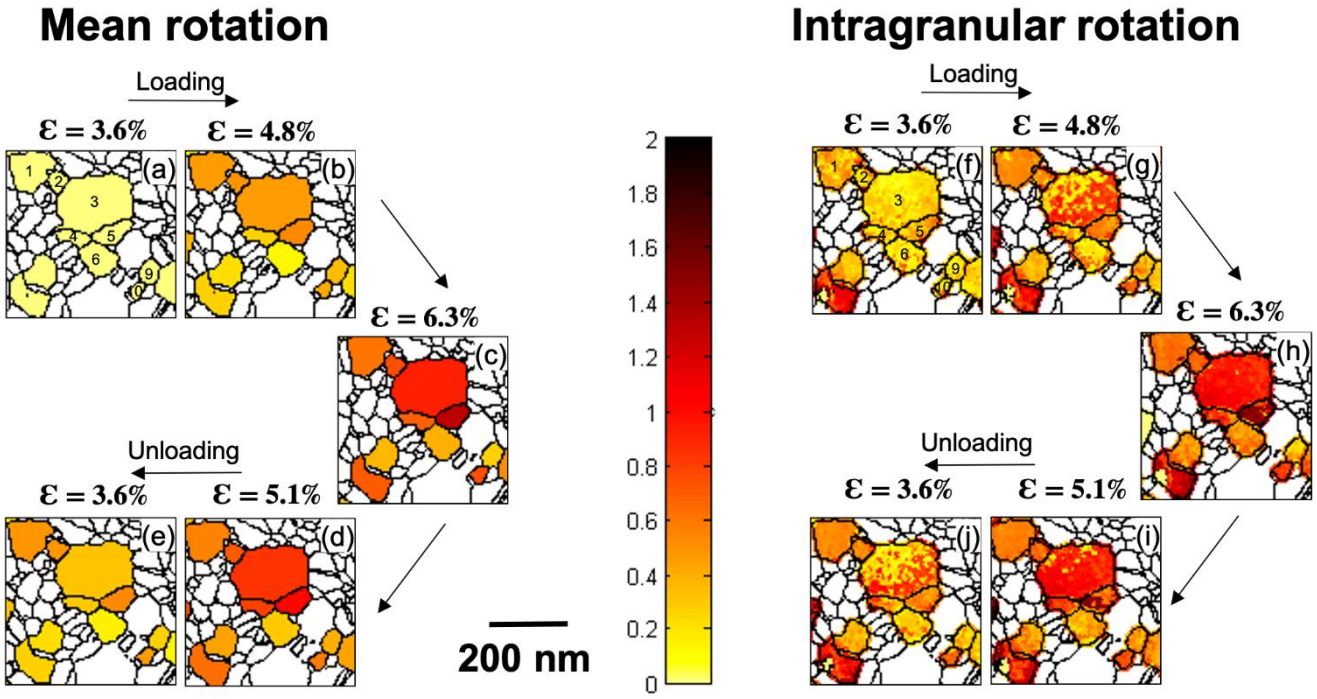

Figure 5-4 Mean and intragranular rotation maps for the grains exhibiting cooperative grain rotation.

To further understand the characteristics of the CGR, critical analyses were performed for the grains marked in the STEM image in Figure 5-2 (a). The mean orientations of the grains for the initial 3.6% and final deformation state at 4.8% strain are shown in Table A-2. Based on these orientations, all the slip directions for each grain were plotted on a stereographic projection at both the deformation states as shown in Figure 5-5. Since the absolute changes are small, for visualization, rotation of the slip directions are indicated by lines that show the rotation enhanced by a factor of 15. To visualize and understand the rotation of these slip directions with reference to the specimen coordinates, the stereographic projection is overlaid on the Wulff net. The loading axis is parallel to the Y-direction. The rotational trajectories of the slip directions of grains 5 and 9 could be seen overlapping with the great circles parallel to the Y-axis, indicating that some specific slip directions of these grains tend to rotate along the global straining direction. This rotational behavior is expected for grains in FCC metals undergoing plastic deformation without significant influence from the local stresses due to neighbors. This shows that the rotation of these grains is most likely influenced by the applied external stress field (σ_e). However, the rotational trajectories of the slip directions of several other grains like 2, 3, 4, and 8 are inclined at a high angle with respect to the great circles parallel to the Y-axis. The slip directions of these grains do not rotate towards the straining

axis. Thus, the rotation of these grains does not appear to be governed by the σ_e. This behavior could be explained by the stress heterogeneity in the specimen leading to generation of a local stress field (σ_l) around these grains which is different from σ_e. The influence of stress heterogeneity on the global grain rotation and the random texture development was discussed in the previous chapter. The stress heterogeneity is mainly expected due to the dislocation pile-up. The formation of dislocation pile-up can lead to a preferential interaction between these grains, one grain influencing the rotation of its neighboring grain as confirmed from the STEM series (Figure 5-2) and the mean grain rotation maps (Figure 5-4). Thus, the CGR can lead to the deviation of rotation paths of the slip directions from the ones that are expected in absence of the CGR during deformation.

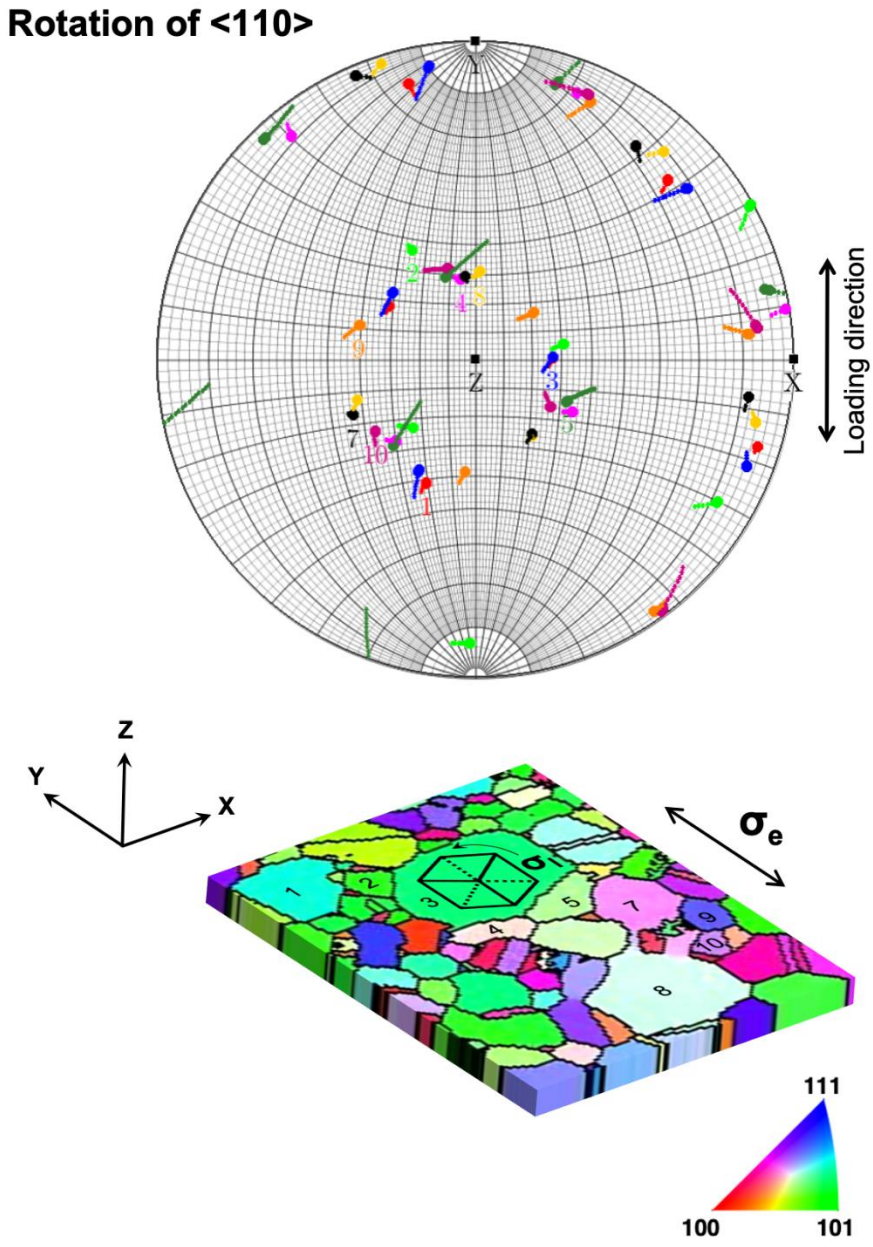

Figure 5-5 Stereographic projection showing the rotation of slip directions for grains 1 to 10. The actual positions of slip directions before and after deformation are shown using circular markers. The rotation of slip directions is indicated by lines, the length of which corresponds to 15 times the rotation angles shown in Table A-2. A schematic of the specimen reference frame is shown with Z-axis along the electron beam direction and X- and Y-axes parallel to the plane of the film. The IPF map is shown with colors representing orientations along the loading axis (Y). σ_e denotes the external applied stress on the specimen along Y-axis. A schematic of an FCC crystal with {111} orientation is shown to rotate under the influence of the local stress field σ_l around it.

5.5 Local Analysis of Geometrically Necessary Dislocations

In the present study, the CGR occurs in a step-wise fashion with significant rearrangement of the sub-grain boundaries suggesting that dislocations are driving the rotation of these grains. It is challenging to track the dislocation activity simultaneously in these nanoscale grains with different orientations using the classical TEM. However, with the ACOM-STEM data, it is far more feasible to analyze the GND density based on the intragrain rotation or the curvature changes within all of these grains. These analyses can facilitate the detailed understanding of the role of dislocation-based processes in CGR.

Locally, as seen from the STEM image series in Figure 5-2, the contrast in the grains undergoing CGR is non-uniform. The intragranular grain rotation maps for the same grains in Figure 5-4 (f)-(j) show a significant rearrangement of the sub-grain or the low-angle grain boundaries during loading and unloading. These observations indicate that there is a change in the curvature within these grains. This curvature is induced by non-uniformity in the rotation of crystallographic planes due to constraints imposed by the neighboring grains across the GBs [225], and it is accommodated by the GNDs. The characteristics of the intragrain rotation can facilitate the understanding of the lattice curvature and thus shed light on the GND activity.

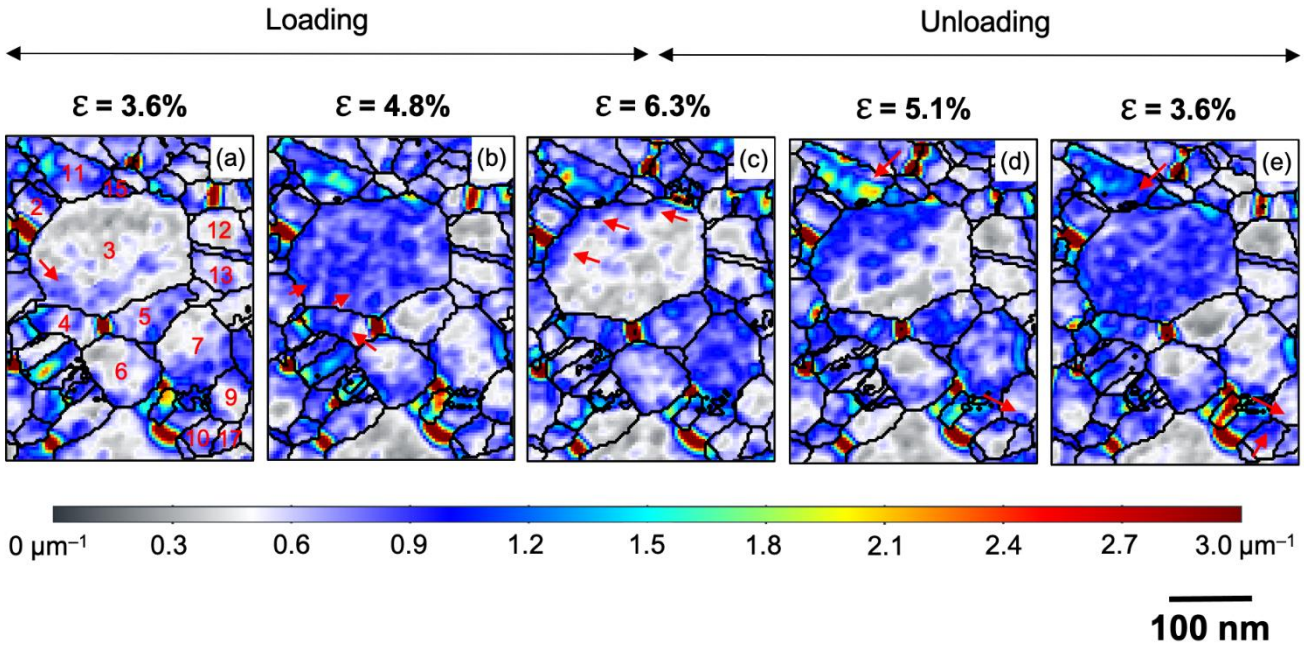

Figure 5-6 Illustration of cooperative grain rotations based on nucleation, propagation, absorption, and piling up of GNDs at or in the vicinity of certain GBs marked using arrows.

Figure 5-6 (a)-(e) show the spatial distribution of the GND density ρ_{GND}^{2D} represented as color maps for varying strain levels during the loading and unloading. Considerable changes in the GND density can be noted in some of the grains whereas others barely show any significant change in the density. Here, the behavior of a few grains is described to understand the CGR. For grains 5 and 7, the overall GND density increases on loading to the peak strain (Figure 5-6 (c)) whereas it reduces on unloading (Figure 5-6 (e)). No significant change of GND density is seen at ε = 4.8% for these grains. On the contrary, the neighboring grain 3 of relatively greater size shows different behavior. During loading, grain 3 with an initially low density at ε = 3.6% (Figure 5-6 (a)), the GND density increases at ε = 4.8% (Figure 5-6 (b)) but reduces as the strain is further increased to ε = 6.3% (Figure 5-6 (c)) and again increases as the specimen in unloaded to ε = 3.6% (Figure 5-6 (e)). Grain 11 shows an almost continuous increase in the GND density during loading and on unloading to ε = 5.1% (Figure 5-6 (d)). It is worth noting that the GND density in grain 11 during deformation is mostly concentrated at the vicinity of its GBs with the other grains and the density

has significantly increased at the GB between grains 3 and 15 on unloading to ε = 5.1% (Figure 5-6 (d)). This sharp rise in the GND density unambiguously reflects the building of dislocation pile-up that is developed in grain 11 at the vicinity of its GB with grains 2, 3, and 15 on unloading from ε = 6.3% to ε = 5.1%. Interestingly, this pile-up at the GB with grains 2, 3, and 15 almost vanishes as the specimen is further unloaded to ε = 3.6% (Figure 5-6 (e)). Grains 9, 12, and 13 do not show significant changes in the GND density during loading and unloading. Thus, the dislocations contribute to the intragrain plasticity at least for those grains in which the GND density was observed to evolve significantly. The evolution of the GND density is significantly different for the analyzed sets of grains in close proximity with each other. This indicates that these grains are subjected to significantly heterogenous stress fields within the length scales of a few tens of nanometers. The increase in the GND density within some grains and especially at the GBs shows that there is a significant generation of back-stresses on unloading the specimen. The development of the dislocation pile-up at GBs and the back-stresses eventually contribute to the observed BE as discussed in chapter 4.

With the presented analysis here, only the GNDs that generate lattice curvature leading to orientation differences and exhibit net Burgers vector were assessed. However, the intragrain plasticity cannot be fully analyzed only based on GNDs or local orientation changes. In absence of lattice curvature or GNDs, the statistically stored dislocations (SSDs) can exist without exhibiting net Burgers vectors and any significant misorientations [217]. The SSDs in the grains were not analyzed owing to the aforementioned experimental limitations. Thus, for the grains that do not exhibit any significant changes in the GND density, the possibility of intragrain plasticity cannot be excluded.

5.6 Mechanism of the Cooperative Grain Rotations

The evolution of GND density is further analyzed to understand the cooperative grain rotations. As seen in Figure 5-6 (a), the initial GND density within most parts of grain 3 is low. However, it can be noticed that in close proximity to the GB with grain 4 (GB 3-4), the density is noticeably higher (as indicated by the arrow in Figure 5-6 (a)) and the GNDs appear to have already transmitted inside grain 3. At this state, it is seen that the GND density at the GB of grain 3 and other neighboring grains is mostly lower. As the strain is increased to ε = 4.8% (Figure 5-6 (b)), there is an abrupt increase in the GND density almost throughout the grain, whereas the density in the proximity to other neighboring GBs is similar to that in the grain interior. These observations suggest that the GNDs preferentially nucleated from the GB 3-4. The stress-field at the GB 3-4 is sufficiently high for the dislocations to propagate from GB 3-4 to the interior of grain 3. The dislocations propagated to large distances from GB 3-4 as can be seen from the continuous density bands (indicated by arrows in Figure 5-6 (b)), almost normal to GB 3-4. At the same deformation state, a parallel set of bands with increased density can be seen in grain 4 as well (Figure 5-6 (b)). Thus, at ε = 4.8%, the GNDs propagated on both sides of GB 3-4 at the same time driving the observed cooperative rotation for grains 3 and 4 which is reflected as a simultaneous contrast change in the STEM series (Figure 5-2 (b)-(c)) and their rotation in the maps shown in Figure 5-4. On further straining to ε = 6.3%, there is a reduction in the GND density within grain 3, and some high density is seen in proximity to the GBs with neighboring grains (indicated by arrows in Figure 5-6 (c)). This shows that the GNDs most likely propagated further and were absorbed in the GBs at the other end of grain 3.

As the specimen is unloaded to ε = 5.1% (Figure 5-6 (d)), the GND density in grain 11 is mostly concentrated in the vicinity of GBs and especially at the GB between grain 3 and 11 (GB 3-11) (as indicated by the arrow in Figure 5-6 (d)). As the specimen is further unloaded to ε = 3.6% (Figure 5-6 (e)) the GND density in grain 11 abruptly reduces and the density within grain 3 is significantly enhanced. Thus, the back-stresses that developed at GB 3-11 and GBs with other neighboring grains during unloading were so severe that the dislocations propagated across grain 3 driving its backward rotation which is seen in Figure 5-4 (i)-(j). This is direct evidence for reverse plastic deformation or plastic recovery that leads to the BE in nc Pd on relaxation. A similar effect is observed for grain pairs 9 and 10 when unloading from ε = 5.1% to ε = 3.6% (Figure 5-6 (d-e)). The GND density reduces at the GB 9-10 in grain 9 and enhances in grain 10 (as indicated by the arrow in Figure 5-6 (d-e)), thus, driving the CGR for these pairs as well. This characteristic feature of CGR is also evident during loading for the grain pairs 3 and 4 in Figure 5-6 (b) which shows that the GND density suddenly enhanced throughout grain 3. Based on the above discussion, it is clear that two

grains that undergo CGR showed nucleation of dislocation at their GBs, followed by their propagation and absorption at the GBs with next neighbors. This process was partially reversible on unloading as the dislocations piled up at the GBs with the same neighbors and there was a 'back-propagation' in the same grain. This is direct evidence of grain interaction in nc metals that shows that rotational deformation in grain is influenced by the grains in its direct neighborhood.

The rotation of grains undergoing CGR in the nc specimen does not only depend on their orientation and grain size but is significantly influenced by their neighbors, the geometric arrangement of GBs, and GB characteristics. To understand the role of these factors, the geometric arrangement of the slip systems in grains 3, 4, and 5 is analyzed. Here, only grains 3 and 4 participate in the CGR as seen from the STEM series (Figure 5-2). Figure 5-7 (a) shows the traces of {111} slip planes of grains 3, 4, and 5. As discussed before, the out-of-plane slip systems have higher Schmid factors (Table A-1) leading to a greater probability of their activation. So, the out-of-plane slip planes have a greater tendency to exhibit the dislocation slip-based processes. It is seen that the out of (film) plane slip planes of grains 4 and 5 are mutually almost orthogonal to the slip planes of grain 3. Similarly, the traces of {111} slip planes for grains 4 and 6 are also at high angles to each other (Figure 5-8). The (almost) orthogonal sets of slip planes constitute geometrically highly incompatible systems for slip transmission, leading to dislocation pile-ups at these GBs as shown schematically in Figure 5-9.

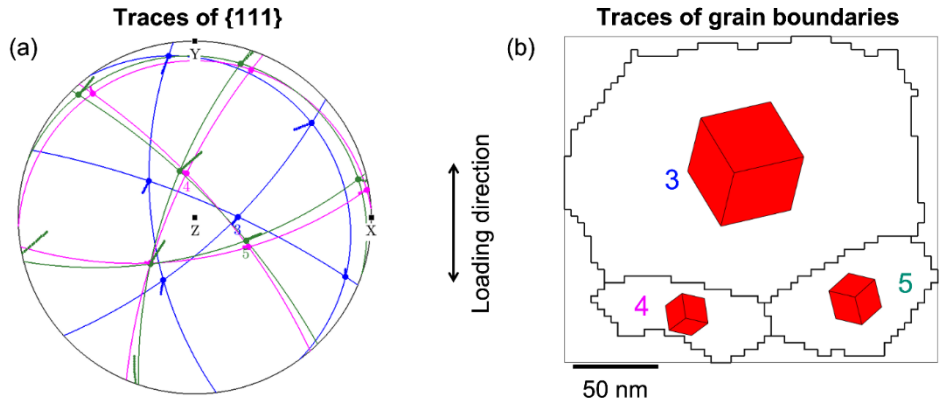

Figure 5-7 (a) Traces of {111} planes of grains 3, 4, and 5, other marking conventions representing the rotation of slip directions are same as shown in Figure 5-5, and (b) grains 3, 4, and 5 with traces of their grain boundaries and unit cells representative of their crystal orientations.

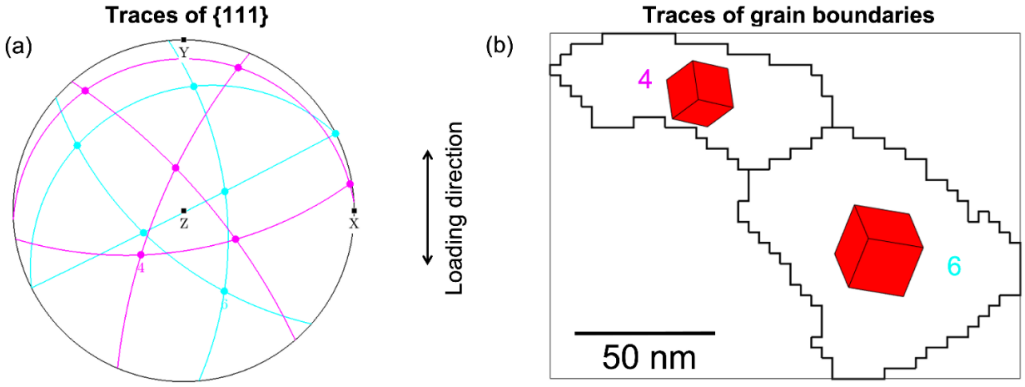

Figure 5-8 Traces of {111} planes of grains 4 and 6, other marking conventions representing slip directions are same as shown in Figure 5-5, and (b) grains 4 and 6 with traces of their grain boundaries and unit cells representative of their crystal orientations.

The compatibility of the active slip systems in adjacent grains can be understood from the compatibility factor (m') as formulated by Luster and Morris [226]. This factor is evaluated by calculating the angle (κ) between the slip directions in grains A and B and the angle (Φ) between the normal to the slip planes. m' is calculated as m = cos Φ . cos κ. For m' = 1, the slip systems are completely compatible since geometrically the slip planes and directions in both the grain are parallel. For m' = 0, the slip systems are completely incompatible as in that case either the slip directions or slip planes are orthogonal. Thus, depending on the geometric arrangement of slip systems, m' can vary between 0 and 1. Table 5-1 shows the compatibility factors evaluated for the most active systems based on the Schmid factor analysis of the grain pairs shown in Figure 5-7 and Figure 5-8. From these factors, it is noted that grain pairs 3-5, 4-5, and 4-6 have very low m' which makes them highly incompatible for slip transmission. Due to their low compatibility, there is a strong barrier imposed for the dislocations for their transmission through the GBs leading to dislocation pile-up formation and stress build-up. As the level of stress is sufficiently high at the GB, dislocations should nucleate into the neighboring grain [144]. m' for grains 3-4 is comparatively higher which makes the slip transmission easier. This is in good agreement with the evolution of dislocation density that shows clear transmission and propagation of dislocations across GB of grains 3 and 4 in Figure 5-6 (a)-(b). This is also reflected from the simultaneous contrast change observed for these grains in the STEM images (Figure 5-2) and their rotation as seen in Figure 5-4. Here, two pairs of grains, 3-4 and 4-6, with incompatible GBs are shown (Figure 5-7 and Figure 5-8). In a series of several grains connected by such incompatible GBs, this should result in the rotation of one grain due to propagation of dislocations and after sufficient stress at GB with the next neighboring grain building up, the rotation in the next grain would be initiated. This process can continue over several grains leading to a long-range cooperative grain rotation as seen in the STEM series (Figure 5-2). From the above analysis, it is concluded that the geometric compatibility of the slip systems across grain boundaries plays a critical role in driving the CGR.

Grain pairs (A-B)	Active slip system (A)	Active slip system (B)	Compatibility factor (m')
3-4	[0 -1 1](-111)	[-110](11-1)	0.71
3-5	[0 -1 1](-111)	[-110](11-1)	0.1
4-5	[-110](11-1)	[-110](11-1)	0.1
4-6	[-110](11-1)	[-1-10](-111)	0.03

Table 5-1 Analysis of the compatibility factor calculated for the most active slip systems based on the Schmid factors presented in Table A-1.

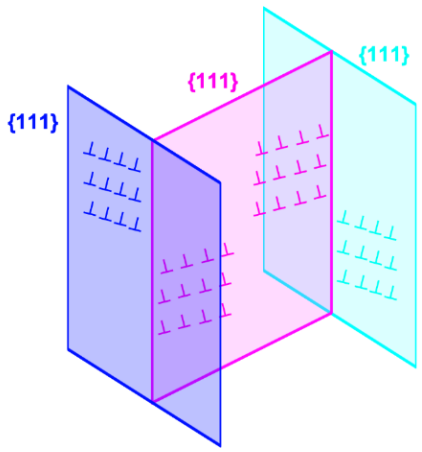

Figure 5-9 Schematic showing the geometric incompatibility of slip systems with their slip planes arranged almost orthogonally leading to dislocation pile-up at the GBs.

A variety of mechanisms on the collective or simultaneous grain rotations in nc metals have been reported in the past using different TEM techniques like dark-field TEM [145], HRTEM [131], and a combination of bright-field and ACOM-TEM [148]. Wang et al. had observed simultaneous (collective) rotation of several grains in the direct neighborhood in a coordinated manner and it was explained by the climbing of dislocations into triple junctions or grain boundaries and no intragranular dislocation processes were observed [131]. These observations were made using HRTEM and were restricted to the analyses of in-plane rotations alone without any detailed consideration of tilting/bending of the specimen. In the present case, with the combination of microprobe STEM imaging and ACOM-STEM, a significant out-of-plane contribution was observed (Figure 5-2 and Figure 5-3). Overall, the results of the GND analysis suggest that the dislocation-based processes are dominant in driving the CGR compared to the GB-mediated processes. To further support this, the characteristics of GBs between the grain pairs were evaluated considering their misorientation axes and angles in the initial (ε = 3.6 %) and final (ε = 4.8 %) deformation states. The results of the analysis are listed in Table A-3 and are plotted on an IPF in Figure 5-10. It is seen that majority of the GBs between grain pairs, for e.g., 2-3, 3-4, 4-6 and 9-10 which exhibited CGR do not change their character significantly. On the other hand, for the grain pair 4-5, there is a change in the misorientation axis, where grain 5 does not participate in the CGR. Grains 4 and 5 have a small misorientation of 5° and are neighbors to each other, nevertheless, there is a change in the GB character between grains 4 and 5. Thus, due to participation in the CGR, grain 4 rotates differently with respect to grain 5 as seen in Figure 4-12 and Figure 5-5. Retention of the GB characteristics during CGR is an indication that the CGR is to a great extent driven by the dislocations.

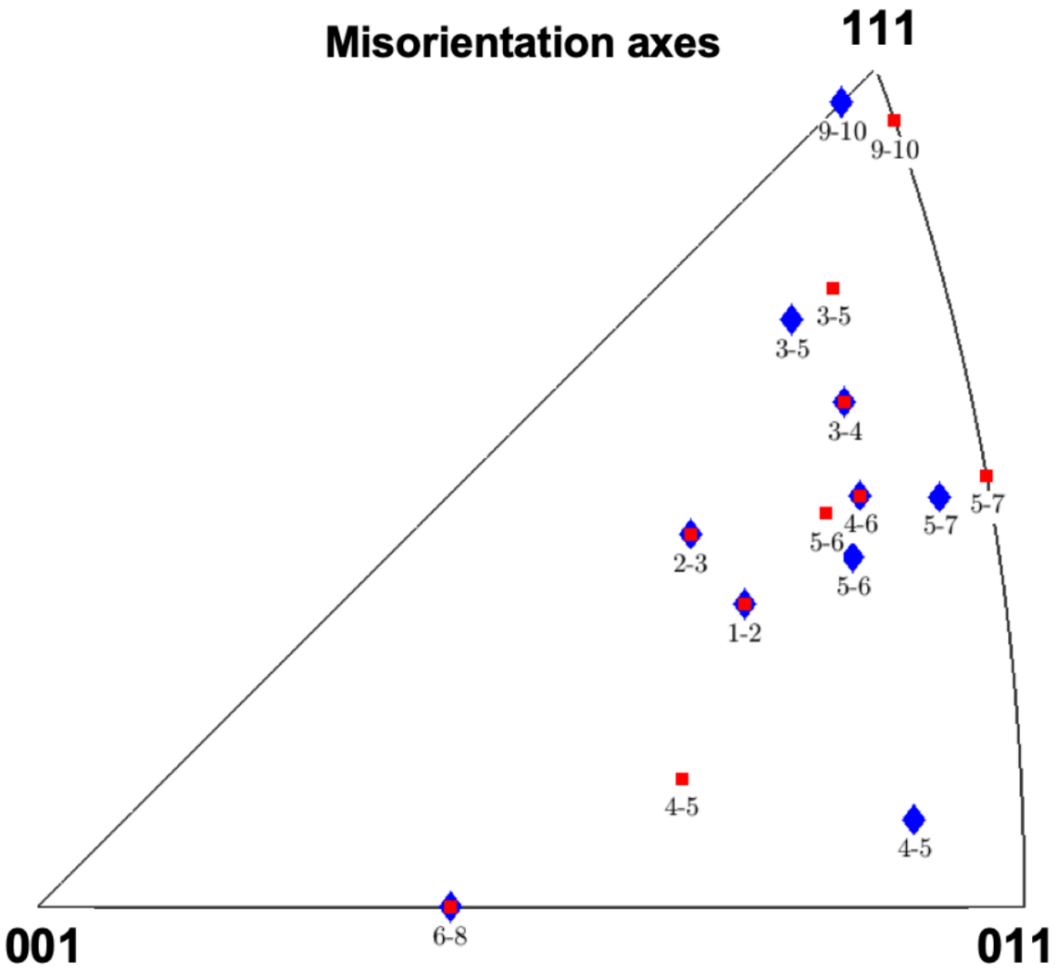

Figure 5-10 Misorientation axes of the selected grain pairs represented in an IPF before and after deformation, denoted by blue and red markers.

5.7 Summary

In this chapter, local analysis of grain interactions was presented for nc palladium during *in situ* cyclic loading-unloading experiments. Microprobe STEM image series showed contrast changes propagating through sets of grains leading to the CGR. These changes were also seen in the quantitative grain rotation analysis. The CGR was mostly reversible which is in agreement with the observed plastic recovery leading to the Bauschinger effect. The CGR occurred in a step-wise cooperative manner with one grain rotating after another, unlike the simultaneous rigid body rotations as typically expected for the GB-mediated rotations. The Nye tensor analysis to estimate GND density confirmed dislocation activity leading to the intragrain rotations in grains. The GND density evolved differently in the grains next to each other during loading and unloading in response to the heterogeneous stress field. The dislocation pile-up formation was confirmed at GBs and GB triple junctions as the specimen was unloaded. This pile-up formation occurred due to the generation of back-stresses on unloading, leading to the BE. The pile-up formation at specific GBs was explained based on geometric incompatibility of the slip systems across the GBs. Based on this model, only after sufficient stress buildup at the GBs, the dislocations are transmitted into the neighboring grain and drive the rotation of this grain. In a series of grains connected by the incompatible grain boundaries, this process may be carried over multiple grains leading to a step-wise CGR which to a significant extent is reversible on unloading. This was justified by an abrupt reduction of the GND density at GBs on unloading together with its increment in a neighboring grain that exhibited CGR. Overall, the CGR is established as a cooperative plastic deformation process extending over multiple grains metals due to complex dislocation-based grain interactions which contribute to the evolution of random texture in nc metals.

6 Deformation Mechanisms in NMCs under Cyclic Tribological Contact

6.1 Introduction

The present chapter aims at exploring the role of heterointerfaces and chemical composition at nanoscales in NMCs deformed under tribological loading. From the perspective of tribological performance, it is essential to understand the role of interfaces in controlling the plastic deformation mechanisms and thus the mechanical characteristics of NMCs. Broadly, the interfacial characteristics can be tailored by modifying their coherency and transparency. Both these factors determine the ease of transmission of dislocations across the interfaces and thus influence their plastic deformation. The microstructural evolution of the component layers in NMC systems can offer significant insights into the plastic deformation processes operating within individual layers as well as in the multilayered system. In this study, comparative investigations were conducted on two NMC systems (Figure 6-1) with different interface structures that were deformed under tribological loading. Figure 6-1 (a) shows the NMC in which both the component layers are pure nc FCC metals Au and Cu with semi-coherent interfaces. On the other hand, Figure 6-1 (b) shows the NMC in which one component is pure nc FCC (Cu) and the other component is pure nc BCC (Cr), thereby forming incoherent interfaces.

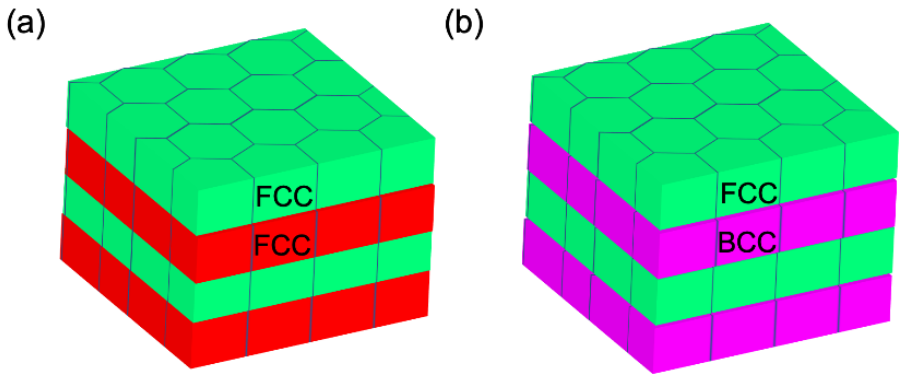

Figure 6-1 Schematic of the NMCs with nc FCC/FCC and FCC/BCC components.

This chapter presents the microstructural investigations with the aid of TEM on the NMC systems shown in Figure 6-1 that were deformed *ex situ* using cyclic sliding contact. From these investigations, a comparative analysis of the unique deformation microstructures obtained in these systems is presented based on various material parameters like crystallography, grain structure, interface characteristics, elastic modulus, hardness, chemical miscibility, etc. The fundamental understanding of the role of these parameters on microstructural evolution has offered greater insights into the active deformation mechanisms.

6.2 Experimental

6.2.1 Preparation of NMC Thin Films

Two batches of NMCs, Au/Cu and Cu/Cr were sputter deposited on a 500 μm thick Si (100) substrate by radio frequency magnetron sputtering under the base pressure of less than 10^{-7} torr and working gas pressure 0.4 Pa. The purity of the Cu, Au, and Cr targets was 99.999 at.%, 99.95 at.%, and 99.95 at.% respectively and their deposition rate was 0.3 nm/s. The Au layer was deposited as the topmost layer in Au-Cu NMC and Cu in the case of Cu-Cr to minimize the effects of surface oxidation. The nominal layer thickness of Cu and Au was 100 nm whereas for Cr the thickness was around 50 nm. The NMCs were prepared by G.-P. Zhang at the Institute of Materials Research, Chinese Academy of Sciences, Shenyang, China.

6.2.2 Cyclic Sliding Experiments

The sliding experiments were performed using a Nanoindenter G200 XP (Agilent technologies) equipped with a spherical diamond tip of 16.7 µm diameter. A constant normal load of 10 mN for Au-Cu and 20 mN for Cu-Cr multilayers was applied. The sample stage was moved back and forth at a rate of 5 µm/s over a distance of 100 µm. Greater details regarding the selection of the normal loads for each system are described in 6.3. Tests were performed up to 100 cycles for Au-Cu NMCs and 1000 cycles for Cu-Cr NMCs with one back and forth movement defined as one sliding cycle. The sliding experiments were performed by Z.-P. Luo and R. Schwaiger at KIT, Germany.

6.2.3 TEM Specimen Preparation

For TEM specimen preparation, the wear tracks corresponding to the specific number of loading cycles were identified. To investigate the anisotropy in microstructural evolution in response to reciprocating stress-field of the indenter, the sections were lifted either parallel or perpendicular to the wear track as shown in Figure 6-2 (a). The TEM specimens were prepared using the standard lift-out technique by FEI Strata 400S Dualbeam FIB. The specimens were prepared jointly by Z.-P. Luo and A. Kashiwar at KIT, Germany.

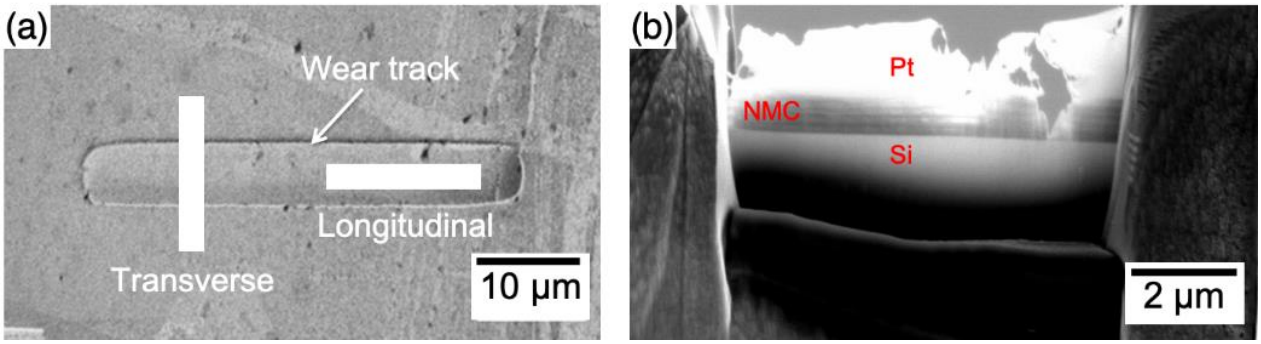

Figure 6-2 (a) SEM image of the sliding track with the schematic of transverse and longitudinal sections chosen for the lift-out, (b) example of a finished FIB lamella from a transverse section of an Au-Cu NMC specimen deformed for 50 sliding cycles.

6.2.4 TEM Microstructural Characterization

ACOM-STEM

ACOM-STEM was performed with precession electron diffraction using the ASTAR system on the FEI Tecnai F20 ST TEM. The TEM was operated at 200 kV in microprobe STEM mode using a 30 µm condenser aperture, 4.5 kV extraction voltage, gun lens 3, spot size 8, and camera length 80 mm. The probe size was around 1 nm with a convergence angle of about 1 mrad. The step size for the maps was selected in the range 1 nm to 1.5 nm depending on the size of the features and overall sampling size for each specimen. The precession angle used was in the range of 0.3-0.5 degrees.

EFTEM-SI

EFTEM spectral imaging (EFTEM-SI) maps were acquired for a Cu-Cr specimen deformed for 200 cycles using the FEI Titan 80-300, equipped with a GIF Tridium spectrometer with a BM-Ultrascan CCD camera. The TEM was operated at 300 kV with 4.5 kV extraction voltage, gun lens 3, and spot size 3. The EFTEM-SI maps were acquired in microprobe EFTEM set-up with the frame size of 512 × 512 and pixel size of 0.86 nm × 0.86 nm. The filtered energy for pre- and post-edges and the corresponding slit widths and exposure time selected for Cu and Cr are indicated in Table A-4. The resulting EFTEM-SI map was obtained using the 3-window method after drift correction. The EFTEM-SI measurements were conducted jointly by A. Kashiwar and X. Mu at KIT, Germany.

6.2.5 Data Processing

The ACOM-STEM results were processed using the ASTAR software package by the template matching procedure. The template banks for both Cu and Cr were generated using DiffGen V2 with the parameters indicated in Table A-5 whereas the indexing was performed using the parameters summarized in Table A-6. After indexing, the resulting maps were corrected for 180° ambiguity [206,208] to correct the ambiguous misorientations in the crystallites. The filtering and processing of the data were performed using the 'Grain Evaluation' in Matlab 2013b.

6.3 Physical and Mechanical Properties of Sputtered NMC Thin Films

Figure 6-3 shows the cross-section images of Au-Cu and Cu-Cr NMCs on Si-substrate in the as-prepared state. The images were acquired using the through-the-lens detector (TLD) and show the contrast which is partly sensitive to the atomic number, contributed by the BSEs. The Cu layers in Figure 6-3 (b) also show the contrast which is slightly sensitive to the orientation of nano-sized crystallites due to channeling effects. The bottom-most layers in Figure 6-3 (a) and (b) are Cu and Cr. The Au-Cu NMC consists of 5 layers each of Au and Cu whereas the Cu-Cr counterpart consists of 5 layers each of Cu and Cr as well.

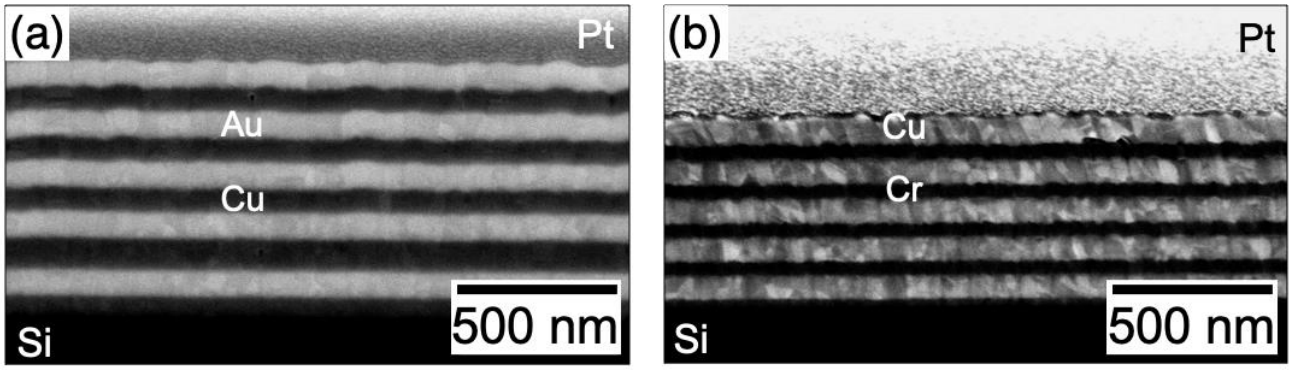

Figure 6-3 Cross-sectional views of as-sputtered (a) Au-Cu, and (b) Cu-Cr NMCs. The images were acquired using an FEI Nova 200 Nanolab. (courtesy of Z.-P. Luo, KIT, Germany).

The physical and mechanical properties of the sputtered multilayers are summarized in Table 6-1. From Table 6-1, it is seen that replacement of Au layers with Cr layers of nearly half the volume fraction results in an enhancement of the hardness of Cu-Cr NMC which is over 200% of the hardness of Au-Cu NMC. On the other hand, the modulus of Cu-Cr NMC is almost 150% of that of Au-Cu NMC.

NMC model system	**Au-Cu**	**Cu-Cr**
Crystal system	Au: FCC, Cu: FCC	Cu: FCC, Cr: BCC
Total thickness (nm)	1062.3 ± 26.9	790.2 ± 16.4
Total number of layers	5 each of Au and Cu	5 each of Cu and Cr
Individual layer thickness (nm)	Au: 110.0 ± 3.2 Cu: 101.6 ± 11.6	Cu: 106.6 ± 6.8 Cr: 53.6 ± 3.0
Modulation period (nm)	~ 210	~ 160
Modulation ratio (η)	Au/Cu ≅ 1.1:1	Cu/Cr ≅ 2:1
Lattice misfit	~ 11.5%	~ 2%
Interface coherency	Semi-coherent	incoherent
Hardness of NMC (GPa)	2.25 ± 0.09	5.67 ± 0.08
Modulus of NMC (GPa)	127.0 ± 1.8	190.4 ± 2.8
Mutual solubility	Miscible	Immiscible

Table 6-1 Multilayer dimensions and their mechanical properties (courtesy of Z.-P. Luo and R. Schwaiger, KIT, Germany).

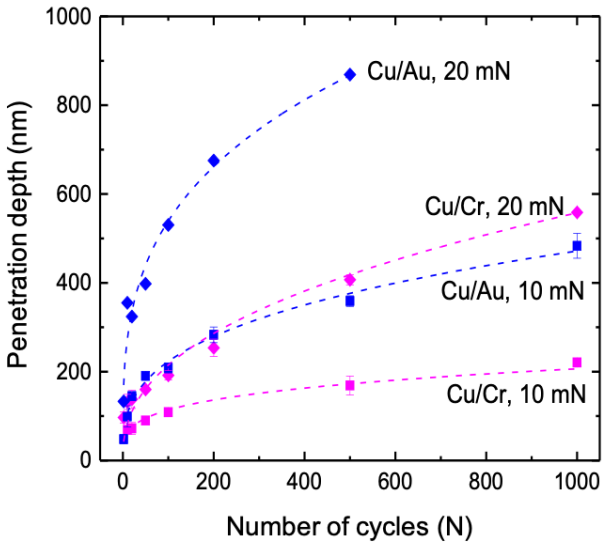

Figure 6-4 Plot of penetration depth versus the number of cycles for Au-Cu and Cu-Cr NMCs at different loads (courtesy of Z.-P. Luo and R. Schwaiger, KIT, Germany).

The normal load for the sliding experiments on each NMC was chosen after considering the penetration depth as a function of the number of cycles for which the specimen is deformed, as shown in Figure 6-4. For a comparative analysis of the deformation microstructures in both NMCs, the normal load was selected in each case such that the penetration depth in both the systems is nearly the same. It is to be noted that similar depths of penetration are achieved not only by appropriate selection of the normal load but also the individual layer thickness and the hardness of both these NMCs as indicated in Table 6-1. The individual layer thickness for both systems was chosen based on the miscibility of the components. At room temperature, Au-Cu constitutes a chemically miscible system with the possibility of formation of ordered phases AuCu, Au_3Cu, or $AuCu_3$. On the other hand, Cu-Cr forms an immiscible system without any chance of formation of intermetallic phase based on the Cu-Cr phase diagram. Assuming complete miscibility of Au and Cu, for the chosen layer thickness of Au, Cu and Cr the effective modulation period of Au-Cu is comparable to that of Cu-Cr. While the thickness of Cu layers in both the NMCs is the same, the thickness of Cr layers is half of that of Au layers and the resulting hardness of Cu-Cr NMC is twice that of Au-Cu NMC. For the selected layer thickness and the hardness of the NMCs, it is seen from Figure 6-4 that at 10 mN load for Cu-Au and 20 mN load for Cu-Cr the penetration depths are nearly the same for a large number of cycles up to at least 500. Similar penetration depths indicate that the depth of the subsurface region within which the deformation is localized could be assumed to be similar and accordingly these normal loads were selected for the present study. Li et al. had also used these NMCs previously with similar modulation ratios, for their comparative analysis with respect to the microstructural length scales, interface structure, strength, and plastic instability [227,228].

6.4 Microstructural and Texture Characteristics of Au-Cu NMC Thin Films

6.4.1 As-sputtered Au-Cu NMC

Figure 6-5 shows the bright-field (BF) and dark-field (DF) images obtained during the ACOM-STEM. The BF-STEM image in Figure 6-5 (a) shows diffraction contrast as well as amplitude contrast sensitive to atomic number and thickness of the specimen. However, unlike the STEM images acquired by HAADF, the heavier element appears darker. The DF-STEM image, unlike the BF counterpart, shows contrast which is sensitive to crystal orientations. The DF image shows a continuous columnar growth of grains with a fairly defined width that extends over multiple layers and these columns are seen mostly in the upper half portion of the NMC specimen. The measured average width of the columns is about 70 nm. Within each column,

several closely spaced nano-scaled twin boundaries (TBs) are seen which are almost orthogonal to the growth direction. Thus, each column consists of Au-Cu interface boundaries with a multitude of TBs, which is further confirmed by ACOM-STEM as shown in Figure 6-6. Figure 6-6 shows the phase map and the IPF maps from the upper 6 layers seen in Figure 6-5. Like the BF-STEM image, the phase map reveals the layers corresponding to Cu and Au with defined interfaces. IPF maps show the crystal orientations of the columnar grains along X, Y, and Z-axes. Each column typically exhibits a uniform orientation with twinned grains embedded in it. Several twinned boundaries exhibited a stepped structure as indicated in the IPF map X. IPF map along Y shows all the columnar grains with a uniform orientation indicating a preferential {111} texture along the growth direction.

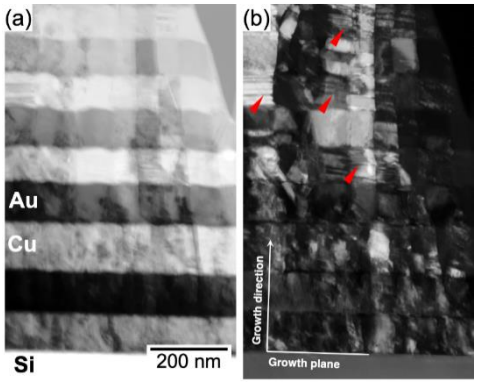

Figure 6-5 Microstructure of as-sputtered Au-Cu NMC thin film: (a) Virtual bright-field, and (b) virtual dark-field STEM images obtained by ACOM-STEM. Growth direction and a trace of the growth plane are shown in (b). Red markers indicate some of the twin boundaries.

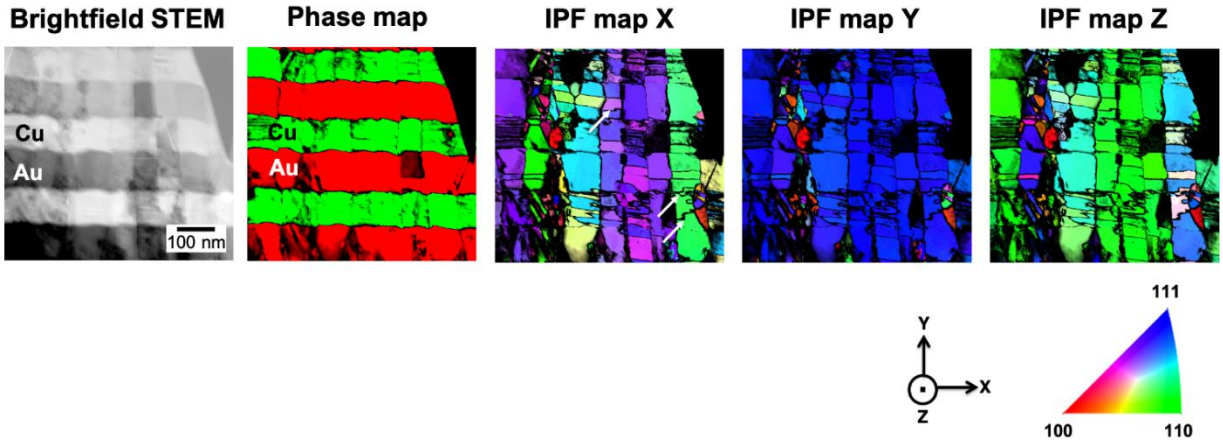

Figure 6-6 Microstructure of Au-Cu NMC in the as-sputtered state as investigated by ACOM-STEM and represented by virtual bright-field STEM, phase map, and IPF maps along X, Y, and Z. Arrows in IPF map X indicate the stepped twin boundaries.

The {111} and {110} pole figures for Au and Cu shown in Figure 6-7 were obtained from the 6 layers (3 layers each of Au and Cu) seen in Figure 6-6. The pole figures show strong {111} density along the growth direction which is almost parallel to the Y-direction. The densities of {111} and {110} for Au and Cu coincide with each other. From the columnar growth (Figure 6-5) and an almost uniform {111} orientation seen in the IPF map Y (Figure 6-6), it is concluded that both Au and Cu layers grow epitaxially in the NMC with the interface orientation relationship as:

$$\text{Au } \{111\} \,//\, \text{Cu } \{111\}$$

$$\text{Au } \langle 110 \rangle \,//\, \text{Cu } \langle 110 \rangle$$

The above relationship is in agreement with the results obtained by Li et al. using XRD for NMCs with varying modulation periods and these confirmed that both Au and Cu exhibited strong (111) diffraction peaks for the modulation period of 200 nm [227]. Further, the almost symmetric distribution of {111} poles about the X-Z plane is in well agreement with the observation of nearly orthogonal nanoscale twins seen in Figure 6-5 (b).

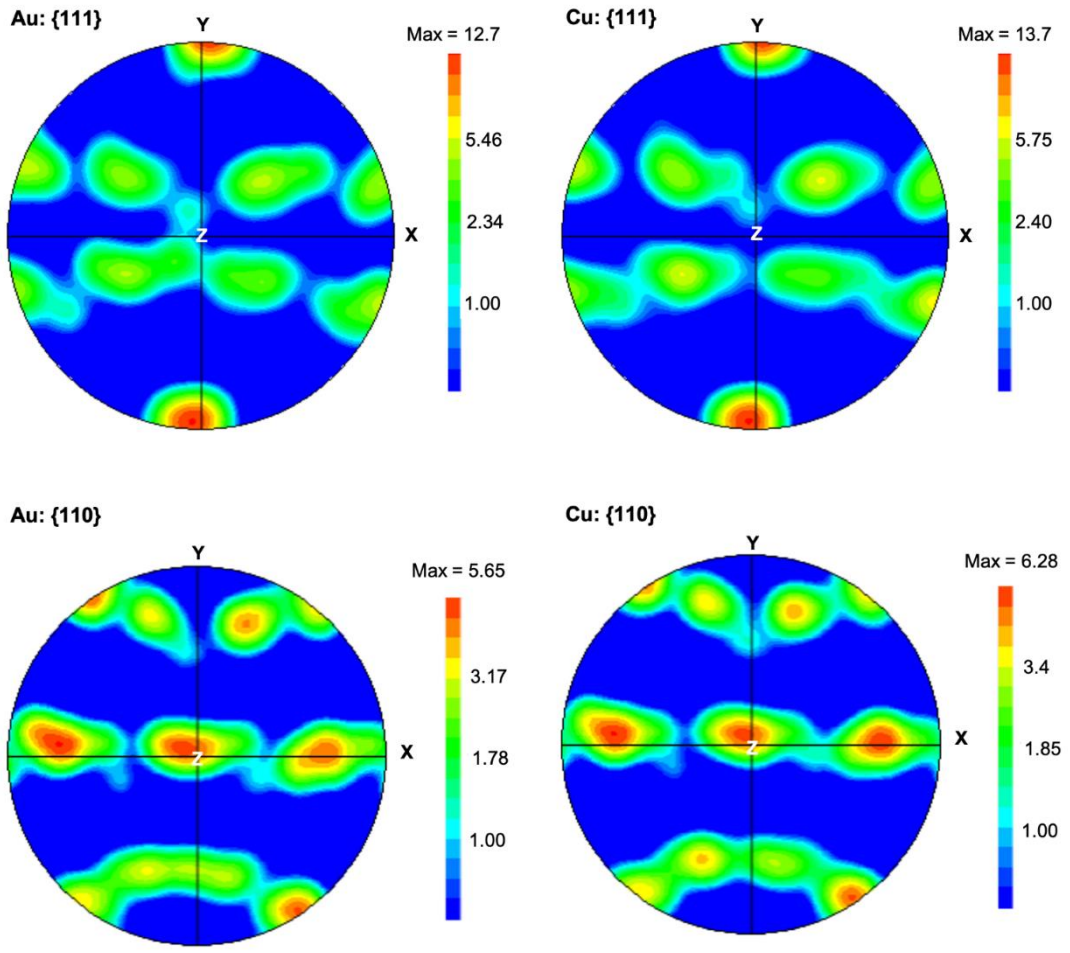

Figure 6-7 Pole figures showing the density of {111} and {110} poles for Au and Cu in as-sputtered Au-Cu NMC. X-Y plane corresponds to the plane of the specimen, where Y is almost parallel to the growth direction.

6.4.2 Deformation Microstructure after 50 Sliding Cycles

Figure 6-8 shows the deformation microstructure of the specimen subjected to 50 sliding cycles at 10 mN. Figure 6-8 (a) shows an overview of the cross-section of the sliding track highlighting the outer and central regions. The sliding direction (SD) in this case is along Z-axis and X-axis is termed as the transverse direction (TD). The film growth direction and the loading direction are almost parallel to Y-axis, which is referred to as the normal direction (ND). Figure 6-8 (b) shows the deformed structure from the outer region whereas Figure 6-8 (c) shows the deformed structure from the central region of the sliding track. The deformation structure is represented here using the STEM image, phase map, and IPF maps. The BF-STEM images in Figure 6-8 (b) and (c) show the deformed zone encompassed by the dotted polygon and the amplitude contrast in these images allows to distinguish the different layers to a certain extent. Within the deformation zone, the thickness of individual layers has changed and especially the upper layers are thinner compared to their original (undeformed) state. The reduction in individual layer thickness is a clear indication of plastic deformation in the deformed zone. The phase maps further confirm the plastic deformation.

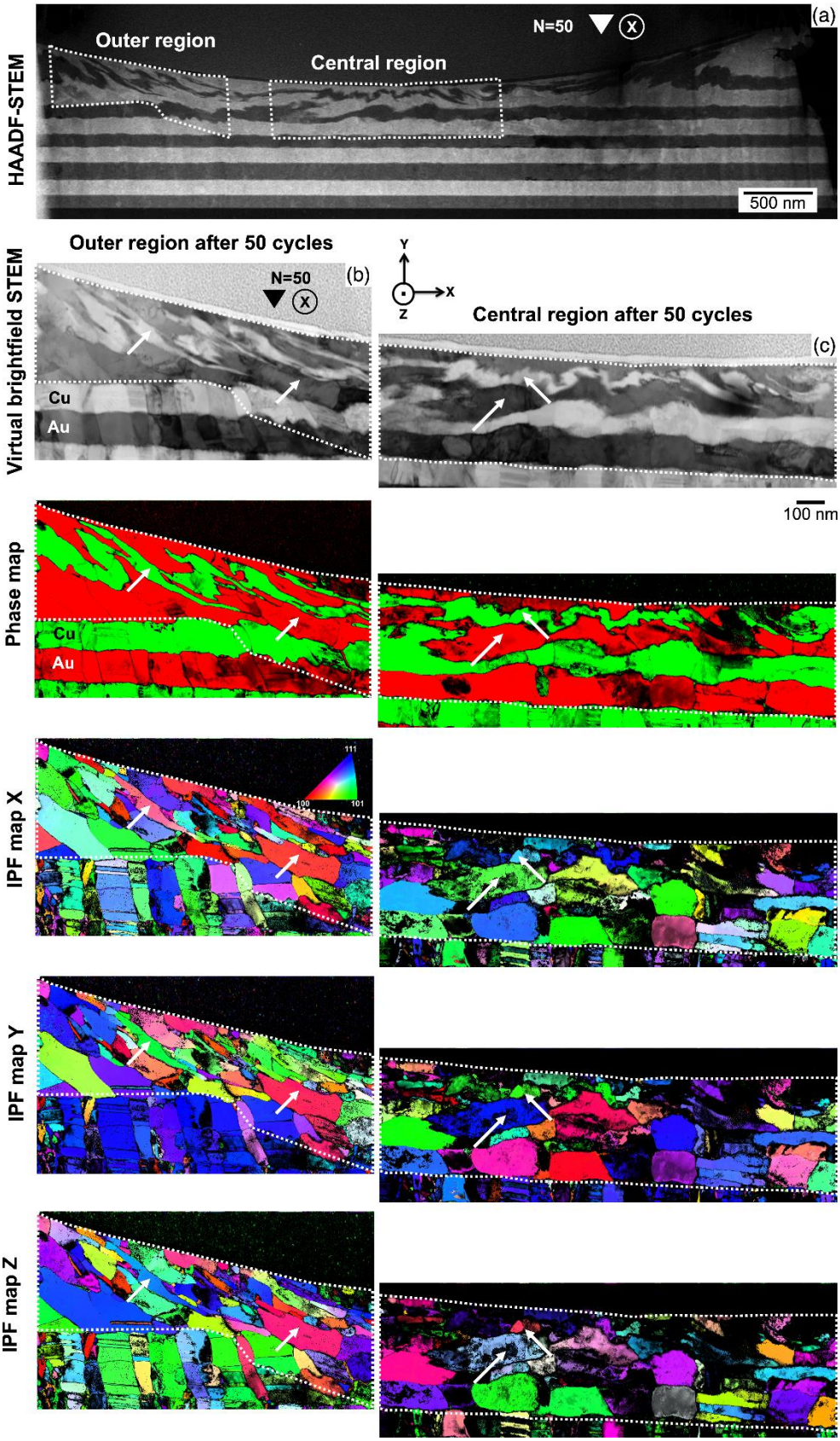

Figure 6-8 (a) HAADF-STEM image showing an overview of the Au-Cu NMC deformed to 50 cycles, (b) and (c) show the outer and central regions where the ACOM-STEM analysis was performed. The results of the ACOM-STEM analysis are illustrated using the virtual bright-field STEM images, phase maps and IPF maps along X, Y, and Z. Dotted polygons in (b) and (c) show the deformed zone with arrows showing the elongated grains. Coordinate axes X, Y, and Z denote the transverse, normal, and sliding directions.

From the STEM images and phase maps, the upper Au and Cu layers are seen to develop a wavy structure and turbulence which are very similar to that observed in the fluids. It is seen that the individual layers accommodate the plastic deformation by co-deforming and organizing themselves to form vortex-like structures leading to their mechanical intermixing as reported previously by Luo et al. [229]. The crystal orientation maps show elongated grains and their shapes are highly anisotropic. The elongation of grains is seen in different directions in Figure 6-8 (b) while the elongation is mostly perpendicular to the loading direction in the central region in Figure 6-8 (c). For most grains, the elongated size (considering the long axis) is greater than the initial average width of the columns. A few examples of such elongated grains have been marked by arrows. Most of these elongated grains are quite thinner (considering short axis) with respect to the initial layer thickness, as prominently seen in the upper portion of the deformed zone. In the lower portion of the deformed zone, the elongated grains are still coarser and comparable to the initial layer thickness. The TBs which were seen in the undeformed specimen in Figure 6-6, are not revealed anymore within the elongated grains in the deformed zone. The absence of TBs indicates that during the plastic deformation there was stress-induced de-twinning in the specimen.

The IPF maps along Y-axis represent the crystal orientation of grains both along the growth direction of the film and the loading direction of the indenter. Thus, the IPF map Y of the undeformed specimen (Figure 6-6) serves as a reference in which the majority of the grains exhibit {111} orientation. At the bottom of the IPF maps Y in the deformed specimens (Figure 6-8 (b)-(c)), where the specimen is mostly undeformed, the TBs persist and the grains show {111} orientation. In the deformed zone, it is evident that during the plastic deformation several grains have changed their orientation along the loading direction. Since the section (lamella) of the undeformed specimen was lifted parallel to the plane of the section of the deformed specimen, the IPF maps along the X and Z axes are also referred for comparison. Both these maps further verify the rotation of grains along the sliding direction (Z) and the transverse direction (X). Thus, all the IPF maps present explicit evidence of the rotation of grains during the plastic deformation induced by sliding contact.

6.4.3 Deformation Microstructure after 100 Sliding Cycles

Figure 6-9 shows the microstructural evolution in a longitudinal section of the deformed specimen subjected to 100 sliding cycles. The STEM image shows the wavy structure and turbulence which is seen further enhanced in the deformed zone as compared to the specimen deformed after 50 cycles. The deformed zone in the BF-STEM image does not show a sharp contrast between Au and Cu interfaces after 100 sliding cycles as it was visible in Figure 6-8 for the specimen after 50 cycles. After 100 cycles, the layers have further deformed and reduced in their thickness and are mechanically intermixed. Since Au and Cu are thermodynamically miscible, it is expected that both these components under severe deformation undergo mechanical alloying with a possibility of formation of solid solution. The alloying aspects involved during the deformation were not explored in the present study. The phase map was generated by using the template banks for pure Au and Cu and provides only an approximation for the spatial distribution for the components. It shows the traces of thin layers of the intermixed phases with reduced reliability at the interfaces most probably because they are not compositionally sharp. However, at the locations where the layers are still thicker, the phase mapping approximation can be considered to be reliable in the interior of the layers, away from the interfaces. The IPF maps show elongated grains mostly perpendicular to the loading direction (Y) and along the sliding direction (X). The TBs are absent in the deformed region. As pointed in 6.4.2, the rotation of grains is also evident in this case. It is worth noting that the plastic deformation leading to the grain growth is fairly confined within a well-defined depth since below this depth the TBs are persisting. Furthermore, the deformed zone is highlighted for the region where most of the grain morphologies have changed, mechanical intermixing and vortex formation is seen and the TBs are mostly absent indicating that the plastic deformation is highly localized within this zone. However, the influence of stress-field may be seen even in the region below the deformed zone as the grain orientations in the IPF map Y are seen deviating from the ideal {111} orientation along the growth direction. This observation suggests that there exists a deformation gradient from the top to the bottom of the NMC with upper layers showing severe deformation.

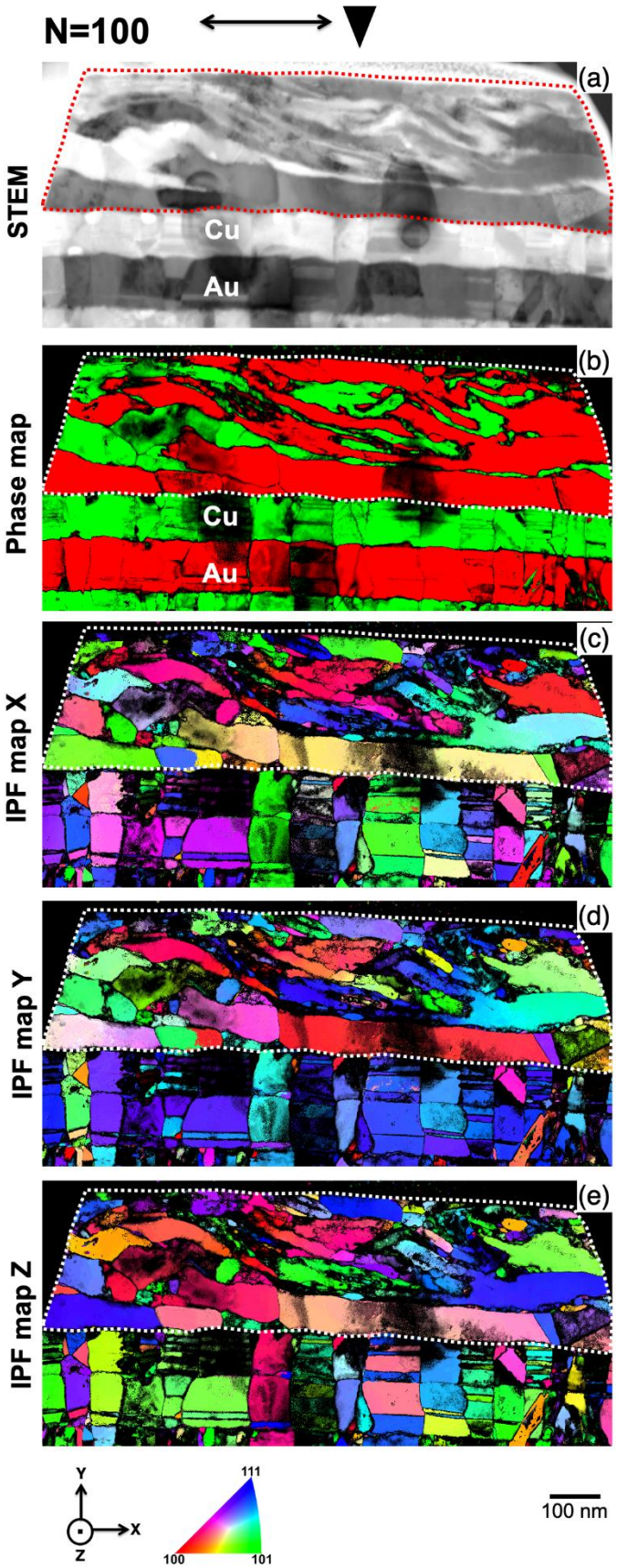

Figure 6-9 Microstructure of the deformed Au-Cu NMC specimen along the longitudinal section of the wear track after 100 sliding cycles investigated by ACOM-STEM and illustrated using virtual BF-STEM, phase map, and IPF maps along X, Y, and Z. The dotted line encompasses the deformed zone. Coordinate axes X, Y, and Z denote the sliding, normal and transverse directions.

6.5 Deformation Mechanisms in Au-Cu NMC

6.5.1 Dislocation-driven Plasticity

The initial size of the columnar grains in individual layers in undeformed Au-Cu NMC is about 100 nm and the average width of columns is about 70 nm. A fundamental observation confirming the plastic deformation in Au-Cu NMC is thinning of individual layers in the deformation zone. A detailed investigation of layer thinning in these Au-Cu NMCs was previously reported by Luo et al. [229]. It was shown that with progressive sliding, the thickness of the upper layers decreased significantly and there was codeformation between the layers. The thickness reduction was attributed to the motion of dislocations within the layers. The generation and emission of dislocations and the evolution of dislocation cell structures in metallic materials under sliding contact are well-known [230–232]. When applied to single-phase coarse-grained metals, reciprocating sliding contact has been shown to emit dislocations several micrometers deep leading to the formation of a plastic deformation zone [230,233]. The size of this zone extends deeper into the material as the loading progresses further. In Au-Cu NMC, the dislocation motion occurs within the individual layers leading to a reduction of the layer thickness. For an initial layer thickness of 100 nm, the Hall-Petch model for semi-coherent interfaces reported by Misra et al. predicts the formation of dislocation pile-up at the interfaces [163,234]. Based on this model, these mobile dislocations are expected to pile up at the interfaces of Au and Cu, the boundaries of the columns, and the twin boundaries within grains. The dislocation pile-up at interfaces is likely to occur considering the initial layer thickness of 100 nm and after thinning up to at least a few tens of nanometers. Although the continuity of slip systems exists at the Au-Cu interfaces, the dislocation pile-up occurs due to the presence of coherency stresses at the interfaces that act as barriers to the transmission of dislocations across these interfaces.

Based on the proposition by Luo et al. [229], local dislocation pile-up at Au-Cu interfaces can lead to step formation. A few steps of smaller height could be seen at the boundaries of the growth twins in the undeformed specimen as well (marked in IPF-X in Figure 6-6). During the deformation, these steps grow as the number of dislocations piling up at the interfaces increases. Beyond certain critical stresses, these dislocations can overcome the coherency stresses and could even transmit Au-Cu interfaces leading to the transfer of slip across these interfaces. The slip transmission across the majority of Au-Cu interfaces is highly feasible as the slip planes and slip directions are parallel, as discussed in 6.4.1. The slip transmission could further promote the growth of the steps at Au-Cu interfaces which is associated with the migration of the interfaces. The plastic instability occurring during the slip transmission most likely causes the development of the waviness of these interfaces. These steps act as some of the potential sites to initiate the vortex formation as discussed later. Similar steps are shown in Figure 6-10 (a)-(b) for the deformed specimen. Figure 6-10 (c) shows the correlation coefficient map showing contrast around the steps due to dislocations. From the observed thinning of layers together with changes in the grain structure leading to their elongation it is concluded that the deformation in Au-Cu NMC is dominated by dislocation-mediated plasticity.

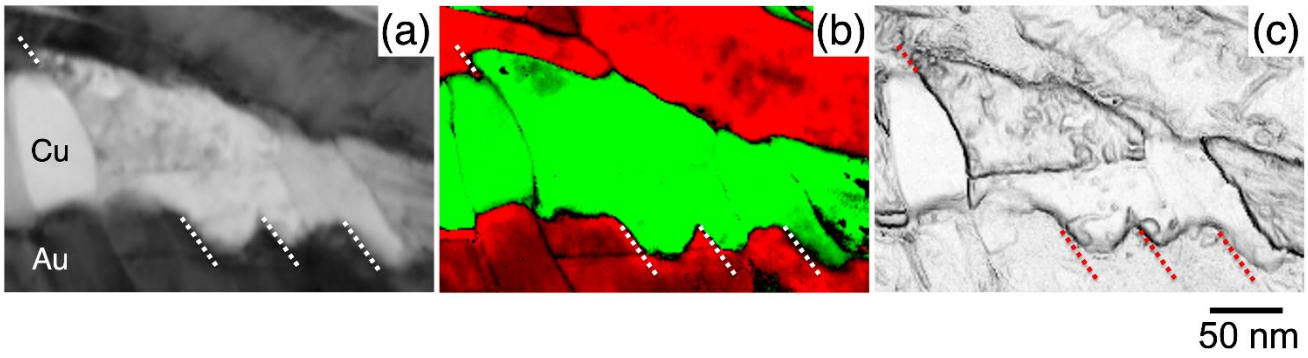

Figure 6-10 Illustration of the step formation denoted using the dotted segments in the transverse section of Au-Cu NMC after 50 sliding cycles: (a) virtual bright-field STEM, (b) phase map, and (c) correlation coefficient map.

6.5.2 Detwinning

Figure 6-11 (a)-(b) represents all the coherent twin boundaries (CTBs) of Σ3 type, with 60°/<111> misorientation, in the undeformed and deformed specimens. It is noted that the Σ3 CTBs constitute a major proportion of intra-layer boundaries in the undeformed specimen. The proportion of other types of coincidence site lattice (CSL) boundaries is negligible and these are not highlighted. Most of the Au-Cu interfaces in the undeformed specimen either exhibit low angle misorientation of less than 5° or these exist as (111) twinned interfaces with high angle misorientation of 60° as shown in Figure 6-11 (c).

The Σ3 CTBs in the deformed zone of the specimen deformed after 50 cycles (Figure 6-11 (b)) are relatively sparse confirming the detwinning process during the plastic deformation. The Σ3 CTBs are expected to be strong barriers to the motion of dislocations and thus very high stresses are required for the slip transmission. In general, the sliding contact is expected to induce large plastic strains and strain gradients [235]. The high stress field introduced in the deformation zone can lead to the detwinning observed therein. The detwinning of single-phase nanotwinned (NT) Cu-Al alloys in the deformation zone under sliding contact was recently reported by Yan et al. [39]. Their investigations on Cu-Al alloys with varying Al content (2 to 6 wt. %) showed the influence of SFE on the microstructural evolution under 5 mN load after 50 sliding cycles. The detwinning was evidenced in all the alloys with varying SFE. SFE influences the mobility of dislocations. In alloys with lower SFE, the mobility of dislocations is reduced as the cross-slip processes become increasingly difficult. The observation of detwinning in alloys with high as well as low SFE validates that the sliding contact generates the stress fields that are sufficient to drive the dislocation activity leading to the detwinning.

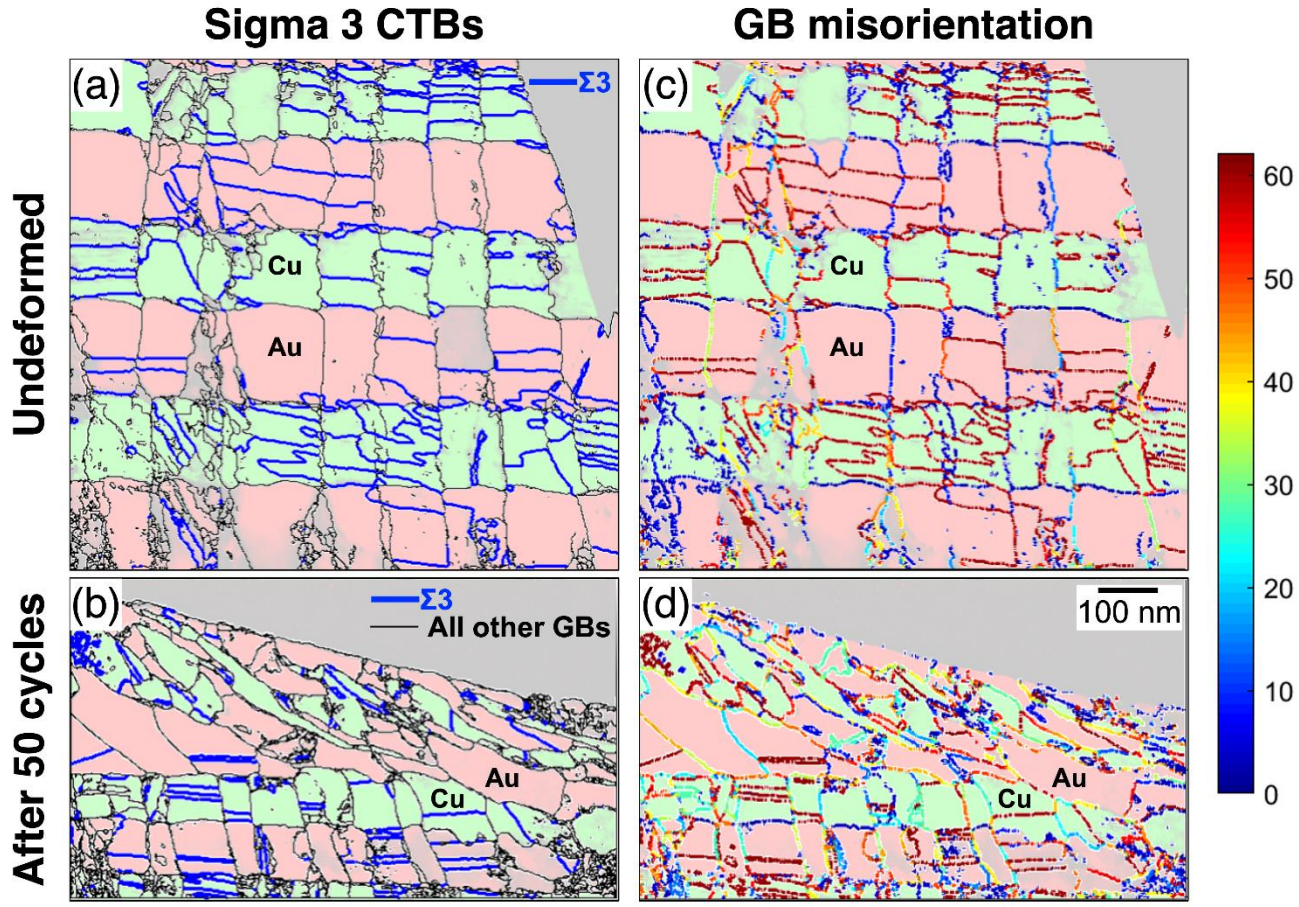

Figure 6-11 Analysis of the grain boundary characteristics in the undeformed Au-Cu NMC: (a) Σ3 GBs shown in blue, and (b) GB misorientation shown according to the color code. Both the GB maps are overlaid on the respective phase maps.

The dislocation-based processes can also explain the detwinning processes at the Σ3 CTBs. Figure 6-12 illustrates a possible mechanism for detwinning. To understand the detwinning, a region around the steps shown in Figure 6-10 is considered. During the step formation, the Au-Cu interface migrates from its original position towards TB1 located in Au (indicated by markers in Figure 6-12 (a)). The Au-Cu interface develops a curvature, and the curved interface meets and crosses the TB1 in Au and generates a discontinuity at the TB1. The segments of the TB1 can be seen exhibiting deviation from 60° misorientation (Figure 6-12 (b)). The presence of the dislocations surrounding these specific steps is already indicated in Figure 6-10 (c). Thus, the piling up of dislocations at the stepped Au-Cu interfaces and their interaction and transmission through the interfaces when the shear stresses are sufficiently high leads to this detwinning. Since the interaction of these dislocations with TBs is causing their detwinning, these are likely to be Shockley partial dislocations that are operative at the Au-Cu interface. Thus, the interaction of partial dislocations with the Σ3 CTBs at the migrating Au-Cu interfaces during the repetitive sliding contact is the basis for this mechanism of detwinning. A similar process is expected for TB3 and TB4 for which a curved Au-Cu interface completely de-twins a segment of the Σ3 CTBs in Cu and migrates into Cu.

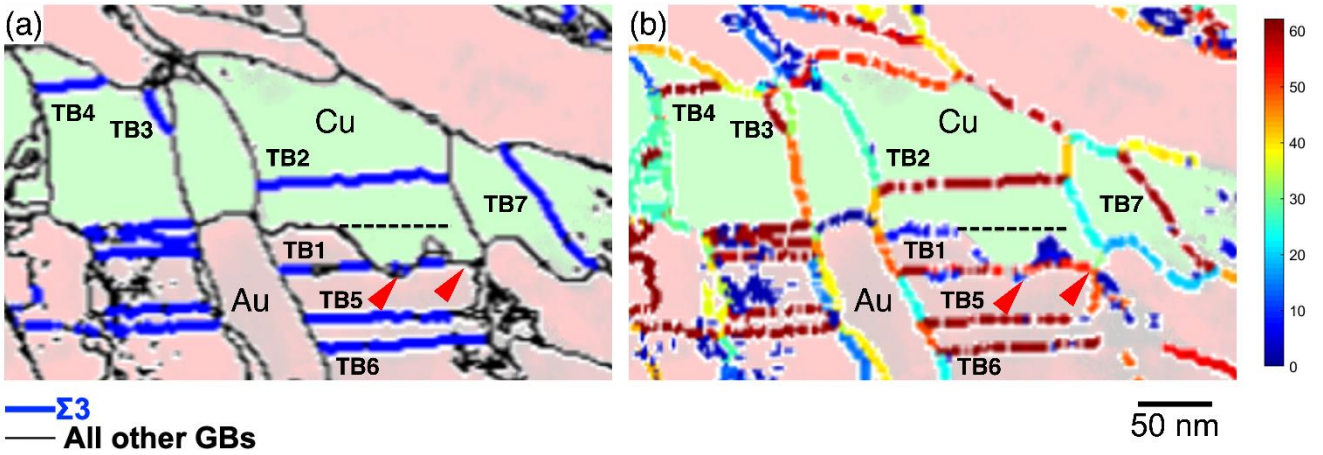

Figure 6-12 Illustration of detwinning (a) map of Σ3 GBs, and (b) GB misorientation map represented according to the color code. Both the GB maps are overlaid on the respective phase maps. The expected original position of an Au-Cu interface is shown by a black-dotted line and the actual migrated interface is shown by red markers.

Detwinning can also be caused by the mobile dislocations within the layers. This is expected for the case in which the Σ3 CTBs that are sufficiently away from the Au-Cu interfaces. The Σ3 CTBs in this case do not interact with the slip processes at the Au-Cu interfaces and the detwinning occurs merely by the intralayer dislocation activity. For the Σ3 CTBs far away from the Au-Cu interfaces, this would be expected during the early stages of layer thinning, while the layers are still thicker. Wang et al. had explained the detwinning of the Σ3 CTBs in NT Cu with columnar grains and a very high density of twins in the individual columns [236]. The model explains the detwinning mechanism for Σ3 CTBs both the ends of which are at the columnar GBs, similar to most of the Σ3 CTBs in the present study. In accordance with this model, single or multiple twinning dislocations (TDs) with Burgers vectors corresponding to Shockley partial dislocations can continuously nucleate at the columnar GBs and glide away on the TB plane under the influence of shear stresses.

6.5.3 Grain Growth and Refinement

The initial grain structure in the undeformed specimen showed columnar grains in each layer. These grains mostly exhibited uniform orientation (within a column) across several layers of Au and Cu with some twinned grains (regions with twinned orientation) in those (Figure 6-6). After deformation, the grain structure in the deformed zone exhibited significant changes, as concerns their sizes and orientation (Figure 6-8 (b) and (c)). The observed grain growth and refinement can be attributed to the layer thinning

concurrent with the migration of Au-Cu interfaces, inter- and intralayer dislocation activity as well as the grain rotation observed in the deformed zone. In the deformed zone, both thicker and thinner layers could be seen at different locations, and coarser as well as finer grains are seen within these as indicated by the arrows in the phase maps corresponding to the central and outer deformed regions (Figure 6-8 (b) and (c)). The grain growth is expected to be highly intensive in the regions of the specimen that are under high stress concentration and its gradient is largest [237], under the tip of the nanoindenter as in the present case. Jin et al. provided the first direct evidence of the deformation-induced grain growth in UFG Al by *in situ* TEM in which the grain sizes were equal to or smaller than the contact area of the indenter [238]. They reported grain growth as a consequence of GB migration, grain rotation, and grain coalescence which could also be supported by the modeling studies by Gutkin et al. [237]. In agreement with these reports, the longitudinal (Figure 6-9) and transverse (Figure 6-8 (c)) sections of the central region directly underneath the sliding indenter exhibit a significant proportion of coarse grains that are elongated normal to sliding direction or the initial growth direction. Formation of such elongated grains in the central region together with detwinning was also reported by Yan et al. in fully NT Cu alloys under similar loading conditions involving the sliding contact [39]. The observation of elongated grains with associated detwinning in NT Cu as well as Au-Cu NMC suggests that the activity of partial dislocations plays a critical role in driving the grain growth during the early stages of deformation in single or two-phase systems. In both these cases, if the Shockley partials are considered to glide across the columnar GBs into neighboring grains, the dissociation of the GBs into new segments might occur. The formation of these mobile segments could accelerate the GB mobility and promote the grain growth.

6.5.4 Vortex Formation and Mechanical Intermixing

Instabilities in shear flow at the interface between layers of two materials are observed in a variety of phenomena in nature which cover a broad range of length scales. The typical examples include wind blowing over water [239], development of turbulence within the ocean [240], atmospheric turbulent billows visible in association with clouds [240,241], deforming rocks by developing kilometer-scale folds during the mountain-building processes [242], etc. In the case of the hydrodynamics of inviscid and incompressible fluids, the transition from calm to wavy interfaces in the presence of velocity gradients leading to their turbulence and mixing is known as the Kelvin-Helmholtz (KH) instability [229,239,243,244].

Mixing instabilities were reported in the case of metallic multilayers subjected to shear deformation by Pouryazdan et al. [242]. Their observations on the vortices emerging from the shear instabilities extended over length scales of several tens of micrometers, far greater than the grain sizes. In the present case, the size of the vortices is within a few 100 nanometers that encompass only a few grains (typically 2 to 4) (Figure 6-8 (c)). Thus, the size of the vortices is quite comparable to the grain sizes. Molecular dynamics simulations by Kim et al. for a tribopair configuration under sliding have clearly shown the development of wave-like instability at atomic scales and the intermixing of materials at the interface [235,245]. As the sliding progressed, the development of vorticity at the nanoscale was reported leading to well-defined eddies in the vicinity of the interfaces. The size of the vortices observed in their simulations was of the order of a few atomic diameters based on which the development of nanocrystalline structure was explained. The mixing of material was shown to be associated with the rotation of these eddies. Further, the flow behavior of materials and the computed velocity profiles at the interfaces were found to be similar to those in the case of the fluid flow. Based on the similarities of the flow patterns, the vorticity induced at the interface of tribopair was compared with the KH instability.

In Au-Cu NMC, the elastic and plastic properties of the two components are different. The elastic shear modulus (G) of Cu is greater than that of Au, whereas the Burgers vector (b) of Au is slightly higher than that of Cu. The force (G.b), required for the gliding of dislocations as calculated by Pugh is higher for Cu than Au [246]. Cu is plastically harder compared to Au thereby resulting in greater resistance to the plastic deformation for Cu than Au. Under the influence of large strain, high strain rates, and strain rate gradients induced underneath the sliding track, differences in the plastic flow rates are likely to be expected between Cu and Au [229,235]. The differences in the plastic flow of Au and Cu lead to the generation of locally inhomogeneous strain fields at their interfaces. These conditions might suffice to initiate the KH instability

in Au-Cu NMC. This is shown schematically in Figure 6-13 for an interface between plastically soft and hard metallic materials A and B under sliding contact. For simplicity, only unidirectional sliding is considered. Initially, for N = 0, the interface is calm without any perturbations. For N = N_1, during the early stages of deformation, the interface develops a sinusoidal wave-like turbulence due to the slip processes across the original undisturbed interface as discussed earlier. Since A is plastically soft, the plastic flow rate of A is expected to be greater compared to B, which is seen from the relative lengths of the arrows. For N = N_2, the perturbations are enhanced due to the plastic flow gradient at the interfaces leading to formation of grooves. The grooves seen in the schematic are similar to those observed experimentally, as highlighted by arrows in Figure 6-12. A rotational deformation occurs in the vicinity of the interface, thereby initiating the mechanical intermixing of the materials. For N = N_3, under KH shear instability, the turbulence and mechanical intermixing of two miscible components (Au and Cu) in the present case, leads to the generation of nanoscale vortices. In agreement with the simulations by Rigney and Karthikeyan, the size of these vortices is comparable to the size of nanocrystals in the present study. The vorticity is also associated with the rotation of crystallites. The observed texture change in the deformed zone thus involves the contribution from dislocation slip processes, associated GB, and interface migration as well as the rotations driven by the vorticity.

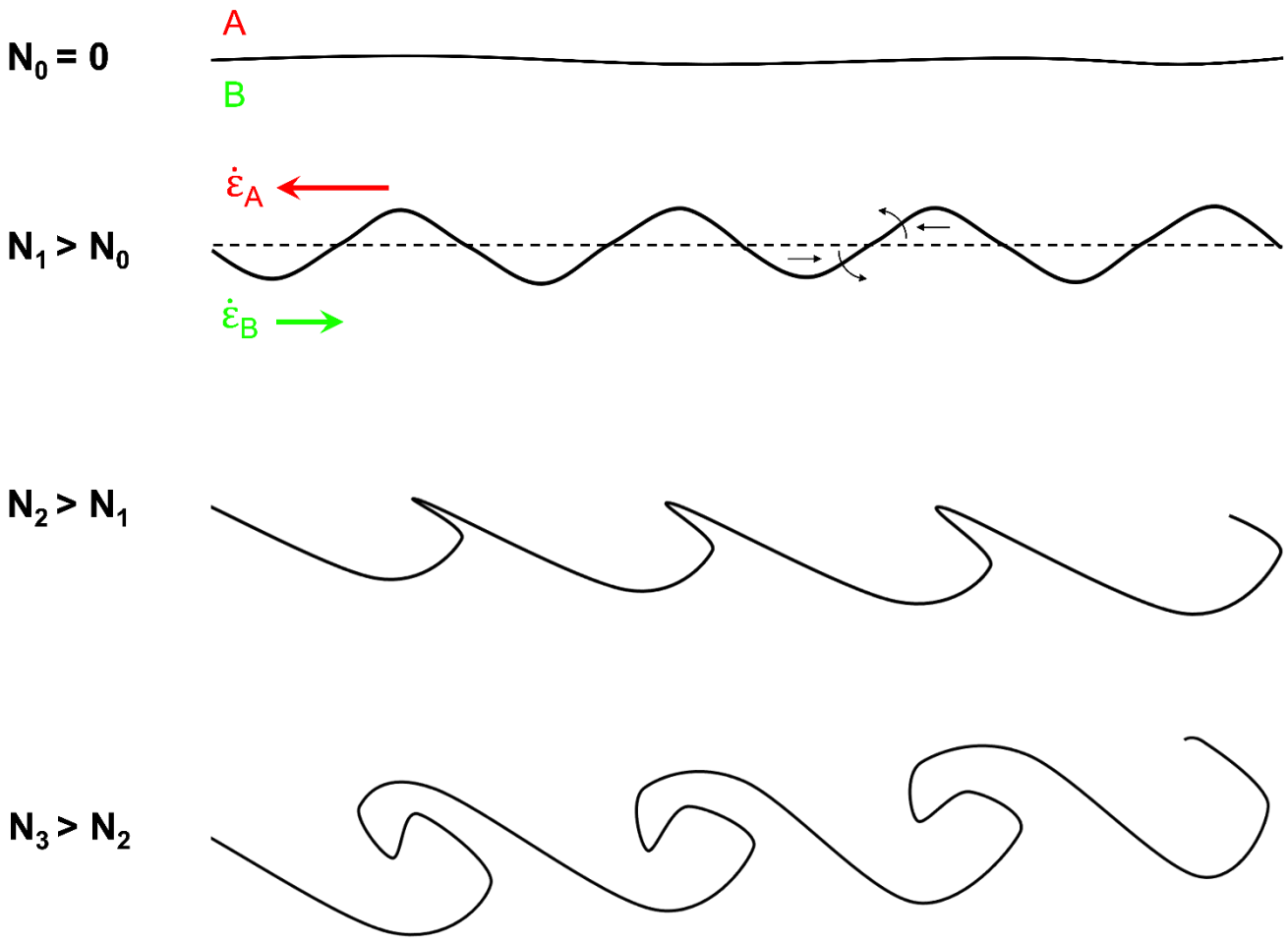

Figure 6-13 Schematic showing the development of plastic instability at the interface of plastically soft and hard metals A and B under sliding contact. The initially undisturbed interface develops turbulence leading to a wavy structure which eventually generates vortices with progressive sliding. The arrows indicate the expected plastic flow profile corresponding to A (red) and B (green) with their lengths representing the relative magnitude of plastic flow rate. The lengths are only schematic and are not true to scale.

6.6 Microstructural and Texture Characteristics of Cu-Cr NMC Thin Films

6.6.1 As-sputtered Cu-Cr NMC

Figure 6-14 (a) and (b) show the BF and DF-STEM images of the as-sputtered Cu-Cr NMC thin film. Both the images show a weaker columnar grain growth in both Cu and Cr layers, as compared with Au-Cu NMCs. It is seen that the grain sizes in Cr layers are relatively smaller than those in Cu layers (Figure 6-14 (c)). As a result, continuous columns of well-defined width are not revealed through the Cu and Cr layers next to each other, unlike those seen in the case of Au-Cu NMC film.

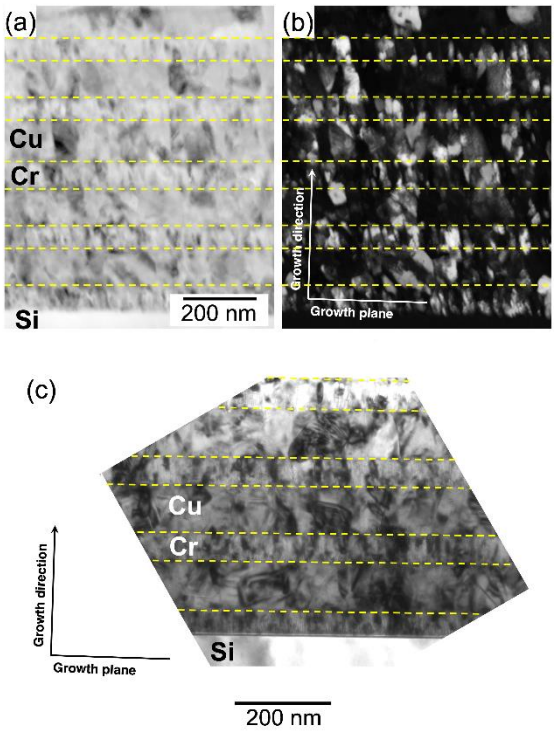

Figure 6-14 Microstructure of as-sputtered Cu-Cr NMC thin film: (a) Virtual bright-field, (b) virtual dark-field STEM images obtained by ACOM-STEM on the same area, and (c) bright-field TEM image. The projections of growth direction and growth plane are shown in (b) and (c). Cu-Cr interfaces are marked using dashed yellow lines.

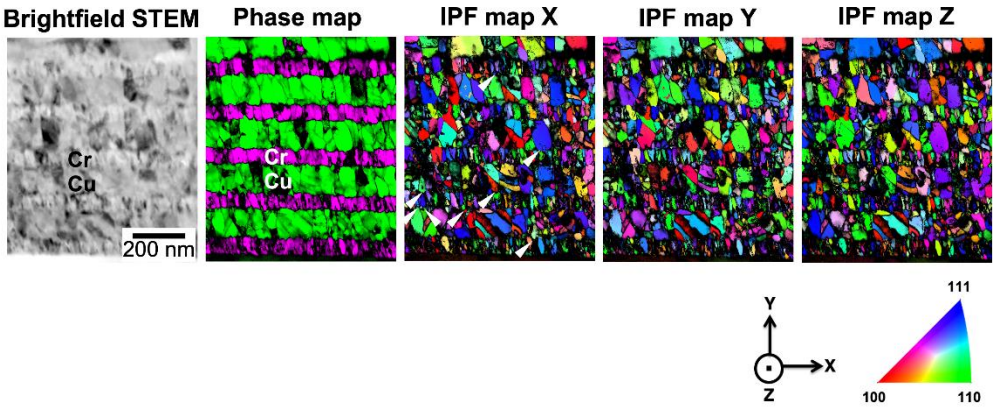

Figure 6-15 Microstructure of Cu-Cr NMC in the as-sputtered state as investigated by ACOM-STEM and represented by virtual bright-field STEM, phase map, and IPF maps along X, Y, and Z. The white markers indicate the grain pairs exhibiting Kurdjmov-Sachs (KS) orientation relationship.

Figure 6-15 shows the phase map and IPF maps of the as-sputtered Cu-Cr NMC. It is seen that Cr layers show finer grain sizes compared to Cu layers. The IPF maps further confirm that there is no continuous columnar growth across the Cu-Cr layers and no preferential orientation along the growth direction is seen in the IPF map Y for Cu and Cr layers. Figure 6-16 shows the {111} and {110} pole figures for Cu and Cr from the specimen shown in Figure 6-15. It is seen that Cu shows a weak {110} texture whereas Cr shows a weak {111} texture along the growth direction which is almost parallel to the Y-axis. The maximum intensities of {111} and {110} poles of Cu do not coincide with the respective {111} and {110} poles of Cr in the pole figures. Instead, it is seen that a few maximum intensities of {111} poles of Cu are coinciding with the maximum intensities of {110} poles of Cr. Similarly, this correlation is also observed for the {110} poles of Cu and {111} poles of Cr. This correlation of the intensities of {111} and {110} poles of Cu and Cr is to some extent related to the existence of the Kurdjmov-Sachs (KS) orientation relationship. The existence of the KS relationship at the Cu-Cr interfaces was confirmed based on the analysis of a few Cu-Cr grains on the pole figures and these pairs are marked in Figure 6-15. However, not all the grain pairs were found to exhibit this relationship. The KS relationship is well-known for Cu-Cr [247] including some other FCC/BCC systems like Cu-Nb [153,248] and Ni-Cr [249] and is expressed as:

{111} FCC // {110} BCC

<110> FCC // <111> BCC

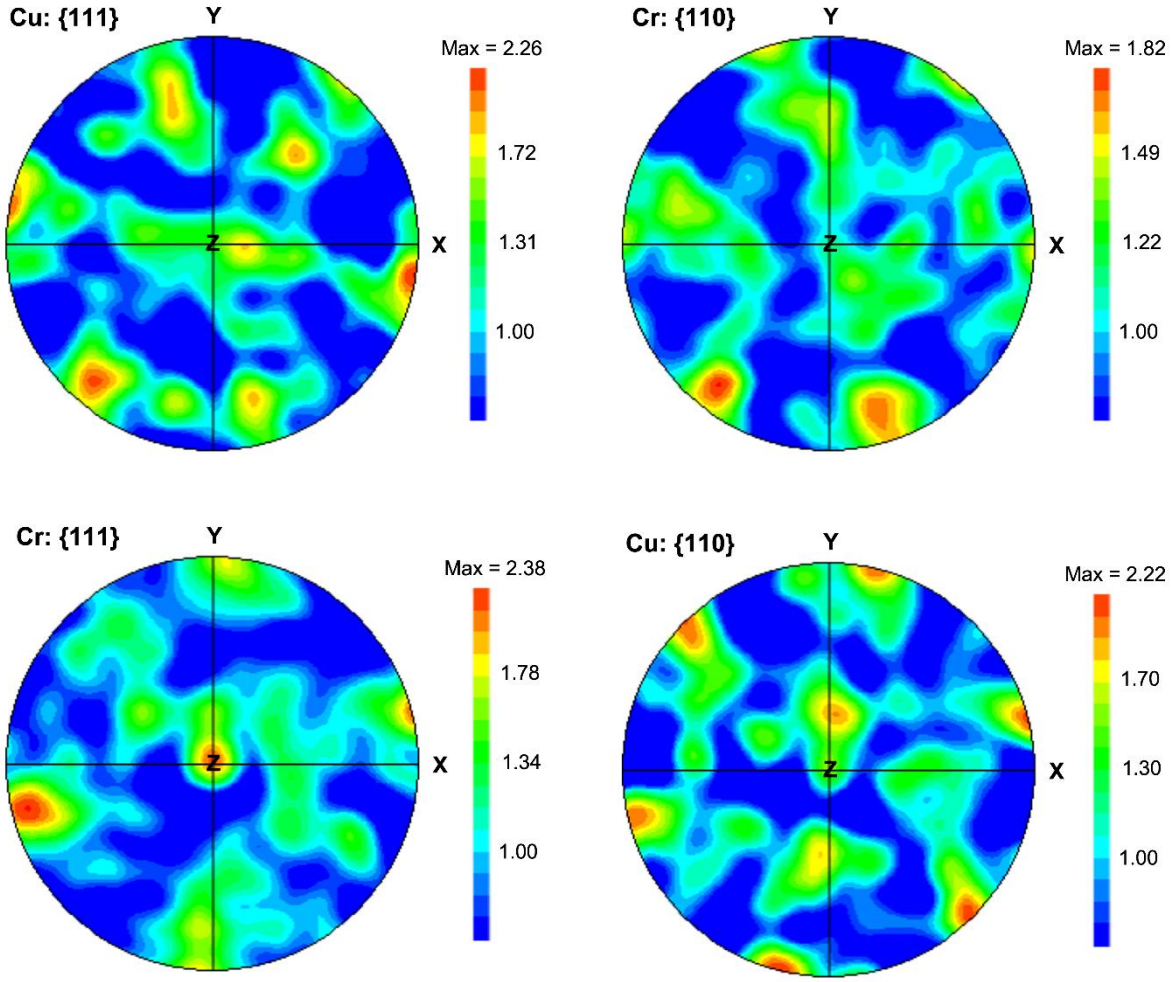

Figure 6-16 Pole figures showing the density of {111} and {110} poles for Cu and Cr in the as-sputtered Cu-Cr NMC. X-Y plane corresponds to the plane of the specimen, where Y is almost parallel with the growth direction.

6.6.2 Deformation Microstructure after 10 and 200 Sliding Cycles

Figure 6-17 shows the microstructural evolution in deformed Cu-Cr NMC after 10 and 200 sliding cycles at 20 mN load with reference to the undeformed specimen (Figure 6-17 (a)) as illustrated in 6.6.1. Figure 6-17 (b) shows the microstructure of the deformed specimen lifted from the transverse section whereas the microstructure in Figure 6-17 (c) corresponds to the longitudinal section of the wear track. The phase maps show 5 layers each of Cu and Cr in the undeformed specimen which are still present in the specimen deformed after 10 cycles. However, after 200 cycles, 5 layers of Cr and only 4 layers of Cu at the bottom of the NMC are visible whereas the uppermost Cu layer is not seen. The uppermost Cu layer wears out and shifts away from the central region of the deformation track as is illustrated in the next section. The phase maps reveal no significant differences in the layer thickness in these specimens investigated in the central region of the deformation track. The individual layers do not change their shapes and remain more or less perpendicular to the normal direction, unlike the case of Au-Cu NMC which showed vortex formation leading to the irregularly shaped layers. In addition, no mechanical intermixing of the layers is observed in Cu-Cr NMC due to the immiscibility of the two components.

The IPF maps show orientations of the grains along the X, Y, and Z axes. The IPF maps after 10 cycles show an elongation of grains in Cu layers perpendicular to the loading or the film growth direction. Compared to the undeformed specimen, it is evident that the Cu layers exhibit grain growth after 10 loading cycles during the sliding contact. Cr layers, on the other hand, show only slight elongation of the grains, however, the grain growth is not as significant as in Cu layers. After 200 cycles, the grains in Cu layers are seen further elongated and their sizes have increased, indicating grain growth with progressive cyclic loading. The grains in the Cr layer still do not exhibit a noticeable change in their sizes. It is worth noting that the cyclic sliding load is applied on the uppermost layer in each case, however, the impact of the stress field is evident even at the bottom-most layer as seen from extensive grain growth in both cases. In terms of the grain structure evolution in Cu-Cr NMC thin film, a clear distinction can be seen here with respect to the deformed Au-Cu NMC thin films, in which the grain structure was mostly unaltered below the deformed zone until 100 loading cycles. In the case of deformed Cu-Cr NMCs, the entire film cross-section is deformed just after 10 loading cycles, although the selected load of 20 mN in Cu-Cr NMC yields a very similar penetration depth as 10 mN in Au-Cu NMC.

To investigate any possible incorporation of elements from a layer into the GBs of its neighboring layer, elemental mapping was performed on a deformed Cu-Cr NMC. Figure 6-18 shows the elemental maps obtained from EFTEM-SI for the deformed Cu-Cr NMC after 200 sliding cycles. The maps were obtained for the same specimen as shown in Figure 6-17 (c). Migration of Cu in the Cr layers can be seen at various locations almost normal to the Cr-layers. Considering the columnar grain structure of Cr, it may be inferred that the migration occurred along the GBs. As marked in Figure 6-18, the Cr layer is seen fragmented and the two fragmented segments are slightly dislocated. The Cu layers, on the other hand, do not exhibit any fragmentation through the layers with their concurrent grain growth during the deformation as seen in Figure 6-17 (c). Thus, there is no trans-layer fragmentation or cracking across the Cu and Cr layers.

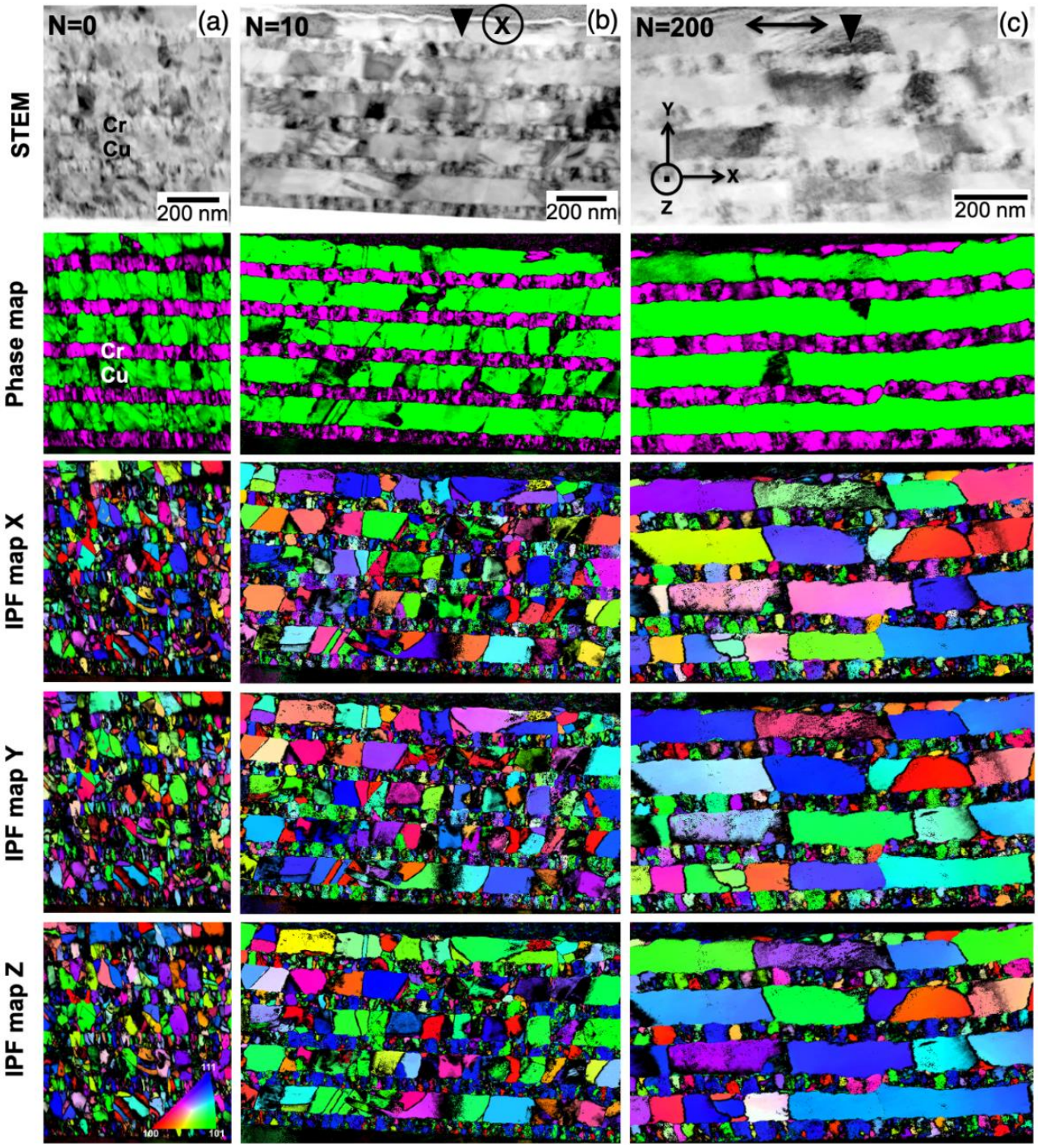

Figure 6-17 Microstructural evolution in the deformed Cu-Cr NMC with reference to the undeformed NMC investigated by ACOM-STEM and illustrated using the virtual brightfield STEM images, phase maps, and IPF maps along X, Y, and Z: (a) undeformed NMC, (b) transverse section after 10 cycles with coordinate axes X, Y and Z indicating the transverse, normal and sliding directions, and (c) showing the longitudinal section after 200 cycles with coordinate axes X, Y and Z indicating the sliding, normal and transverse directions.

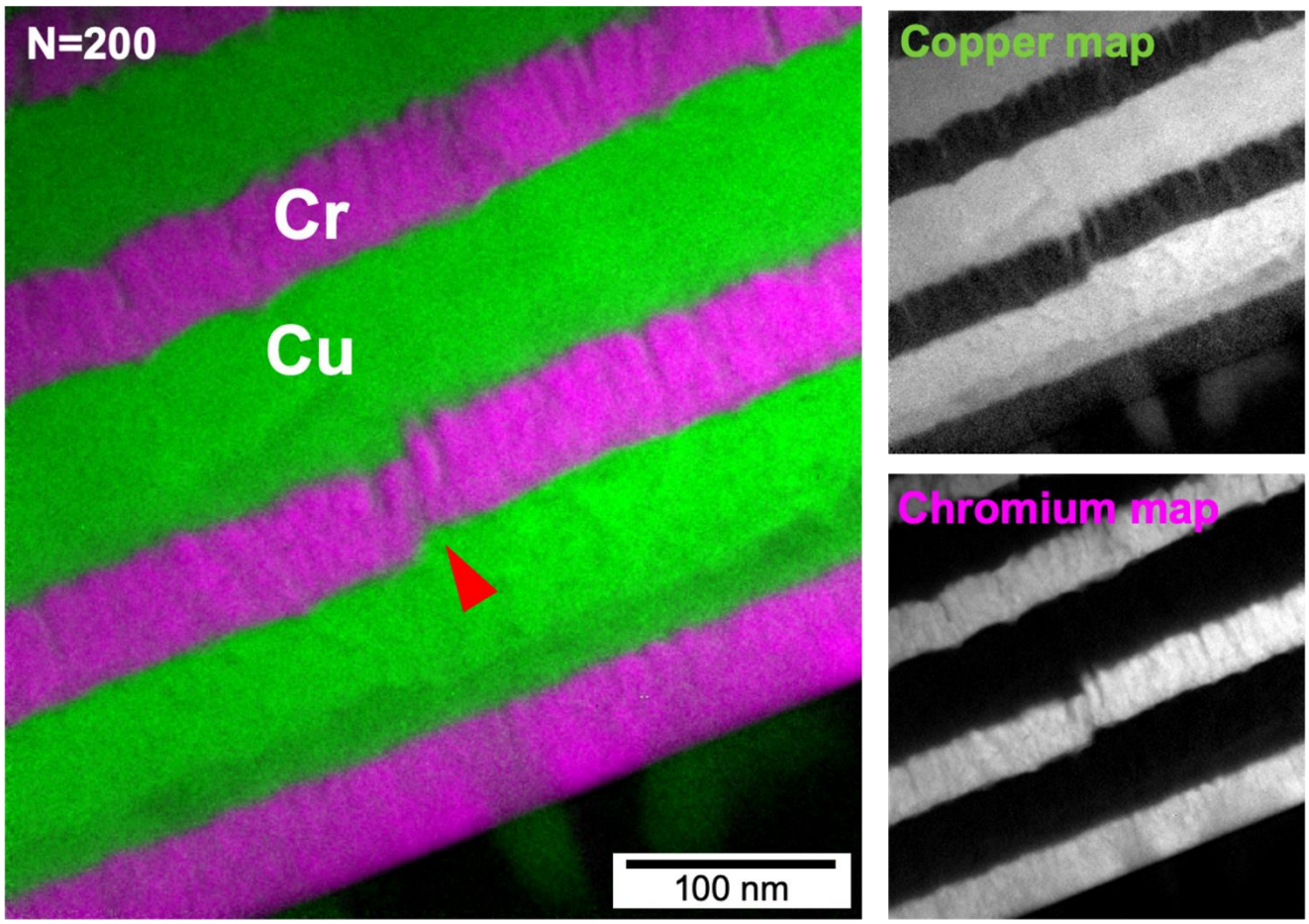

Figure 6-18 EFTEM-SI maps for Cu and Cr in the deformed Cu-Cr NMC after 200 sliding cycles.

6.6.3 Deformation Microstructure after 500 and 1000 Sliding Cycles

The initial microstructure of Cu-Cr NMC consisted of 5 layers each of Cu and Cr whereas the microstructure of the NMC deformed up to 200 cycles showed 5 Cr layers and 4 Cu layers (Figure 6-17 (c)). After 200 cycles, the Cr layers are mostly seen intact with intergranular cracking but without noticeable separation of the cracked regions. Figure 6-19 (a) shows the microstructure of the deformed Cu-Cr NMC after 500 sliding cycles with 3 Cr layers (layers 1 to 3) at the bottom which are more or less intact and are seen broken apart with a separation of their fragments at a few locations. The upper 2 Cr layers (layers 4 and 5) have cracked extensively, and a fraction of their separated fragments can be seen in the upper part as confirmed by the phase map in Figure 6-20 acquired from the specimen shown in Figure 6-19 (a). From the fragmented Cr layers seen after 500 cycles, it is concluded that the cracking processes continue further leading to the separation and fragmentation of the layers. A considerable fraction of the material appears to have lost due to extensive wear in the central regions seen in Figure 6-19 (a)-(b). In Figure 6-19 (a), only a single layer of Cu is seen preserved in the central region at the bottom with a fraction of the volume of Cu on the top which is most likely contributed by the merging of the upper 3 Cu layers (layers 2, 3 and 4). The Cu layer 2 has partly 'squeezed out' in the central region (Figure 6-19 (a)) and displaced away from the center and the Cr layers 2 and 3 come in contact with each other during the deformation.

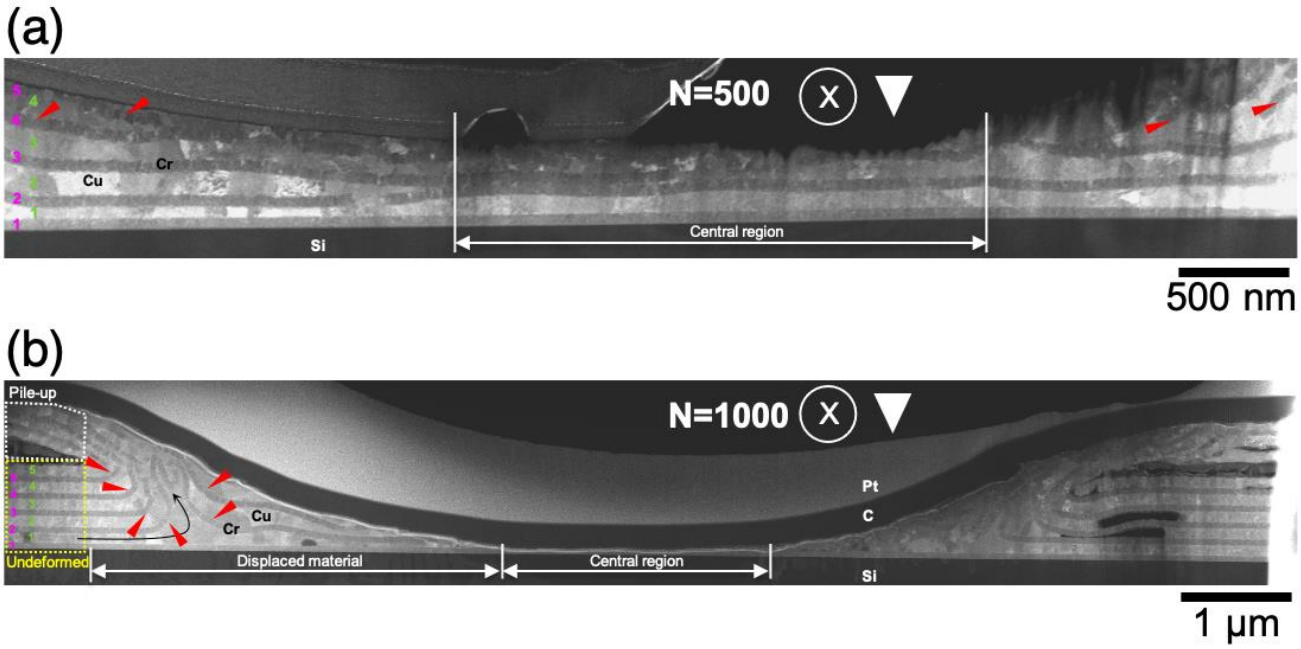

Figure 6-19 HAADF-STEM images of the transverse section of the deformed Cu-Cr NMC after (a) 500 cycles and (b) 1000 cycles. The Cu and Cr layers are numbered in green and pink. The central region is approximately marked for the portion of NMC where the overall thickness is minimum. Red markers indicate the displacement and bending or folding of the Cr layers. The undeformed region is marked using the yellow dotted box, the white dotted box marks the region where the material is piled up and the approximate folding path of the Cr is marked by the black curved arrow in (b).

Figure 6-20 shows the results of the ACOM-STEM on the same Cu-Cr NMC specimen as shown in Figure 6-19 (a). The STEM image in Figure 6-20 does not show any noticeable mechanical intermixing as it was seen in the case of Au-Cu NMC. Cu layers can be seen penetrating through the space between the Cr fragments in the phase map. Cr layers, like the previous deformed specimens (10 and 200 cycles) do not show any significant change in the layer thickness as well as no grain growth is observed. Cu layers on the other hand show extensive grain elongation. The longest grain observed within Cu layers in this specimen is over 1.4 µm. In general, the longest grains are mostly observed in the Cu layer 1 (Figure 6-19 (a) and Figure 6-20) at the bottom of the NMC where the Cr are layers are still more or less intact. This observation leads to an inference that the confinement of Cu grains within two Cr layers is possibly driving this extensive grain growth during which the initial columnar grains with a starting width of less than 100 nm have elongated to sizes of more than 1000%. Such elongated grains in the Cu layers were revealed in the longitudinal section (Figure A) of the specimen after 500 cycles as well. From the observation of these elongated grains in the specimens from two perpendicular sections, it is concluded that Cu layers during the sliding contact tend to exhibit extended 2D grain growth spanning several 100 nanometers with a thickness of less than 100 nm. The GBs in Cu layers are mostly seen vertical which is likely to occur due to their parallel migration with respect to the film normal during reciprocating loading. A few twin boundaries (Figure 6-20) are seen in the upper Cu layers indicating stress-driven twinning as a mechanism during the plastic deformation in Cu.

The thickness of the NMCs subjected to sliding contact is expected to be minimum at the center of the wear track where the depth of penetration during the plastic deformation is greatest. This is seen in the transverse section after 500 cycles in Figure 6-19 (a). The plastic deformation due to the normal load applied via indenter together with the wear during its sliding leads to the displacement of material away from the central region of the wear track. After extreme deformation up to 1000 cycles, this central portion barely consists of any material, except for a fraction of the bottom-most Cr layer as seen in Figure 6-19 (b) and almost the entire volume of material is displaced away from the center. In the region far away from the central region seen in Figure 6-19 (b), the displaced material gets deposited or piled up on top of the

unaffected or undeformed region at the boundary of the wear track. It is noted that within this piled-up material, the individual layers have folded and turned upside down. The Cu and Cr layers (layer 5 of Cu and Cr in Figure 6-19 (b)) which are at the upper-most part of the NMC in the undeformed portion get deposited such that they are the bottom-most in the piled-up material.

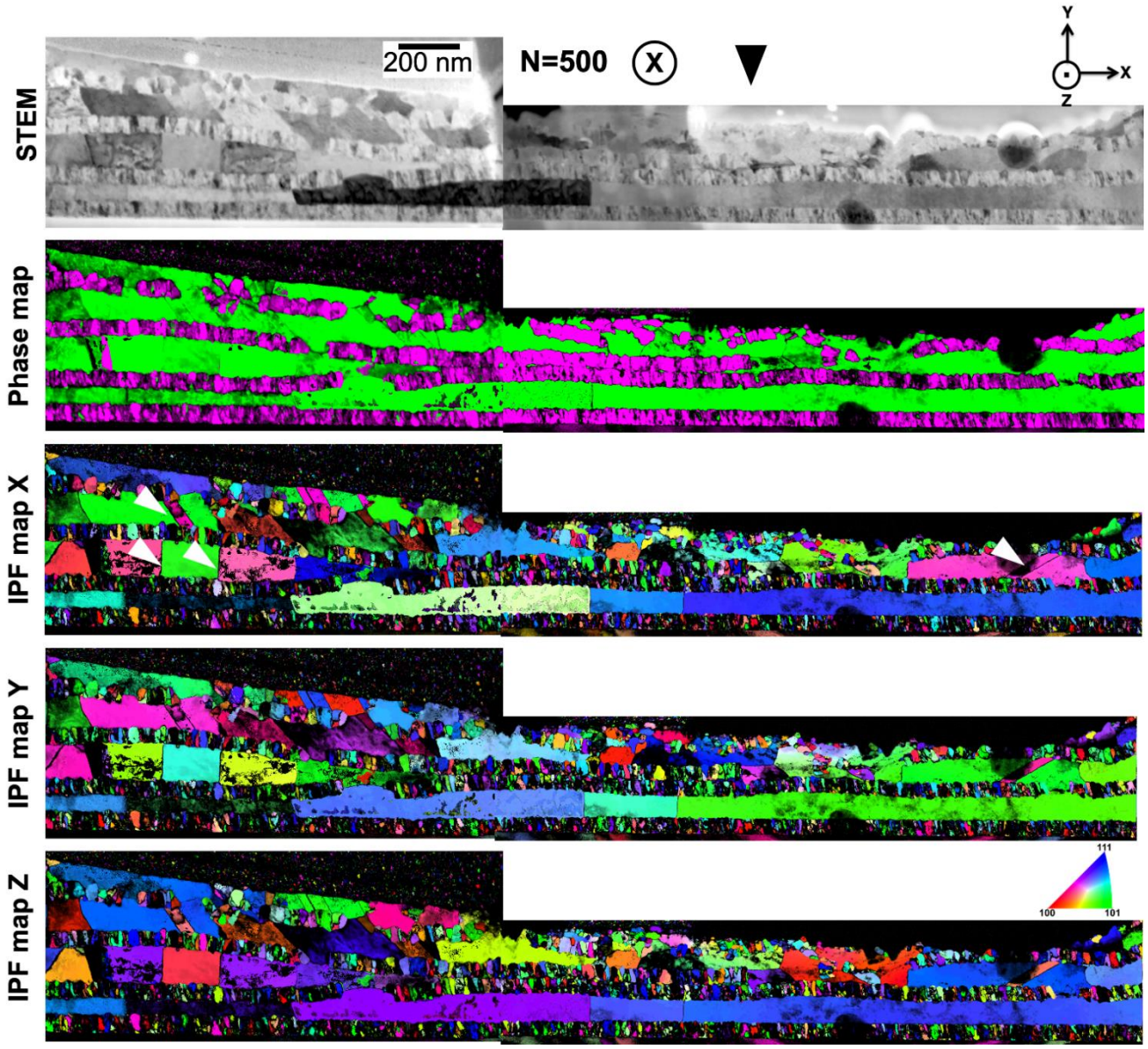

Figure 6-20 Microstructural evolution in the transverse section of the deformed Cu-Cr NMC after 500 cycles investigated by ACOM-STEM and illustrated using a montage of virtual bright-field STEM images, phase maps, and IPF maps along X, Y, and Z obtained from the central region (right) and a part of the region encompassing the displaced material (left). Coordinate axes X, Y, and Z indicate the transverse, normal, and sliding directions. White markers in the IPF map X denote the twin boundaries.

Within the volume of the displaced material away from the central region, bending or folding of the Cr layers occurs as highlighted by markers shown in Figure 6-19 (a). The bending of Cr layers is also confirmed in the phase map of the same specimen deformed after 500 sliding cycles (Figure 6-20). The grain structure of Cu within the displaced material far away from the central region is illustrated in Figure 6-21. It is interesting to observe the accommodation of Cu within the bent Cr layers or fragments. During this accommodation, the layers remain adhered to each other and no separation of Cu and Cr layers is visible, in contrast to the observation at the central region (Figure 6-19 (a)) where Cu layer 2 completely separates

itself from Cr layers 2 and 3. This indicates that all the layers mutually accommodate the plastic deformation while they are displaced away from the center of the wear track and subsequently develop the curvature or bending within the NMC.

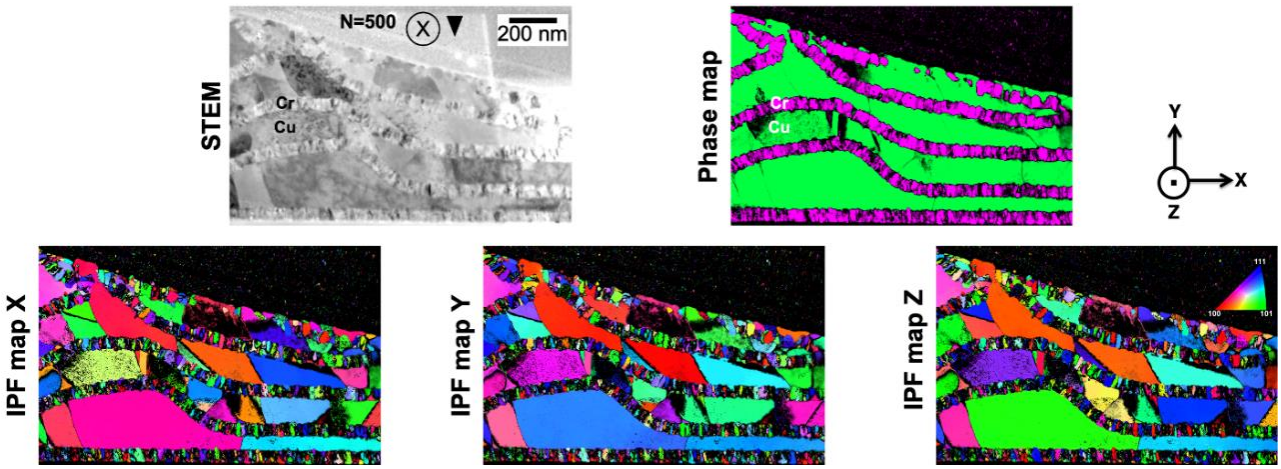

Figure 6-21 Microstructural evolution in the transverse section of the displaced region in the deformed Cu-Cr NMC after 500 cycles investigated by ACOM-STEM and illustrated using the virtual bright-field STEM image, phase map, and IPF maps along X, Y, and Z. Coordinate axes X, Y, and Z indicate the transverse, normal and sliding directions.

6.7 Deformation Mechanisms in Cu-Cr NMC

6.7.1 Grain Growth: Copper versus Chromium

Significant plastic deformation can be seen preferentially for all 5 Cu layers through the deformation sequences in Cu-Cr NMC. The principal evidence for this plastic deformation is extensive grain growth which is seen for all the Cu layers from the early stages of deformation after 10 sliding cycles. The thickness of the individual layers does not change significantly at least until 200 cycles and no codeformation or waviness of the interfaces is seen. These are some of the fundamental aspects that distinguish Cu-Cr NMC from Au-Cu NMC which showed a well-defined deformation zone exhibiting changes in thickness as well as grain structure and below that zone the grain structure was almost unaltered. Further, the depth of the deformation zone gradually increased for Au-Cu NMC as the deformation progressed. On the other hand, with a similar estimated depth of penetration for the selected load and thickness of individual layers, Cu-Cr NMC shows plasticity even at the bottom-most Cu layer. It is conceivable that the grain growth in 100 nm thick Cu layers is driven by dislocations. Strong evidence for the activity of dislocations is that the longest grains seen at the bottom after extreme deformation have {110} orientation along the loading direction as seen in the IPF map Y in Figure 6-20 and Figure A. This demonstrates that during loading, the majority of grains tend to rotate to attain crystal orientation along the primary slip direction. The activity of dislocations is also supported by the observation of some twins during deformation. The grain growth is seen even in the bottom-most Cu layer. This indicates that the applied stress field during the sliding contact in Cu-Cr NMC is sufficient to nucleate and propagate dislocations, transfer the slip across Cu-Cu GBs and cause the migration of Cu-Cu GBs within all Cu layers.

The largest Cu grains in Cu-Cr NMC are seen in the specimen deformed up to 500 cycles at the bottom-most Cu layer which is confined between 2 Cr layers that are still intact (Figure 6-20). It appears that the Cu-Cr interfaces have a crucial role in promoting the preferential grain growth in Cu in Cu-Cr NMCs. The Cu-Cr interfaces are opaque and offer strong resistance to slip transmission due to the discontinuity of slip systems across the interfaces. As a result, the activity of dislocations is expected to be mainly confined within each layer leading to confined layer slip (CLS). The CLS within Cu layers could promote extensive grain growth. The dislocation activity is expected to be relatively lower in Cr layers as Cr is plastically

harder than Cu. Furthermore, the migration of Cu along the cracks formed at the Cr-Cr GBs (Figure 6-18) restricts the slip within Cr layers as well as the mobility of Cr-Cr GBs. As a result, Cr layers barely exhibit grain growth. After extensive deformation, the fragments of cracked Cr layers separate and the neighboring Cu layers merge through the gaps between these fragments. These fragments of Cr offer strong resistance to the motion of Cu-Cu GBs. Thus, the grain growth in the upper Cu layers is limited compared to the lowest one (seen in Figure 6-20). The lowest Cu layer is confined within Cr layers that are not fully fragmented and does not face any resistance from the Cr fragments, unlike the upper ones thereby promoting the migration of random GBs leading to preferential grain growth in Cu.

The thermodynamic driving force for grain growth in nc Cu is the reduction of interfacial energy at Cu-Cu GBs, leading to the reduction in total energy of the system. The chemical miscibility of Cr in Cu is almost negligible. As a result, the Cu layers are not expected to be alloyed with Cr solute atoms. This is well supported by the EFTEM-SI results (Figure 6-18), which do not show the presence of Cr at GBs within the Cu layers. Under these conditions, the nanoscale Cu-Cu GBs are expected to be 'pure' and no solute atoms (Cr) are expected at the GBs. The absence of any solute impurities at the GBs implies the absence of elements that might potentially stabilize the GBs by reducing their free energy and thus their mobility [250,251]. The influence of purity of GBs could be understood from the limited grain growth in the case of Au-Cu NMC considering the miscibility of Au and Cu. Au and Cu constitute a chemically miscible system, with a greater tendency of the solute atoms at GBs to introduce the solute-drag effects that affect the kinetics by inhibiting the grain growth. Following the thermodynamic approach in the case of nc Cu at cryogenic temperatures, Li formulated that increasing the purity at the GBs eases the removal of dislocations due to a reduction in the required external shear stresses [252]. Further, considering a simple case of tilt boundary, Li proposed that due to the removal of dislocations from GBs, the angle of misfit at GB reduces leading to the stress-driven motion of GB. Another possibility could be the disintegration of the GBs by emission of dislocations. As a result, the grain coarsening may proceed in a way that the smaller grains are replaced by the growing grains that are more favorably oriented with respect to the applied stress field [238].

The thermodynamic considerations also explain the limited grain coarsening in Au-Cu NMC as compared with Cu-Cr NMC. Au-Cu NMC consisted of epitaxially grown twin boundaries through the thickness that are expected to be energetically quite stable as opposed to random grain boundaries in the case of Cu-Cr NMC. The mobility of Σ3 CTBs is far lesser compared to the random GBs and these boundaries are well-known for stabilizing the nc metals. As a result, the stress-driven detwinning, interface migration, and grain growth mostly remain confined within a well-defined zone where the stress field is extremely high. The role of CTBs in stabilizing and inhibiting extensive grain growth across the multilayered structure could be emphasized from the behavior of single-phase NT metals. The microstructures obtained by Yan et al. in alloyed NT Cu under tribological loading show similar grain morphologies in the deformed zone [39]. The grains in their case tend to show lateral growth and the long axis of these grains is comparable to the width of individual columns. The detwinning and grain growth in their case are also confined to a defined zone marking a clear separation between the original microstructure and the deformed region.

6.7.2 Fragmentation Cr Layers and Separation of Cu and Cr Layers

The fragmentation processes were seen only in the Cr layers and no trans-layer cracking processes across Cu-Cr NMCs were evidenced. Macroscopically, this shows that under the sliding contact, the Cu-Cr composite system does not exhibit brittle behavior. This is also supported by the extensive plasticity shown by the Cu layers and accommodation of Cu within Cr fragments. The thickness of the Cr layers is about 50 nm and the grain sizes in those are much finer. Further, due to very high hardness of Cr, the plastic deformation due to the gliding of dislocations is limited. Strong evidence for very limited dislocation-based plasticity in Cr is that the sizes of the Cr grains remain almost unaltered even after extreme deformation up to 1000 cycles. Secondly, due to the high hardness of Cr and the discontinuity of slip systems across the Cu-Cr interfaces, the stresses required for transmission of dislocations from Cu in Cr are expected to be quite high. This limits the activity of dislocations to the Cu layers leading to extensive grain growth in Cu as discussed earlier.

Similar Cu-Cr NMCs were probed by Li et al. by 3-point bending test with Cu layer thickness varying between 25 to 250 nm and Cu/Cr ratio of 2:1 [228]. All the Cu-Cr NMCs in their case exhibited a macroscopic brittle fracture with limited plastic deformation. The fracture initially occurred in the stiffer Cr layers along the columnar GBs with localized necking in Cu which occurred between the cracks in the Cr. This behavior was explained based on the weakly bonded columnar GBs in Cr. Thus, if the cohesive strength of the Cr-Cr columnar GBs is weak, these GBs could act as potential sites of crack initiation. In the present study, however, the stress field is complex due to the normal (compressive) load from the intender as well as the shear loading due to the sliding of the indenter. Therefore, the limited gliding of dislocations in Cr coupled with weaker Cr-Cr columnar GBs would lead to the fragmentation along GBs in Cr layers. On the other hand, due to the compressive component of the applied stress-field and extensive dislocation-driven plasticity in Cu layers, the fragmentation initiated in the Cr-Cr GBs is accommodated by Cu. As a result, no macroscopic trans-layer cracking processes or brittle behavior is seen in the Cu-Cr NMCs.

As stated earlier, Cu-Cr interfaces are incoherent and thus the coherency stresses are negligible. In general, these FCC/BCC incoherent interfaces are supposedly 'weak interfaces' owing to their low shear strength. This shear strength corresponds to the critical stress at which the irreversible sliding of a crystal initiates with respect to the other along the interface [151]. Atomistic modeling for Cu-Nb nanolayered composite by Wang et al. has shown that the atomic structure, geometry, and energetics at the interfaces with KS orientation relation leads to low interfacial shear strength [151,162]. These interfaces are thus easily sheared under the influence of the stress field of the glide dislocations. This offers a potential explanation for the separation of Cu from Cr layers directly underneath the sliding indenter.

The negligible plastic flow within Cr layers due to their high hardness and limited slip processes across Cu-Cr interfaces do not lead to their co-deformation and instability at the interfaces that would result in their waviness. The development of cracks along the GBs generates discontinuities within Cr layers. In addition, under extreme deformation Cu and Cr separate from each other. All these conditions do not favor the plastic flow instabilities that would lead to the generation of vortices similar to those observed in the case of Au-Cu NMC.

6.8 Summary

In the present study, the microstructural evolution under cyclic tribological loading was investigated in two NMC systems: Au-Cu and Cu-Cr. Based on the systematic analysis of the microstructural characteristics in the deformed NMCs, varying deformation behaviors and mechanisms were analyzed in these two systems. Au-Cu NMCs with initially an epitaxial and columnar growth of grains with several CTBs deformed by layer thinning and co-deformation. The plastic deformation occurred within a zone with a well-defined penetration depth. Significant detwinning was observed during the plastic deformation. Based on the CTBs observed in the deformed region, two possible mechanisms were proposed to explain the detwinning. According to mechanism 1, the detwinning occurs due to the migrating Au-Cu interface and the interaction and transmission of the dislocations across the layers. Mechanism 2, on the other hand, is based on the detwinning due to the nucleation and gliding of TDs from both the ends of the columnar GBs. Mechanism 2 is expected to be less dominant due to the possibility of annihilation of the partial dislocations as they recombine or are absorbed during the sliding in opposite direction. The plastic deformation was further confirmed by the observation of both grain growth and grain refinement in the deformed zone. These were explained based on the migration of Au-Cu interfaces and inter and intralayer dislocation activity. Apart from the changes in the grain structure, a prominent change in crystallographic texture was seen in the deformed zone which confirmed the grain rotation as an operating deformation mechanism during the sliding contact. The grain rotation may be a result of both the dislocation activity as well as the GB mediated processes. Within the deformed region, mechanical intermixing of Au and Cu and vortex formation analogous to the one resulting Kelvin-Helmholtz instability was evidenced. This vortex formation is also expected to lead to the rotation of grains and thus the observed change in texture.

Cu-Cr NMCs with columnar grains in both Cu and Cr exhibited much different deformation behavior. The plastic deformation was not confined within a specific zone, but it occurred across the entire thickness of the NMC. This was confirmed by the extensive grain growth seen preferentially in all the Cu layers during the early and later stages of deformation. No mechanical intermixing of the Cu and Cr layers was seen. The

preferential grain growth in Cu is driven by the dislocation, migration of GBs, and grain coalescence. This was further explained based on the absence of solute impurities (Cr) at the Cu-Cu GBs which would prevent the stabilization of GBs and promote their mobility. Cr layers, on the other hand, did not show any noticeable change in the grain sizes, indicating very limited dislocation plasticity and GB migration leading to grain growth. Preferential cracking of the Cr layers was seen along their GBs which was attributed to the weak bonding at the columnar Cr-Cr GBs. Cu was seen to penetrate within the cracks of the Cr-Cr GBs which further inhibits the mobility of Cr-Cr GBs and thus, even after extreme stages of deformation, the grain growth in Cr is inhibited. The cracks in Cr layers were not seen to propagate across the Cu-Cr interfaces, which confirmed that Cu-Cr NMCs do not exhibit trans-layer or brittle fracture. The disengagement of Cu and Cr layers was observed which was explained based on the weak shear strength of Cu-Cr interfaces.

7 Conclusions and Outlook

The presented thesis work was focused on in-depth microstructural investigations in nc metallic materials with the aid of *in situ* and *ex situ* TEM techniques and has offered several insights into the deformation mechanisms in these materials. The thesis initially focused on exploring the mechanisms behind the plastic recovery in nc metal thin films and demonstrated the BE using state-of-the-art *in situ* nanomechanical testing. An nc Pd thin film showed a characteristic deviation from the elastic response as it was unloaded during *in situ* cyclic loading and unloading experiments inside TEM. This was evidence of plastic recovery and the BE in the film which progressively became more pronounced as the maximum applied strain in the film was increased. The BE in the film occurred as a result of the stress build-up due to the piling up of dislocations at GBs and film-substrate interface. The thesis unraveled the complex dynamics of the dislocation-based processes that lead to the plastic recovery and the BE and the local grain interactions in the nc metallic materials.

The BE in the film was associated with reversible changes in the microstructural characteristics which were observed with BFTEM imaging. The reversible contrast changes in the TEM images showed an indication of rotation of grains. The contrast changes were seen in the film even after complete relaxation which indicated a time-dependent behavior of the deformation processes in the film. For a quantitative understanding of the mechanisms underlying these microstructural changes, a unique combination of *in situ* cyclic loading-unloading with precession-based 4D STEM to perform crystal orientation mapping inside TEM was implemented. A systematic data processing routine based on the MTEX program was adopted that enabled a reliable quantitative analysis and interpretation of the global and local deformation microstructures in real-time. Analysis of the global deformation structure during loading and unloading revealed the characteristics of rotational deformation of a large number of grains representative of the specimen. The grain rotation maps were initially used to track and exclude the systematic bending/tilting effects in the specimen thereby exposing the true deformation response of the material. The global average rotation of grains in the film increased on loading and reduced on unloading. This showed that the BE in nc Pd thin films is associated with rotational deformation of the grains. From the analysis based on intragrain rotation maps, the majority of grains exhibited a significant rearrangement of the sub-grain boundaries occurring due to dislocation-based processes. These maps thus proved to be critical for tracing the dislocation activity simultaneously in a multitude of grains irrespective of their orientations. This served as an effective approach for understanding the role of dislocation or GB-mediated processes on a statistically significant basis compared to classical BF/DFTEM, nanobeam electron diffraction, or HRTEM-based investigations as reported in the past. The partially reversible arrangement of the sub-grain boundary structure during loading and unloading is in agreement with the observed BE in the nc thin film.

Furthermore, the global analysis of grain rotations during loading and unloading showed a distinct texture evolution unlike the textures observed in cg metals as predicted by Taylor, Sachs, or other classical models. Tensile axes of the majority of the grains showed a directionally reversible response fitting to the BE. The distinct rotation of grains in terms of magnitude and direction showed the generation of locally heterogeneous stress fields. The reversible rotation of grains presented evidence of the localized plastic recovery leading to the BE. Overall, an orientation independent and random texture evolution was evidenced in the nc thin film. The random texture in the present study was attributed to the grain rotation driven by dislocation-based processes in the presence of stress build-up at GBs as well as strong interactions between grains. The present study has raised an alternative possibility to the GB-mediated processes that are commonly known to result in a random texture. Further dedicated *in situ* experiments and analysis might aid in a better understanding of the texture characteristics which is expected to refine the current plasticity models for predicting textures in nc metals.

In the quest of understanding the observed texture behavior, the thesis investigated the grain interactions and the influence of rotation of grain on its neighboring grains. Direct evidence of a unique mechanism involving grain interactions that result in a cooperative rotation of grains in nc thin metal film was presented. From the *in situ* observations using ADF-STEM imaging inside TEM, sets of neighboring grains were shown to rotate cooperatively one after another and these rotations were reversible as the specimen was loaded and unloaded. These rotations were markedly different from the collective or simultaneous rotations occurring due to the GB-mediated processes reported in the past. The grains

rotated with a strong out-of-plane component due to the presence of free surfaces and preferential activation of the out-of-plane slip systems. The evolution of GND density for the grains in the direct neighborhood was significantly different due to the deformation heterogeneity. The GND analysis confirmed the formation of dislocation pile-ups at GBs as a result of the generation of back-stresses on the unloading of the specimen. The formation of dislocation pile-up at specific GBs was found to be closely linked with the geometric arrangement of slip systems and the GBs. The geometric incompatibility of slip systems at the GBs was shown to be the basis for the pile-up formation. The dislocation pile-up at GBs significantly influenced the GND density in the neighboring grains. With the progressive deformation, by increasing or decreasing the strain, the transmission of dislocations was evidenced from grain to its next neighboring grain. This process was shown to occur over multiple grains leading to cooperative grain rotations associated with the BE. Based on these results, direct experimental evidence of dislocation-based grain interactions was presented in nc metals. From these interactions, it is concluded that the rotational deformation and texture in nc metals are complex processes that depend on stress build-up or relaxation, geometric arrangement and character of GBs, and compatibility of the slip systems across GBs. The complex dislocation-dominated grain interactions also rationalize the orientation independent rotation of nanosized grains and the random texture evolution even if the GB-mediated processes do not dominate the global deformation characteristics.

The intragrain orientation spread and grain interactions in bulk nc metals are barely reported or understood. A principal reason for this is the limitations of the experimental methods and a general agreement or assumption that the deformation in nc metals is likely to be dominated by GB-mediated processes. The presented study on the grain interactions in thin nc metal films lays a foundation for extending these investigations in 3D or bulk nc metals. Due to the increased number of neighbors, the interactions in the bulk materials will be far more complex compared to the 2D thin films which have the neighbors confined within the film plane. A detailed investigation of these interactions could be achieved by advanced studies on texture by experiments and simulations. The key factors that might aid to the development of advanced models include the geometric compatibility between the slip systems, its variation across the neighbors, mean free path of mobile dislocations, and GB characteristics.

Besides understanding the grain interactions in pure nc Pd, the thesis investigated the role of grain structure and heterointerfaces to understand the interaction of two phases in NMCs subjected to tribological loading. Au-Cu NMCs with semi-coherent interfaces were initially deformed by thinning of Au and Cu layers. The thinning of layers was observed within a well-defined zone confirming the plastic deformation in both layers. With an initially high density of CTBs in the undeformed Au-Cu NMC, extensive detwinning was evident in the deformed zone. The detwinning occurred as a result of the activity of partial dislocations within the individual layers as well as at the migrating interfaces. Codeformation of layers with a concurrent grain growth as well as grain refinement presented evidence of migration of GBs and Au-Cu interfaces. The Au-Cu interfaces developed waviness and with subsequent deformation, a vortex structure was formed resulting in the mechanical intermixing of Au and Cu. The formation of the vortex structure was attributed to the instabilities in the plastic flow between Au and Cu. The plastic flow instabilities arise primarily due to the differential resistance to the dislocation-based slip processes in Au and Cu due to the differences in their shear modulus and Burgers vectors. The grain rotations and the texture evolution in the deformed zone occurred due to the complex contributions from the dislocation slip, GB-mediated processes as well as due to the rotational deformation induced by vorticity. The fundamental understanding of the deformation characteristics in Au-Cu NMC has opened several avenues for prospective research. A detailed mechanistic understanding of the interface instability and generation of vorticity can be achieved by simulation studies. Simulations might further aid to explain the activity of dislocations at the interfaces and their interactions with CTBs leading to detwinning and grain structure evolution. A closer investigation of the chemical interaction at the interface of the miscible phases may be achieved by analytical electron microscopy. Exploring these interactions might aid in the understanding of the incorporation of solutes, their possible alloying effects, and their impact on the mobility of GBs and interfaces.

In the end, the thesis explored the microstructural evolution and deformation mechanisms in Cu-Cr NMCs with incoherent interfaces. Cu-Cr NMCs showed a clear disparity in the deformation behavior compared to Au-Cu NMC. Cu-Cr NMCs did not exhibit any major change in the layer thickness and no

codeformation and mechanical intermixing were evident. However, widespread stress-driven planar grain growth was preferentially seen in all Cu layers from the early deformation stages. This confirmed the plastic deformation in Cu layers that was mainly attributed to the preferential dislocation activity in Cu due to confined layer slip. After large deformation, Cu-Cu GBs were seen to exist without the incorporation of Cr due to the chemical immiscibility which promoted the migration of random GBs based on the thermodynamic considerations. Cr did not show any noticeable grain growth. One of the reasons for that is its high hardness that led to a large resistance in the dislocation-slip processes. Secondly, intergranular cracking at Cr-Cr GBs was shown and the cracks were accommodated due to migration of Cu. The migrated Cu offered resistance to the motion of Cr-Cr GBs thereby inhibiting the grain growth in all Cr layers. The cracks at Cr-Cr GBs led to a discontinuity in Cr layers and at extreme deformation resulted in the fragmentation of these layers. The restricted slip processes across the opaque Cu-Cr interfaces, limited plastic flow in Cr, and discontinuity in Cr layers due to cracking were proposed as the principal reasons behind the absence of plastic instability at Cu-Cr interfaces and no manifestation of vortex structures. In terms of prospective research, investigation of the grain structure in Cr at atomic scales might aid in a greater understanding of the deformation mechanisms in Cr layers including the cracking processes at Cr-Cr GBs. Detailed global texture analysis on a larger sampling size might be helpful to explain the rotational behavior of Cr grains. For Cu layers, it might be interesting to study the grain structure evolution in greater depth to understand the competition between grain growth and refinement and confirm the existence of an equilibrium grain size. Atomistic simulations might explain the interaction of Cu and Cr at interfaces and the migration of Cu within the cracks at Cr-Cr GBs. In addition, the separation process of Cu from Cr at extreme deformation needs greater investigation.

With these concluding remarks and outlook, the thesis has attempted to add some novel insights into the nanomechanics of nc metals and multilayered composites. These outcomes are expected to promote the existing theories and models of plasticity aimed at developing nanostructured metallic materials with superior mechanical characteristics.

Appendix

Slip Components	Slip directions	Slip planes	Schmid's factor									
	<uvw>	{hkl}	1	2	3	4	5	6	7	8	9	10
In- plane	[0 -1 1]	(1 1 1)	0.097	0.057	0.05	0.11	0.09	0.15	0.07	0.04	0.006	0.007
	[1 0 -1]	(1 1 1)	0.13	0.113	0.08	0.02	0.02	0.29	0.013	0.014	0.05	0.056
	[-1 1 0]	(1 1 1)	0.04	0.055	0.03	0.09	0.07	0.14	0.09	0.059	0.05	0.05
Out-of- plane	[-1 1 0]	(1 1 -1)	0.27	0.417	0.33	0.48	0.49	0.4	0.35	0.28	0.34	0.46
	[-1 0 -1]	(1 1 -1)	0.005	0.07	0.01	0.29	0.32	0.21	0.18	0.15	0.1	0.16
	[0 -1 -1]	(1 1 -1)	0.28	0.34	0.34	0.18	0.16	0.19	0.17	0.13	0.23	0.3
	[0 -1 1]	(-1 1 1)	0.42	0.38	0.43	0.34	0.28	0.32	0.48	0.48	0.08	0.1
	[-1 0 -1]	(-1 1 1)	0.003	0.06	0.009	0.17	0.14	0.16	0.29	0.33	0.26	0.26
	[-1 -1 0]	(-1 1 1)	0.42	0.45	0.43	0.17	0.14	0.48	0.18	0.14	0.18	0.36
	[1 0 -1]	(1 -1 1)	0.14	0.02	0.1	0.14	0.2	0.07	0.12	0.19	0.42	0.36
	[-1 -1 0]	(1 -1 1)	0.1	0.01	0.06	0.4	0.42	0.05	0.26	0.19	0.09	0.15
	[0 -1 -1]	(1 -1 1)	0.04	0.011	0.04	0.26	0.21	0.016	0.39	0.39	0.32	0.21

Table A-1 Schmid factor for in-plane and out-of-plane slip components for grains 1 to 10 as marked in Figure 5-1.

Grain ID	Mean orientation in Euler angles (°) during loading						Angle of rotation
	Initial (ε = 3.6%)			Final (ε = 4.8%)			
	Phi1	Phi	Phi2	Phi1	Phi	Phi2	
1	346.81	135.26	230.85	346.82	135.11	230.81	0.2°
2	28.49	46.86	45.93	28.81	46.96	45.69	0.3°
3	343.10	132.83	231.68	342.83	132.38	231.56	0.5°
4	124.98	50.94	52.00	124.94	51.05	52.18	0.2°
5	131.36	50.05	48.22	131.76	49.07	48.29	1.1°
7	110.64	44.27	47.92	110.85	44.34	47.83	0.2°
8	106.29	47.18	47.05	106.24	47.29	46.95	0.2°
9	59.83	49.24	54.30	59.93	49.39	53.90	0.4°
10	307.85	132.46	226.37	307.18	132.31	226.11	0.6°

Table A-2 Crystal orientation data before and after deformation and the corresponding angles of the rotation of individual grains.

Grain pairs ID	Misorientation axis-angle pairs			
	Initial (i) (ε = 3.6 %)		Final (f) (ε = 4.8 %)	
	Axis	Angle	Axis (f) ∠ (i)	Angle
1-2	[-3 7 11] (i)	20.1°	[-3 7 11] (f) ∠1.9° [-3 7 11] (i)	19.9°
2-3	[-7 4 12] (i)	15.4°	[-7 4 12] (f) ∠0.2° [-7 4 12] (i)	14.8°
3-4	[-8 5 10] (i)	31.1°	[-8 5 10] (f) ∠0.8° [-8 5 10] (i)	30.9°
3-5	[-9 7 12] (i)	26.4°	[-9 7 11] (f) ∠3° [-9 7 12] (i)	25.6°
4-5	[-1 10 12] (i)	5°	[-1 5 9] (f) ∠10.8° [-1 10 12] (i)	5.6°
5-6	[-3 7 9] (i)	50°	[-3 6 8] (f) ∠1.1° [-3 7 9] (i)	50.6°
4-6	[-2 4 5] (i)	45.1°	[-2 4 5] (f) ∠0.2° [-2 4 5] (i)	45.1°
6-8	[-1 0 3] (i)	30.8°	[-1 0 3] (f) ∠0.3° [-1 0 3] (i)	30.7°
5-7	[-5 11 12] (i)	21.7°	[-11 5 11] (f) ∠2.9° [-5 11 12] (i)	21.7°
9-10	[-11 11 12] (i)	58.6°	[-12 11 12] (f) ∠0.2° [-11 11 12] (i)	59°
7-9	[-11 11 12] (i)	46.9°	[-10 10 11] (f) ∠0.3° [-11 11 12] (i)	47.2°

Table A-3 Misorientation axis and angle of the selected pair of grains before and after deformation. The angles between the misorientation axes in the final (f) state are shown relative to the initial (i) state.

Components	Pre edge 1 (eV)	Pre edge 2 (eV)	Post edge (eV)	Slit width (eV)	Exposure time (s)
Cu	861	906	953	40	40
Cr	520	550	585	30	30

Table A-4 Filter energy selected for the pre- and post-edges of Cu and Cr and the corresponding slit width and exposure time.

NMC model system	Au-Cu		Cu-Cr	
Component	Au	Cu	Cu	Cr
Lattice constant (Å)	4.078	3.615	3.615	2.884
TEM voltage (kV)	200	200	200	200
Maximum angle (°)	3	3	3	3
Excitation error	0.6	0.5	0.5-1	0.5-1
Step count	50-60	50-60	50	50
Templates count	1326-1891	1326-1891	1326	1326

Table A-5 Summary of parameters used for generating the template banks for Au, Cu, and Cr in the NMC systems.

NMC model system	Au-Cu	Cu-Cr
Softening loops	2	1
Spot enhance loops	1	3
Spot detection radius	5	5
Noise threshold	10	10
Gamma correction	0.5	0.5
Maximum working radius	115	115
Camera length (cm)	8	8

Table A-6 Summary of parameters used for indexing the block files by template matching.

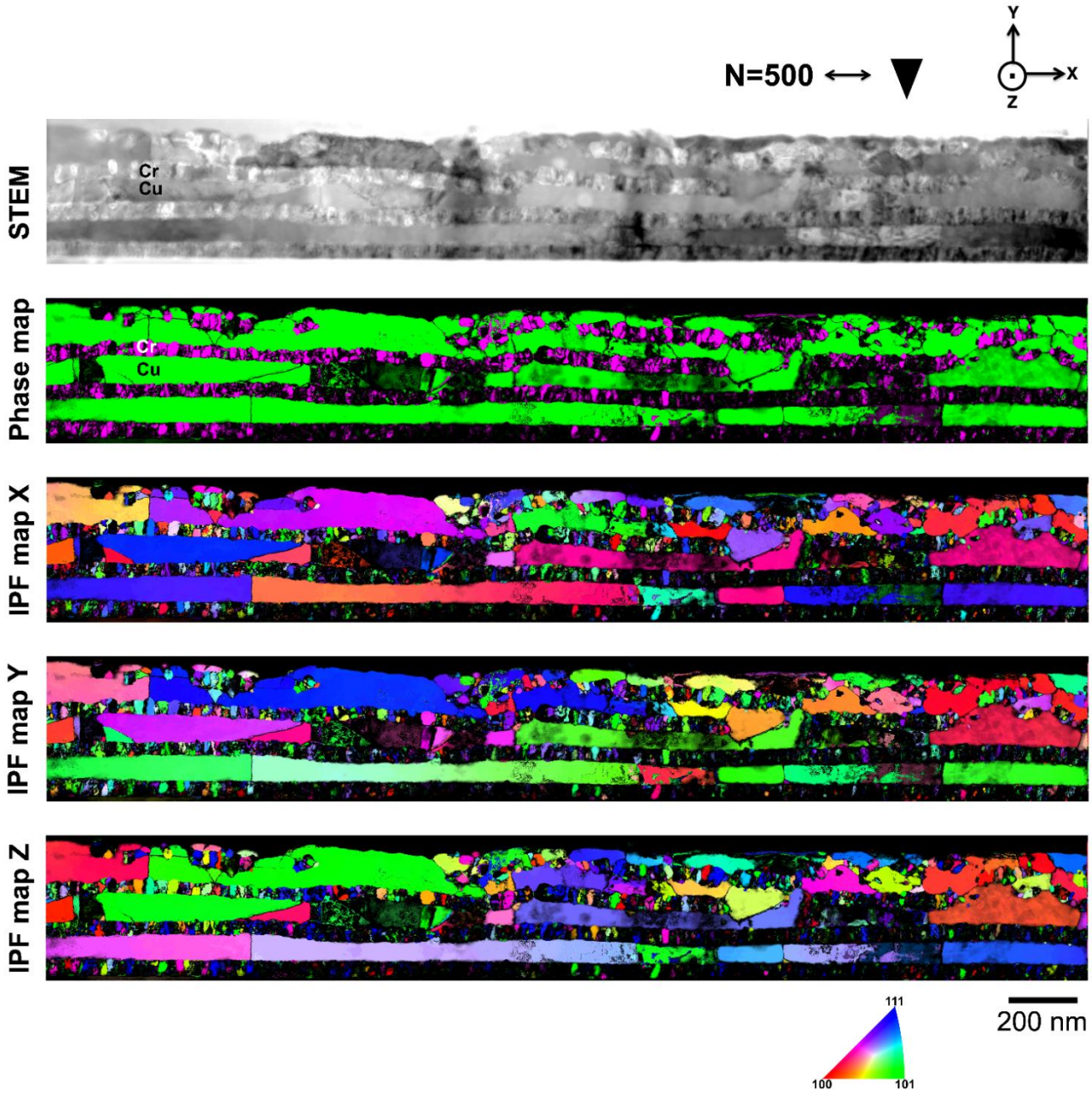

Figure A-1 Microstructural evolution in the longitudinal section of the deformed Cu-Cr NMC after 500 cycles investigated by ACOM-STEM and illustrated using virtual bright-field STEM images, phase maps, and IPF maps along X, Y, and Z. Coordinate axes X, Y, and Z indicate the transverse, normal and sliding directions.

References

[1] T. Rehren, T. Belgya, A. Jambon, G. Káli, Z. Kasztovszky, Z. Kis, I. Kovács, B. Maróti, M. Martinón-Torres, G. Miniaci, V.C. Pigott, M. Radivojević, L. Rosta, L. Szentmiklósi, Z. Szokefalvi-Nagy, 5,000 years old Egyptian iron beads made from hammered meteoritic iron, Journal of Archaeological Science. 40 (2013) 4785–4792. doi:10.1016/j.jas.2013.06.002.

[2] World Steel Association, The Steel Story, (n.d.).

[3] V. Shinde, R.J. Willis, A New Type of Inscribed Copper Plate from Indus Valley (Harappan) Civilisation, Ancient Asia. 5 (2014) 1–10. doi:10.5334/aa.12317.

[4] Indus Civilization, Centre for Cultural Resources and Training, Ministry of Culture, Government of India. http://ccrtindia.gov.in/indusciviliscul p.php%0D%0A.

[5] R. Balasubramaniam, On the corrosion resistance of the Delhi iron pillar, Corrosion Science. 42 (2000) 2103–2129. doi:10.1016/S0010-938X(00)00046-9.

[6] J. Schifman, The entire history of steel, (2018). https://www.popularmechanics.com/technology/infrastructure/a20722505/history-of-steel/%0D%0A.

[7] Boeing, Boeing 777. https://www.boeing.com/commercial/777/.

[8] Y. Colombe, National Institute of Standards and Technology. https://commons.wikimedia.org/wiki/File:Quantum_Computing;_Ion_Trapping_(5941055642).jpg

[9] C. Yusheng, Pure Titanium Slab Rolling Study & Practice on Twin-stand Hot Steckel Mill, in: Titanium 2012, Georgia, Atlanta, 2012.

[10] A. Kashiwar, 3D Microstructural characterization in some alloys using serial sectioning techniques, Indian Institute of Science, Bangalore, 2014. doi:10.13140/RG.2.2.20794.03524.

[11] P. Agrawal, S. Karthikeyan, D. Banerjee, Effect of Dynamic Strain Ageing on Creep in Titanium Alloy, IMI 834, Proceedings of the 13th World Conference on Titanium. (2016) 707–710. doi:10.1002/9781119296126.ch118.

[12] Rolls-Royce, Trent 7000, (n.d.). https://www.rolls-royce.com/products-and-services/civil-aerospace/airlines/trent-7000.aspx?utm_source=LinkedIn&utm_medium=Organic&utm_campaign=CS_PowerOfTrent_Trent7000&utm_content=Video#section-technologyhttps://www.compositesworld.com/news/rolls-royce-b.

[13] G. Markovich, D. V. Left, S.W. Chung, H.M. Soyez, B. Dunn, J.R. Heath, Parallel fabrication and single-electron charging of devices based on ordered, two-dimensional phases of organically functionalized metal nanocrystals, Applied Physics Letters. 70 (1997) 3107–3109. doi:10.1063/1.119105.

[14] Z. Liu, C. Lee, V. Narayanan, G. Pei, E.C. Kan, Metal nanocrystal memories - Part I: Device design and fabrication, IEEE Transactions on Electron Devices. 49 (2002) 1606–1613. doi:10.1109/TED.2002.802617.

[15] B. Wang, H. Idrissi, M. Galceran, M.S. Colla, S. Turner, S. Hui, J.P. Raskin, T. Pardoen, S. Godet, D. Schryvers, Advanced TEM investigation of the plasticity mechanisms in nanocrystalline freestanding palladium films with nanoscale twins, International Journal of Plasticity. 37 (2012) 140–156. doi:10.1016/j.ijplas.2012.04.003.

[16] A. Castrup, C. Kübel, T. Scherer, H. Hahn, Microstructure and residual stress of magnetron sputtered nanocrystalline palladium and palladium gold films on polymer substrates, Journal of Vacuum Science & Technology A: Vacuum, Surfaces, and Films. 29 (2011) 021013. doi:10.1116/1.3554265.

[17] J. Lohmiller, R. Spolenak, P.A. Gruber, Alloy-dependent deformation behavior of highly ductile nanocrystalline AuCu thin films, Materials Science and Engineering A. 595 (2014) 235–240. doi:10.1016/j.msea.2013.12.021.

[18] S. Simoes, R. Calinas, M.T. Vieira, M.F. Vieira, P.J. Ferreira, In situ TEM study of grain growth in nanocrystalline copper thin films, Nanotechnology. 21 (2010) 145701. doi:10.1088/0957-4484/21/14/145701.

[19] Y. Wang, M. Chen, F. Zhou, E. Ma, High tensile ductility in a nanostructured metal, Nature. 419 (2002) 912–915. doi:10.1038/nature01133.

[20] J. Lohmiller, M. Grewer, C. Braun, A. Kobler, C. Kübel, K. Schüler, V. Honkimäki, H. Hahn, O. Kraft, R. Birringer, P.A. Gruber, Untangling dislocation and grain boundary mediated plasticity in nanocrystalline

nickel, Acta Materialia. 65 (2014) 295–307. doi:10.1016/j.actamat.2013.10.071.
[21] E. Hosseinian, O.N. Pierron, Quantitative in situ TEM tensile fatigue testing on nanocrystalline metallic ultrathin films, Nanoscale. 5 (2013) 12532–12541. doi:10.1039/c3nr04035f.
[22] M.S. Colla, B. Wang, H. Idrissi, D. Schryvers, J.P. Raskin, T. Pardoen, High strength-ductility of thin nanocrystalline palladium films with nanoscale twins: On-chip testing and grain aggregate model, Acta Materialia. 60 (2012) 1795–1806. doi:10.1016/j.actamat.2011.11.054.
[23] E. Hosseinian, M. Legros, O.N. Pierron, Quantifying and observing viscoplasticity at the nanoscale: Highly localized deformation mechanisms in ultrathin nanocrystalline gold films, Nanoscale. 8 (2016) 9234–9244. doi:10.1039/c6nr00710d.
[24] H. Gleiter, Nanostructured materials: state of the art and perspectives, Nanostructured Materials. 6 (1995) 3–14. doi:10.1016/0965-9773(95)00025-9.
[25] H. Gleiter, Nanocrystalline materials, Progress in Materials Science. 33 (1989) 223–315. doi:10.1016/0079-6425(89)90001-7.
[26] K.S. Kumar, H. Van Swygenhoven, S. Suresh, Mechanical behavior of nanocrystalline metals and alloys, Acta Materialia. 51 (2003) 5743–5774. doi:10.1016/j.actamat.2003.08.032.
[27] C.S. Pande, K.P. Cooper, Nanomechanics of Hall-Petch relationship in nanocrystalline materials, Progress in Materials Science. 54 (2009) 689–706. doi:10.1016/j.pmatsci.2009.03.008.
[28] M.A. Meyers, A. Mishra, D.J. Benson, Mechanical properties of nanocrystalline materials, Progress in Materials Science. 51 (2006) 427–556. doi:10.1016/j.pmatsci.2005.08.003.
[29] R. Valiev, Nanostructuring of metals by severe plastic deformation for advanced properties, Nature Materials. 3 (2004) 511–516. doi:10.1038/nmat1180.
[30] G. Liu, G.J. Zhang, F. Jiang, X.D. Ding, Y.J. Sun, J. Sun, E. Ma, Nanostructured high-strength molybdenum alloys with unprecedented tensile ductility, Nature Materials. 12 (2013) 344–350. doi:10.1038/nmat3544.
[31] L. Waltz, D. Retraint, A. Roos, P. Olier, J. Lu, High strength nanocrystallized multilayered structure obtained by SMAT and co-rolling, Materials Science Forum. 614 (2009) 249–254. doi:10.4028/www.scientific.net/MSF.614.249.
[32] J. Wang, F. Sansoz, J. Huang, Y. Liu, S. Sun, Z. Zhang, S.X. Mao, Near-ideal theoretical strength in gold nanowires containing angstrom scale twins, Nature Communications. 4 (2013) 1742. doi:10.1038/ncomms2768.
[33] A. Pineau, A. Amine Benzerga, T. Pardoen, Failure of metals III: Fracture and fatigue of nanostructured metallic materials, Acta Materialia. 107 (2016) 508–544. doi:10.1016/j.actamat.2015.07.049.
[34] E.W. Qin, L. Lu, N.R. Tao, J. Tan, K. Lu, Enhanced fracture toughness and strength in bulk nanocrystalline Cu with nanoscale twin bundles, Acta Materialia. 57 (2009) 6215–6225. doi:10.1016/j.actamat.2009.08.048.
[35] K.M. Youssef, R.O. Scattergood, K.L. Murty, J.A. Horton, C.C. Koch, Ultrahigh strength and high ductility of bulk nanocrystalline copper, Applied Physics Letters. 87 (2005). doi:10.1063/1.2034122.
[36] H. Ueno, K. Kakihata, Y. Kaneko, S. Hashimoto, A. Vinogradov, Enhanced fatigue properties of nanostructured austenitic SUS 316L stainless steel, Acta Materialia. 59 (2011) 7060–7069. doi:10.1016/j.actamat.2011.07.061.
[37] T. Hanlon, Y.N. Kwon, S. Suresh, Grain size effects on the fatigue response of nanocrystalline metals, Scripta Materialia. 49 (2003) 675–680. doi:10.1016/S1359-6462(03)00393-2.
[38] T. Hanlon, E.D. Tabachnikova, S. Suresh, Fatigue behavior of nanocrystalline metals and alloys, International Journal of Fatigue. 27 (2005) 1147–1158. doi:10.1016/j.ijfatigue.2005.06.035.
[39] J. Yan, A. Lindo, R. Schwaiger, A.M. Hodge, Sliding wear behavior of fully nanotwinned Cu alloys, Friction. 7 (2019) 260–267. doi:10.1007/s40544-018-0220-z.
[40] A.W. Ruff, D.S. Lashmore, Effect of layer spacing on wear of Ni/Cu multilayer alloys, Wear. 151 (1991) 245–253. doi:10.1016/0043-1648(91)90252-P.
[41] Z.X. Wu, Y.W. Zhang, D.J. Srolovitz, Dislocation-twin interaction mechanisms for ultrahigh strength and ductility in nanotwinned metals, Acta Materialia. 57 (2009) 4508–4518. doi:10.1016/j.actamat.2009.06.015.
[42] Y. Wei, Y. Li, L. Zhu, Y. Liu, X. Lei, G. Wang, Y. Wu, Z. Mi, J. Liu, H. Wang, H. Gao, Evading the strength-

ductility trade-off dilemma in steel through gradient hierarchical nanotwins, Nature Communications. 5 (2014) 3580. doi:10.1038/ncomms4580.
[43] I.A. Ocid'Ko, T.G. Langdon, Enhanced ductility of nanocrystalline and ultrafine-grained metals, Reviews on Advanced Materials Science. 30 (2012) 103–111.
[44] Y. Champion, C. Langlois, S. Guérin-Mailly, P. Langlois, J.L. Bonnentien, M.J. Hÿtch, Near-perfect elastoplasticity in pure nanocrystalline copper, Science (New York, N.Y.). 300 (2003) 310–311. doi:10.1126/science.1081042.
[45] E. Ma, Controlling plastic instability, Nature Materials. 2 (2003) 7–8. doi:10.1038/nmat797.
[46] Y. Li, L. Zhu, Y. Liu, Y. Wei, Y. Wu, D. Tang, Z. Mi, On the strain hardening and texture evolution in high manganese steels: Experiments and numerical investigation, Journal of the Mechanics and Physics of Solids. 61 (2013) 2588–2604. doi:10.1016/j.jmps.2013.08.007.
[47] M.A. Meyers, A. Mishra, D.J. Benson, Mechanical properties of nanocrystalline materials, Progress in Materials Science. 51 (2006) 427–556. doi:10.1016/j.pmatsci.2005.08.003.
[48] E.O. Hall, The Deformation and Ageing of Mild Steel: III Discussion of Results, Proceedings of the Physical Society. Section B. 64 (1951) 747–753.
[49] Y. Xiang, J.J. Vlassak, Bauschinger effect in thin metal films, Scripta Materialia. 53 (2005) 177–182. doi:10.1016/j.scriptamat.2005.03.048.
[50] I. Bauschinger, Ueber die Veranderung der Elasticitatsgrenze und des Elasticitatsmoduls ver-schiedener Metalle, Civilingeneur. 27 (1881) 289–348.
[51] K. Miyauchi, Deformation path effect on stress-strain relation in sheet metals, Journal of Materials Processing Tech. 34 (1992) 195–200. doi:10.1016/0924-0136(92)90107-4.
[52] R. Sowerby, D.K. Uko, Y. Tomita, A review of certain aspects of the Bauschinger effect in metals, Materials Science and Engineering. 41 (1979) 43–58. doi:10.1016/0025-5416(79)90043-0.
[53] D. Zhu, H. Zhang, D.Y. Li, Effects of nano-scale grain boundaries in Cu on its Bauschinger's effect and response to cyclic deformation, Materials Science and Engineering A. 583 (2013) 140–150. doi:10.1016/j.msea.2013.06.050.
[54] J.F. Curry, T.F. Babuska, T.A. Furnish, P. Lu, D.P. Adams, A.B. Kustas, B.L. Nation, M.T. Dugger, M. Chandross, B.G. Clark, B.L. Boyce, C.A. Schuh, N. Argibay, Achieving Ultralow Wear with Stable Nanocrystalline Metals, Advanced Materials. 30 (2018). doi:10.1002/adma.201802026.
[55] C. Subramanian, K.N. Strafford, Review of multicomponent and multilayer coatings for tribological applications, Wear. 165 (1993) 85–95. doi:10.1016/0043-1648(93)90376-W.
[56] R. Maaß, P.M. Derlet, Micro-plasticity and recent insights from intermittent and small-scale plasticity, Acta Materialia. 143 (2018) 338–363. doi:10.1016/j.actamat.2017.06.023.
[57] E.F. Dudarev, E.E. Deryugin, Microplastic deformation and yield strength of polycrystals, Soviet Physics Journal. 25 (1982) 510–519. doi:10.1007/BF00898747.
[58] S. Brandstetter, H. Van Swygenhoven, S. Van Petegem, B. Schmitt, R. Maaß, P.M. Derlet, From micro- to macroplasticity, Advanced Materials. 18 (2006) 1545–1548. doi:10.1002/adma.200600397.
[59] L. Thilly, S. Van Petegem, P.O. Renault, F. Lecouturier, V. Vidal, B. Schmitt, H. Van Swygenhoven, A new criterion for elasto-plastic transition in nanomaterials: Application to size and composite effects on Cu-Nb nanocomposite wires, Acta Materialia. 57 (2009) 3157–3169. doi:10.1016/j.actamat.2009.03.021.
[60] E. Bitzek, P.M. Derlet, P.M. Anderson, H. Van Swygenhoven, The stress-strain response of nanocrystalline metals: A statistical analysis of atomistic simulations, Acta Materialia. 56 (2008) 4846–4857. doi:10.1016/j.actamat.2008.05.043.
[61] J. Rajagopalan, C. Rentenberger, H. Peter Karnthaler, G. Dehm, M.T.A. Saif, In situ TEM study of microplasticity and Bauschinger effect in nanocrystalline metals, Acta Materialia. 58 (2010) 4772–4782. doi:10.1016/j.actamat.2010.05.013.
[62] J. Rajagopalan, J.H. Han, M.T.A. Saif, On plastic strain recovery in freestanding nanocrystalline metal thin films, Scripta Materialia. 59 (2008) 921–926. doi:10.1016/j.scriptamat.2008.02.060.
[63] J. Rajagopalan, J.H. Han, M.T.A. Saif, Bauschinger effect in unpassivated freestanding nanoscale metal films, Scripta Materialia. 59 (2008) 734–737. doi:10.1016/j.scriptamat.2008.06.010.
[64] F. Mompiou, D. Caillard, M. Legros, H. Mughrabi, In situ TEM observations of reverse dislocation motion upon unloading in tensile-deformed UFG aluminium, Acta Materialia. 60 (2012) 3402–3414.

doi:10.1016/j.actamat.2012.02.049.
[65] G.E. Dieter, Mechanical metallurgy., McGraw-Hill Book Company, Inc., New York, USA, 2011. doi:10.5962/bhl.title.35895.
[66] M. Dao, L. Lu, R.J. Asaro, J.T.M. De Hosson, E. Ma, Toward a quantitative understanding of mechanical behavior of nanocrystalline metals, Acta Materialia. 55 (2007) 4041–4065. doi:10.1016/j.actamat.2007.01.038.
[67] L. Lu, Z.S. You, K. Lu, Work hardening of polycrystalline Cu with nanoscale twins, Scripta Materialia. 66 (2012) 837–842. doi:10.1016/j.scriptamat.2011.12.046.
[68] C.C. Koch, D.G. Morris, K. Lu, A. Inoue, Ductility of nanostructured materials, MRS Bulletin. 24 (1999) 54–58. doi:10.1557/S0883769400051551.
[69] K. Wierzbanowski, M. Wroński, A. Baczmański, B. Bacroix, P. Lipinski, A. Lodini, Problem of lattice rotation due to plastic deformation. Example of rolling of F.C.C materials, Archives of Metallurgy and Materials. 56 (2011) 575–584. doi:10.2478/v10172-011-0061-5.
[70] N.J. Petch, The Cleavage Strength of Polycrystals, Journal of the Iron and Steel Institute. 174 (1953) 25–28.
[71] R.A. Masumura, P.M. Hazzledine, C.S. Pande, Yield stress of fine grained materials, Acta Materialia. 46 (1998) 4527–4534. doi:10.1016/S1359-6454(98)00150-5.
[72] C.E. Carlton, P.J. Ferreira, What is behind the inverse Hall-Petch effect in nanocrystalline materials?, Acta Materialia. 55 (2007) 3749–3756. doi:10.1016/j.actamat.2007.02.021.
[73] A.H. Cottrell, Dislocations and Plastic Plow in Crystals, Oxford University Press, 1953.
[74] S.N. Buckley, K.M. Entwistle, The bauschinger effect in super-pure aluminum single crystals and polycrystals, Acta Metallurgica. 4 (1956).
[75] F.A. McClintock, A.S. Argon, Mechanical Behaviour of Materials, Addison-Wesley, 1966.
[76] H.G. van Bueren, Imperfections in Crystal, Amsterdam, 1960.
[77] A. Abel, H. Muir, The bauschinger effect and discontinuous yielding, Philosophical Magazine. 26 (1972) 489–504. doi:10.1080/14786437208227444.
[78] S. Mader, A. Seeger, C. Leitz, Work hardening and dislocation arrangement of fcc single crystals. I. Plastic deformation and slip line studies of nickel single crystals, Journal of Applied Physics. 34 (1963) 3368–3375. doi:10.1063/1.1729194.
[79] E. Orowan, Symposium on internal stresses in metals and alloys, Institute of Metals, London. (1948).
[80] E. Orowan, Causes, and Effects of Int. Stresses, Internal Stresses, and Fatigue in Metals, Symposium, Detroit, New York: Elsevier Co. (1959).
[81] H.W. Höppel, M. Kautz, C. Xu, M. Murashkin, T.G. Langdon, R.Z. Valiev, H. Mughrabi, An overview: Fatigue behaviour of ultrafine-grained metals and alloys, International Journal of Fatigue. 28 (2006) 1001–1010. doi:10.1016/j.ijfatigue.2005.08.014.
[82] Y. Xiang, J.J. Vlassak, Bauschinger and size effects in thin-film plasticity, Acta Materialia. 54 (2006) 5449–5460. doi:10.1016/j.actamat.2006.06.059.
[83] G. Winther, Slip systems, dislocation boundaries and lattice rotations in deformed metals, 2009.
[84] E. Ma, Watching the nanograins roll, Science (New York, N.Y.). 305 (2004) 623–624. doi:10.1126/science.1101589.
[85] G. Winther, L. Margulies, S. Schmidt, H.F. Poulsen, Lattice rotations of individual bulk grains Part II: Correlation with initial orientation and model comparison, Acta Materialia. 52 (2004) 2863–2872. doi:10.1016/j.actamat.2004.02.045.
[86] H.F. Poulsen, L. Margulies, S. Schmidt, G. Winther, Lattice rotations of individual bulk grains. Part I: 3D X-ray characterization, Acta Materialia. 51 (2003) 3821–3830. doi:10.1016/S1359-6454(03)00206-4.
[87] G.I. Taylor, Plastic strain in metals, Journal of the Institute of Metals. 62 (1938) 307–324. doi:not found.
[88] G.I. Sachs, Zur ableitung einer fleissbedingun, Zeichschrift Verein Deutscher Ingenieur. 72 (1928) 734–736.
[89] J. Hirsch, K. Lücke, Overview no. 76. Mechanism of deformation and development of rolling textures in polycrystalline f.c.c. metals-II. Simulation and interpretation of experiments on the basis of Taylor-type theories, Acta Metallurgica. 36 (1988) 2883–2904. doi:10.1016/0001-6160(88)90173-3.
[90] L. Margulies, G. Winther, H.F. Poulsen, In situ measurement of grain rotation during deformation of

polycrystals, Science (New York, N.Y.). 291 (2001) 2392–2394. doi:10.1126/science.1057956.
[91] U.F. Kocks, Independent slip systems in crystals, Philosophical Magazine. 10 (1964) 187–193. doi:10.1080/14786436408225657.
[92] J.F.W. Bishop, R. Hill, XLVI. A theory of the plastic distortion of a polycrystalline aggregate under combined stresses., The London, Edinburgh, and Dublin Philosophical Magazine and Journal of Science. 42 (1951) 414–427. doi:10.1080/14786445108561065.
[93] W. Mao, On the Taylor principles for plastic deformation of polycrystalline metals, Frontiers of Materials Science. 10 (2016) 335–345. doi:10.1007/s11706-016-0358-4.
[94] W. Mao, The currently predominant Taylor principles should be disregarded in the study of plastic deformation of metals, Frontiers of Materials Science. 12 (2018) 322–326. doi:10.1007/s11706-018-0434-z.
[95] C. Thorning, M.A.J. Somers, J.A. Wert, Grain interaction effects in polycrystalline Cu, Materials Science and Engineering A. 397 (2005) 215–228. doi:10.1016/j.msea.2005.02.043.
[96] G. Winther, J.P. Wright, S. Schmidt, J. Oddershede, Grain interaction mechanisms leading to intragranular orientation spread in tensile deformed bulk grains of interstitial-free steel, International Journal of Plasticity. 88 (2017) 108–125. doi:10.1016/j.ijplas.2016.10.004.
[97] W. Robert, D. Piot, J.H. Driver, A rapid deformation texture model incorporating grain interactions, Scripta Materialia. 50 (2004) 1215–1219. doi:10.1016/j.scriptamat.2004.02.007.
[98] S. Panchanadeeswaran, R.D. Doherty, R. Becker, Direct observation of orientation change by channel die compression of polycrystalline aluminum—Use of a split sample, Acta Materialia. 44 (1996) 1233–1262. doi:10.1016/1359-6454(95)00186-7.
[99] S.R. Kalidindi, A. Bhattacharyya, R.D. Doherty, Detailed analyses of grain-scale plastic deformation in columnar polycrystalline aluminium using orientation image mapping and crystal plasticity models, Proceedings of the Royal Society A: Mathematical, Physical and Engineering Sciences. 460 (2004) 1935–1956. doi:10.1098/rspa.2003.1260.
[100] W. Mao, Influence of intergranular mechanical interactions on orientation stabilities during rolling of pure aluminum, Metals. 9 (2019) 477. doi:10.3390/met9040477.
[101] S. Mu, F. Tang, G. Gottstein, A cluster-type grain interaction deformation texture model accounting for twinning-induced texture and strain-hardening evolution: Application to magnesium alloys, Acta Materialia. 68 (2014) 310–324. doi:10.1016/j.actamat.2013.12.007.
[102] P. Van Houtte, S. Li, M. Seefeldt, L. Delannay, Deformation texture prediction: From the Taylor model to the advanced Lamel model, International Journal of Plasticity. 21 (2005) 589–624. doi:10.1016/j.ijplas.2004.04.011.
[103] J. Oddershede, J.P. Wright, A. Beaudoin, G. Winther, Deformation-induced orientation spread in individual bulk grains of an interstitial-free steel, Acta Materialia. 85 (2015) 301–313. doi:10.1016/j.actamat.2014.11.038.
[104] P. Van Houtte, L. Delannay, I. Samajdar, Quantitative Prediction of Cold Rolling Textures in Low-Carbon Steel by Means of the Lamel Model, Textures and Microstructures. 31 (1999) 109–149. doi:10.1155/tsm.31.109.
[105] M. Crumbach, G. Pomana, P. Wagner, G. Gottstein, Recrystallisation and grain growth, Recrystallization and Grain Growth. (2001) 1053–1060.
[106] A. Kobler, J. Lohmiller, J. Schäfer, M. Kerber, A. Castrup, A. Kashiwar, P.A. Gruber, K. Albe, H. Hahn, C. Kübel, Deformation-induced grain growth and twinning in nanocrystalline palladium thin films, Beilstein Journal of Nanotechnology. 4 (2013) 554–566. doi:10.3762/bjnano.4.64.
[107] Y. Ivanisenko, L. Kurmanaeva, J. Weissmueller, K. Yang, J. Markmann, H. Rösner, T. Scherer, H.J. Fecht, Deformation mechanisms in nanocrystalline palladium at large strains1, Acta Materialia. 57 (2009) 3391–3401. doi:10.1016/j.actamat.2009.03.049.
[108] M.Y. Gutkin, A.L. Kolesnikova, I.A. Ovid'ko, N. V. Skiba, Rotational Deformation Mechanism in Fine-Grained Materials Prepared by Severe Plastic Deformation, Journal of Metastable and Nanocrystalline Materials. 12 (2002) 47–58. doi:10.4028/www.scientific.net/jmnm.12.47.
[109] M.Y. Gutkin, I.A. Ovid'ko, N. V. Skiba, Crossover from grain boundary sliding to rotational deformation in nanocrystalline materials, Acta Materialia. 51 (2003) 4059–4071. doi:10.1016/S1359-6454(03)00226-

X.
[110] B.N. Kim, K. Hiraga, K. Morita, H. Yoshida, B.W. Ahn, Viscous grain-boundary sliding with rotating particles or grains, Acta Materialia. 57 (2009) 5730–5738. doi:10.1016/j.actamat.2009.08.001.
[111] Y.J. Wei, L. Anand, Grain-boundary sliding and separation in polycrystalline metals: Application to nanocrystalline fcc metals, Journal of the Mechanics and Physics of Solids. 52 (2004) 2587–2616. doi:10.1016/j.jmps.2004.04.006.
[112] Y. Ivanisenko, W. Skrotzki, R. Chulist, T. Lippmann, L. Kurmanaeva, Texture development in a nanocrystalline Pd-Au alloy studied by synchrotron radiation, Scripta Materialia. 66 (2012) 131–134. doi:10.1016/j.scriptamat.2011.10.004.
[113] K.S. Kumar, S. Suresh, M.F. Chisholm, J.A. Horton, P. Wang, Deformation of electrodeposited nanocrystalline nickel, Acta Materialia. 51 (2003) 387–405. doi:10.1016/S1359-6454(02)00421-4.
[114] H. Hahn, P. Mondal, K.A. Padmanabhan, Plastic deformation of nanocrystalline materials, Nanostructured Materials. 9 (1997) 603–606. doi:10.1016/S0965-9773(97)00135-9.
[115] J. Markmann, P. Bunzel, H. Rösner, K.W. Liu, K.A. Padmanabhan, R. Birringer, H. Gleiter, J. Weissmüller, Microstructure evolution during rolling of inert-gas condensed palladium, Scripta Materialia. 49 (2003) 637–644. doi:10.1016/S1359-6462(03)00401-9.
[116] D. V. Bachurin, P. Gumbsch, Accommodation processes during deformation of nanocrystalline palladium, Acta Materialia. 58 (2010) 5491–5501. doi:10.1016/j.actamat.2010.06.026.
[117] Y. Ivanisenko, N.A. Enikeev, K. Yang, A. Smoliakov, V.P. Soloviev, H. Fecht, H. Hahn, Contribution of grain boundary related strain accommodation to deformation of ultrafine-grained palladium, Materials Science and Engineering A. 668 (2016) 255–262. doi:10.1016/j.msea.2016.05.036.
[118] A. Vuppuluri, Theory and simulation of microstructure evolution due to simultaneous grain boundary migration and grain rotation with misorientation dependent energy and mobility, Materials Science and Engineering A. 713 (2018) 118–124. doi:10.1016/j.msea.2017.12.031.
[119] L. Wang, T. Xin, D. Kong, X. Shu, Y. Chen, H. Zhou, J. Teng, Z. Zhang, J. Zou, X. Han, In situ observation of stress induced grain boundary migration in nanocrystalline gold, Scripta Materialia. 134 (2017) 95–99. doi:10.1016/j.scriptamat.2017.03.003.
[120] D.S. Gianola, D.H. Warner, J.F. Molinari, K.J. Hemker, Increased strain rate sensitivity due to stress-coupled grain growth in nanocrystalline Al, Scripta Materialia. 55 (2006) 649–652. doi:10.1016/j.scriptamat.2006.06.002.
[121] Z.T. Trautt, Y. Mishin, Grain boundary migration and grain rotation studied by molecular dynamics, Acta Materialia. 60 (2012) 2407–2424. doi:10.1016/j.actamat.2012.01.008.
[122] P.F. Rottmann, K.J. Hemker, Experimental quantification of mechanically induced boundary migration in nanocrystalline copper films, Acta Materialia. 140 (2017) 46–55. doi:10.1016/j.actamat.2017.08.022.
[123] M. Legros, D.S. Gianola, K.J. Hemker, In situ TEM observations of fast grain-boundary motion in stressed nanocrystalline aluminum films, Acta Materialia. 56 (2008) 3380–3393. doi:10.1016/j.actamat.2008.03.032.
[124] A.J. Haslam, S.R. Phillpot, D. Wolf, D. Moldovan, H. Gleiter, Mechanisms of grain growth in nanocrystalline fcc metals by molecular-dynamics simulation, Materials Science and Engineering A. 318 (2001) 293–312. doi:10.1016/S0921-5093(01)01266-7.
[125] I.A. Ovid'ko, A.G. Sheinerman, Free surface effects on stress-driven grain boundary sliding and migration processes in nanocrystalline materials, Acta Materialia. 121 (2016) 117–125. doi:10.1016/j.actamat.2016.08.082.
[126] A. Hasnaoui, H. Van Swygenhoven, P.M. Derlet, Cooperative processes during plastic deformation in nanocrystalline fcc metals: A molecular dynamics simulation, Physical Review B - Condensed Matter and Materials Physics. 66 (2002) 1–8. doi:10.1103/PhysRevB.66.184112.
[127] V. Yamakov, D. Wolf, S.R. Phillpot, H. Gleiter, Grain-boundary diffusion creep in nanocrystalline palladium by molecular-dynamics simulation, Acta Materialia. 50 (2002) 61–73. doi:10.1016/S1359-6454(01)00329-9.
[128] A.J. Haslam, D. Moldovan, V. Yamakov, D. Wolf, S.R. Phillpot, H. Gleiter, Stress-enhanced grain growth in a nanocrystalline material by molecular-dynamics simulation, Acta Materialia. 51 (2003) 2097–2112. doi:10.1016/S1359-6454(03)00011-9.

[129] A.H. Chokshi, A. Rosen, J. Karch, H. Gleiter, On the validity of the hall-petch relationship in nanocrystalline materials, Scripta Metallurgica. 23 (1989) 1679–1683. doi:10.1016/0036-9748(89)90342-6.
[130] T. Shimokawa, A. Nakatani, H. Kitagawa, Grain-size dependence of the relationship between intergranular and intragranular deformation of nanocrystalline Al by molecular dynamics simulations, Physical Review B - Condensed Matter and Materials Physics. 71 (2005) 1–8. doi:10.1103/PhysRevB.71.224110.
[131] L. Wang, J. Teng, P. Liu, A. Hirata, E. Ma, Z. Zhang, M. Chen, X. Han, Grain rotation mediated by grain boundary dislocations in nanocrystalline platinum, Nature Communications. 5 (2014) 4402. doi:10.1038/ncomms5402.
[132] P. Liu, S.C. Mao, L.H. Wang, X.D. Han, Z. Zhang, Direct dynamic atomic mechanisms of strain-induced grain rotation in nanocrystalline, textured, columnar-structured thin gold films, Scripta Materialia. 64 (2011) 343–346. doi:10.1016/j.scriptamat.2010.10.029.
[133] M. Ke, S.A. Hackney, W.W. Milligan, E.C. Aifantis, Observation and measurement of grain rotation and plastic strain in nanostructured metal thin films, Nanostructured Materials. 5 (1995) 689–697. doi:10.1016/0965-9773(95)00281-I.
[134] Y.B. Wang, B.Q. Li, M.L. Sui, S.X. Mao, Deformation-induced grain rotation and growth in nanocrystalline Ni, Applied Physics Letters. 92 (2008) 2006–2009. doi:10.1063/1.2828699.
[135] A. Kobler, C. Brandl, H. Hahn, C. Kübel, In situ observation of deformation processes in nanocrystalline face-centered cubic metals, Beilstein Journal of Nanotechnology. 7 (2016) 572–580. doi:10.3762/bjnano.7.50.
[136] D. Jang, J.R. Greer, Size-induced weakening and grain boundary-assisted deformation in 60 nm grained Ni nanopillars, Scripta Materialia. 64 (2011) 77–80. doi:10.1016/j.scriptamat.2010.09.010.
[137] F. Mompiou, M. Legros, A. Boé, M. Coulombier, J.P. Raskin, T. Pardoen, Inter- and intragranular plasticity mechanisms in ultrafine-grained Al thin films: An in situ TEM study, Acta Materialia. 61 (2013) 205–216. doi:10.1016/j.actamat.2012.09.051.
[138] H. Van Swygenhoven, P.M. Derlet, A. Hasnaoui, Atomistic modeling of strength of nanocrystalline metals, Advanced Engineering Materials. 5 (2003) 345–350. doi:10.1002/adem.200310080.
[139] V. Yamakov, D. Wolf, S.R. Phillpot, A.K. Mukherjee, H. Gleiter, Deformation-mechanism map for nanocrystalline metals by molecular-dynamics simulation, Nature Materials. 3 (2004) 43–47. doi:10.1038/nmat1035.
[140] X.Z. Liao, F. Zhou, E.J. Lavernia, S.G. Srinivasan, M.I. Baskes, D.W. He, Y.T. Zhu, Deformation mechanism in nanocrystalline Al: Partial dislocation slip, Applied Physics Letters. 83 (2003) 632–634. doi:10.1063/1.1594836.
[141] L. Fu, C. Yang, R. Wei, X. Pei, J. Teng, D. Kong, Y. Lu, Y. Guo, T. Liu, Y. Hu, B. Yin, Z. Zhang, A. Li, L. Wang, X. Han, In Situ Atomic-scale Observation of AuCu Alloy Nanowire with Superplasticity and High Strength at Room Temperature, Materials Today Nano. (2021) 100123. doi:10.1016/j.mtnano.2021.100123.
[142] H. Van Swygenhoven, M. Spaczer, A. Caro, Microscopic description of plasticity in computer generated metallic nanophase samples: A comparison between Cu and Ni, Acta Materialia. 47 (1999) 3117–3126. doi:10.1016/S1359-6454(99)00109-3.
[143] X.K. Guo, Z.P. Luo, X.Y. Li, K. Lu, Plastic deformation induced extremely fine nano-grains in nickel, Materials Science and Engineering A. 802 (2021) 140664. doi:10.1016/j.msea.2020.140664.
[144] D. Farkas, M. Spaczer, Competing plastic deformation mechanisms in nanophase metals, Physical Review B - Condensed Matter and Materials Physics. 60 (1999) 22–25. doi:10.1103/PhysRevB.60.22.
[145] Z. Shan, E.A. Stach, J.M.K. Wiezorek, J.A. Knapp, D.M. Follstaedt, S.X. Mao, Grain boundary-mediated plasticity in nanocrystalline nickel, Science (New York, N.Y.). 305 (2004) 654–657. doi:10.1126/science.1098741.
[146] K. Yang, H.J. Fecht, Y. Ivanisenko, First direct in situ observation of grain boundary sliding in ultrafine grained noble metal, Advanced Engineering Materials. 16 (2014) 517–521. doi:10.1002/adem.201300413.
[147] Y.L. Yang, N. Jia, Y.D. Wang, Y.F. Shen, H. Choo, P.K. Liaw, Simulations of texture evolution in heavily deformed bulk nanocrystalline nickel, Materials Science and Engineering A. 493 (2008) 86–92.

doi:10.1016/j.msea.2007.11.083.
[148] F. Mompiou, M. Legros, Quantitative grain growth and rotation probed by in-situ TEM straining and orientation mapping in small grained Al thin films, Scripta Materialia. 99 (2015) 5–8. doi:10.1016/j.scriptamat.2014.11.004.
[149] K. Holmberg, A. Matthews, H. Ronkainen, Coatings tribology - Contact mechanisms and surface design, Tribology International. 31 (1998) 107–120. doi:10.1016/S0301-679X(98)00013-9.
[150] H.M. Zbib, C.T. Overman, F. Akasheh, D. Bahr, Analysis of plastic deformation in nanoscale metallic multilayers with coherent and incoherent interfaces, International Journal of Plasticity. 27 (2011) 1618–1639. doi:10.1016/j.ijplas.2011.03.006.
[151] J. Wang, A. Misra, An overview of interface-dominated deformation mechanisms in metallic multilayers, Current Opinion in Solid State and Materials Science. 15 (2011) 20–28. doi:10.1016/j.cossms.2010.09.002.
[152] L. Nan, J. Wang, A. Misra, J.Y. Huang, Direct observations of confined layer slip in Cu/Nb multilayers, Microscopy and Microanalysis. 18 (2012) 1155–1162. doi:10.1017/S143192761200133X.
[153] K. Yu-Zhang, J.D. Embury, K. Han, A. Misra, Transmission electron microscopy investigation of the atomic structure of interfaces in nanoscale Cu-Nb multilayers, Philosophical Magazine. 88 (2008) 2559–2567. doi:10.1080/14786430802380485.
[154] A. Misra, M. Verdier, Y.C. Lu, H. Kung, T.E. Mitchell, M. Nastasi, J.D. Embury, Structure and mechanical properties of Cu-X (X = Nb,Cr,Ni) nanolayered composites, Scripta Materialia. 39 (1998) 555–560. doi:10.1016/S1359-6462(98)00196-1.
[155] Y. Liu, D. Bufford, H. Wang, C. Sun, X. Zhang, Mechanical properties of highly textured Cu/Ni multilayers, Acta Materialia. 59 (2011) 1924–1933. doi:10.1016/j.actamat.2010.11.057.
[156] R.G. Hoagland, R.J. Kurtz, C.H. Henager, Slip resistance of interfaces and the strength of metallic multilayer composites, Scripta Materialia. 50 (2004) 775–779. doi:10.1016/j.scriptamat.2003.11.059.
[157] J.Y. Zhang, X. Zhang, G. Liu, G.J. Zhang, J. Sun, Scaling of the ductility with yield strength in nanostructured Cu/Cr multilayer films, Scripta Materialia. 63 (2010) 101–104. doi:10.1016/j.scriptamat.2010.03.024.
[158] M.A. Phillips, B.M. Clemens, W.D. Nix, A model for dislocation behavior during deformation of Al/Al3Sc (fcc/L12) metallic multilayers, Acta Materialia. 51 (2003) 3157–3170. doi:10.1016/S1359-6454(03)00127-7.
[159] J.Y. Zhang, X. Zhang, R.H. Wang, S.Y. Lei, P. Zhang, J.J. Niu, G. Liu, G.J. Zhang, J. Sun, Length-scale-dependent deformation and fracture behavior of Cu/X (X = Nb, Zr) multilayers: The constraining effects of the ductile phase on the brittle phase, Acta Materialia. 59 (2011) 7368–7379. doi:10.1016/j.actamat.2011.08.016.
[160] S. Shao, S.N. Medyanik, Dislocation-interface interaction in nanoscale fcc metallic bilayers, Mechanics Research Communications. 37 (2010) 315–319. doi:10.1016/j.mechrescom.2010.03.007.
[161] J. Wang, R.G. Hoagland, A. Misra, Mechanics of nanoscale metallic multilayers: From atomic-scale to micro-scale, Scripta Materialia. 60 (2009) 1067–1072. doi:10.1016/j.scriptamat.2008.11.035.
[162] J. Wang, R.G. Hoagland, J.P. Hirth, A. Misra, Atomistic modeling of the interaction of glide dislocations with “weak” interfaces, Acta Materialia. 56 (2008) 5685–5693. doi:10.1016/j.actamat.2008.07.041.
[163] A. Misra, J.P. Hirth, R.G. Hoagland, Length-scale-dependent deformation mechanisms in incoherent metallic multilayered composites, Acta Materialia. 53 (2005) 4817–4824. doi:10.1016/j.actamat.2005.06.025.
[164] J. Wang, I.J. Beyerlein, N.A. Mara, D. Bhattacharyya, Interface-facilitated deformation twinning in copper within submicron Ag-Cu multilayered composites, Scripta Materialia. 64 (2011) 1083–1086. doi:10.1016/j.scriptamat.2011.02.025.
[165] S.J. Zheng, J. Wang, J.S. Carpenter, W.M. Mook, P.O. Dickerson, N.A. Mara, I.J. Beyerlein, Plastic instability mechanisms in bimetallic nanolayered composites, Acta Materialia. 79 (2014) 282–291. doi:10.1016/j.actamat.2014.07.017.
[166] J.A. Thornton, High Rate Thick Film Growth., Annual Review of Materials Science. 7 (1977) 239–260. doi:10.1146/annurev.ms.07.080177.001323.
[167] P.J. Kelly, R.D. Arnell, Magnetron sputtering: A review of recent developments and applications,

Vacuum. 56 (2000) 159–172. doi:10.1016/S0042-207X(99)00189-X.
[168] G. Bräuer, B. Szyszka, M. Vergöhl, R. Bandorf, Magnetron sputtering - Milestones of 30 years, in: Vacuum, Elsevier Ltd, 2010: pp. 1354–1359. doi:10.1016/j.vacuum.2009.12.014.
[169] J.A. Thornton, Influence of Apparatus Geometry and Deposition Conditions on the Structure and Topography of Thick Sputtered Coatings., J Vac Sci Technol. 11 (1974) 666–670. doi:10.1116/1.1312732.
[170] A.J. Detor, A.M. Hodge, E. Chason, Y. Wang, H. Xu, M. Conyers, A. Nikroo, A. Hamza, Stress and microstructure evolution in thick sputtered films, Acta Materialia. 57 (2009) 2055–2065. doi:10.1016/j.actamat.2008.12.042.
[171] M. Knoll, E. Ruska, Das Elektronenmikroskop, Zeitschrift Für Physik. 78 (1932) 318–339. doi:10.1055/s-0028-1122268.
[172] J. Goldstein, D. Newbury, D. Joy, L. Charles, P. Echlin, E. Lifshin, L. Sawyer, J. Michael, Scanning electron microscopy and X-ray microanalysis, Third, Kluwer Academic/Plenum Publishers, New York, 2003. doi:10.2307/3225926.
[173] D.B. Williams, C.B. Carter, Transmission Electron Microscopy, 2nd ed., Springer, 2009.
[174] L. Reimer, H. Kohl, Transmission Electron Microscopy: Physics of Image Formation, Fifth, Springer, 2008. doi:10.1007/978-0-387-34758-5.
[175] M. Sugiyama, G. Sigesato, A review of focused ion beam technology and its applications in transmission electron microscopy, Journal of Electron Microscopy. 53 (2004) 527–536. doi:10.1093/jmicro/dfh071.
[176] J. Li, The focused-ion-beam microscope - More than a precision ion milling machine, Jom. 58 (2006) 27–31. doi:10.1007/s11837-006-0156-z.
[177] J. Mayer, L.A. Giannuzzi, T. Kamino, J. Michael, TEM sample preparation and FIB-induced damage, MRS Bulletin. 32 (2007) 400–407. doi:10.1557/mrs2007.63.
[178] J.M. Zuo, J.C.H. Spence, Advanced Transmission Electron Microscopy, Springer Science New York, 2017. doi:10.1007/978-1-4939-6607-3.
[179] J. Biskupek, J. Leschner, P. Walther, U. Kaiser, Optimization of STEM tomography acquisition - A comparison of convergent beam and parallel beam STEM tomography, Ultramicroscopy. 110 (2010) 1231–1237. doi:10.1016/j.ultramic.2010.05.008.
[180] J. Loos, E. Sourty, K. Lu, B. Freitag, D. Tang, D. Wall, Electron tomography on micrometer-thick specimens with nanometer resolution, Nano Letters. 9 (2009) 1704–1708. doi:10.1021/nl900395g.
[181] J.M. Cowley, Electron nanodiffraction methods for measuring medium-range order, Ultramicroscopy. 90 (2002) 197–206. doi:10.1016/S0304-3991(01)00130-9.
[182] P.A. Midgley, M. Weyland, J. Meurig Thomas, B.F.G. Johnson, Z-contrast tomography: A technique in three-dimensional nanostructural analysis based on Rutherford scattering, Chemical Communications. (2001) 907–908. doi:10.1039/b101819c.
[183] W. McBride, D.J.H. Cockayne, D. Nguyen-Manh, Electron diffraction from nanovolumes of amorphous material using coherent convergent illumination, Ultramicroscopy. 96 (2003) 191–200. doi:10.1016/S0304-3991(03)00007-X.
[184] F. Uesugi, A. Hokazono, S. Takeno, Evaluation of two-dimensional strain distribution by STEM/NBD, Ultramicroscopy. 111 (2011) 995–998. doi:10.1016/j.ultramic.2011.01.035.
[185] D. Alloyeau, C. Ricolleau, T. Oikawa, C. Langlois, Y. Le Bouar, A. Loiseau, STEM nanodiffraction technique for structural analysis of CoPt nanoparticles, Ultramicroscopy. 108 (2008) 656–662. doi:10.1016/j.ultramic.2007.10.006.
[186] R. Vincent, P.A. Midgley, Double conical beam-rocking system for measurement of integrated electron diffraction intensities, Ultramicroscopy. 53 (1994) 271–282. doi:10.1016/0304-3991(94)90039-6.
[187] T.A. White, A.S. Eggeman, P.A. Midgley, Is precession electron diffraction kinematical? Part I: “Phase-scrambling” multislice simulations, Ultramicroscopy. 110 (2010) 763–770. doi:10.1016/j.ultramic.2009.10.013.
[188] J.S. Barnard, D.N. Johnstone, P.A. Midgley, High-resolution scanning precession electron diffraction: Alignment and spatial resolution, Ultramicroscopy. 174 (2017) 79–88. doi:10.1016/j.ultramic.2016.12.018.
[189] S. Zaefferer, A critical review of orientation microscopy in SEM and TEM, in: Crystal Research and Technology, 2011: pp. 607–628. doi:10.1002/crat.201100125.

[190] E.F. Rauch, J. Portillo, S. Nicolopoulos, D. Bultreys, S. Rouvimov, P. Moeck, Automated nanocrystal orientation and phase mapping in the transmission electron microscope on the basis of precession electron diffraction, Zeitschrift Fur Kristallographie. 225 (2010) 103–109. doi:10.1524/zkri.2010.1205.
[191] P. Moeck, S. Rouvimov, E.F. Rauch, M. Véron, H. Kirmse, I. Häusler, W. Neumann, D. Bultreys, Y. Maniette, S. Nicolopoulos, High spatial resolution semi-automatic crystallite orientation and phase mapping of nanocrystals in transmission electron microscopes, Crystal Research and Technology. 46 (2011) 589–606. doi:10.1002/crat.201000676.
[192] E.F. Rauch, M. Veron, Coupled microstructural observations and local texture measurements with an automated crystallographic orientation mapping tool attached to a tem, in: Materialwissenschaft Und Werkstofftechnik, 2005: pp. 552–556. doi:10.1002/mawe.200500923.
[193] E.F. Rauch, M. Véron, Automated crystal orientation and phase mapping in TEM, Materials Characterization. 98 (2014) 1–9. doi:10.1016/j.matchar.2014.08.010.
[194] AppFive, Topspin Calibration Manual, Version 2. (2015).
[195] J.S. Jones, P.R. Swann, Specimen heating holder for electron microscopes, 4,996,433, 1991.
[196] Gatan Inc., Heating In-Situ Holders, Media Library. (n.d.). www.gatan.com.
[197] S.H. Oh, M. Legros, D. Kiener, P. Gruber, G. Dehm, In situ TEM straining of single crystal Au films on polyimide: Change of deformation mechanisms at the nanoscale, Acta Materialia. 55 (2007) 5558–5571. doi:10.1016/j.actamat.2007.06.015.
[198] A. Kobler, A. Kashiwar, H. Hahn, C. Kübel, Combination of in situ straining and ACOM TEM: A novel method for analysis of plastic deformation of nanocrystalline metals, Ultramicroscopy. 128 (2013) 68–81. doi:10.1016/j.ultramic.2012.12.019.
[199] Y. Oh, E. Cyrankowski, Z. Shan, A. Syed Asif, Micro/Nano-mechanical test system employing tensile test holder with push-to-pull transformer, United States Patent US 8,434,370 B2, 2013.
[200] HYSITRON Inc., PI 95 TEM PicoIndenter User Manual, Revision 9 (2016).
[201] O. Engler, V. Randle, Introduction to texture analysis : macrotexture, microtexture, and orientation mapping, 2nd Editio, Taylor & Francis Group, 2010.
[202] H.-J. Bunge, P.R. Morris, Texture Analysis in Materials Science: Mathematical Methods, English Ed, Cuvilliar Verlag, Göttingen, 1993.
[203] E.F. Rauch, DiffGen, NanoMEGAS SPRL, www.nanomegas.com, (2016).
[204] E.F. Rauch, Index, NanoMEGAS SPRL, www.nanomegas.com, (2016).
[205] A. Kobler, A. Kashiwar, H. Hahn, C. Kübel, Combination of in situ straining and ACOM TEM: A novel method for analysis of plastic deformation of nanocrystalline metals, Ultramicroscopy. 128 (2013) 68–81. doi:10.1016/j.ultramic.2012.12.019.
[206] A. Kobler, C. Kübel, Challenges in quantitative crystallographic characterization of 3D thin films by ACOM-TEM, Ultramicroscopy. 173 (2017) 84–94. doi:10.1016/j.ultramic.2016.07.007.
[207] E.F. Rauch, Mapviewer, NanoMEGAS SPRL, www.nanomegas.com, (2016).
[208] E.F. Rauch, M. Veron, Solving the 180 Degree Orientation Ambiguity Related to Spot Diffraction Patterns in Transmission Electron Microscopy, Microscopy and Microanalysis. 19 (2013) 324–325. doi:10.1017/s1431927613003619.
[209] E. Rauch, A. Kiss, J. Labar, The use of Correlation Coefficient maps to enhance visibility of internal structure for nanocrystalline thin foils, in: European Microscopy Congress 2016: Proceedings, 2016. doi:10.1002/9783527808465.EMC2016.6564.
[210] Á.K. Kiss, E.F. Rauch, J.L. Lábár, Highlighting material structure with transmission electron diffraction correlation coefficient maps, Ultramicroscopy. 163 (2016) 31–37. doi:10.1016/j.ultramic.2016.01.006.
[211] F. Bachmann, R. Hielscher, H. Schaeben, Texture analysis with MTEX- Free and open source software toolbox, Solid State Phenomena. 160 (2010) 63–68. doi:10.4028/www.scientific.net/SSP.160.63.
[212] A. Kobler, Untersuchung von Deformationsmechanismen in nanostrukturierten Metallen und Legierungen mit Transmissionselektronenmikroskopie, TU Darmstadt, 2014.
[213] B. Beausir, J.J. Fundenberger, Analysis Tools for Electron and X-ray diffraction, ATEX - software, www.atex-software.eu, Université de Lorraine - Metz, (2017). doi:www.atex-software.eu.
[214] D. Mastronarde, R. Gaudette, S. Held, J. Kremer, Q. Xiong, J. Heumann, IMOD, (2017). doi:https://bio3d.colorado.edu/imod/index.html.

[215] J.F. Nye, Some geometrical relations in dislocated crystals, Acta Metallurgica. 1 (1953) 153–162. doi:https://doi.org/10.1016/0001-6160(53)90054-6.
[216] W. Pantleon, Resolving the geometrically necessary dislocation content by conventional electron backscattering diffraction, Scripta Materialia. 58 (2008) 994–997. doi:10.1016/j.scriptamat.2008.01.050.
[217] L.S. Toth, C.F. Gu, B. Beausir, J.J. Fundenberger, M. Hoffman, Geometrically necessary dislocations favor the Taylor uniform deformation mode in ultra-fine-grained polycrystals, Acta Materialia. 117 (2016) 35–42. doi:10.1016/j.actamat.2016.06.062.
[218] C.F. Gu, L.S. Tóth, B. Beausir, Modeling of large strain hardening during grain refinement, Scripta Materialia. 66 (2012) 250–253. doi:10.1016/j.scriptamat.2011.11.002.
[219] T. Malis, S.C. Cheng, R.F. Egerton, EELS log-ratio technique for specimen-thickness measurement in the TEM, Journal of Electron Microscopy Technique. 8 (1988) 193–200. doi:https://doi.org/10.1002/jemt.1060080206.
[220] K. Lakoubovskii, K. Mitsuishi, Y. Nakayama, K. Furuya, Mean free path of inelastic electron scattering in elemental solids and oxides using transmission electron microscopy: Atomic number dependent oscillatory behavior, Physical Review B - Condensed Matter and Materials Physics. 77 (n.d.). doi:https://doi.org/10.1103/PhysRevB.77.104102.
[221] P. Moeck, S. Rouvimov, E.F. Rauch, M. Véron, H. Kirmse, I. Häusler, W. Neumann, D. Bultreys, Y. Maniette, S. Nicolopoulos, High spatial resolution semi-automatic crystallite orientation and phase mapping of nanocrystals in transmission electron microscopes, in: Crystal Research and Technology, 2011: pp. 589–606. doi:10.1002/crat.201000676.
[222] A.C. Leff, C.R. Weinberger, M.L. Taheri, Estimation of dislocation density from precession electron diffraction data using the Nye tensor, Ultramicroscopy. 153 (2015) 9–21. doi:10.1016/j.ultramic.2015.02.002.
[223] T. Tsuru, Y. Aoyagi, Y. Kaji, T. Shimokawa, Heterogeneous plastic deformation and Bauschinger effect in ultrafine-grained metals: Atomistic simulations, Modelling and Simulation in Materials Science and Engineering. 24 (2016) 035010. doi:10.1088/0965-0393/24/3/035010.
[224] J. Oddershede, J.P. Wright, A. Beaudoin, G. Winther, Deformation-induced orientation spread in individual bulk grains of an interstitial-free steel, Acta Materialia. 85 (2015) 301–313. doi:10.1016/j.actamat.2014.11.038.
[225] L.S. Tóth, Y. Estrin, R. Lapovok, C. Gu, A model of grain fragmentation based on lattice curvature, Acta Materialia. 58 (2010) 1782–1794. doi:10.1016/j.actamat.2009.11.020.
[226] J. Luster, M.A. Morris, Compatibility of deformation in two-phase Ti-Al alloys: Dependence on microstructure and orientation relationships, Metallurgical and Materials Transactions A. 26 (1995) 1745–1756. doi:10.1007/BF02670762.
[227] Y.P. Li, X.F. Zhu, J. Tan, B. Wu, W. Wang, G.P. Zhang, Comparative investigation of strength and plastic instability in Cu/Au and Cu/Cr multilayers by indentation, Journal of Materials Research. 24 (2009) 728–735. doi:10.1557/jmr.2009.0092.
[228] Y.P. Li, G.P. Zhang, On plasticity and fracture of nanostructured Cu/X (X = Au, Cr) multilayers: The effects of length scale and interface/boundary, Acta Materialia. 58 (2010) 3877–3887. doi:10.1016/j.actamat.2010.03.042.
[229] Z.P. Luo, G.P. Zhang, R. Schwaiger, Microstructural vortex formation during cyclic sliding of Cu/Au multilayers, Scripta Materialia. 107 (2015) 67–70. doi:10.1016/j.scriptamat.2015.05.022.
[230] C. Greiner, Z. Liu, L. Strassberger, P. Gumbsch, Sequence of Stages in the Microstructure Evolution in Copper under Mild Reciprocating Tribological Loading, ACS Applied Materials and Interfaces. 8 (2016) 15809–15819. doi:10.1021/acsami.6b04035.
[231] C. Greiner, Z. Liu, R. Schneider, L. Pastewka, P. Gumbsch, The origin of surface microstructure evolution in sliding friction, Scripta Materialia. 153 (2018) 63–67. doi:https://doi.org/10.1016/j.scriptamat.2018.04.048.
[232] A.B. Parsa, M. Walter, W. Theisen, D. Bürger, G. Eggeler, On the evolution of dislocation cell structures in two Al-alloys (Al-5Mg and Al-11Zn) during reciprocal sliding wear at high homologous temperatures, Wear. 418–419 (2019) 1–12. doi:https://doi.org/10.1016/j.wear.2018.10.018.

[233] C. Haug, F. Ruebeling, A. Kashiwar, P. Gumbsch, C. Kübel, C. Greiner, Early deformation mechanisms in the shear affected region underneath a copper sliding contact, Nature Communications. 11 (2020). doi:10.1038/s41467-020-14640-2.
[234] J.P.H.& H.K. A. Misra, Single-dislocation-based strengthening mechanisms in nanoscale metallic multilayers Single-dislocation-based strengthening mechanisms in nanoscale metallic multilayers, Philosophical Magazine. 8610 (2002). doi:10.1080/0l4l86102.
[235] D.A. Rigney, S. Karthikeyan, The evolution of tribomaterial during sliding: A brief introduction, Tribology Letters. 39 (2010) 3–7. doi:10.1007/s11249-009-9498-3.
[236] J. Wang, N. Li, O. Anderoglu, X. Zhang, A. Misra, J.Y. Huang, J.P. Hirth, Detwinning mechanisms for growth twins in face-centered cubic metals, Acta Materialia. 58 (2010) 2262–2270. doi:10.1016/j.actamat.2009.12.013.
[237] M.Y. Gutkin, K.N. Mikaelyan, I.A. Ovid'ko, Grain growth and collective migration of grain boundaries during plastic deformation of nanocrystalline materials, Physics of the Solid State. 50 (2008) 1266–1279. doi:10.1134/S1063783408070135.
[238] M. Jin, A.M. Minor, E.A. Stach, J.W. Morris, Direct observation of deformation-induced grain growth during the nanoindentation of ultrafine-grained Al at room temperature, Acta Materialia. 52 (2004) 5381–5387. doi:10.1016/j.actamat.2004.07.044.
[239] Lord Kelvin, Hydrodynamics and General Dynamics, Mathematical and Physical Papers Vol. 4, Cambridge University Press, Cambridge, England, 1910, 1910.
[240] W.D. Smyth, J.N. Moum, Ocean mixing by Kelvin-Helmholtz instability, Oceanography. 25 (2012) 140–149. doi:10.5670/oceanog.2012.49.
[241] H. Luce, L. Kantha, M. Yabuki, H. Hashiguchi, Atmospheric Kelvin–Helmholtz billows captured by the MU radar, lidars and a fish-eye camera, Earth, Planets and Space. 70 (2018). doi:10.1186/s40623-018-0935-0.
[242] M. Pouryazdan, B.J.P. Kaus, A. Rack, A. Ershov, H. Hahn, Mixing instabilities during shearing of metals, Nature Communications. 8 (2017) 1–7. doi:10.1038/s41467-017-01879-5.
[243] R. Blaauwgeers, V.B. Eltsov, G. Eska, A.P. Finne, R.P. Haley, M. Krusius, J.J. Ruohio, L. Skrbek, G.E. Volovik, Shear Flow and Kelvin-Helmholtz Instability in Superfluids, Physical Review Letters. 89 (2002) 2–5. doi:10.1103/PhysRevLett.89.155301.
[244] H.L.F. von Helmholtz, Monatsberichte der königlichen Akademie der Wissenschaften zu Berlin vom April, 215 (1868).
[245] H.J. Kim, S. Karthikeyan, D. Rigney, A simulation study of the mixing, atomic flow and velocity profiles of crystalline materials during sliding, Wear. 267 (2009) 1130–1136. doi:10.1016/j.wear.2009.01.030.
[246] S.F. Pugh, XCII. Relations between the elastic moduli and the plastic properties of polycrystalline pure metals, The London, Edinburgh, and Dublin Philosophical Magazine and Journal of Science. 45 (1954) 823–843. doi:10.1080/14786440808520496.
[247] M.G. Hall, H.I. Aaronson, The fine structure f.c.c./b.c.c. boundaries in a Cu-0.3% Cr alloy, Acta Metallurgica. 34 (1986) 1409–1418. doi:https://doi.org/10.1016/0001-6160(86)90029-5.
[248] T.E. Mitchell, Y.C. Lu, A.J.G. Jr, M. Nastasi, H. Kung, Structure and Mechanical Properties of Copper/Niobium Multilayers, (n.d.) 1673–1676.
[249] J.K. Chen, D. Farkas, W.T. Reynolds, Atomistic simulation of an f.c.c./b.c.c. interface in Ni□Cr alloys, Acta Materialia. 45 (1997) 4415–4421. doi:https://doi.org/10.1016/S1359-6454(97)00159-6.
[250] A.J. Detor, C.A. Schuh, Grain boundary segregation, chemical ordering and stability of nanocrystalline alloys: Atomistic computer simulations in the Ni-W system, Acta Materialia. 55 (2007) 4221–4232. doi:10.1016/j.actamat.2007.03.024.
[251] J. Weissmüller, Alloy effects in nanostructures, Nanostructured Materials. 3 (1993) 261–272. doi:https://doi.org/10.1016/0965-9773(93)90088-S.
[252] J.C.M. Li, Mechanical grain growth in nanocrystalline copper, Physical Review Letters. 96 (2006) 2–5. doi:10.1103/PhysRevLett.96.215506.

Curriculum Vitae

Education and Research Experience

10.2020 – present	**Research Assistant** at Electron Microscopy for Materials Science Department of Physics, University of Antwerp, Belgium
10.2020 – present	**Research Assistant** at Institute of Mechanics, Materials and Civil Engineering Université catholique de Louvain, Belgium
07.2015 – 02.2022	**Ph.D.**, Materials Science, Technical University of Darmstadt, Germany
07.2015 – 09.2020	**Research Fellow** at Electron Microscopy and Spectroscopy Laboratory Institute of Nanotechnology, Karlsruhe Institute of Technology, Germany
08.2015 – 09.2015	**German Language Course (A2 waystage)**, did deutsch-institut Frankfurt, Germany
07.2014 – 04.2015	**Project Assistant** at Interdisciplinary Center for Energy Research Indian Institute of Science, Bangalore, India
08.2012 – 07.2014	**M.E.**, Materials Engineering, Indian Institute of Science, Bangalore, India
05.2012 – 06.2012	**Student Research Assistant** at Institute of Nanotechnology Karlsruhe Institute of Technology, Germany
07.2008 – 06.2012	**B.Tech.**, Metallurgical & Materials Engineering, Visvesvaraya National Institute of Technology, Nagpur, India
05.2011 – 07.2011	**Student Research Assistant** at Institute of Nanotechnology Karlsruhe Institute of Technology, Germany

Fellowships and Grants

01.08.2015 – 31.12.2019	Doctoral scholarship by German Academic Exchange Service (DAAD)
2018, 2019	Travel grants by German Society for Electron Microscopy (DGE)
01.08.2012 – 31.07.2014	Master's scholarship by Ministry of Human Resource Development (MHRD), Government of India

List of Publications

1. R. Shi, D. Choudhuri, **A. Kashiwar**, S. Dasari, Y. Wang, R. Banerjee, D. Banerjee, *α phase growth and branching in titanium alloys*, Philosophical Magazine 2021, 1–24.

2. **A. Kashiwar**, H. Hahn, C. Kübel, *In situ TEM observation of cooperative grain rotations and the Bauschinger effect in nanocrystalline palladium*, Nanomaterials 2021, 11, 432.

3. S. Gorji, **A. Kashiwar**, L.S. Mantha, R. Kruk, R. Witte, P. Marek, H. Hahn, C. Kübel, T. Scherer, *Nanowire facilitated transfer of sensitive TEM samples in a FIB*, Ultramicroscopy, 2020, 219, 113075.

4. C. Haug, F. Ruebeling, **A. Kashiwar**, P. Gumbsch, C. Kübel, C. Greiner, *Early deformation mechanisms in the shear affected region underneath a copper sliding contact*, Nature Communications, 2020, 11, 839.

5. L. Ahmels, **A. Kashiwar**, T. Scherer, C. Kübel, E. Bruder, *Grain growth mechanisms in ultrafine-grained steel: an electron backscatter diffraction and in situ TEM study*, Journal of Materials Science, 2019, 54, 10489–10505.

6. C.S. Tiwary, **A. Kashiwar**, S. Bhowmick, K.C. Hari Kumar, K. Chattopadhyay, D. Banerjee, *Engineering an ultrafine intermetallic eutectic ternary alloy for high strength and high temperature applications*, Scripta Materialia, 2018, 157, 67–71.

7. C. Kübel, A. Kobler, **A. Kashiwar**, H. Hahn, *Imaging the structural evolution in nanocrystalline metals during mechanical deformation*, Microscopy and Microanalysis, 2017, 23, 748–749.

8. S. Balachandran, **A. Kashiwar**, A. Choudhury, D. Banerjee, R. Shi, Y. Wang, *On variant distribution and coarsening behavior of the α phase in a metastable β titanium alloy*, Acta Materialia, 2016, 106, 374–387.

9. A. Kobler, J. Lohmiller, J. Schäfer, M. Kerber, A. Castrup, **A. Kashiwar**, P. Gruber, K. Albe, H. Hahn, C. Kübel, *Deformation-induced grain growth and twinning in nanocrystalline palladium thin films*, Beilstein Journal of Nanotechnology, 2013, 4, 554–566.

10. A. Kobler, **A. Kashiwar**, H. Hahn, C. Kübel, *Combination of in situ straining and ACOM TEM: A novel method for analysis of plastic deformation of nanocrystalline metals*, Ultramicroscopy, 2013, 128, 68–81.

11. **A. Kashiwar**, N. Phani Vennela, S.L. Kamath, R.K. Khatirkar, *Effect of solution annealing temperature on precipitation in 2205 duplex stainless steel*, Materials Characterization, 2012, 74, 55–63.

Conference Presentations

1. **A. Kashiwar**, C. Kübel, *Quantitative orientation and phase mapping of nanostructured materials in TEM: in situ and ex situ applications*, Workshop on Electrochemistry in Liquid TEM and on Orientation/Phase Mapping in Liquid, 27-29 May 2019, University of Picardy Jules Verne, Amiens, France.

2. **A. Kashiwar**, H. Hahn, C. Kübel, *In situ observation of grain rotation and the Bauschinger effect in nanocrystalline palladium thin films using ACOM-STEM*, 2019 MRS Spring Meeting & Exhibit, 22-26 April 2019, Phoenix, Arizona, USA.

3. **A. Kashiwar**, H. Hahn, C. Kübel, *In situ cyclic deformation studies on nanocrystalline Pd thin films using ACOM-TEM*, NANO 2018, 24-29 June 2018, Hong Kong.

4. **A. Kashiwar**, H. Hahn, C. Kübel, *In situ thermal and mechanical studies using quantitative orientation mapping in TEM*, HGI–INT International Training Workshop on Nanostructured Materials, 19-22 June 2018, Nanjing, China.

5. **A. Kashiwar**, A. Kobler, H. Hahn, C. Kübel, *Imaging structural evolution in nanocrystalline metals during mechanical deformation*, EMMC16, 26-28 March 2018, Nantes, France.

6. **A. Kashiwar**, A. Kobler, H. Hahn, C. Kübel, *In situ TEM imaging and quantitative orientation mapping of the structural evolution in nanocrystalline metals during mechanical deformation*, TMS 2018, 11-15 March 2018, Phoenix, Arizona, USA.

7. **A. Kashiwar**, L. Morsdorf, A. Kobler, H. Hahn, C. Kübel, C. Cem Tasan, *Observation of nano-scaled carbide precipitation in low carbon lath martensite by in situ TEM heating coupled with ACOM-STEM*, ICEAM 2017, 10-12 October 2017, Erlangen, Germany.

8. **A. Kashiwar**, L. Morsdorf, A. Kobler, H. Hahn, C. Kübel, C. Cem Tasan, *In situ TEM heating in combination with ACOM-STEM to follow the precipitation of nano-scaled carbides in lath martensite*, EUROMAT 2017, 17-22 September 2017, Thessaloniki, Greece.

9. **A. Kashiwar**, Z.P. Luo, X. Mu, H. Hahn, C. Kübel, R. Schwaiger, *Deformation behavior in multilayered thin films with different interface structures under sliding contact*, EUROMAT 2017, 17-22 September 2017, Thessaloniki, Greece.

10. **A. Kashiwar**, Z.P. Luo, X. Mu, H. Hahn, C. Kübel, R. Schwaiger, *Microstructural evolution in multilayered thin films with different interface structure under sliding contact*, DPG Spring Meeting, 19-24 March 2017, Dresden, Germany.

11. **A. Kashiwar**, *Electron Microscopy in Materials Science*, DAAD Scholarship Holder's Meeting, 1-3 April 2016, Munich, Germany.

Thesis Declaration

I have included a list of all references used in my doctoral thesis. I hereby declare that I have, with the exception of the help that has been clearly mentioned in the thesis, completed this work on my own.

Antwerp, 23.02.2022

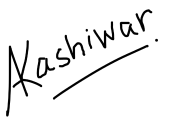

Place, Date

Ankush Kashiwar